



Delft University of Technology

## Development of a high-performing spectropolarimeter for space usage

Mr. Vasilescu, B.V.

### DOI

[10.4233/uuid:17d27e45-9625-400d-b25a-ad13c3b6a6d0](https://doi.org/10.4233/uuid:17d27e45-9625-400d-b25a-ad13c3b6a6d0)

### Publication date

2025

### Document Version

Final published version

### Citation (APA)

Mr. Vasilescu, B. V. (2025). *Development of a high-performing spectropolarimeter for space usage*. [Dissertation (TU Delft), Delft University of Technology]. <https://doi.org/10.4233/uuid:17d27e45-9625-400d-b25a-ad13c3b6a6d0>

### Important note

To cite this publication, please use the final published version (if applicable). Please check the document version above.

### Copyright

Other than for strictly personal use, it is not permitted to download, forward or distribute the text or part of it, without the consent of the author(s) and/or copyright holder(s), unless the work is under an open content license such as Creative Commons.

### Takedown policy

Please contact us and provide details if you believe this document breaches copyrights. We will remove access to the work immediately and investigate your claim.

# **DEVELOPMENT OF A HIGH-PERFORMING SPECTROPOLARIMETER FOR SPACE USAGE**



# **DEVELOPMENT OF A HIGH-PERFORMING SPECTROPOLARIMETER FOR SPACE USAGE**

## **Dissertation**

for the purpose of obtaining the degree of doctor  
at Delft University of Technology  
by the authority of the Rector Magnificus, prof. dr. ir. T.H.J.J. van der Hagen,  
chair of the Board for Doctorates  
to be defended publicly on  
Wednesday 7, May 2025, at 10:00 o'clock

by

**Bogdan VASILESCU**

Master in Space Sciences, University of Liège, Belgium  
born in Craiova, Romania

This dissertation has been approved by the promotor:

promotor: Prof. Dr. J. D. Loicq

promotor: Prof. Dr. Ir. P. N. A. M. Visser

copromotor: Asst. Prof. Dr. P. Piron

Composition of the doctoral committee:

Rector Magnificus,	chairperson
Prof. Dr. J. D. Loicq,	Delft University of Technology, <i>promotor</i>
Prof. Dr. Ir. P. N. A. M. Visser,	Delft University of Technology, <i>promotor</i>
Asst. Prof. Dr. P. Piron,	Delft University of Technology, <i>copromotor</i>

*Independent members:*

Prof. Dr. B. Vermeersen	Delft University of Technology
Prof. Dr. B. Brandl	Leiden University
Asst. Prof. Dr. A. Menicucci	Delft University of Technology
Dr. C. Neiner	Observatoire de Paris



*Keywords:* polarization, polarimetry, spectropolarimetry, imaging spectropolarimetry, Stokes polarimetry, Mueller calculus, polarimetric modulation, modulation matrix, birefringence

*Printed by:* Proefschriftspecialist

*Cover image:* Shutterstock.com

*Cover design:* <http://www.mihavladguta.eu>

Copyright © 2024 by B. Vasilescu

ISBN 978-94-6384-738-4

An electronic copy of this dissertation is available at  
<https://repository.tudelft.nl/>.

*If light is man's most useful tool, polarized light is the quintessence of utility.*

W. A. Shurcliff



# CONTENTS

<b>Summary</b>	<b>xi</b>
<b>Samenvatting</b>	<b>xv</b>
<b>Nomenclature</b>	<b>xix</b>
<b>Introduction</b>	<b>xxi</b>
<b>I Part I</b>	<b>xxv</b>
<b>1 Polarizing processes and the polarization usage</b>	<b>1</b>
1.1 Sources of polarization	2
1.1.1 Rayleigh scattering	2
1.1.2 Thomson scattering	4
1.1.3 Mie scattering	4
1.1.4 Zeeman effect	5
1.1.5 Hanle effect	7
1.2 Polarization in astronomy	7
1.3 Other applications	9
<b>2 Description of polarization</b>	<b>15</b>
2.1 The polarization of light	16
2.1.1 The Poincaré representation	18
2.2 Birefringent materials	22
2.3 Mueller calculus	26
2.3.1 Physical interpretation of the Mueller matrix	27
2.3.2 Mueller matrices of ideal components	28
2.3.3 Measuring the Mueller matrix of an arbitrary element	29
2.4 Fresnel terms	32
<b>3 Methods for the measurement of polarization</b>	<b>37</b>
3.1 Measuring the polarization	38
3.2 The assessment of the modulation scheme	41
3.2.1 The concept of efficiency of the modulation	41
3.2.2 Condition number and Equally weighted variance	45
3.3 Examples of instruments	50
3.3.1 DOAP spectropolarimeter	51
3.3.2 SFSIP imaging spectropolarimeter	53
3.4 Spectropolarimetry and imaging spectropolarimetry	55
3.4.1 Integral Field Spectrometry with Lenslet array (IFS-L)	56
3.4.2 Integral Field Spectrometry with Slicing Mirrors (IFS-M)	57



3.5	Polarimetry with metasurfaces . . . . .	58
<b>4</b>	<b>A new design of spectropolarimeter</b>	<b>63</b>
4.1	The starting point. . . . .	64
4.2	Towards a compact structure . . . . .	67
4.3	The working principle. . . . .	74
4.4	Retrieving the polarization of the incoming light . . . . .	78
4.5	Sampling criteria . . . . .	89
4.6	Towards Imaging Spectropolarimetry. . . . .	91
<b>5</b>	<b>The uniqueness of the solution and the behavior in noisy conditions</b>	<b>97</b>
5.1	The uniqueness of the solution: the rank of the modulation matrix. . . . .	100
5.2	The uniqueness of the solution: the Wronskian of the modulation functions . . . . .	101
5.3	The orthogonality of the modulation functions . . . . .	120
5.4	Conclusion . . . . .	122
<b>6</b>	<b>The analysis of the modulation scheme</b>	<b>125</b>
<b>7</b>	<b>Optimal configurations</b>	<b>143</b>
7.1	Identifying the optimal configurations . . . . .	144
7.2	Conclusions. . . . .	149
<b>8</b>	<b>Preliminary confirmation of the concept</b>	<b>153</b>
8.1	Compatibility of the models. . . . .	154
8.2	Case study: the identification of space objects . . . . .	158
8.3	Conclusions. . . . .	162
<b>II</b>	<b>Part II</b>	<b>167</b>
<b>9</b>	<b>Instrumental setup and first light</b>	<b>169</b>
9.1	Fabrication of the modulator . . . . .	170
9.1.1	Experimental objectives and the basic optical setup . . . . .	175
9.2	Characterization of the source . . . . .	177
9.3	General procedure for the polarimetric part . . . . .	178
9.4	A step forward: TNO's implementation of the concept . . . . .	181
<b>10</b>	<b>Characterization of the modulator</b>	<b>183</b>
10.1	Method 1: The fit of the intensity ratio . . . . .	184
10.2	Method 2: The Mueller matrix decomposition . . . . .	187
10.3	Test of the method 1 . . . . .	190
10.4	Experimental results for Prims 1 . . . . .	191
10.5	Experimental results for Prims 3 . . . . .	195
10.6	Verification of the results . . . . .	196
10.7	Test for the Mueller matrix decomposition . . . . .	198
10.8	Mueller matrix decomposition: prism 1. . . . .	199
10.9	Characterization of the Modulator . . . . .	204

---

<b>11 Instrumental matrix determination</b>	<b>211</b>
11.1 Method I: Singular value decomposition . . . . .	213
11.2 Assessing the incoming Stokes vectors . . . . .	215
11.3 Method II: Opposed states of polarization . . . . .	224
<b>12 Conclusions and Perspectives</b>	<b>229</b>
12.1 Next steps . . . . .	233
<b>A Addendum</b>	<b>235</b>
A.1 Mueller calculus . . . . .	236
A.2 SPEX Spectropolarimeter . . . . .	239
A.3 Optical properties of Magnesium Fluoride . . . . .	242
A.4 Experimental setup: The main properties of the optical components . . . . .	246
<b>Acknowledgements</b>	<b>255</b>
<b>Curriculum Vitae</b>	<b>257</b>
<b>List of Publications</b>	<b>259</b>



# SUMMARY

The polarization of light has become a powerful tool for scientists in recent years, a key that opens countless doors to knowledge. Astronomy, climatology, chemistry, and medicine are only a few sectors turning toward this light feature to produce a finer description of the media they study.

Despite the growing number of applications that use the knowledge of polarization, measuring this property of light remains a problematic task placed on the shoulders of opticians. When it comes to measuring polarization in the space environment, where the operating conditions of optical instruments are among the harshest, the difficulty of producing reliable instruments is even greater.

Until now, the polarization measurement method has evolved in two directions: one that uses a static approach, with fixed optical elements occupying a rather significant volume, and a dynamic direction that uses rotating or variable optical elements. Both methods are bulky and risky when it comes to use in space. The volume occupied by such instruments, the large number of components, and the presence of rotating parts are very challenging considering space missions' ergonomic and safety constraints.

It is in this context that this research was initiated. The main goal was to find a method of measuring any type of polarization at different wavelengths that could be translated into reliable instruments for use in space.

The starting point of our quest was a solution proposed by William Sparks et al.<sup>1</sup> Employing several prisms from a birefringent material, this approach was promising for most of the space constraints: it was compact, robust, stable, and able to cover all polarization states instantly.

However, a solid scientific foundation for this way of accessing the polarization was still needed. In addition, because it was a general procedure, countless possibilities of implementing it could be foreseen. It was still unknown if some optical designs are better than others or if they must be avoided. After all, it was utterly unknown if this method could be implemented experimentally and if it could lead to good instruments with respect to the existing ones.

We embarked with curiosity and interest in the analysis of this idea. We wanted to see if it can be scientifically supported and if it can lead not only to robust and compact instruments but also to performant ones.

Five scientific questions guided this research:

1. Does the signal detected with an instrument using this method correspond to a single state of polarization?
2. How do potential instruments built according to this method behave in noisy conditions?

---

<sup>1</sup>W. Sparks et al., "Compact and robust method for full Stokes spectropolarimetry". In: Applied Optics 51, No. 22 (Aug. 1, 2012), p. 5495, doi: 10.1364/AO.54.007377

3. Which procedures can be applied to retrieve the polarization, and how reliable are they?
4. Can this method be experimentally implemented?
5. How can it be exploited in the future?

To answer these questions, a plan in four steps was implemented:

1. The first step was dedicated to the problem of the uniqueness of the solution. We searched to see if an univocal relation can be established between the detected signal and the type of polarization. Multiple equivalent proofs were brought to this question.
2. Once the possibility of an instrument using this method was established, it remained to be seen how well it would perform under real conditions when noise is also present. The analysis of behavior in noisy conditions also provides the first hints about the requirements that should be met to achieve robust instruments for complete polarization measurement.
3. Furthermore, the polarization retrieval based on this new method should use specific algorithms to demodulate the detected signal. These algorithms depend on the potential characteristics of the optical system: spectral resolution, number of pixels from the detector, etc. This thesis investigated how these factors influenced the measurement process and identified additional practical requirements for building high-performance instruments.
4. After the theoretical foundation of the project and the determination of the technical requirements for obtaining reliable instruments, the last step was taken: the experimental implementation of the project. The new device was tested to measure the polarization following a detailed experimental characterisation. It fully confirmed the expectations.

Overall, this thesis introduces a new method for measuring any type of polarization at various wavelengths. It describes the theoretical principle of this method and, with the help of a laboratory prototype, provides an experimental validation.

The advantages of this new polarization measurement method are significant. With its help, robust and compact instruments can be built, thus meeting the needs of the space domain.

Perhaps the most important advantage is versatility. It is a complete polarization determination method that can be transposed into different types of instruments (with or without wide spectral coverage, with or without imaging capabilities), always keeping its compact and robust character.

For this reason, the possible applications go beyond the space domain. Instruments built based on this method can be relatively easily assembled on ground-based astronomical telescopes, equip drones or be adapted for medical investigations.

The most important stage in the development of this new method of spectropolarimetry was completed through this thesis. However, there is still a long way to go.

The imaging working mode needs to be further developed. The demodulation procedures of the polarimetric information must be perfected, and for the different types of applications calibration methods must also be developed.



# SAMENVATTING

De polarisatie van licht is de afgelopen jaren een krachtig hulpmiddel geworden voor wetenschappers, een sleutel die talloze deuren naar kennis opent. Astronomie, klimatologie, scheikunde en geneeskunde zijn slechts enkele sectoren die zich tot deze lichteigenschap wenden om een fijnere beschrijving te produceren van de media die ze bestuderen.

Ondanks het groeiende aantal toepassingen dat gebruik maakt van de kennis van polarisatie, blijft het meten van deze eigenschap van licht een problematische taak die op de schouders van opticiens rust. Als het gaat om het meten van polarisatie in de ruimte, waar de omstandigheden van de optische instrumenten tot de zwaarste behoren, is het nog moeilijker om betrouwbare instrumenten te produceren.

Tot nu toe is de technologie om polarisatie te meten in twee richtingen ontwikkeld: een die gebruikmaakt van een statische methode, met vaste optische elementen die een groot volume innemen, en een dynamische richting die gebruikmaakt van roterende of variabele optische elementen. Beide methoden zijn omvangrijk en riskant als het gaat om gebruik in de ruimte. Het volume dat door dergelijke instrumenten wordt ingenomen, het grote aantal componenten en de aanwezigheid van roterende onderdelen vormen een grote uitdaging gezien de ergonomische en veiligheidsbeperkingen van ruimtemissies.

In deze context is dit onderzoek gestart. Het hoofddoel was om een methode te vinden om de polarisatie bij verschillende golflengten te meten, die vertaald kan worden naar betrouwbare instrumenten voor gebruik in de ruimte.

Het startpunt van onze zoektocht was een oplossing voorgesteld door William Sparks et al.<sup>2</sup>. Deze aanpak, waarbij gebruik werd gemaakt van meerdere prisma's van een dubbelbrekend materiaal, was veelbelovend voor de meeste beperkingen voor een instrument in de ruimte: het was compact, robuust, stabiel en in staat om direct alle polarisatietoestanden te dekken.

Er was echter nog steeds een solide wetenschappelijke basis nodig voor deze manier om de polarisatie te meten. Bovendien konden, omdat het een algemene procedure was, talloze mogelijkheden voor implementatie worden voorzien. Het was nog steeds onbekend of sommige optische ontwerpen die er gebruik van maakten beter waren dan andere of dat ze moesten worden vermeden. Het was immers volkomen onbekend of het experimenteel kon worden geïmplementeerd en of het kon leiden tot goede instrumenten in vergelijking met de bestaande methodes.

We zijn met nieuwsgierigheid en interesse begonnen aan de analyse van dit idee. We wilden zien of het wetenschappelijk onderbouwd kon worden en of het niet alleen tot robuuste en compacte instrumenten kon leiden, maar ook tot instrumenten met goede

---

<sup>2</sup>W. Sparks et al., "Compact and robust method for full Stokes spectropolarimetry". In: Applied Optics 51, nr. 22 (1 aug. 2012), p. 5495



prestaties. Vijf wetenschappelijke vragen vormden de leidraad voor dit onderzoek. Deze vragen zijn:

1. Komt het signaal dat met een instrument met deze methode wordt gedetecteerd overeen met één enkele polarisatietoestand?
2. Hoe gedragen potentiële instrumenten die volgens deze methode zijn gebouwd zich in lawaaiërië omstandigheden?
3. Welke procedures kunnen worden gebruikt om de polarisatie te meten en hoe betrouwbaar zijn ze?
4. Kan deze methode experimenteel worden geïmplementeerd?
5. Hoe kan deze in de toekomst worden benut?

Om deze vragen te beantwoorden, werd een plan in vier stappen geïmplementeerd:

1. De eerste stap was gewijd aan het probleem van de uniciteit van de oplossing. We onderzochten of er een eenduidige relatie kon worden vastgesteld tussen het gedetecteerde signaal en het type polarisatie. Er werden meerdere equivalente benwijzen voor deze vraag aangedragen.
2. Nadat de haalbaarheid van een instrument dat deze methode gebruikte was vastgesteld, moest nog worden afgewacht hoe goed het zou presteren onder reële omstandigheden wanneer er ook ruis aanwezig is. De analyse van gedrag in omstandigheden met veel ruis geeft ook de eerste hints over de vereisten waaraan moet worden voldaan om robuuste instrumenten te verkrijgen voor volledige polarisatiemeting.
3. Bovendien moet de polarisatie meting op basis van deze nieuwe methode specifieke algoritmen gebruiken om het gedetecteerde signaal te demoduleren. Deze algoritmen zijn afhankelijk van de potentiële kenmerken van het optische systeem: golflengte, spectrale resolutie, aantal pixels van de detector, enz. Dit proefschrift onderzocht hoe deze factoren het meetproces beïnvloedden en identificeerde aanvullende praktische vereisten voor het bouwen van hoogwaardige instrumenten.
4. Na de theoretische basis van het project en de bepaling van de technische vereisten voor het verkrijgen van betrouwbare instrumenten, werd de laatste stap gezet: de experimentele implementatie. Na een gedetailleerde experimentele karakterisering werd het nieuwe apparaat getest om de polarisatie te meten. Het bevestigde volledig de verwachtingen.

Over het geheel genomen brengt dit proefschrift een nieuwe methode aan het licht voor het meten van elk type polarisatie bij verschillende golflengten. Het beschrijft het theoretische principe van deze methode en biedt, met behulp van een laboratoriumprototype, een experimentele validatie. De voordelen van deze nieuwe polarisatiemeetmethode zijn aanzienlijk. Met behulp hiervan kunnen robuuste en uiterst compacte instrumenten worden gebouwd, die voldoen aan de behoeften van ruimtemissies.

Het belangrijkste voordeel is echter misschien wel de veelzijdigheid. Het is een complete polarisatiebepalingsmethode die kan worden omgezet in verschillende soorten instrumenten (met of zonder brede spectrale dekking, met of zonder beeldvormingsmogelijkheden), waarbij het altijd zijn compacte en robuuste karakter behoudt. Om deze reden gaan de mogelijke toepassingen verder dan het ruimtedomein. Instrumenten die op basis van deze methode zijn gebouwd, kunnen relatief eenvoudig worden gemonteerd op aardse astronomische telescopen, kunnen gemonteerd worden op drones of kunnen worden aangepast voor medisch onderzoek. De belangrijkste fase in de ontwikkeling van deze nieuwe methode van spectropolarimetrie werd voltooid met dit proefschrift. Er is echter nog een lange weg te gaan. De beeldvormingswerkmodus moet verder worden ontwikkeld. De demodulatieprocedures van de polarimetrische informatie moeten worden geperfectioneerd en voor de verschillende soorten toepassingen moeten ook kalibratiemethoden worden ontwikkeld.



# NOMENCLATURE

## ABBREVIATIONS

AoLP	Angle of linear polarization
DoCP	Degree of circular polarization
DoLP	Degree of linear polarization
DoP	Total degree of polarization
FoV	Field of view
QWP	Quarter-wave plate
HWP	Half-wave plate
WP	Wave plate
TNO	Netherlands Organisation for Applied Scientific Research
PSG	Polarization state generator
SNR	Signal to noise ratio

## SYMBOLS AND NOTATIONS

$\phi_x$	Phase of the component $\vec{E}_x$ of the electric field
$\phi_y$	Phase of the component $\vec{E}_y$ of the electric field
$\Delta\phi$	Phase difference between $\vec{E}_y$ and $\vec{E}_x$
$\phi_1$	Phase difference between $\vec{E}_y$ and $\vec{E}_x$ for the prism 1 of the modulator
$\phi_3$	Phase difference between $\vec{E}_y$ and $\vec{E}_x$ for the prism 3 of the modulator
$M$	Mueller matrix of an arbitrary optical element
$\vec{S}$	Stokes vector
$S_i$	Stokes parameters ( $i = 0, 1, 2, 3$ )
$W$	Modulation matrix
$W^{-1}$	Instrumental matrix
$\xi$	Apex angle prism 1
$\psi$	Apex angle prism 3
$\theta$	Orientation of the analyzer
$\lambda$	Wavelength
$d_0$	Additional thickness for the wedges
$h$	Height of the modulator
$n_e$	Extraordinary index of refraction
$n_o$	Ordinary index of refraction
$m, n, p$	Modulation functions
$N$	Number of pixels used to sample the signal

$LP_1$	First linear polarizer
$LP_2$	Second linear polarizer
$\Delta n$	Birefringence
$M_\Delta$	Mueller matrix of a depolarizer
$M_R$	Mueller matrix of a retarder
$M_D$	Mueller matrix of a diattenuator
$\vec{P}$	Polarizance vector
$\vec{D}_t$	Diattenuation vector
$\Delta$	Depolarization
$\sigma_R$	Cross-section Rayleigh scattering
$\sigma_T$	Cross-section Thomson scattering
$\vec{E}$	Electric field
$\vec{B}$	Magnetic field
$\psi_e$	Orientation of the polarization ellipse
$\chi_e$	Ellipticity of the polarization ellipse
$\xi_i$	Efficiency of the Stokes parameters ( $i = 0, 1, 2, 3$ )
$\xi_{tot}$	Total efficiency of the modulation scheme
$R_f$	Ratio of the intensities obtained with crossed and parallel polarizers
$\rho_{s,p}$	Fresnel terms for reflection
$\tau_{s,p}$	Fresnel terms for transmission
$\sigma_i$	Uncertainty on the Stokes parameters ( $i = 0, 1, 2, 3$ )
$Y_{min}$	Minimum sampling distance
$\Delta y_{max}$	Maximum pixel size
$m_{i,j}$	Terms of the normalized Mueller matrix ( $i, j = 0, 1, 2, 3$ )
$M_{i,j}$	Terms of the Mueller matrix ( $i, j = 0, 1, 2, 3$ )

# INTRODUCTION

Polarization is a property of light that can open countless doors for knowledge. In addition to the detection of light intensity, this property can tell much more about the medium interacting with the waves reaching us. Scientists have realized this potential since the formulation of the wave theory of light.

The use of light polarization has grown continuously since then and continues to grow.

Astronomy was among the first fields to benefit from the help of this optical phenomenon. A surge of polarimetric studies of celestial bodies marked the beginning of the 20th century. The Sun, the solar system's planets, and the asteroids underwent a polarimetric analysis. This helped us gather much more knowledge about them. Properties inaccessible otherwise, such as the intensity of the magnetic field, the concentration of specific elements, or the graininess of distant bodies, could be inferred. Based on such details, essential steps forward, like the Moon landing or the understanding of the Sun's activity, became possible.

However, the use of polarimetry was not limited to astronomy. Other fields gradually discovered its importance. Biology, chemistry, climate study, and medicine are some examples. Thus, polarimetry plays a critical role today in detecting and characterizing aerosols in the atmosphere, which are crucial in influencing the climate. In medicine, the contribution is also significant. Polarimetry has proven to be a powerful tool for near-instantaneous detection of cancer-affected tissues by reducing diagnostic times and precise localisation of the affection.

Despite this undeniable contribution to a better knowledge of the world around us, this branch of optics remains somewhat exotic. The main reason for this fact is the very manifestation of the polarization of light. Most often, polarization reaches us in small quantities: only a tiny part of the detected light shows a specific type of polarization. The rest has an entirely random polarimetric behavior. This brought high pressure on those trying to build devices to detect polarization. They had to find solutions to extract information about this small polarized part while reducing the impact of noise or the effect of polarization induced by the detecting instrument itself.

The challenges faced by opticians seeking new methods to improve polarization detection have grown with the needs of science and the expansion of fields of applicability. Thus, for instance, the use of polarimetry in space comes with significant constraints related to the structure and performance of the instrument. These instruments' compactness, rigidity, and thermal behavior are as important as their performance. They must occupy a small volume, withstand launch into space, perform optimally in that harsh environment, and not bring supplementary risks to the space mission. In addition, they must detect as many types of polarization as possible. Designing an instrument that satisfies all these constraints becomes a challenging task. This is probably the main reason why we do not have a spectropolarimeter able to cover any state of polarization and

operate in space.

Having space-based access to all types of polarization at different wavelengths can open the way to new approaches in astronomy or simplify the monitoring of various processes. For instance, in monitoring the Sun, simultaneous and instantaneous access to the polarization's linear and circular components can streamline the magnetic field's measurement. The same types of polarization, but doubled by a high sensitivity of the instrument, can be used to observe exoplanets directly. Polarization has long been theorized as a possible solution for detecting life on other planets. In addition, access to elliptical polarization over a large wavelength band can contribute to space monitoring activities by helping to characterise distant objects in orbit around the Earth.

Adding imaging capabilities to spectral and polarimetric detection could also be a big step forward. Processes and observations that require precise localization of spectral and polarimetric features can benefit from this. Cloud polarimetry and remote sensing are two possible fields that could benefit from such development.

Unfortunately, most of today's access to polarization procedures do not fully comply with the demands of the space sector. The main techniques use voluminous structures or risky elements that can bring supplementary risk and jeopardize the missions.

Our research is included in this context of the challenges in the space field and the need for excellent and complete polarimetric knowledge at various wavelengths. Starting from the fundamental constraints that must be satisfied by a polarimeter intended for use in space, we set out in search of a solution for these problems faced by polarimetry.

We identified a potential candidate for this solution in a method of complete spectropolarimetry proposed in 2012 by Sparks et al <sup>3</sup>. Using a compact structure without rotating elements, which could bring additional risks for a space mission, this approach seems to answer most of the requirements of the space field. The critical component was the polarization modulator. Imagined being built from three prisms of Magnesium Fluoride ( $\text{MgF}_2$ ), glued together in a compact optical part, this component was responsible for the capacity to detect any polarization. It was a novel optical design, an attractive proposal from an engineering point of view, but it still needed scientific proof. In this idea, we saw an instrument and a method for conceiving countless new spectropolarimeters, which can be easily tuned for various applications.

Our efforts have been directed then toward exploring this new method of accessing the polarization of light. In a certain way, it was an uncharted territory, a new method of spectropolarimetry. It required a continuous adaptation of the classical analysis methods, a constant interrogation about what is essential and what is less important, what is critical and what can be neglected. Five questions guided our research:

1. Does the signal detected with an instrument using this method correspond to a single state of polarization?
2. How do potential instruments built according to this method behave?
3. Which procedures can be used to retrieve the polarization, and how reliable are they?

---

<sup>3</sup>W. Sparks et al., "Compact and robust method for full Stokes spectropolarimetry". In: Applied Optics 51, No. 22 (Aug. 1, 2012), p. 5495

4. Could this method be experimentally implemented?
5. How can it be exploited in the future?

To answer these questions, this thesis was divided into two parts. The first part deals with the theoretical aspects of the research, while the second part closely follows the experimental testing of a prototype of the instrument. The theoretical approach is divided into eight chapters, while the experimental activities are detailed in three.

The first chapter reviews the primary uses of polarization, which were only briefly mentioned in this introduction. The second chapter is a foray into the formalism used to describe polarization. Stokes' formalism, Mueller's calculus, and the fundamental notions of birefringent media are introduced here. The third chapter deals with the issue of light polarization measurement. We detail the preferred methods developed over time and the figures of merit that allow an understanding of how polarization is measured in various conditions. Some examples of instruments are presented and compared at this point, along with their main characteristics.

In the fourth chapter of the first part, step by step, we describe the key component of the spectropolarimeter analyzed within this work, the modulator. The geometry, optical properties, polarimetric properties, and mode of operation are reviewed. Using numerical simulations, we show how different types of polarization can be determined with such a method based on the modulation it can generate at the light intensity level in a particular direction.

The main criteria such a concept must fulfil to become a reliable instrument are related to the modulation scheme's uniqueness and excellent noise mitigation. A special effort was dedicated to this analysis. The results, published in the *Journal of Astronomical Telescopes, Instruments, and Systems (JATIS)* <sup>4</sup>, indicate a unique character of the modulation scheme and the existence of optical configurations capable of ensuring almost ideal noise mitigation. All these discoveries are presented in the fifth chapter.

Despite being a static approach, where no movement or modification of the optical properties of the components is required to generate the modulation of intensity, parameters like the size of pixels, number of pixels, binning of pixels, or spectral resolution play a vital role in the reliability of the measurements. In chapter six, we discover how all these parameters influence the key figures that describe the modulation scheme. In their turn, these researches are the subject of an article published in *Optics Express* <sup>5</sup>.

One crucial question must be answered in preparation for the practical implementation of this new method for measuring polarization: how do we choose a design? This question is answered in chapter seven.

Before passing to the experimental activity, which benefited from the ample support of the Netherlands Organisation for Applied Scientific Research (TNO), a series of simulations were performed in parallel in Zemax and MATLAB. The compatibility of the results once again proved the reliability of the concept. This topic is covered in chapter eight.

---

<sup>4</sup>Bogdan Vasilescu, Yaël Nazè, Jérôme Loicq, "Solution uniqueness and noise impact in a static spectropolarimeter based on birefringent prisms for full Stokes parameter retrieval," *J. Astron. Telesc. Instrum. Syst.* 6(2), 028001 (2020), doi: 10.1117/1.JATIS.6.2.028001

<sup>5</sup>Bogdan Vasilescu, Pierre Piron, and Jérôme Loicq, "Performance analysis of a spectropolarimeter employing a continuous phase variation," *Opt. Express* 31, 21078-21092 (2023), doi: 10.1364/OE.487335



The second part of the thesis is dedicated to the experimental validation of the proposed concept. With the help of TNO, the central part of our instrument, the modulator, was procured.

Chapter nine presents the main components of the optical setup used throughout the different stages of the tests. The configurations for characterizing the modulator and its wedges are also offered here.

Being about optical elements produced from  $\text{MgF}_2$  and having a geometry of critical importance for the operation of the instrument, the first round of experiments aimed at characterizing the separate components of the modulator. A series of tests and new procedures have been developed to optically and geometrically characterize these optical prisms. Global characterization of the assembled modulator followed the separate characterization at several wavelengths from the visible spectrum. Due to the complex structure, traditional characterization methods have limited applicability. For this reason, new characterization procedures had to be developed, and their results are presented in chapter ten.

After analyzing the optical components of the modulator and the response under the incidence of different polarizations, the instrumental matrix of the spectropolarimeter was determined for a wavelength of 514 nm. Later, multiple demodulation tests of various types of elliptical polarizations were performed. All these tests proved to be a success. They demonstrated the instrument's ability to serve to determine any polarization in a single shot. The results of these last and crucial inquiries are presented in chapter 11.

The last chapter is dedicated to the conclusions. We present here the lessons learned, underlying what can be done differently, what should be improved, and what should be deepened to benefit from this concept fully. In addition, we explore briefly the future potential developments, like the imaging working mode, which can drastically enlarge the field of applicability for such a concept.

# I

## PART I



# 1

## POLARIZING PROCESSES AND THE POLARIZATION USAGE

*Everything excellent is as difficult as it is rare.*

B. Spinoza

## 1.1. SOURCES OF POLARIZATION

Polarization is a widespread phenomenon in nature. For the light described as an electromagnetic transverse wave, this property refers to the orientation of the electric field. It is a property that goes completely unnoticed by our eyes and most optical detectors. We need complex instruments to observe it. Wherever light encounters a dichroic or birefringent medium, is reflected or scattered, a total or partial polarization is also generated. Sometimes, light emission is characterized by a specific polarization, as in the Zeeman or Hanle effects (Crutcher and Kemball, 2019). However, these are much rarer phenomena, of particular interest to astronomers. From the point of view of the shape described by the vector associated with the electric field at a given location along the propagation path and during an interval of time, the polarization can be elliptical, circular, or linear. The next chapter will offer a deeper incursion into the formalism of polarization and a proper description of this property of light.

### 1.1.1. RAYLEIGH SCATTERING

Rayleigh scattering is probably the most widespread and well-theorized phenomenon. It refers to molecules' absorption and re-emission of light and has been theorized since 1899. Using a simplified representation of molecules as spherical dipoles, Rayleigh demonstrated that the intensity of light emitted by molecules depends on  $1/\lambda^4$ , where  $\lambda$  is the wavelength of the incident light. Simply put, short wavelengths are more strongly scattered than large wavelengths, whose medium is much more transparent. This is also why, in general, the color of the sky is blue (Bucholtz, 1995).

The Rayleigh scattering cross-section of the particles situated in the air is:

$$\sigma_R = \frac{8\pi}{3} \left( \frac{2\pi}{\lambda} \right)^4 \left( \frac{n^2 - 1}{n^2 + 1} \right)^2 r^2, \quad (1.1)$$

where  $\lambda$  is the wavelength of the incident beam,  $n$  is the refractive index of the spheres used to represent the molecules, and  $r$  is the radius of the spheres. The Rayleigh scattering does not explain only the variation of scattered light intensity with the wavelength. It also explains the appearance of certain types of polarization through this process. A simplified representation of the formation of different kinds of polarization is shown in Fig. 1.1. Therefore, let us consider the case of a non-polarized incident wave, which propagates from left to right along the  $Oz$  axis and meets a molecule located at the origin of the chosen reference system. The electric field components of the incident wave can be represented as two vibrations in orthogonal directions ( $Ox$  and  $Oy$ ) and of equal amplitude. The molecule's behavior under each action can be explained by considering the two orthogonal vibrations independently. Thus, the electric field of the light along the  $x$ -axis will cause an oscillation of the dipole in the same direction and light emission with the same frequency and wavelength as the incident light. However, the emission will occur in a plane perpendicular to the direction of oscillation of the electric field of the incoming light, i.e., in the  $yz$  plane (see components (1)) of the emission). On the other hand, the field component of the incident wave oscillating along the  $Oy$  line will determine an emission of the dipole in the  $(xz)$  plane in the form of component (2). Looking closely at the global result of this phenomenon of absorption and re-emission, we notice that the re-emitted light is completely linearly polarized in specific directions

to the direction of the incident light.

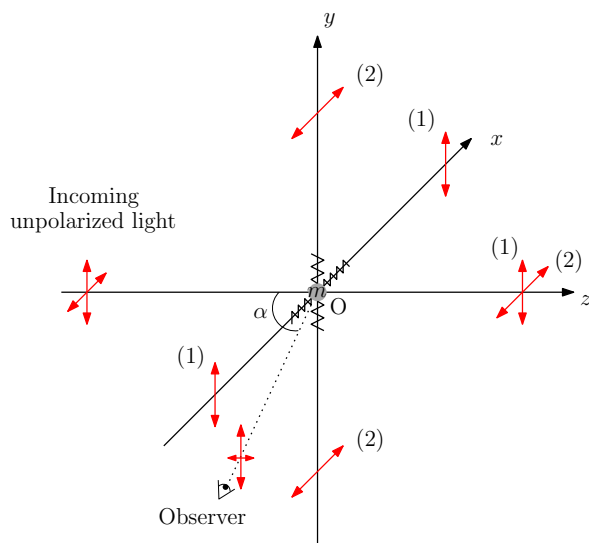


Figure 1.1: Schematic representation of the Rayleigh scattering

The degree of linear polarization, which is nothing else but the fraction of light being linearly polarized, varies like (Leroy, 2000):

$$P = \frac{\sin^2(\alpha)}{1 + \cos^2(\alpha)}, \quad (1.2)$$

where  $\alpha$  is the angle between the incident ray and the direction of observation. According to formula (1.2), an observer located at  $90^\circ$  about the direction of the incident light will be able to detect a complete linear polarization coming from the molecule. However, in practice, the degree of polarization that can be detected is generally lower. In fact, the light reaching the observer is not a single photon scattered by a single molecule but the cumulative effect of multiple scatterings on multiple molecules of many photons. Consequently, instead of a single angle  $\alpha$ , we have to associate the beam of light with various values for  $\alpha$ . This will result in a detected degree of polarization inferior to 1 for almost any observing conditions.

Combined with polarization, the photometric study of scattered light at different wavelengths and different angles can allow the characterization of molecules. The refractive index or the diameter of the molecules can thus be deduced.

Different types of polarization can be produced when the molecules' shape no longer corresponds to a sphere. Therefore, chiral molecules are known as a source of circular polarization when the incident light is non-polarized or linearly polarized (Gassó and Knobelspiesse, 2022). In addition, multiple scattering taking place before reaching the observer can also be a source of circular polarization (Slonaker et al., 2005).

### 1.1.2. THOMSON SCATTERING

When charged particles replace the molecule previously considered, and the wavelength of the scattered light is much greater than the Compton wavelength of the particle ( $\lambda_C = h/mc$ , where  $h$  is the Planck constant,  $m$  is the mass of the particle and  $c$  the speed of light), we speak of Thomson scattering. This follows the same principle as Rayleigh scattering, the only difference being that the cross-section is no longer related to the wavelength:

$$\sigma_T = \frac{8\pi}{3} r_e^2 \quad (1.3)$$

where  $r_e$  is the radius of the charged particle.

The difference is significant and widely used in astronomy. It allows, among others, to separate the polarization generated by the interstellar medium from the polarization of the light coming from the stars. In general, the polarization coming directly from the stars is produced by Thomson scattering and, therefore, independent of the wavelength. Therefore, by making observations at several wavelengths, the polarization produced by the interstellar medium can be separated from the polarization coming from the stars.

### 1.1.3. MIE SCATTERING

When the particles responsible for light scattering have a diameter smaller than  $0.1\lambda$ , the Rayleigh model accurately describes the phenomena and can predict the value of the intensity detected in different places. When the particles in question have a size greater than  $0.1\lambda$ , the Rayleigh approach can no longer provide correct values of the intensity of the diffused light. The Mie model must be used in this case.

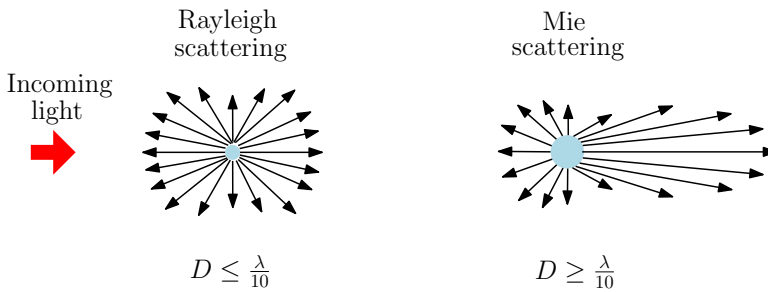


Figure 1.2: Intensity distribution for Rayleigh and Mie scattering. The diameter of particles ( $D$ ) determines the type of scattering.

In Mie scattering, the expression of the intensity becomes a sum of series with an infinite number of terms. This results from describing the interaction of electromagnetic radiation with the particle using the Maxwell equations (Born et al., 1999). Because of its complicated expression, the value of the scattered intensity is most often inferred using a numerical approach and well-established algorithms.

As with Rayleigh scattering, Mie scattering depends on the wavelength, particle shape parameters, and viewing angle. The near-spherical symmetry manifested in the case of Rayleigh scattering is no longer valid here. In Mie scattering, at least two asymmetric

lobes are present in the intensity pattern, with a maximum distribution in the direction of light propagation. As with Rayleigh scattering, the diffuse light is linearly polarized, with a degree of polarization depending on the scattering direction. However, in this case, the degree of polarization is also affected by the shape factor and the particle concentration. This is why the maximum degree of polarization is no longer located at  $90^\circ$  to the direction of light propagation and is less than 100%. In this way, Mie scattering becomes an excellent tool for estimating particle concentration and size.

It should be emphasized, however, that if both Rayleigh and Mie scattering refers only to linear polarization, this does not mean that only this type of polarization deserves attention. Circular and elliptical polarization can be equally detected following multiple scattering or pointed out in specific directions. The presence of molecules or organic substances, for instance, in the path of light, can, in turn, generate a circular polarization (Gassó and Knobelspiesse, 2022). For this reason, a complete determination of the polarization is necessary even when observing the scattering phenomenon (van der Laan et al., 2015).

#### 1.1.4. ZEEMAN EFFECT

The Zeeman effect is one of the most investigated phenomena in the spectropolarimetric study of stars and the interstellar medium. Starting from determining the linear and circular polarization components, this effect allows the measurement of the star's magnetic field projection in the plane of the sky or along the line of sight.

The Zeeman effect consists of splitting the spectral lines of an atom (in emission or absorption) in the presence of an intense magnetic field. The emitted light can be linearly or circularly polarized. The type of detected polarization provides a clear indication of the orientation of the magnetic field in which the atom is placed. A clear distinction between spectral lines is sometimes challenging in a weak magnetic field. For these situations, a spectropolarimeter can help to differentiate between the lines.

In its initial formulation, the Zeeman effect only considers the existence of the orbital angular momentum of the electron. As a result, the transition energy is split into  $m_l$  levels in the presence of a magnetic field, where:

$$m_l = -l, -l + 1, \dots, l - 1, l \quad , \quad (1.4)$$

in which  $l$  is the angular momentum number:

$$l = 0, 1, 2, \dots, n \quad , \quad (1.5)$$

where  $n$  is the principal quantum number.

When the electron's spin angular momentum is also considered, the transition energy will be split into  $m_j$  levels instead of  $m_l$ . For the case of the electron, of spin  $s = \pm \frac{1}{2}$ , we have:

$$\begin{cases} j = l \pm \frac{1}{2} \\ m_j = -j, -j + 1, \dots, j - 1, j \end{cases} \quad (1.6)$$

Therefore, according to the selection rules of transitions in the dipole approximation, we can have only  $\Delta m_j = 0, \pm 1$ .



- $\Delta m_j = 0$  ( $\pi$  transition): in a transverse view (perpendicular to  $\vec{B}$ ) the emitted radiation is linearly polarized in a direction parallel to  $\vec{B}$ ; in a longitudinal view (parallel to  $\vec{B}$ ) the transition is forbidden.
- $\Delta m_j = \pm 1$  ( $\sigma$  transition): in a transverse view, the emitted radiation is linearly polarized in a plane perpendicular to the field; in a longitudinal view, the polarization is circular.

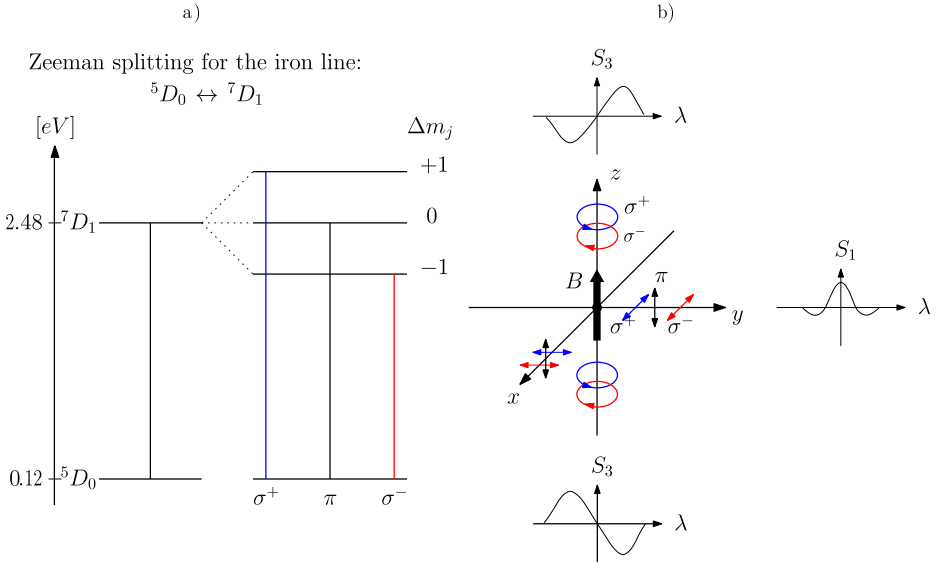


Figure 1.3: a) Zeeman splitting for the iron line ( ${}^5D_0 \leftrightarrow {}^7D_1$ ), at  $\lambda = 525.02 \text{ nm}$ . b) Schematic representation of the detected polarizations for different directions of observation.

The separation of the spectral lines depends on the intensity of the magnetic field. The Stokes parameters, commonly used to describe the polarization and corresponding to the detected emission (or absorption), are also related to the magnetic field<sup>1</sup>:

$$\begin{cases} S_1 \propto B^2 \\ S_3 \propto B \end{cases}, \quad (1.7)$$

where  $S_1$  is the Stokes parameter that describes the fraction of light that is linearly horizontal or vertically polarized, and  $S_3$  is the circularly polarized fraction. Measuring  $S_1$  and  $S_3$  parameters of the Stokes vector can give access to the value of the magnetic field. The geometry of the problem, together with the example of the Zeeman effect for iron at 525.02 nm, are presented in Fig. 1.3. We notice here how an observer located in the plane  $(xy)$ , perpendicular to the direction of  $\vec{B}$ , will detect three emissions (or absorption) lines, all carrying a linear polarization (horizontal or vertical). On the contrary, an

<sup>1</sup>More details about Stokes's formalism can be retrieved in the next chapter.

observer looking along the magnetic field will detect only two circular polarizations corresponding to  $\sigma$  transitions. In this case, the sign of the polarization will be influenced by the direction of the magnetic field.

A spectropolarimeter able to measure any polarization at various wavelengths will be paramount in studying the Zeeman effect and determining the magnetic fields of stars.

### 1.1.5. HANLE EFFECT

Besides the Zeeman effect, the Hanle effect is also a widely used phenomenon that can reveal the magnitude of a star's magnetic field (Bommier, 2012). However, in contrast to the Zeeman effect, the Hanle effect needs a much weaker magnetic field to be visible. In principle, this is nothing else than a scattering effect taking place in the presence of a magnetic field. Therefore, using the representation of a vibrating dipole excited by electromagnetic radiation in the presence of a magnetic field, given the existence of the Larmor precession, this dipole will have two movements: a vibration and a precession. The emission of this dipole will also move constantly, as it should always stay perpendicular to the direction of movement. The following situations can occur (see Fig. 1.4):

- $\vec{B} = 0$ : if there is no magnetic field (situation a)), then we are in the presence of Rayleigh scattering. An observer looking in the  $y$  direction will perceive a linearly polarized wave oriented along the  $x$ -axis.
- $\vec{B} \neq 0$  and  $\vec{B}$  along  $x$ -axis (situation b)): in this case, there will be no change in the detected polarization.
- $\vec{B} \neq 0$  and  $\vec{B}$  along  $z$ -axis (situation c)): if  $B$  is very small or very big, then it does not affect the detected polarization. Otherwise, it will determine a decrease in the degree of polarization detected.
- $\vec{B} \neq 0$  and  $\vec{B}$  along  $y$ -axis (situation d)): if  $B$  is weak, then the detected linear polarization will be tilted. If  $B$  is strong, a complete depolarization will happen.

In practice, the Hanle effect is used to diagnose magnetic fields between several G and until 100 G. Thus, for the Sun corona, where  $B \approx 100$  G, it is the most suited (Raouafi et al., 2016).

In contrast with the Zeeman effect, the Hanle effect yields only linear polarization components ( $S_1$  and  $S_2$ ).

## 1.2. POLARIZATION IN ASTRONOMY

The use of polarization in astronomy has a long tradition. It is probably the field that first used this property of light to gather information about distant bodies. The first astronomical polarimetric observations were made more than a century ago by Arago, who was curious to look at the Moon through a polarimeter (Dollfus et al., 1971). However, in the beginning, the relevance of these observations was negligible, considering that plausible information could hardly be deduced starting only from the polarimetric measurements. It took time and laborious experimental work to establish an empirical relationship between the texture and composition of reflective surfaces and the polarization of light (Spadaccia et al., 2022).

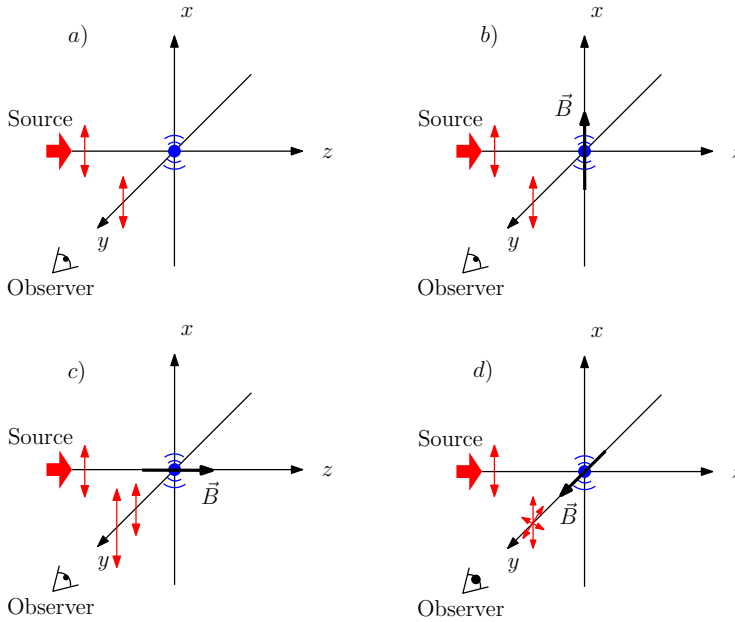


Figure 1.4: Hanle effect under excitation with a linearly polarized wave.

The most used effects and processes in astronomy that use the polarization of light are, apart from those already described previously, the Umov effect, the inversion angle, and the opposition effect.

The Umov effect refers to the relationship between the linear polarization of an atmosphereless body and albedo. According to this empirical correlation, for large phase angles, the degree of linear polarization of a celestial body is inversely proportional to its albedo (Mazarbhuiya et al., 2021). This behavior is mainly related to the multiple scattering in the regolith. In the case of the bodies with an atmosphere or of the comets, this effect is visible only for small phase angle values (Zubko et al., 2018). Another phenomenon used extensively in astronomy is the inversion angle. This corresponds to the phase angle<sup>2</sup> accompanied by a rotation with 90° of the linear polarization of the reflected light. This phase angle depends on the granularity of the reflective surface as well as the wavelength. It is a range rather than a single value. Thus, for instance, for the Moon, the inversion angle is situated between 15° and 27°.

Another polarimetric phenomenon related to the observed object's phase is the opposition phenomenon or opposition surge (Belskaya and Shevchenko, 2000; Shkuratov et al., 2002). This phenomenon manifests itself for phase angles close to zero and consists of a strong increase in the intensity of the light reflected by the observed body. The phenomenon is explained by an interference of the incident light with the light reflected from the surface. It occurs for particles with a dimension comparable to the wavelength of the incident light and a distance in between greater than this wavelength. When these

<sup>2</sup>Just like in the Rayleigh scattering, the phase angle is the angle between the direction of the incident light and the direction of observation.

conditions are fulfilled, the incident light can interfere with the scattered light, increasing brightness (Akkermans et al., 1986; Hapke et al., 1993). Information about the particles' size can be obtained based on the polarimetric observations of the inversion phenomenon.

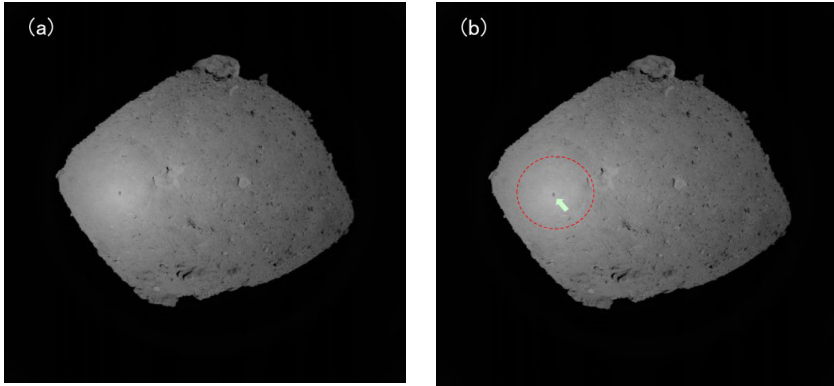


Figure 1.5: Opposition effect observed by Hayabusa2 probe on the surface of the asteroid Ryugu. In the image b) the opposition effect is encircled in red. The black dot represents the shadow of the space probe. (Image credit: JAXA)

The use of polarization in astronomy is not limited to the characterization of the surfaces of distant bodies or the determination of the magnetic field. With the help of linear and circular polarization measured on a broad spectrum, for instance, the interstellar medium can be characterized (Jones and Whittet, 2015). In addition, polarization can be used to confirm the detection of exoplanets and to search for their biosignature (Wiktorowicz and Stam, 2015). The mechanism is based on the fact that the light coming from the stars is unpolarized when considered for the entire disk. However, the light reflected by the planets has a degree of linear polarization that depends on the scattering phenomenon that occurs and on the phase angle (Buenzli and Schmid, 2009). The evidence of this linear polarization remains difficult, considering that the light flux is dominated by the light coming from the star. Applications can go even further, aiming to detect the presence of organic compounds or the signature of life on other planets (Keller et al., 2020).

### 1.3. OTHER APPLICATIONS

Astronomy is not the only field that intensively uses the polarization of light. In recent years, fields such as climatology, defense, and medicine have begun to call more and more attention to this property of light. In the defense sector, for example, it can become a formidable tool for identifying camouflaged targets (Hickman et al., 2017; Jin-Zuo, 2007). In climatology, it allows the identification and characterization of aerosols in the atmosphere or the characterization of the surface of the oceans (El-Habashi et al., 2021; Zubko et al., 2024). However, one of the most remarkable and impactful applications is the one in medicine. Here, spectropolarimetry has proven a noteworthy contribution to cancer detection (Novikova et al., 2012). Initially, the applications targeted

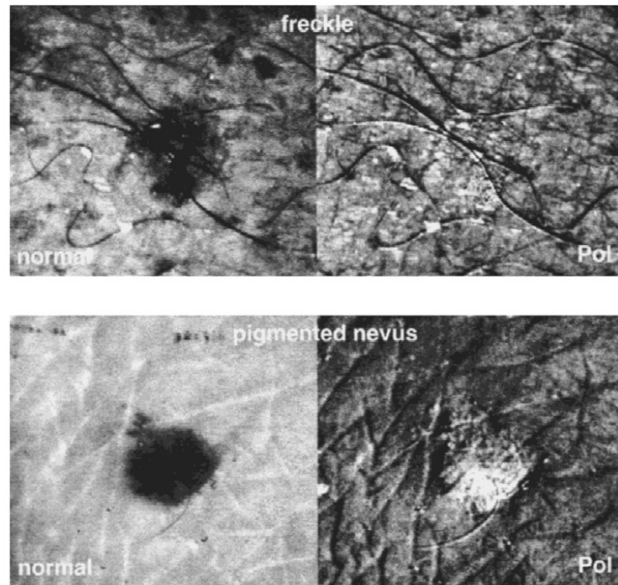


Figure 1.6: Skin cancer detection using linear polarization. Source: (Jacques et al., 2000)

only skin conditions (Jacques et al., 2002). Later, however, it was discovered that it could also be used to detect other types of cancer (Ivanov et al., 2020; Le Gratiot et al., 2021; Vizet et al., 2017). The novelty brought by polarimetry is that it allows for the rapid identification, in vivo, of the affected tissues, thus allowing for the rapid onset of treatment or usage during the surgery.

# BIBLIOGRAPHY

- Akkermans, E., Wolf, P. E., & Maynard, R. (1986). Coherent backscattering of light by disordered media: Analysis of the peak line shape. *Phys. Rev. Lett.*, 56, 1471–1474. <https://doi.org/10.1103/PhysRevLett.56.1471>
- Belskaya, I., & Shevchenko, V. (2000). Opposition effect of asteroids. *Icarus*, 147(1), 94–105. <https://doi.org/https://doi.org/10.1006/icar.2000.6410>
- Bommier, V. (2012). Hanle effect from a dipolar magnetic structure: The case of the solar corona and the case of a star. *Astronomy & Astrophysics*, 539, A122. <https://doi.org/10.1051/0004-6361/201118245>
- Born, M., Wolf, E., Bhatia, A. B., Clemmow, P. C., Gabor, D., Stokes, A. R., Taylor, A. M., Wayman, P. A., & Wilcock, W. L. (1999). *Principles of optics: Electromagnetic theory of propagation, interference and diffraction of light* (7th ed.). Cambridge University Press.
- Bucholtz, A. (1995). Rayleigh-scattering calculations for the terrestrial atmosphere. *Appl. Opt.*, 34(15), 2765. <https://doi.org/10.1364/AO.34.002765>
- Buenzli, E., & Schmid, H. M. (2009). A grid of polarization models for Rayleigh scattering planetary atmospheres. *Astronomy & Astrophysics*, 504(1), 259–276. <https://doi.org/10.1051/0004-6361/200911760>
- Crutcher, R. M., & Kemball, A. J. (2019). Review of zeeman effect observations of regions of star formation. *Frontiers in Astronomy and Space Sciences*, 6, 66. <https://doi.org/10.3389/fspas.2019.00066>
- Dollfus, A., Bowell, E., & Titulaer, C. (1971). Polarimetric Properties of the Lunar Surface and its Interpretation. Part II. Terrestrial Samples in Orange Light. *Astronomy and Astrophysics*, 10, 450.
- El-Habashi, A., Bowles, J., Foster, R., Gray, D., & Chami, M. (2021). Polarized observations for advanced atmosphere-ocean algorithms using airborne multi-spectral hyper-angular polarimetric imager. *Journal of Quantitative Spectroscopy and Radiative Transfer*, 262, 107515. <https://doi.org/https://doi.org/10.1016/j.jqsrt.2021.107515>
- Gassó, S., & Knobelspiesse, K. D. (2022). Circular polarization in atmospheric aerosols. *Atmospheric Chemistry and Physics*, 22(20), 13581–13605. <https://doi.org/10.5194/acp-22-13581-2022>
- Hapke, B. W., Nelson, R. M., & Smythe, W. D. (1993). The Opposition Effect of the Moon: The Contribution of Coherent Backscatter. *Science*, 260(5107), 509–511. <https://doi.org/10.1126/science.260.5107.509>
- Hickman, D., Smith, M. I., Kim, K. S., & Choi, H.-J. (2017). The utility of polarimetry within passive military imaging systems. *Security + Defence*. <https://doi.org/10.1117/12.2279524>
- Ivanov, D., Dreminev, V., Bykov, A., Borisova, E., Genova, T., Popov, A., Ossikovski, R., Meglinski, I., & Novikova, T. (2020). Colon cancer detection by using poincaré sphere

- and 2d polarimetric mapping of ex vivo colon samples. *Journal of Biophotonics*, 13(8). <https://doi.org/10.1002/jbio.202000082>
- Jacques, S. L., Ramella-Roman, J. C., & Lee, K. (2002). Imaging skin pathology with polarized light. *Journal of Biomedical Optics*, 7(3), 329. <https://doi.org/10.1117/1.1484498>
- Jacques, S. L., Roman, J. R., & Lee, K. (2000). Imaging superficial tissues with polarized light. *Lasers in Surgery and Medicine*, 26(2), 119–129. [https://doi.org/10.1002/\(SICI\)1096-9101\(2000\)26:2<119::AID-LSM3>3.0.CO;2-Y](https://doi.org/10.1002/(SICI)1096-9101(2000)26:2<119::AID-LSM3>3.0.CO;2-Y)
- Jin-Zuo, S. (2007). Study of target identification based on polarization imaging. *Journal of Yantai University*. <https://api.semanticscholar.org/CorpusID:124404674>
- Jones, T. J., & Whittet, D. C. B. (2015). Interstellar polarization. In L. Kolokolova, J. Hough, & A.-C. Levasseur-Regourd (Eds.), *Polarimetry of stars and planetary systems* (pp. 147–161). Cambridge University Press. <https://doi.org/10.1017/CBO9781107358249>
- Keller, C., Snik, F., Patty, C., Klindzic, D., Krasteva, M., Doelman, D., Wijnen, T., Pallichadath, V., Stam, D., & More Authors. (2020). Design of the life signature detection polarimeter lsdpol. In M. Lystrup & M. Perrin (Eds.), *Space telescopes and instrumentation 2020* (Vol. 11443). SPIE. <https://doi.org/10.1117/12.2562656>
- Le Gratiet, A., Mohebi, A., Callegari, F., & Bianchini, A., Paolo and Diaspro. (2021). Review on complete mueller matrix optical scanning microscopy imaging. *Applied Sciences*, 11(4). <https://doi.org/10.3390/app11041632>
- Leroy, J.-L. (2000). *Polarization of light and astronomical observation*. CRC Press.
- Mazarbhuiya, A. M., Das, H. S., & Halder, P. (2021). The Umov effect in cosmic dust analogue fluffy aggregates. *Monthly Notices of the Royal Astronomical Society*, 502(2), 2536–2540. <https://doi.org/10.1093/mnras/stab230>
- Novikova, T., Pierangelo, A., De Martino, A., Benali, A., & Validire, P. (2012). Polarimetric imaging for cancer diagnosis and staging. *Optics and Photonics News*, 23(10), 26. <https://doi.org/10.1364/OPN.23.10.000026>
- Raouafi, N. E., Riley, P., Gibson, S., Fineschi, S., & Solanki, S. K. (2016). Diagnostics of coronal magnetic fields through the hanle effect in UV and IR lines. *Frontiers in Astronomy and Space Sciences*, 3. <https://doi.org/10.3389/fspas.2016.00020>
- Shkuratov, Y., Ovcharenko, A., Zubko, E., Miloslavskaya, O., Muinonen, K., Piironen, J., Nelson, R., Smythe, W., Rosenbush, V., & Helfenstein, P. (2002). The opposition effect and negative polarization of structural analogs for planetary regoliths. *Icarus*, 159(2), 396–416. <https://doi.org/https://doi.org/10.1006/icar.2002.6923>
- Slonaker, R. L., Takano, Y., Liou, K.-N., & Ou, S.-C. (2005, August 18). Circular polarization signal for aerosols and clouds. In H.-L. A. Huang, H. J. Bloom, X. Xu, & G. J. Dittberner (Eds.), *Atmospheric and environmental remote sensing data processing and utilization: Numerical atmospheric prediction and environmental monitoring* (58900B). <https://doi.org/10.1117/12.619576>
- Spadaccia, S., Patty, C. H. L., Capelo, H. L., Thomas, N., & Pommerol, A. (2022). Negative polarization properties of regolith simulants: Systematic experimental evaluation of composition effects. *Astronomy & Astrophysics*, 665, A49. <https://doi.org/10.1051/0004-6361/202243844>

- van der Laan, J. D., Wright, J. B., Scrymgeour, D. A., Kemme, S. A., & Dereniak, E. L. (2015). Evolution of circular and linear polarization in scattering environments. *Opt. Express*, 23(25), 31874–31888. <https://doi.org/10.1364/OE.23.031874>
- Vizet, J., Rehbinder, J., Deby, S., Roussel, S., Nazac, A., Soufan, R., Genestie, C., Haie-Meder, C., Fernandez, H., Moreau, F., & Pierangelo, A. (2017). In vivo imaging of uterine cervix with a mueller polarimetric colposcope. *Scientific Reports*, 7(1), 2471. <https://doi.org/10.1038/s41598-017-02645-9>
- Wiktorowicz, S. J., & Stam, D. M. (2015). Exoplanets. In L. Kolokolova, J. Hough, & A.-C. Levasseur-Regourd (Eds.), *Polarimetry of stars and planetary systems* (pp. 439–461). Cambridge University Press. <https://doi.org/10.1017/CBO9781107358249>
- Zubko, E., Videen, G., Zubko, N., & Shkuratov, Y. (2018). The Umov effect in application to an optically thin two-component cloud of cosmic dust. *Monthly Notices of the Royal Astronomical Society*, 477(4), 4866–4873. <https://doi.org/10.1093/mnras/sty938>
- Zubko, E., Zheltobryukhov, M., Chornaya, E., Shmirko, K. A., Lisitsa, V. V., Pavlov, A. N., Kochergin, A., Kornienko, G., & Videen, G. (2024). Characterizing atmospheric aerosols using polarimetry and shadow hiding. *Frontiers in Remote Sensing*, 4. <https://doi.org/10.3389/frsen.2023.1321621>





# 2

## DESCRIPTION OF POLARIZATION

*Evolution is not a cause but the description of a process*

George Gabriel Stokes

The polarization of light was observed long ago. Its story is related to the discovery of the Icelandic spar, a crystal through which, in certain conditions, the image of objects seems to be doubled. Famous scholars bumped their heads at this renowned rock, trying to explain what was happening with the light that passed through. Rasmus Bartholin, Christiaan Huygens, Biot, Young, Brewster, Arago, and Malus are just a few names. However, hundreds of years were necessary to explain the optical processes in such media. This was possible only after Fresnel formulated the wave theory of light. After that, the concept of polarization was forged and received a complete mathematical description, which agreed with the observations. In this way, the light split in the Iceland spar was also explained and related to the polarization phenomenon.

Despite its long history and the well-established analytical apparatus that describes it, polarization remains a complex concept. To deal with polarization and achieve its measurement, we need to use a special mathematical formalism and particular materials capable of altering or converting the polarization into an observable property.

This chapter summarizes the physical interpretation of the polarization of light. In addition, it offers the mathematical apparatus necessary to deal with this property of light in the research framework conducted here.

We concentrate our attention on Stokes and Mueller's formalism even though one can also consider Jones's formalism. The reason behind our choice for the Stokes formalism is related to the need to cover the partial polarization, which is only possible with the help of the Stokes vector.

## 2.1. THE POLARIZATION OF LIGHT

The formalism used in this research is the Mueller-Stokes formalism. This is one of the most widely used mathematical apparatus to describe the different polarizations of light and the transformations undergone by the polarization when light passes through various media. Numerous sources exist that provide an in-depth presentation of this formalism. We can cite here, for instance (Goldstein, 2011), (Hecht, 2017), or (Collett, 2005).

Let us consider light as an electromagnetic transverse wave, for which the electric and magnetic fields vibrate in orthogonal planes. Then, the polarization can be defined with the help of the orientation of the electric field of light, as seen by an observer looking along the direction of propagation of the beam (see Fig. 2.1). Therefore, to explain the concept of polarization scientifically, we need to understand how the electric field of light propagates.

The Maxwell's equations represent the starting point of this story. In summary, by adopting a harmonic solution for the electromagnetic disturbances in Maxwell's equations, we can find that the  $x$  and  $y$  components of an electric field propagating in the direction  $\vec{k}$  can be expressed as:

$$\begin{cases} E_x(\vec{r}, t) = E_{0x} \cos(\omega t - \vec{k} \cdot \vec{r} + \phi_x) \\ E_y(\vec{r}, t) = E_{0y} \cos(\omega t - \vec{k} \cdot \vec{r} + \phi_y) \end{cases} \quad (2.1)$$

Considering, for simplicity, that the direction of propagation  $\vec{k}$  is parallel to the  $z$ -axis of the cartesian system, then we have:

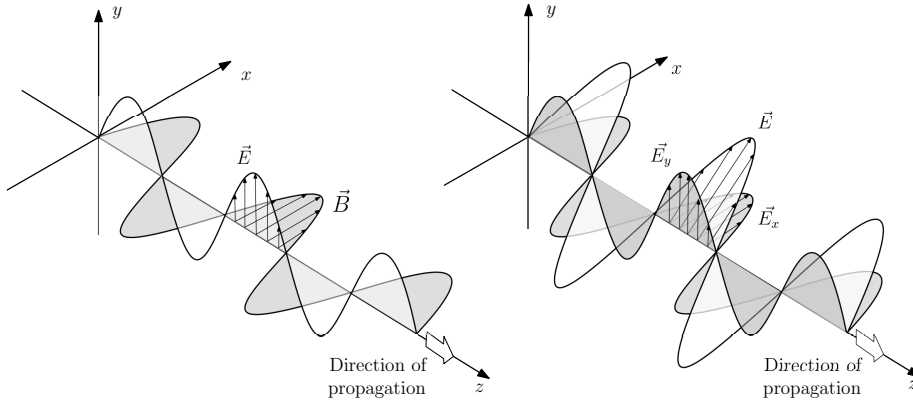


Figure 2.1: At left: representation of an electromagnetic wave in a reference frame where the direction of the  $x$ -axis coincides with the direction of  $\vec{B}$ ,  $y$ -axis with  $\vec{E}$ ,  $z$ -axis shows the direction of propagation. At right, the electric field is decomposed in an arbitrary reference frame  $xyz$ , where the  $z$ -axis is oriented towards the wave's propagation direction. The case of  $\vec{E}$  oscillating in a single plane is depicted here.

$$\begin{cases} \vec{k} = k \cdot \vec{e}_z = \frac{2\pi}{\lambda} \cdot \vec{e}_z \\ \vec{r} = z \cdot \vec{e}_z \end{cases}, \quad (2.2)$$

where  $\lambda$  is the wavelength of light. For a wave with a frequency  $f = 1/\tau$ , where  $\tau$  is the period of the oscillation, we obtain from the two sets of equations:

$$\begin{cases} E_x(z, t) = E_{0x} \cos(\omega t - kz + \phi_x) \\ E_y(z, t) = E_{0y} \cos(\omega t - kz + \phi_y) \end{cases} \quad (2.3)$$

where  $k = 2\pi/\lambda$  is the wavenumber,  $\omega = 2\pi f$  is the angular frequency,  $E_{0x}$  and  $E_{0y}$  are the maximum values of the amplitudes along  $x$  and  $y$  directions, and  $\phi_x, \phi_y$  are the phases. Taking  $\Delta\phi = \phi_y - \phi_x$ , the phase difference between the two components of the electric field, and eliminating the propagator  $(\omega t - kz)$ , the expressions (2.3) lead to:

$$\frac{E_x(z, t)^2}{E_{0x}^2} + \frac{E_y(z, t)^2}{E_{0y}^2} - \frac{2E_x(z, t)E_y(z, t)}{E_{0x}E_{0y}} \cos(\Delta\phi) = \sin^2(\Delta\phi) \quad (2.4)$$

which is the general expression of an ellipse in the plane  $(x, y)$ . Freezing a point in space along the  $z$ -axis, an observer looking in the direction of propagation will see the variation of  $E_x$  and  $E_y$  components during the observing time (see Fig. 2.2).

Equation (2.4) tells us that the two components of the electric field will generally describe an ellipse. However, for certain values of  $\delta$ ,  $E_{0x}$  and  $E_{0y}$ , the shape described by the Eq. (2.4) can embrace degenerate forms, becoming a circle or a line with a specific orientation. This shape is referred to as the polarization state of light. The linear and circular polarization states are the most encountered in practice. For the circular states, a clockwise movement of the field, as seen by an observer on the  $z$ -axis, is called right circular polarization (RCP). The counter-clockwise development of the field is the left circular polarization (LCP).

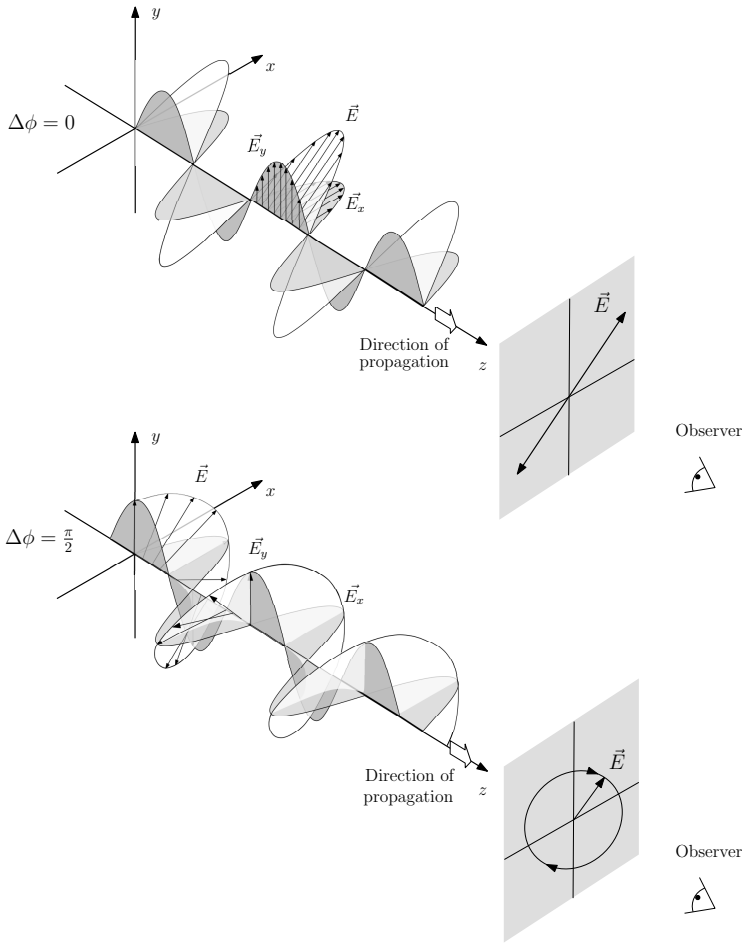


Figure 2.2: Intuitive representation of linear and right-circular states of polarizations. We notice that to have a linear state of polarization, the two components of the field should be in phase ( $\Delta\phi = 0$ ). On the contrary, a circular or elliptical polarization state is generated when the phase difference is different from zero ( $\Delta\phi = \pi/2$ ). Several possible orientations of the E vector are highlighted to help visualize the general shape described by the electric field.

### 2.1.1. THE POINCARÉ REPRESENTATION

The main parameters of the ellipse described by Eq. (2.4) are the orientation angle ( $\psi_e$ ) and the ellipticity ( $\chi_e$ ). These angles are defined by:

$$\begin{cases} \tan(2\psi_e) = \frac{2E_{0x}E_{0y}}{E_{0x}^2 - E_{0y}^2}, & \psi_e \in (0, \pi] \\ \tan(2\chi_e) = \frac{2E_{0x}E_{0y} \sin(\Delta\phi)}{E_{0x}^2 + E_{0y}^2}, & \chi_e \in (-\frac{\pi}{4}, \frac{\pi}{4}], \quad \Delta\phi \in (0, 2\pi] \end{cases} \quad (2.5)$$

An orientation angle and an ellipticity then define any polarization state. Based on this property, Poincaré proposed an alternative representation of polarization in a three-

dimensional system (see Fig. 2.3). Any state of polarization can then be represented by a point on a sphere of radius unity and having as coordinates:

$$\begin{cases} x = \cos(2\chi_e) \cos(2\psi_e) \\ y = \cos(2\chi_e) \sin(2\psi_e) \\ z = \sin(2\chi_e) \end{cases} . \quad (2.6)$$

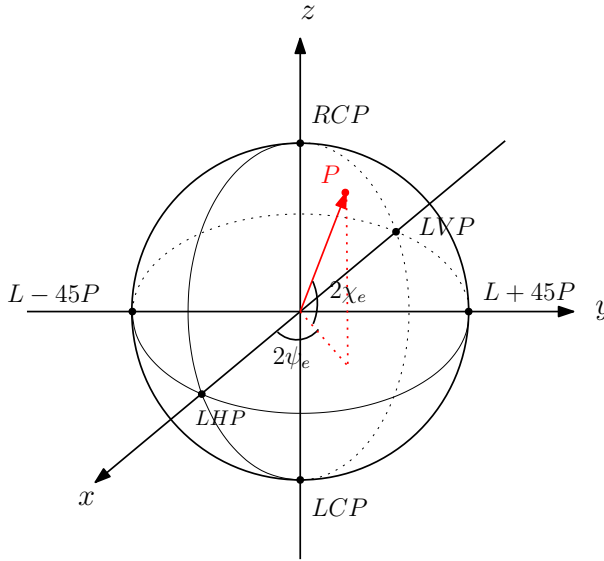


Figure 2.3: Poincaré representation of a polarization state  $P$  and of the main degenerate states. The location of any polarization state on the sphere can be directly retrieved using Eq. (2.5) and (2.6).

The Poincaré sphere is essential in visualizing the polarization states and is a handy instrument in the algebra that deals with polarization transformations. Nevertheless, it does not help us to measure this property of light. All the parameters involved in this representation are not directly measurable.

The optical detectors are sensitive to the intensity of light. Because of this, the assessment of polarization should also be reduced to the intensity measurement. To solve this challenge, Stokes proposed using four parameters embedding all the information about polarization and having the dimension of intensity.

Thus, after taking the time average of the relation (2.4), one can introduce the further notation:

$$\begin{cases} S_0 = E_{0x}^2 + E_{0y}^2 \\ S_1 = E_{0x}^2 - E_{0y}^2 \\ S_2 = 2E_{0x}E_{0y} \cos(\Delta\phi) \\ S_3 = 2E_{0x}E_{0y} \sin(\Delta\phi) \end{cases} . \quad (2.7)$$

The first Stokes parameter,  $S_0$ , stays for the total intensity of light,  $S_1$  describes the difference between the horizontal and the vertical polarization, and the  $S_2$  term represents the difference between the polarization at  $45^\circ$  and  $-45^\circ$ . In contrast, the last term,  $S_3$ , measures the difference between *RCP* and *LCP*. Overall, any polarization state will be described by a vector:

$$\vec{S} = \begin{pmatrix} S_0 \\ S_1 \\ S_2 \\ S_3 \end{pmatrix}. \quad (2.8)$$

A very common notation for the Stokes vector, often used in the specialized literature, is:

$$\vec{S} = \begin{pmatrix} I \\ Q \\ U \\ V \end{pmatrix}.$$

Therefore, the degenerate states of polarization most often used are described by the following vectors:

- Linear horizontal polarization (LHP):

$$\vec{S} = S_0 \begin{pmatrix} 1 \\ 1 \\ 0 \\ 0 \end{pmatrix}$$

- Linear vertical polarization (LVP):

$$\vec{S} = S_0 \begin{pmatrix} 1 \\ -1 \\ 0 \\ 0 \end{pmatrix}$$

- Linear  $45^\circ$  polarization (L+45P):

$$\vec{S} = S_0 \begin{pmatrix} 1 \\ 0 \\ 1 \\ 0 \end{pmatrix}$$

- Linear  $-45^\circ$  polarization (L-45P):

$$\vec{S} = S_0 \begin{pmatrix} 1 \\ 0 \\ -1 \\ 0 \end{pmatrix}$$

- Right circular polarization (RCP):

$$\vec{S} = S_0 \begin{pmatrix} 1 \\ 0 \\ 0 \\ 1 \end{pmatrix}$$

- Left circular polarization (LCP):

$$\vec{S} = S_0 \begin{pmatrix} 1 \\ 0 \\ 0 \\ -1 \end{pmatrix}$$

The parameters  $S_1$ ,  $S_2$ , and  $S_3$  describe the state of polarization like  $x$ ,  $y$ , and  $z$  in the relation (2.6). It can be easily shown that:

$$\begin{cases} S_1 = S_0 \cos(2\chi_e) \cos(2\psi_e) \\ S_2 = S_0 \cos(2\chi_e) \sin(2\psi_e) \\ S_3 = S_0 \sin(2\chi_e) \end{cases} \quad (2.9)$$

Equation 2.1 describes an infinite wave train of constant frequency and constant value of phase difference. An observer located in the direction of propagation will always see a unique pattern described by the oscillation of the electric field. As we have seen, this pattern can be a line, a circle, or an ellipse. However, the emission of light by an atom is a very short process. It takes about  $10^{-8}$ s for an atom to radiate. We would perceive a certain polarization if we could observe the wave train in this short interval. However, our eyes or electronic detectors use an integration time much greater than the emission time. We are detecting the result of multiple emissions. If the orientation of the electric field of these separate emissions contained in the detected light varies continuously, then we are talking about unpolarized light. This is the case with natural light. However, when a pattern appears in the random orientations of the electric field, we are talking about partially polarized light. In the extreme case, when all the emitted wave trains are characterized by the same orientation of the electric field, then we are dealing with total polarization.

One of the most essential advantages of Stokes formalism is that it can describe equally the complete and the partial states of polarization. Thus, the degree of polarization ( $DoP$ ) is defined by:

$$DoP = \frac{\sqrt{S_1^2 + S_2^2 + S_3^2}}{S_0}, \quad DoP \in [0, 1] \quad (2.10)$$

and the light can be represented all the time as the sum of a fraction that is not polarized and of a fraction that is completely polarized:



$$\vec{S} = \begin{pmatrix} S_0 \\ S_1 \\ S_2 \\ S_3 \end{pmatrix} = (1 - DoP) \begin{pmatrix} S_0 \\ 0 \\ 0 \\ 0 \end{pmatrix} + DoP \begin{pmatrix} S_0 \\ S_1 \\ S_2 \\ S_3 \end{pmatrix} \quad (2.11)$$

When  $DoP = 1$ , we deal with completely polarized light, whereas  $DoP = 0$  stays for the unpolarized light. In addition, the degree of linear polarization is defined as:

$$DoLP = \frac{\sqrt{S_1^2 + S_2^2}}{S_0} \quad (2.12)$$

and the degree of circular polarization:

$$DoCP = \frac{|S_3|}{S_0}. \quad (2.13)$$

Using Eq. (2.5) and (2.7), the orientation of the ellipse ( $\psi_e$ ) and the ellipticity ( $\chi_e$ ) can also be expressed in terms of Stokes parameters:

$$\begin{cases} \psi_e = \frac{1}{2} \tan^{-1} \left( \frac{S_2}{S_1} \right) \\ \chi_e = \frac{1}{2} \sin^{-1} \left( \frac{S_3}{S_0} \right) \end{cases} \quad (2.14)$$

The ellipticity sign also determines the polarization's handedness (right for positive and left for negative). Thus, the orientation angle provides information about the ratio between ( $45^\circ, 135^\circ$ ) linear polarizations and linear horizontal or vertical polarization. On the other hand, the ellipticity shows the ratio of the light that is circularly polarized.

## 2.2. BIREFRINGENT MATERIALS

When the light reaches an optical medium, the electrons will absorb and reemit the light. Driven by the vibration of the electric field of the incoming wave, these electrons will start to vibrate in the same direction as the electric field and then will radiate. In an isotropic medium, the same binding forces manifest in all directions. This will be translated into the existence of a single refractive index and the same speed of propagation in all directions within the medium.

When this symmetry in the binding forces is no longer present, we are talking about an anisotropic material. Of particular importance are, in this category, the optical crystals that still present a symmetry direction characterized by the same binding forces of the electrons. These are uniaxial crystals. We can cite calcium carbonate ( $\text{CaCO}_3$ ) or calcite, magnesium fluoride ( $\text{MgF}_2$ ), or calcium fluoride ( $\text{CaF}_2$ ) here.

Around this symmetry direction, also called the optical axis of the crystal, the atomic arrangement is symmetrical. Because of this, the same optical properties will manifest within this plane of symmetry, thus in a direction perpendicular to the optical axis. On the contrary, in all other crystal directions, the optical properties will differ from one point to another.

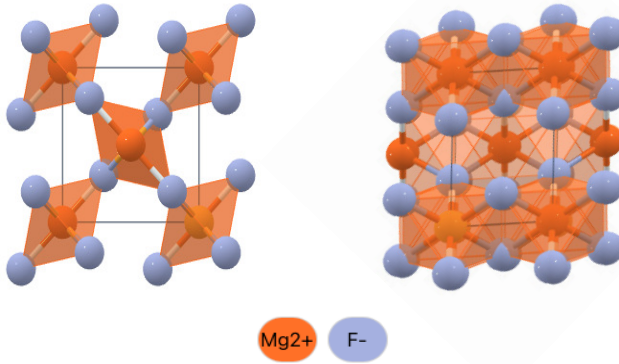


Figure 2.4: Crystalline structure of MgF<sub>2</sub>. The left image shows the structure seen looking down along the optical axis, while the right image is a view perpendicular to the optical axis. Credits: (“The Materials Project”, 2024)

The mathematical description of the wave propagating through such materials can be complex. Therefore, it can be helpful to summarize the main effects of such a crystal through an imaginative exercise.

First, let us consider the case of an electron situated inside such a uniaxial crystal and excited by a natural source of light (unpolarized light) (see Fig. 2.5).

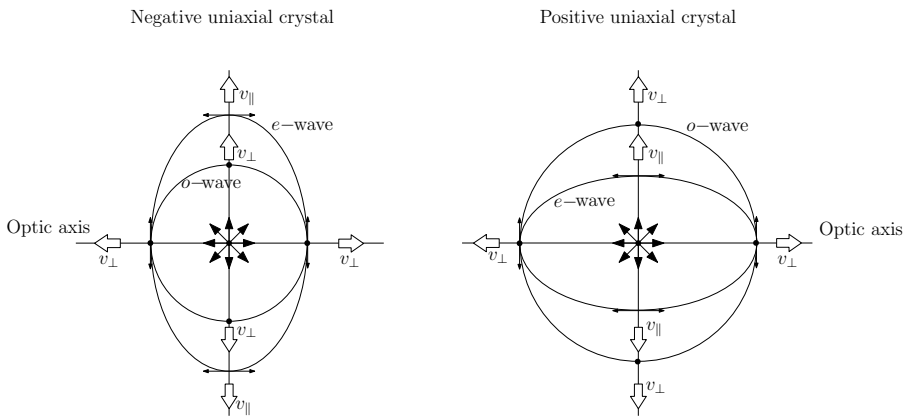


Figure 2.5: Propagation of wavelets in uniaxial negative and positive crystals. Representation adapted after (Hecht, 2017)

Because the electric field of the incoming wave vibrates randomly in all directions, the electron will also vibrate and emit in all directions. The wavelets originating in this electron that present an electric field perpendicular to the optical axis of the crystal in

all directions will see the medium like an isotropic one. Because of this, they will form spherical wavelets, expanding with the same speed in all directions,  $v_{\perp}$ . This is called the ordinary wave ( $o$ -wave).

On the contrary, the wavelets with an electric field perpendicular to the optical axis when propagating along this direction and parallel to this when moving orthogonally will encounter different optical conditions. This wave is called the extraordinary wave ( $e$ -wave).

As we can notice from Fig. 2.5, the  $e$ -wave will propagate in a direction perpendicular to the optical axis with speed  $v_{\parallel}$ , whereas along the optical axis, it will present a speed  $v_{\perp}$ . The difference in speed is determined by the difference in the refractive indices along the two directions. In turn, this originates in the anisotropy of the material and, more precisely, in the variation of the permittivity with the direction. We notice that the wavelets are no longer spherical in the case of the  $e$ -wave. They have an ellipsoidal shape. The indices of refraction these wavelets encounter also evolve on an ellipsoid.

The difference  $\Delta n = n_e - n_o$ , where  $n_o = c/v_{\perp}$  and  $n_e = c/v_{\parallel}$  is called birefringence. The crystals having  $\Delta n \neq 0$  are called birefringent crystals. If  $\Delta n < 0$ , and there is a single axis of symmetry, we are dealing with a negative uniaxial crystal, whereas if  $\Delta n > 0$ , the crystal is uniaxial positive. The direction of propagation corresponding to the highest speed of light, thus having the smallest refractive index, is called the fast axis of the crystal. In contrast, the direction characterized by the higher refractive index is called the slow axis. Thus, following the examples presented in Fig. 2.5, for a negative crystal, where  $n_e < n_o$ , the fast axis is perpendicular to the optical axis of the crystal, whereas, for a positive crystal, the fast axis is in the direction of the optical axis. Even though the Huygens constructions used to describe the propagation of waves in an isotropic material are not the most accurate instrument when describing the situation of birefringent media, they are still used today. They can help to build a very intuitive representation that is easy to follow. Therefore, let us consider the case in Fig. 2.6, where a plane wave passes from the air into a birefringent crystal. We assume that the incoming wave is unpolarized.

Each atom from the interface of the material excited by the wavefront  $AB$  will become a source of wavelets inside the crystal. When these sources are excited by the  $o$ -wave, characterized by an electric field vibrating perpendicular to the optical axis in any direction, then the wavelets propagating in the crystal will have a spherical shape. The time necessary for the wavelet to travel from  $A$  to  $D$  equals the time necessary for the wavefront to travel from  $B$  to  $C$ . The tangent from  $C$  to the circle of radius  $AD$  provides the direction of propagation of the  $o$ -ray inside the crystal ( $\vec{S}_o$ ). Given that the  $o$ -ray encounters an isotropic medium, its precise direction of propagation can be inferred from Snell's law.

Let us focus on the extraordinary ray (right schema in Fig. 2.6). We know that in a direction perpendicular to the optical axis, we have an isotropic medium with a refractive index  $n_o$  for this ray. In a direction parallel to the optical axis, the refractive index is  $n_e$ . Assuming we are dealing with a negative uniaxial crystal,  $n_e < n_o$ . The time from the wavefront  $AB$  to arrive from  $B$  to  $C$  now equals the time of the disturbance propagating from  $A$  to  $E$ , where  $AE$  is the semi-major axis of the ellipse described by the wavelet. Given that we have  $n_e < n_o$ , then  $AE > AD$ . Just like in the previous case, the direction of

propagation of the energy inside the material will be provided by the tangent to the ellipses centered on the points along  $AC$  distance and having the major axis perpendicular to the optical axis of the crystal ( $\vec{S}_e$ ).

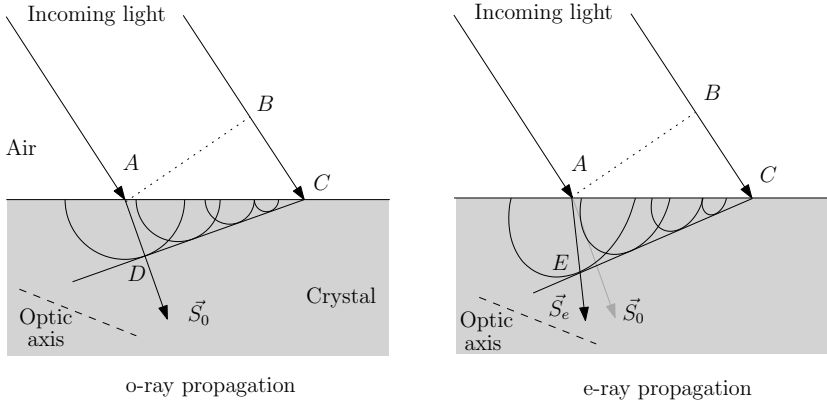


Figure 2.6: Huygens constructions for light propagation inside the birefringent negative crystal. The drawing on the left shows the propagation of  $o$ -waves, while the drawing on the right illustrates the case of  $e$ -waves. The two cases have been separated to make the schematic easier to follow. Representation adapted after (Hecht, 2017)

Due to the different directions of propagation for the  $e$ - and  $o$ -waves inside a birefringent material, an incoming light that is not polarized can emerge, in certain conditions, as two beams carrying orthogonal states of linear polarization. Returning to the story of the Icelandic spar from the beginning, this explains the formation of two images while looking through such crystal and the relation with the polarization process.

Even more, if the incoming ray is orthogonal to the optical axis, like in the situation depicted in Fig. 2.7, the  $o$ - and  $e$ -ray will travel in the same direction inside the crystal. The  $o$ -ray, generated by the field's  $\vec{E}_x$  component, which is always perpendicular to the optical axis, will see a refractive index  $n_o$  inside the material. The  $e$ -ray, in exchange, will encounter a medium of refractive index  $n_e$ . Thus, when exiting the slab of material of thickness  $d$ , a phase difference  $\Delta\phi$  will exist between the  $\vec{E}_x$  and  $\vec{E}_y$  components of the field, characterizing  $o$ - and  $e$ -rays:

$$\Delta\phi = \frac{2\pi}{\lambda} \Delta n(\lambda) d, \quad (2.15)$$

where  $\lambda$  is the wavelength of light, and  $\Delta n(\lambda)$  is the birefringence of the crystal:

$$\Delta n(\lambda) = n_e(\lambda) - n_o(\lambda) \quad (2.16)$$

In this way, by choosing an appropriate angle of incidence and orientation of the optical axis, a birefringent crystal can be used to control the phase difference between the orthogonal components of the field. It is by this principle that optical retarders are produced.

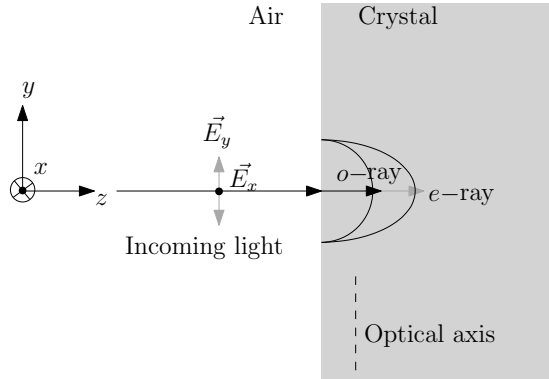


Figure 2.7: Huygens constructions for light propagation inside the birefringent crystal when the plane of incidence is perpendicular to the direction described by the optical axis and to the surface of the crystal.

The most notorious examples are the quarter-wave plate (*QWP*,  $\Delta\phi = \pi/2$ ), half-wave plate (*HWP*,  $\Delta\phi = \pi$ ), or the full-wave plate (*FWP*,  $\Delta\phi = 2\pi$ ). If, instead of changing the propagation speed for one of the orthogonal components of the field, the crystal can attenuate one of them completely, we are speaking about a property called dichroism. Such crystals are used to produce linear polarization.

### 2.3. MUELLER CALCULUS

One must use Mueller's or Jones's calculus to deal with polarization propagation through different media. Both approaches can quantify how a given medium can affect the electric field's orthogonal projections and how it can polarize/depolarize a wave or induce a specific phase difference between the field components. The advantage of Mueller calculus is that it can also contain the scattering effect (Shurcliff, 1962) and deal with the light partially polarized. The two approaches are compatible, and there is a simple and elegant way of switching between them. However, because we chose Stokes formalism to represent the states of polarization, the most appropriate tool now is Mueller calculus. According to this, any optical element acting on the polarization state of light can be represented by a  $4 \times 4$  matrix:

$$M = \begin{pmatrix} M_{00} & M_{01} & M_{02} & M_{03} \\ M_{10} & M_{11} & M_{12} & M_{13} \\ M_{20} & M_{21} & M_{22} & M_{23} \\ M_{30} & M_{31} & M_{32} & M_{33} \end{pmatrix} = M_{00} \begin{pmatrix} 1 & m_{01} & m_{02} & m_{03} \\ m_{10} & m_{11} & m_{12} & m_{13} \\ m_{20} & m_{21} & m_{22} & m_{23} \\ m_{30} & m_{31} & m_{32} & m_{33} \end{pmatrix}, \quad (2.17)$$

The lowercase notation,  $m_{ij}$ , with  $i, j = 0, \dots, 3$ , is often used for the normalized Mueller matrix. The Mueller matrix is the transformation matrix of a Stokes vector from a particular position on the Poincaré sphere to another location on another Poincaré sphere. This transformation is given by:

$$\vec{S}_{out} = M \cdot \vec{S}_{in}, \quad (2.18)$$

where  $\vec{S}_{in}$  is the state of polarization of the light entering the system described by  $M$ , and  $\vec{S}_{out}$  is the state of polarization of the emerging light.

### 2.3.1. PHYSICAL INTERPRETATION OF THE MUELLER MATRIX

The previous relation can help us understand the meaning of the terms from a Mueller matrix. An easy imaginary exercise can be carried out for this. Adopting the notation  $\vec{S}_{out} = (S'_0, S'_1, S'_2, S'_3)^T$  for the resulting Stokes vector, where  $T$  denotes the transposition operator, and  $\vec{S}_{in} = (S_0, S_1, S_2, S_3)^T$  for the incident vector, it is useful to rewrite Eq. 2.18:

$$\begin{pmatrix} S'_0 \\ S'_1 \\ S'_2 \\ S'_3 \end{pmatrix} = \begin{pmatrix} M_{00}S_0 + M_{01}S_1 + M_{02}S_2 + M_{03}S_3 \\ M_{10}S_0 + M_{11}S_1 + M_{12}S_2 + M_{13}S_3 \\ M_{20}S_0 + M_{21}S_1 + M_{22}S_2 + M_{23}S_3 \\ M_{30}S_0 + M_{31}S_1 + M_{32}S_2 + M_{33}S_3 \end{pmatrix}. \quad (2.19)$$

Let us suppose that the incoming light is completely unpolarized now. The incoming Stokes vector is  $\vec{S}_{in} = (S_0, 0, 0, 0)^T$ . When this light passes through the medium characterized by the matrix  $M$ , it will result in a new polarization state:

$$\begin{pmatrix} S'_0 \\ S'_1 \\ S'_2 \\ S'_3 \end{pmatrix} = S_0 \begin{pmatrix} M_{00} \\ M_{10} \\ M_{20} \\ M_{30} \end{pmatrix}. \quad (2.20)$$

Recalling the meaning of the different parameters of a Stokes vector, the term  $M_{00}$  tells us how light intensity is attenuated when passing through the medium. The next term,  $M_{10}$ , tells what fraction of the incoming light is converted into linear horizontal or vertical polarization,  $M_{20}$  what fraction becomes  $\pm 45^\circ$  polarized, and  $M_{30}$  what fraction is circularly polarized. Because the incoming light is nonpolarized, whereas the resulting light is polarized, the vector  $(M_{10}, M_{20}, M_{30})^T$  is called the polarizance vector. Shortly said, it describes how the optical medium polarizes an unpolarized wave.

Let us consider that the incoming state is a linear horizontal or vertical polarization,  $\vec{S}_{in} = (S_0, S_1, 0, 0)^T$ . Consequently, the resulting Stokes vector is:

$$\begin{pmatrix} S'_0 \\ S'_1 \\ S'_2 \\ S'_3 \end{pmatrix} = S_0 \begin{pmatrix} M_{00} \\ M_{10} \\ M_{20} \\ M_{30} \end{pmatrix} + S_1 \begin{pmatrix} M_{01} \\ M_{11} \\ M_{21} \\ M_{31} \end{pmatrix}. \quad (2.21)$$

Therefore, aside from polarizing the incoming light, the optical medium can also convert, in this case, that fraction of the incoming light that is linearly polarized at  $0^\circ$ ,  $90^\circ$  in all the other types of polarizations. Therefore,  $M_{01}$  tells us what fraction of  $S_1$  is attenuated,  $M_{11}$  what fraction remains polarized at  $0^\circ$ ,  $90^\circ$ ,  $M_{21}$  what part of  $S_1$  becomes  $\pm 45^\circ$  polarized, and  $M_{31}$  what part is converted into circular polarization. Therefore,  $M_{21}$  and  $M_{31}$  can be considered as crosstalk terms. Repeating this exercise for hypothetical incoming vectors like  $(S_0, 0, S_2, 0)^T$  and  $(S_0, 0, 0, S_3)^T$  we will see that the third column of the Mueller matrix describes the transformation of the  $S_2$  into other states of polarizations. In contrast, the last column shows the transformation of the circular polarization. Summarizing all these effects, we can represent the Mueller matrix in terms

of the transformation of the incoming state  $\vec{S}_{in} = (S_0, S_1, S_2, S_3)^T$  into the outgoing state  $\vec{S}_{out} = (S'_0, S'_1, S'_2, S'_3)^T$ :

$$M = \begin{pmatrix} S_0 \rightarrow S'_0 & S_1 \rightarrow S'_0 & S_2 \rightarrow S'_0 & S_3 \rightarrow S'_0 \\ S_0 \rightarrow S'_1 & S_1 \rightarrow S'_1 & S_2 \rightarrow S'_1 & S_3 \rightarrow S'_1 \\ S_0 \rightarrow S'_2 & S_1 \rightarrow S'_2 & S_2 \rightarrow S'_2 & S_3 \rightarrow S'_2 \\ S_0 \rightarrow S'_3 & S_1 \rightarrow S'_3 & S_2 \rightarrow S'_3 & S_3 \rightarrow S'_3 \end{pmatrix}. \quad (2.22)$$

Aside from the polarizance vector located in the matrix's first column, we can now notice that the first line describes how the optical medium attenuates the different polarization states. For this reason, this row forms the diattenuation vector. The diagonal terms of the matrix tell what part of the incoming polarization passes unaltered. The rest of the terms, as already underlined, are crosstalk terms. They inform about transforming an incoming polarization state into a different one.

As underlined by (del Toro Iniesta, 2003), the Mueller matrix terms must fulfill several necessary conditions<sup>1</sup>:

- The attenuation term is always positive:  $M_{00} \geq 0$

- $M_{00} \geq \sqrt{M_{01}^2 + M_{02}^2 + M_{03}^2}$

The vector  $\vec{D}_t = (M_{01} \ M_{02} \ M_{03})^T$  is called the diattenuation vector. For more details about the properties of this vector, see (Lu and Chipman, 1996).

- $M_{00} \geq \sqrt{M_{10}^2 + M_{20}^2 + M_{30}^2}$

The polarizance vector also belongs to the Poincaré sphere.

When the optical system is composed of multiple elements, described by the matrices  $M_1, M_2, \dots, M_n$ , through which the light passes in the same order, then the total Mueller matrix of the compound is:

$$M_{tot} = M_n \cdot M_{n-1} \cdot \dots \cdot M_1 \quad (2.23)$$

with  $M_1$  being the first element in the stream of light.

### 2.3.2. MUELLER MATRICES OF IDEAL COMPONENTS

Two optical components are particularly interesting: linear polarizers and waveplates. The linear polarizers allow the passage of the electrical field component that vibrates in a given direction, which is called the transmission direction. At the same time, they block the vibration in the orthogonal direction. The linear polarizers do not change the handedness of the polarization. They only allow the passage of a fraction of polarization or completely block this passage.

Both the waveplates and polarizers are usually made from a birefringent material. The difference is that we use materials that can attenuate one electric field component for polarizers. The capacity to induce a phase difference between these components

<sup>1</sup>The necessary and sufficient condition that a Mueller matrix must fulfill to become physically realizable was exposed by (Givens and Kostinski, 1993).

is exploited for waveplates. A nonpolarized light passes unaffected, from the point of view of polarization, through a waveplate. The polarizance vector of such a medium is  $\vec{0}$ . In addition, because it only changes the phase difference without absorbing one component of the field or another, the diattenuation vector of such a medium is also zero.

The precise Mueller matrices for these types of optical elements are:

- Linear polarizer oriented at an angle  $\theta$ :

$$\frac{1}{2} \begin{pmatrix} 1 & C & S & 0 \\ C & C^2 & CS & 0 \\ S & CS & S^2 & 0 \\ 0 & 0 & 0 & 0 \end{pmatrix} \quad (2.24)$$

where  $C = \cos(2\theta)$ ,  $S = \sin(2\theta)$ .

- Wave-plate of phase difference  $\Delta\phi$  and orientation of the fast-axis (optical-axis)  $\theta$ :

$$\begin{pmatrix} 1 & 0 & 0 & 0 \\ 0 & C^2 + S^2 \cos(\Delta\phi) & CS(1 - \cos(\Delta\phi)) & -S \sin(\Delta\phi) \\ 0 & CS(1 - \cos(\Delta\phi)) & S^2 + C^2 \cos(\Delta\phi) & C \sin(\Delta\phi) \\ 0 & S \sin(\Delta\phi) & -C \sin(\Delta\phi) & \cos(\Delta\phi) \end{pmatrix} \quad (2.25)$$

Examples of matrices corresponding to linear polarizers or particular waveplates, like the quarter-wave plate (*QWP*) and half-wave plate (*HWP*), are presented in the Addendum of this thesis.

### 2.3.3. MEASURING THE MUELLER MATRIX OF AN ARBITRARY ELEMENT

Multiple methods have been developed for measuring an optical element's Mueller matrix (Hielscher et al., 1998; Manhas et al., 2006). All are based on the measurement of the intensity of light when different incoming states of polarization, chosen from the Poincaré sphere, are used. The fastest and most imprecise method uses 16 measurements to infer the 16 terms of the matrix, whereas the most complex uses 49 measurements. The available optical elements (polarizers, *QWP*, *HWP*, etc.) can be the driving reason for choosing one method or another. Hereafter, we present the method used during the experimental part of our research. It makes use of two linear polarizers and two quarter-waveplates. A linear polarizer followed by a quarter-waveplate that can be rotated for different orientations forms what is here called a polarization state generator (*PSG*). This combination of optical elements allows us to obtain any polarization starting from unpolarized light.

#### 1. Determination of line 1: $M_{00}$ , $M_{01}$ , $M_{02}$ , $M_{03}$

- Necessary setup: *PSG*+Test element+Detector

Assuming that the Mueller matrix of the optical element under test is provided by the relation (2.17), then the first line of  $M$  can be measured using a polarization state



generator (*PSG*), and the element to be tested. If various incoming states generated with the help of the *PSG* are passing through the element under study, and then the intensity is detected by an optical detector, we have:

$$S'_0 = M_{00}S_0 + M_{01}S_1 + M_{02}S_2 + M_{03}S_3. \quad (2.26)$$

Therefore, choosing successively as incoming states of polarization

$$\begin{pmatrix} S_0 \\ 0 \\ 0 \\ 0 \end{pmatrix}, \begin{pmatrix} S_0 \\ \pm S_1 \\ 0 \\ 0 \end{pmatrix}, \begin{pmatrix} S_0 \\ 0 \\ \pm S_2 \\ 0 \end{pmatrix}, \begin{pmatrix} S_0 \\ 0 \\ 0 \\ \pm S_3 \end{pmatrix}, \quad (2.27)$$

with 100% degree of polarization, then the parameters  $M_{00}$ ,  $M_{01}$ ,  $M_{02}$ ,  $M_{03}$  can be immediately inferred.

### 2. Determination of line 2: $M_{10}$ , $M_{11}$ , $M_{12}$ , $M_{13}$

- Necessary setup: *PSG*+Test element+ *LP*( $\beta$ )+Detector
- $\beta=(0^\circ, 90^\circ)$

### 3. Determination of line 3: $M_{20}$ , $M_{21}$ , $M_{22}$ , $M_{23}$

- Necessary setup: *PSG*+Test element+ *LP*( $\beta$ )+Detector
- $\beta=(45^\circ, 135^\circ)$

To measure the terms of the second and the third lines, a rotating linear polarizer (*LP*) should be inserted into the optical system between the element to be characterized and the detector. This component plays the role of a polarimetric analyzer. The orientation of its transmission axis is  $\beta$ . The expression of the detected intensity becomes then:

$$\begin{aligned} S'_0 = & \frac{1}{2} \left( S_0 \left( M_{00} + M_{10} \cos(2\beta) + M_{20} \sin(2\beta) \right) + \right. \\ & S_1 \left( M_{01} + M_{11} \cos(2\beta) + M_{21} \sin(2\beta) \right) + \\ & S_2 \left( M_{02} + M_{12} \cos(2\beta) + M_{22} \sin(2\beta) \right) + \\ & \left. S_3 \left( M_{03} + M_{13} \cos(2\beta) + M_{23} \sin(2\beta) \right) \right), \end{aligned} \quad (2.28)$$

where  $\beta$  is the orientation of the analyzer to the horizontal. The rest of the terms can be retrieved using the same incoming polarization as in the previous series of measurements and choosing the appropriate values for the angle  $\beta$ . In order to retrieve the terms of the first line, one series of measurements for all the polarization states (2.27) should be conducted with *LP* oriented at  $\beta=0^\circ$ , and a second series with  $\beta=90^\circ$ .

The analyzer must be oriented at  $\beta=45^\circ$  and  $\beta=135^\circ$  to measure the Mueller matrix third line. The minimum number of measurements to retrieve all the terms  $M_{i,j}$ , for

$i = 1, 2$  and  $j = 0, \dots, 3$  is 16. However, higher precision can be achieved by varying  $\beta$  between  $0^\circ$  and  $360^\circ$  with a small step (for instance,  $1^\circ$ ) and fitting then the expression (2.28) to the experimental data.

#### 4. Determination of line 4: $M_{30}, M_{31}, M_{32}, M_{33}$

- Necessary setup:  $PSG + \text{Test element} + QWP(90^\circ) + LP(\beta) + \text{Detector}$
- $\beta = (45^\circ, 135^\circ)$

In the end, the last line of the Mueller matrix can be accessed by placing a quarter-wave plate ( $QWP$ ) oriented at  $90^\circ$  with respect to the horizontal of the optical system between the element under study and the analyzer. This helps us to convert the circular component resulting from the passage through the medium under study into a linear component, which can then be modulated with the rotating analyzer. The expression of the intensity emerging from such a system is:

$$S'_0 = \frac{1}{2} \left( S_0 \left( M_{00} + M_{10} \cos(2\beta) + M_{30} \sin(2\beta) \right) + S_1 \left( M_{01} + M_{11} \cos(2\beta) + M_{31} \sin(2\beta) \right) + S_2 \left( M_{02} + M_{12} \cos(2\beta) + M_{32} \sin(2\beta) \right) + S_3 \left( M_{03} + M_{13} \cos(2\beta) + M_{33} \sin(2\beta) \right) \right), \quad (2.29)$$

therefore, using orientations at  $0^\circ$  and  $90^\circ$  for the analyzer, the four remaining terms,  $M_{30}, M_{31}, M_{32}, M_{33}$  can be determined using at least eight measurements. Overall, the entire Mueller matrix can be retrieved with 32 measurements.

However, just like in the case of lines two and three, the fourth line can also be retrieved from the fit of the expression (2.29) to the experimental data collected for multiple values of  $\beta$  between  $0^\circ$  and  $360^\circ$ . This procedure will ensure the minimization of the errors. The detailed procedure for determining the Mueller matrix is presented in Table 2.1, where we adopted a notation of the detected intensity with  $I$  instead of  $S'_0$  to simplify the reading. For each term of the matrix, we explain in this table the required states of the polarization used as input, the number of measurements, and the system's composition between a non-polarized source and the detector.

The formula used to compute each term is presented in the last column of the Table 2.1. The notations  $I^+$  and  $I^-$  refer to the intensities measured for the two configurations of the system required. Therefore, when the two options concern the angles  $(45^\circ, 135^\circ)$ , the  $I^+$  corresponds to the configuration  $45^\circ$ , and the  $I^-$  to  $135^\circ$ . By extension, the same principle applies to the options  $(0^\circ, 90^\circ)$ . The values of the terms  $A$  and  $B$ , present in the computation of  $M_{ij}$ , are displayed in Table 2.2.

### Mueller matrix measurement

Terms	Pol.	Nr.	System	Formula
$M_{00}$	-	1	$M$	$M_{00} = \frac{I}{S_0}$
$M_{01}$	$\pm S_1$	2	$LP_1(0^\circ, 90^\circ) + M$	$M_{01} = M_{00} \frac{I^+ - I^-}{I^+ + I^-}$
$M_{02}$	$\pm S_2$	2	$LP_1(45^\circ, 135^\circ) + M$	$M_{02} = M_{00} \frac{I^+ - I^-}{I^+ + I^-}$
$M_{03}$	$\pm S_3$	2	$LP_1(0^\circ) + QWP(45^\circ, 135^\circ) + M$	$M_{03} = M_{00} \frac{I^+ - I^-}{I^+ + I^-}$
$M_{10}$	-	2	$M + LP_2(0^\circ, 90^\circ)$	$M_{10} = M_{00} \frac{I^+ - I^-}{I^+ + I^-}$
$M_{20}$	-	2	$M + LP_2(45^\circ, 135^\circ)$	$M_{20} = M_{00} \frac{I^+ - I^-}{I^+ + I^-}$
$M_{30}$	-	2	$M + QWP(90^\circ) + LP_2(45^\circ, 135^\circ)$	$M_{30} = M_{00} \frac{I^+ - I^-}{I^+ + I^-}$
$M_{11}$	$+S_1$	2	$LP_1(0^\circ) + M + LP_2(0^\circ, 90^\circ)$	$M_{11} = \frac{B_1 I^+ - A_1 I^-}{I^+ + I^-}$
$M_{21}$	$+S_1$	2	$LP_1(0^\circ) + M + LP_2(45^\circ, 135^\circ)$	$M_{21} = \frac{B_2 I^+ - A_2 I^-}{I^+ + I^-}$
$M_{12}$	$+S_2$	2	$LP_1(45^\circ) + M + LP_2(0^\circ, 90^\circ)$	$M_{12} = \frac{B_3 I^+ - A_3 I^-}{I^+ + I^-}$
$M_{22}$	$+S_2$	2	$LP_1(45^\circ) + M + LP_2(45^\circ, 135^\circ)$	$M_{22} = \frac{B_4 I^+ - A_4 I^-}{I^+ + I^-}$
$M_{31}$	$+S_1$	2	$LP_1(0^\circ) + M + QWP(90^\circ) + LP_2(45^\circ, 135^\circ)$	$M_{31} = \frac{B_5 I^+ - A_5 I^-}{I^+ + I^-}$
$M_{32}$	$+S_2$	2	$LP_1(45^\circ) + M + QWP(90^\circ) + LP_2(45^\circ, 135^\circ)$	$M_{32} = \frac{B_6 I^+ - A_6 I^-}{I^+ + I^-}$
$M_{13}$	$+S_3$	2	$LP_1(0^\circ) + QWP(45^\circ) + M + LP_2(0^\circ, 90^\circ)$	$M_{13} = \frac{B_7 I^+ - A_7 I^-}{I^+ + I^-}$
$M_{23}$	$+S_3$	2	$LP_1(0^\circ) + QWP(45^\circ) + M + LP_2(45^\circ, 135^\circ)$	$M_{23} = \frac{B_8 I^+ - A_8 I^-}{I^+ + I^-}$
$M_{33}$	$+S_3$	2	$LP_1(0^\circ) + QWP(45^\circ) + M + QWP(90^\circ) + LP_2(45^\circ, 135^\circ)$	$M_{33} = \frac{B_9 I^+ - A_9 I^-}{I^+ + I^-}$

Table 2.1: Mueller matrix measurement procedure for an arbitrary optical element,  $M$ .

$A_1 = M_{00} + M_{10} + M_{01}$	$B_1 = M_{00} - M_{10} + M_{01}$
$A_2 = M_{00} + M_{20} + M_{01}$	$B_2 = M_{00} - M_{20} + M_{01}$
$A_3 = M_{00} + M_{10} + M_{02}$	$B_3 = M_{00} - M_{10} + M_{02}$
$A_4 = M_{00} + M_{20} + M_{02}$	$B_4 = M_{00} - M_{20} + M_{02}$
$A_5 = M_{00} + M_{30} + M_{01}$	$B_5 = M_{00} - M_{30} + M_{01}$
$A_6 = M_{00} + M_{30} + M_{02}$	$B_6 = M_{00} - M_{30} + M_{02}$
$A_7 = M_{00} + M_{10} + M_{03}$	$B_7 = M_{00} - M_{10} + M_{03}$
$A_8 = M_{00} + M_{20} + M_{03}$	$B_8 = M_{00} - M_{20} + M_{03}$
$A_9 = M_{00} + M_{30} + M_{03}$	$B_9 = M_{00} - M_{30} + M_{03}$

Table 2.2: Additional terms used in the computation of the Mueller matrix.

## 2.4. FRESNEL TERMS

When the light encounters a surface at an oblique angle, the transmitted and the reflected beams are linearly polarized. The degree of polarization depends on the medium's refractive index and the incidence angle. The phenomenon is described by the Fresnel equations and, by extension, by the Mueller-Stokes formalism applied to Fresnel reflection and transmission.

Therefore, if we consider a beam of light incident at an angle  $i$  on a surface of refractive index  $n$ , then the degree of polarization of the reflected beam will be:

$$DoP_r = \left| \frac{\cos^2(\alpha_-) - \cos^2(\alpha_+)}{\cos^2(\alpha_-) + \cos^2(\alpha_+)} \right|, \quad (2.30)$$

whereas for the transmitted beam, we have

$$DoP_t = \left| \frac{\cos^2(\alpha_-) - 1}{\cos^2(\alpha_-) + 1} \right|, \quad (2.31)$$

where  $\alpha_- = i - r$ , and  $\alpha_+ = i + r$ , for  $r$  the refraction angle.

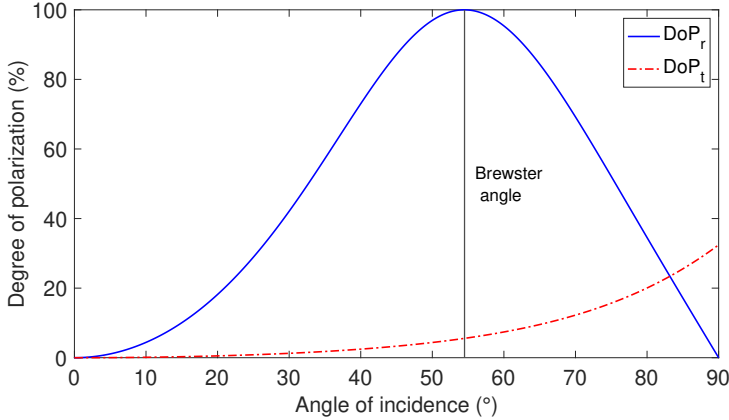


Figure 2.8: The degree of polarization corresponding to the reflected and transmitted beam after encountering a medium of refractive index  $n=1.4$ .

The reflected beam's polarization reaches a maximum of 100% when  $i + r = 90^\circ$ . The corresponding incidence angle is the Brewster angle (see Fig. 2.8). A surface acts like a linear polarizer. Because of this, its effect depends on the polarization of the incident light. Thus, considering that  $E_s$  and  $E_p$  are the components of the incident field which are perpendicular, respectively parallel to the plane of incidence, and  $R_s$ ,  $R_p$  the corresponding reflected components, then, using the notations proposed by (Collett, 1971, 2005), we have:

$$\begin{cases} \rho_s = \left( \frac{R_s}{E_s} \right)^2 = \left( \frac{\sin(\alpha_-)}{\sin(\alpha_+)} \right)^2 \\ \rho_p = \left( \frac{R_p}{E_p} \right)^2 = \left( \frac{\tan(\alpha_-)}{\tan(\alpha_+)} \right)^2 \end{cases} \quad (2.32)$$

Similarly, if  $T_s$ ,  $T_p$  are the transmitted components of the field, then, for transmission, we have:

$$\begin{cases} \tau_s = \left( \frac{T_s}{E_s} \right)^2 = \frac{\sin(2i)\sin(2r)}{\sin^2(\alpha_+)} \\ \tau_p = \left( \frac{T_p}{E_p} \right)^2 = \frac{\sin(2i)\sin(2r)}{\sin^2(\alpha_+)\cos^2(\alpha_-)} \end{cases} \quad (2.33)$$

How the Fresnel coefficients depend on the angle of incidence can be observed in Fig. 2.9. We notice here that the effect of the passage from one medium to another

depends on the polarization of the incident light. At the Brewster angle, the reflection of an incoming light polarized parallel to the incidence plane vanishes completely. This phenomenon can be used to establish the orientation of the transmission axis of a linear polarizer.

2

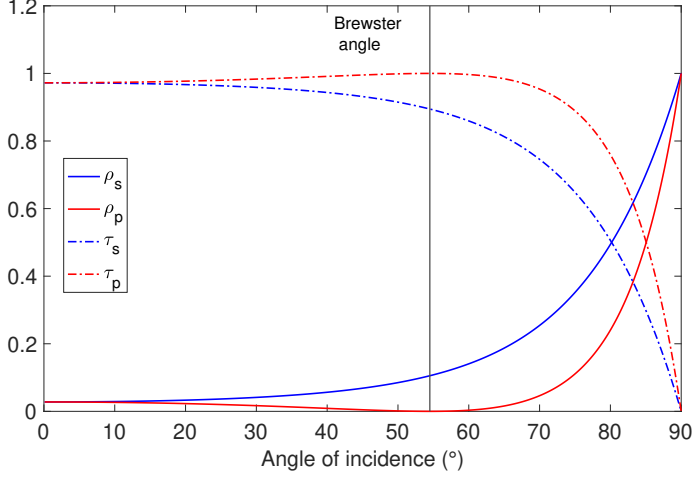


Figure 2.9: Fresnel coefficients for reflection ( $\rho$ ) and transmission ( $\tau$ ), for  $p$  and  $s$  states of polarization of the incoming beam.

The Mueller matrices associated with the reflection and transmission are:

$$M_{\rho} = \frac{1}{2} \begin{pmatrix} \rho_s + \rho_p & \rho_s - \rho_p & 0 & 0 \\ \rho_s - \rho_p & \rho_s + \rho_p & 0 & 0 \\ 0 & 0 & 2\sqrt{\rho_s \rho_p} & 0 \\ 0 & 0 & 0 & 2\sqrt{\rho_s \rho_p} \end{pmatrix} \quad (2.34)$$

$$M_{\tau} = \frac{1}{2} \begin{pmatrix} \tau_s + \tau_p & \tau_s - \tau_p & 0 & 0 \\ \tau_s - \tau_p & \tau_s + \tau_p & 0 & 0 \\ 0 & 0 & 2\sqrt{\tau_s \tau_p} & 0 \\ 0 & 0 & 0 & 2\sqrt{\tau_s \tau_p} \end{pmatrix} \quad (2.35)$$

In the case of the incidence on a birefringent material, the two light components are seeing different media; therefore, they are refracted differently. Consequently,  $\alpha_+$  and  $\alpha_-$  terms should be computed separately for the two components. In addition, an eventual split of rays would also require two different matrices for each type of ray.

# BIBLIOGRAPHY

- Collett, E. (1971). Mueller-stokes matrix formulation of fresnel's equations. *American Journal of Physics*, 39(5), 517–528. <https://doi.org/10.1119/1.1986205>
- Collett, E. (2005). *Field guide to polarization*. SPIE. <https://doi.org/10.1117/3.626141>
- del Toro Iniesta, J. C. (2003). *Introduction to spectropolarimetry*. Cambridge University Press.
- Givens, C. R., & Kostinski, A. B. (1993). A simple necessary and sufficient condition on physically realizable mueller matrices. *Journal of Modern Optics*, 40(3), 471–481. <https://doi.org/10.1080/09500349314550471>
- Goldstein, D. H. (2011). *Polarized light*. Taylor; Francis Group.
- Hecht, E. (2017). *Optics* (5 ed). Pearson Education, Inc.
- Hielscher, A., Eick, A., Mourant, J., Shen, D., Freyer, J., & Bigio, I. (1998). Diffuse backscattering mueller matrices of highly scattering media. *Optics express*, 1, 441–53. <https://doi.org/10.1364/OE.1.000441>
- Lu, S.-Y., & Chipman, R. A. (1996). Interpretation of Mueller matrices based on polar decomposition. *J. Opt. Soc. Am. A*, 13(5), 1106. <https://doi.org/10.1364/JOSAA.13.001106>
- Manhas, S., Swami, M. K., Buddhiwant, P., Ghosh, N., Gupta, P. K., & Singh, K. (2006). Mueller matrix approach for determination of optical rotation in chiral turbid media in backscattering geometry. *Opt. Express*, 14(1), 190–202. <https://doi.org/10.1364/OPEX.14.000190>
- The Materials Project* [Online; accessed August 06, 2024]. (2024). <https://next-gen.materialsproject.org/materials/mp-1249?formula=MgF2>
- Shurcliff, A. W. (1962). *Polarized light, production and use*. Harvard University Press.



# 3

## METHODS FOR THE MEASUREMENT OF POLARIZATION

*Polarizers come in many different configurations (...). There is, however, one underlying property that they all share: there must be some form of asymmetry associated with the process.*

E. Hecht



We saw in the previous chapter that any polarization state can be described using the four parameters of the Stokes vector. Polarization measurement means determining these parameters. Consequently, when the polarization recovery can be formulated as a system of equations, at least four measurements are required. In practice, however, the complete determination of polarization may require more than four measurements. The presence of noise is one of the main factors that dictate the use of a larger number of measurements. Over time, two significant directions emerged for the polarization measurement (del Toro Iniesta, 2003; Dong and Zhou, 2020; Mignani et al., 2019; Tyo et al., 2006). One, called division of aperture, supposes light split into multiple channels with different optical configurations. Each channel provides access to a Stokes parameter or a well-established combination of them. Finally, polarization determination is generally done by solving equations that have as unknown the Stokes parameters. Since constructing optical channels with different configurations usually requires a larger volume of deployment of the optical elements and can also become extremely expensive, this procedure tends to use the minimum number of necessary equations. The second approach, called time division, operates by sequential measurements. Particular modulation schemes are produced by rotating specific components within the instrument or changing their properties (birefringence, fast axis orientation) with a defined temporal frequency. Each new measurement provides a light intensity value that depends on the instantaneous configuration of the optical system as well as the polarization state of the incident light. The measured intensity values constitute a modulation containing information about the light's polarization state. Using different demodulation techniques of this signal, such as fitting with a theoretical function or Fourier transforms, the four Stokes parameters can finally be recovered. When addressing the need to determine the full Stokes vector, both methods are difficult to use in the space environment and have significant drawbacks (Hagen and Kudenov, 2013; Tyo et al., 2006). Therefore, the first method often involves considerable bulk and possible redundancy of some optical components. Its drawbacks are the risk of misalignment or limitations related to the visual field. Over time, however, this approach became increasingly compact and adapted much better to the rigors of use in outer space. The second method presents a higher risk, especially due to the rotating elements.

### 3.1. MEASURING THE POLARIZATION

Perhaps one of the easiest ways to measure any polarization is to take several measurements using only a linear polarizer, then add a quarter-wave plate (*QWP*) in front of this element, and take one more measurement (Collett, 2005). Therefore, if one uses only a linear polarizer oriented at an angle  $\theta$  to the  $x$ -axis of the reference frame (see Fig. 3.1), then, according to Eqs. (2.18, 2.25), the detected intensity is:

$$I = \frac{1}{2} \left( S_0 + S_1 \cos(2\theta) + S_2 \sin(2\theta) \right). \quad (3.1)$$

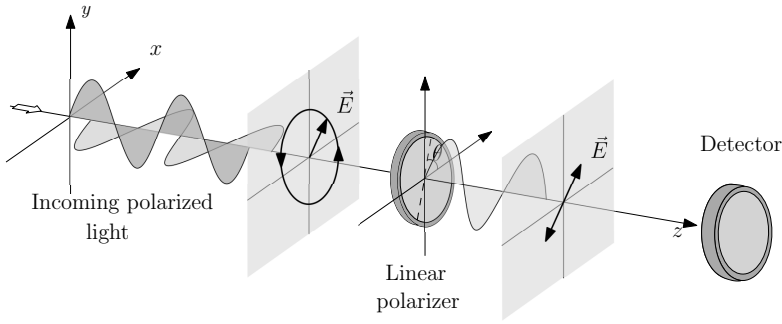


Figure 3.1: The first setup structure required for polarization measurement comprises only a linear polarizer and a detector. The dashed line indicates the orientation of the transmission axis of the linear polarizer.

The unknowns  $S_0$ ,  $S_1$ , and  $S_2$  can be retrieved using three different values for  $\theta$ . For instance, one can use:

$$\begin{cases} \theta = 0^\circ \Rightarrow I_0 = \frac{1}{2}(S_0 + S_1) \\ \theta = 90^\circ \Rightarrow I_{90} = \frac{1}{2}(S_0 - S_1) \\ \theta = 45^\circ \Rightarrow I_{45} = \frac{1}{2}(S_0 + S_2) \end{cases}, \quad (3.2)$$

where  $I_0$ ,  $I_{90}$ , and  $I_{45}$  are the detected intensities for the three different orientations of the linear polarizer. Solving for  $S_0$ ,  $S_1$  and  $S_2$  we obtain:

$$\begin{cases} S_0 = I_0 + I_{90} \\ S_1 = I_0 - I_{90} \\ S_2 = 2I_{45} - (I_0 + I_{90}) \end{cases}. \quad (3.3)$$

Of course, no information about the circular state of polarization can be obtained with only a linear polarizer. Adding instead a *QWP*, oriented at  $0^\circ$ , in front of the polarizer allows us to convert the circular polarization into linear and to change the handedness of the circular polarization (see Fig. 3.2). Thus, the expression of intensity becomes:

$$I = \frac{1}{2} \left( S_0 + S_1 \cos(2\theta) + S_3 \sin(2\theta) \right). \quad (3.4)$$

With this configuration,  $S_3$  can be accessed. Placing, for instance, the linear polarizer with the transmission axis at  $45^\circ$  to the horizontal, we obtain:

$$\theta = 45^\circ \Rightarrow I_{Q45} = \frac{1}{2}(S_0 + S_3), \quad (3.5)$$

where  $I_{Q45}$  is the detected intensity with this optical configuration.

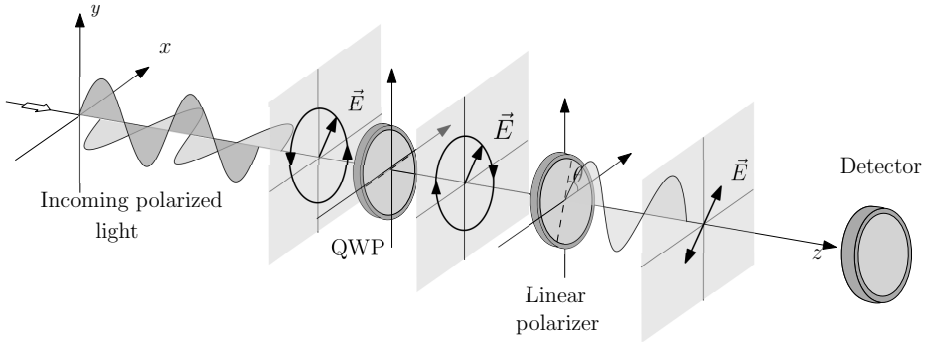


Figure 3.2: The second setup structure required for the retrieval of the  $S_3$  parameter. A *QWP* was added in front of the linear polarizer.

Using (3.3) the value of  $S_3$  is immediately retrieved:

$$S_3 = 2I_{Q45} - (I_0 + I_{90}). \quad (3.6)$$

The equations (3.2) and (3.5) can be written in a system:

$$\begin{cases} I_0 = \frac{1}{2}(S_0 \cdot 1 + S_1 \cdot 1 + S_2 \cdot 0 + S_3 \cdot 0) \\ I_{90} = \frac{1}{2}(S_0 \cdot 1 + S_1 \cdot (-1) + S_2 \cdot 0 + S_3 \cdot 0) \\ I_{45} = \frac{1}{2}(S_0 \cdot 1 + S_1 \cdot 0 + S_2 \cdot 1 + S_3 \cdot 0) \\ I_{Q45} = \frac{1}{2}(S_0 \cdot 1 + S_1 \cdot 0 + S_2 \cdot 0 + S_3 \cdot 1) \end{cases}. \quad (3.7)$$

This is a very simple procedure for measuring the polarization of light. However, even such a rudimentary approach can be challenging to be converted into a robust and reliable instrument. First, it must be underlined that this procedure does not measure the polarization instantly. It supposes the existence of four independent measurements conducted with different configurations at different moments in time. In addition, we saw that three rotations of the linear polarizer are required, as well as the insertion of a *QWP* for the last measurement. All these rotations and changes in the optical configuration can become extremely challenging and risky when implementing the method in a space instrument. Coming back to the Eq. (3.7), by using a matrix form, one can write:

$$\begin{pmatrix} I_0 \\ I_{90} \\ I_{45} \\ I_{Q45} \end{pmatrix} = \frac{1}{2} \begin{pmatrix} 1 & 1 & 0 & 0 \\ 1 & -1 & 0 & 0 \\ 1 & 0 & 1 & 0 \\ 1 & 0 & 0 & 1 \end{pmatrix} \cdot \begin{pmatrix} S_0 \\ S_1 \\ S_2 \\ S_3 \end{pmatrix}. \quad (3.8)$$

Let us consider that  $\vec{I} = (I_0, I_{90}, I_{45}, I_{Q45})^T$  is the vector of intensities detected during this polarization measurement procedure,  $T$  representing the transposition operator, and  $\vec{S} = (S_0, S_1, S_2, S_3)^T$  is the incoming Stokes vector. The overall determination of  $\vec{S}$ , embraces then the following form:

$$\vec{I} = \frac{1}{2} \underbrace{\begin{pmatrix} 1 & 1 & 0 & 0 \\ 1 & -1 & 0 & 0 \\ 1 & 0 & 1 & 0 \\ 1 & 0 & 0 & 1 \end{pmatrix}}_W \cdot \vec{S}, \quad (3.9)$$

where  $W$  is called the procedure's modulation scheme (or the modulation matrix). When four measurements are performed to measure the incoming Stokes vector,  $W$  is invertible if it is not singular, and the polarization can be immediately assessed:

$$\vec{S} = W^{-1} \cdot \vec{I}. \quad (3.10)$$

It should be underlined that in the literature, the factor  $1/2$  is very often omitted from the definition of the modulation scheme, even if it is present in the modulation and the demodulation procedure.

### 3.2. THE ASSESSMENT OF THE MODULATION SCHEME

Most polarimeters designed for the complete measurement of polarizations use the previously described principle, based on the production of a modulation scheme,  $W$ . Since this modulation can take countless forms, leading all the time to the same Stokes parameters, insightful procedures for comparing different modulation schemes have been developed over time. This allows the comparison of the working principle of the instruments as well as the achievable performance. However, it should be stressed that these figures of merit apply only to what we call full Stokes polarimetry, i.e., the methods capable of retrieving any state of polarization. Instruments that only aim to determine linear or circular polarizations elude these procedures. However, this has no consequence on the quality of such instruments. A great example from this category is the SPEX instrument, described in the Addendum of this thesis.

#### 3.2.1. THE CONCEPT OF EFFICIENCY OF THE MODULATION

The modulation matrix  $W$  dictates the quality of a method for retrieving the Stokes parameters (del Toro Iniesta and Collados, 2000). It describes which kinds of measurements are conducted and which changes are operated in the optical system during the measurement procedure, and it also provides information about how external factors like misalignment, spectral resolution, or noise could influence polarization determination. All these factors are translated into a change of the recorded intensity, which propagates during the demodulation process in the retrieval of the Stokes parameters. Therefore, the quality of a method for determining polarization is related to how a variation of intensity, depending on various external factors, is transmitted in the computed Stokes parameters. An optimal modulation scheme was defined as one able to minimize the propagation of errors and, accordingly, to minimize the uncertainty on the Stokes parameters (del Toro Iniesta, 2003; del Toro Iniesta and Collados, 2000).

If for the  $W$  matrix we use most often the name of modulation matrix, then  $W^{-1}$  is known as the demodulation (or instrumental matrix). For simplicity, we adopt here the notation  $D = W^{-1}$ .

Significant theoretical advancements have been made in assessing the modulation matrices when the source of uncertainties is the photon noise. Thus, if all the readings of intensity comprised in the vector  $\vec{I}$  have the same uncertainty  $\sigma$ , due to the photon noise, then, according to (del Toro Iniesta and Collados, 2000), the uncertainties on the Stokes parameters are:

$$\sigma_i^2 = \sigma^2 \sum_{j=0}^{N-1} D_{ij}^2, \quad i = 0, 1, 2, 3, \quad (3.11)$$

where  $N$  represents the number of measurements (here,  $N = 4$ ),  $i$  refers to the Stokes parameters, and  $\sigma$  is the photon noise, which is the same for all the measurements.

For the example studied above and having the modulation matrix  $W$  from Eq. (3.9), the demodulation matrix is:

$$D = W^{-1} = \begin{pmatrix} 1 & 1 & 0 & 0 \\ 1 & -1 & 0 & 0 \\ -1 & -1 & 2 & 0 \\ -1 & -1 & 0 & 2 \end{pmatrix}. \quad (3.12)$$

That means the uncertainty corresponding to the four Stokes parameters are:

$$\begin{cases} \sigma_0^2 = 2\sigma^2 \\ \sigma_1^2 = 2\sigma^2 \\ \sigma_2^2 = 6\sigma^2 \\ \sigma_3^2 = 6\sigma^2 \end{cases}. \quad (3.13)$$

We learn from this that, despite the fact that the system of equations built to retrieve the Stokes parameters grants equal access to all four terms of the Stokes vector, it does not form the best method. The linear ( $45^\circ$ ,  $135^\circ$ ) polarizations and the circular left and right are more affected by noise than the other two parameters.

Comparing the uncertainties of different modulation schemes is a good strategy to assess the quality of a method for the determination of polarization as long as the number of measurements remains unchanged. When the modulation schemes use different numbers of measurements, the associated  $W$  matrices have different numbers of lines, and consequently,  $D$  will have different numbers of columns. In order to make possible a correct comparison of the modulation schemes, Toro Iniesta (del Toro Iniesta and Collados, 2000) introduced then the modulation scheme's efficiency concept. It is closely related to the uncertainty, but it is normalized with the number of measurements,  $N$ :

$$\begin{cases} \xi_i = \frac{1}{\sqrt{N \sum_{j=0}^{N-1} D_{ij}^2}}, \quad i = 0, 1, 2, 3 \\ \xi_{tot} = \sqrt{\xi_1^2 + \xi_2^2 + \xi_3^2} \end{cases}, \quad (3.14)$$

where  $\xi_i$  are the efficiencies associated to the Stokes parameters, and  $\xi_{tot}$  is the total efficiency of the modulation scheme. If the factor  $1/2$  is not comprised in the definition of  $W$ , as is often the case in the literature, then the previous expression must be multiplied

by 2. A certain efficiency  $\xi_i$  characterizes each parameter of the Stokes vector. It can be proved (del Toro Iniesta, 2003), that the average uncertainty affecting a Stokes parameter is related to the efficiency of the modulation scheme through:

$$\overline{\sigma_i}^2 = \frac{\sigma^2}{\xi_i^2}, \quad (3.15)$$

which means that the accuracy of the Stokes parameters increases with the efficiency. The higher the efficiency for a Stokes parameter, the lower the uncertainty that we may have for this parameter.

Returning to our example from the beginning of the chapter, we can compute these efficiencies with the help of the matrix  $D$  (Eq. (3.12)) and  $N = 4$ :

$$\begin{cases} \xi_0 = 0.7071 \\ \xi_1 = 0.7071 \\ \xi_2 = 0.4082 \\ \xi_3 = 0.4082 \\ \xi_{tot} = \sqrt{\xi_1^2 + \xi_2^2 + \xi_3^2} = 0.9129 \end{cases} . \quad (3.16)$$

That means the imagined polarimeter can provide better results for measuring  $S_0$  and  $S_1$  terms than for  $S_2$  and  $S_3$ . This will be translated into an uncertainty almost double for  $S_2$  and  $S_3$  than for the rest of the Stokes terms in the presence of noise. This result perfectly agrees with Eq. (3.13).

Having a criterion to compare different methods for determining polarization is not enough. We have also to know where to stop the process of amelioration. For this purpose, an optimum modulation matrix is needed. Two situations may occur:

1. *The polarimeter is an ideal one.*

In this case, the lines of the matrix  $W$ , representing the diattenuation vector of the Mueller matrix of the polarimeter, have the property:

$$\sum_{i=1}^3 W_{ji}^2 = 1, \quad j = 0, 1, 2, \dots, N-1, \quad (3.17)$$

For this case, it has been proved (del Toro Iniesta, 2003; del Toro Iniesta and Collados, 2000) that  $W$  is an optimal modulation matrix if it converges towards a value satisfying the relation:

$$W^T W = N \begin{pmatrix} 1 & 0 & 0 & 0 \\ 0 & \xi_1^2 & 0 & 0 \\ 0 & 0 & \xi_2^2 & 0 \\ 0 & 0 & 0 & \xi_3^2 \end{pmatrix}, \quad (3.18)$$

where  $\sqrt{\xi_1^2 + \xi_2^2 + \xi_3^2} = 1$ .

The maximum values of the efficiencies which can be attained are:

$$\xi_{max,i}^2 = \frac{\sum_{j=0}^{N-1} W_{ji}^2}{N}, \quad i = 0, 1, 2, 3, \quad (3.19)$$

In the best case, when efficiencies on the Stokes parameters are the same, we have  $\xi_i = 1/\sqrt{3}$ , for all three parameters  $S_1$ ,  $S_2$ , and  $S_3$ . This optimal modulation matrix ( $W$ ) has been defined starting from the idea that the  $D_{ij}$  terms must be minimized in order to obtain the highest efficiencies. The optimum demodulation matrix has then the form:

$$D = (W^T W)^{-1} \cdot W^T. \quad (3.20)$$

This expression is not a random one. As we will see in the next section, this is nothing else but the formulation of the pseudoinverse matrix of  $W$  when  $W$  has more than four lines.

## 2. The polarimeter is a non-ideal one.

In this case, the lines of the matrix  $W$  have the property:

$$\sum_{i=1}^3 W_{ji}^2 < 1, \quad j = 0, 1, 2, \dots, N-1, \quad (3.21)$$

Minimizing the  $D_{ij}$  terms is not a trivial task in this case. However, it has been proved that a matrix  $W$  that satisfies the relation:

$$W^T W = N \begin{pmatrix} \frac{\sum_{j=0}^{N-1} W_{j0}^2}{N} & 0 & 0 & 0 \\ 0 & \frac{\sum_{j=0}^{N-1} W_{j1}^2}{N} & 0 & 0 \\ 0 & 0 & \frac{\sum_{j=0}^{N-1} W_{j2}^2}{N} & 0 \\ 0 & 0 & 0 & \frac{\sum_{j=0}^{N-1} W_{j3}^2}{N} \end{pmatrix}, \quad (3.22)$$

where the diagonal terms represent the maximum accessible efficiencies. Like in the ideal scenario, the optimum demodulation matrix is defined by:

$$D = (W^T W)^{-1} \cdot W^T. \quad (3.23)$$

From the relations (3.18), (3.19) and (3.22), it results that ideal and non-ideal cases are converging towards the same values of the efficiencies.

### 3.2.2. CONDITION NUMBER AND EQUALLY WEIGHTED VARIANCE

Other figures of merit that can help us assess the quality of the modulation matrix in the presence of noise are the condition number ( $CN$ ) and the equally weighted variance ( $EWV$ ) (Foreman and Goudail, 2019; Goudail, 2016). The theoretical studies that treat these concepts generally use two interpretations of noise. On the one hand, it is considered the case where the noise is additive, originating in some of the components of the optical system (like the detector or the electronics). Such noise has a normal distribution and is called Additive White Gaussian Noise ( $AWGN$ ). This noise can be seen then as independent of the detected signal. On the other hand, the noise is related to the signal and, most precisely, to the counting of photons done with the help of the detector. This noise tends to be more significant at small signal values (small number of photons) and decreases with the number of photons. Both concepts, the condition number and the equally weighted variance, are discussed in the literature in relation to these two types of noise. Despite their mathematical equivalence, demonstrated by (Foreman and Goudail, 2019), the interpretations of the two concepts are slightly different. Thus, if the condition number informs about how well-suited a matrix is for inversion, the equally weighted variance, as defined in the case of a polarimeter, provides direct information on how optimal the modulation matrix is and which covariances on the Stokes parameters could be expected. In other words, the condition number tells us how the variations in the detected intensity due to the presence of noise are propagated into the retrieved values of the Stokes parameters. The equally weighted variance in exchange tells us if the modulation matrix we are using is close to an optimal one in terms of the previously described efficiency.

#### THE EQUALLY WEIGHTED VARIANCE (EWV)

In section 3.1, we saw the example of a method for determining polarization, which employs a configuration based on a linear polarizer and, eventually, a  $QWP$ . Using the Mueller calculus, we retrieved the modulation matrix  $W$  corresponding to this application. Considering now that a general Mueller matrix describes the instrument (see Eq. 2.17), then  $W$  can be written as:

$$W = \frac{1}{2} \begin{pmatrix} 1 & m_{01}^0 & m_{02}^0 & m_{03}^0 \\ 1 & m_{01}^1 & m_{02}^1 & m_{03}^1 \\ 1 & m_{01}^2 & m_{02}^2 & m_{03}^2 \\ \cdot & \cdot & \cdot & \cdot \\ \cdot & \cdot & \cdot & \cdot \\ 1 & m_{01}^{N-1} & m_{02}^{N-1} & m_{03}^{N-1} \end{pmatrix}, \quad (3.24)$$

where  $m_{0i}$  ( $i = 1, 2, 3$ ) are the terms of the diattenuation vector from the Mueller matrix of the optical system, and the superscript indicates the system's configuration.

In an ideal case, we need to have (del Toro Iniesta and Collados, 2000):

$$\sum_{i=1}^3 (m_{0i}^j)^2 = 1, \quad j = 0, 1, \dots, N-1. \quad (3.25)$$

Adopting the contracted notation used by (Foreman and Goudail, 2019), the relation (3.24) can be written as:



$$W = \frac{1}{2} \begin{pmatrix} 1 & \vec{w}_0^T \\ 1 & \vec{w}_1^T \\ \cdot & \cdot \\ \cdot & \cdot \\ 1 & \vec{w}_{N-1}^T \end{pmatrix} = \frac{1}{2} (\vec{r} \quad \mathbb{Q}), \quad (3.26)$$

where  $\vec{r}$  is a  $N \times 1$  vector with all the elements equal to 1, while  $\mathbb{Q}$  is a  $N \times 3$  matrix composed of the diattenuation vectors of the modulation scheme (see Eq. (3.24)). In other words, we have:

$$\vec{r} = \begin{pmatrix} 1 \\ 1 \\ \cdot \\ \cdot \\ 1 \end{pmatrix}, \quad \text{and} \quad \mathbb{Q} = \begin{pmatrix} \vec{w}_0^T \\ \vec{w}_1^T \\ \cdot \\ \cdot \\ \vec{w}_{N-1}^T \end{pmatrix} = \begin{pmatrix} m_{01}^0 & m_{02}^0 & m_{03}^0 \\ m_{11}^0 & m_{12}^0 & m_{13}^0 \\ m_{21}^0 & m_{22}^0 & m_{23}^0 \\ \cdot & \cdot & \cdot \\ \cdot & \cdot & \cdot \\ m_{01}^{N-1} & m_{02}^{N-1} & m_{03}^{N-1} \end{pmatrix}, \quad (3.27)$$

where, just like before, the superscript  $T$  designates the transposition operator. One of the problems with polarimeters using more than four measurements is that the modulation matrix  $W$  is no longer invertible. Consequently, relation (3.10) cannot be applied directly. We can use either the left inverse (the pseudoinverse) or the singular value decomposition to retrieve the inverse of  $W$ . According to the left inverse method, the pseudoinverse of  $W$  is:

$$W^\dagger = (W^T W)^{-1} W^T, \quad (3.28)$$

which is nothing else than the optimum demodulation matrix presented in the previous section. This expression can be used if the product  $W^T W$  is well-conditioned for inversion. When this is no longer possible, the singular value decomposition (SVD) can be used. For the moment, however, we will consider that the left inverse could be applied successfully.

Therefore, coming back to the problem of the measurement in the presence of noise, if we imagine that we are dealing with additive Gaussian noise, then the detected intensity is:

$$\vec{I} = W \cdot \vec{S} + \vec{\Delta}I, \quad (3.29)$$

where  $\vec{\Delta}I$  is a  $N \times 1$  random vector of covariance  $\sigma^2 \cdot \mathbb{1}$ . Multiplying at left (3.29) with  $W^\dagger$  we obtain:

$$W^\dagger \vec{I} = \vec{S} + W^\dagger \sigma^2. \quad (3.30)$$

Adopting the notation  $\hat{S} = W^\dagger \vec{I}$ , this relation becomes:

$$\hat{S} = \vec{S} + W^\dagger \sigma^2. \quad (3.31)$$

Therefore,  $\hat{S}$  is nothing else but a maximum likelihood estimate of  $\vec{S}$ . It is a vector that has  $\vec{S}$  as a mean value, and the covariance matrix:

$$\mathbb{K}_{\vec{s}} = \sigma^2 W^\dagger (W^\dagger)^T. \quad (3.32)$$

Using the algebraic properties of the transposition operator it is immediate that:

$$\mathbb{K}_{\vec{s}} = \sigma^2 (W^T W)^{-1}. \quad (3.33)$$

The diagonal elements of  $\mathbb{K}_{\vec{s}}$  represent the variances on the Stokes parameters. A modulation matrix  $W$  is then considered optimal when the covariances on the Stokes parameters reach the minimum. In other words, we need to have  $Tr(\mathbb{K}_{\vec{s}}) = \min$ , where  $Tr$  is the trace operator. This condition is identical to the one used by del Toro Iniesta to evaluate the optimal modulation scheme, as we already saw in the previous section.

The concept of equally weighted variance ( $EWV$ ) has been introduced in this context. It represents the trace of the covariance matrix and should be minimal for optimal modulation.

$$EWV(W) = Tr(\mathbb{K}_{\vec{s}}). \quad (3.34)$$

In the presence of additive Gaussian noise,  $EWV$  is:

$$EWV(W) = \sigma^2 Tr[(W^T W)^{-1}]. \quad (3.35)$$

It has been proven (Foreman and Goudail, 2019) that the product  $(W^T W)$  which can minimize the  $EWV$  has the form:

$$W^T W = \frac{N}{12} \begin{pmatrix} 3 & 0 & 0 & 0 \\ 0 & 1 & 0 & 0 \\ 0 & 0 & 1 & 0 \\ 0 & 0 & 0 & 1 \end{pmatrix}. \quad (3.36)$$

Consequently, the covariance matrix of an optimal modulation scheme is:

$$\mathbb{K}_{\vec{s}} = \frac{4}{N} \sigma^2 \begin{pmatrix} 1 & 0 & 0 & 0 \\ 0 & 3 & 0 & 0 \\ 0 & 0 & 3 & 0 \\ 0 & 0 & 0 & 3 \end{pmatrix}. \quad (3.37)$$

Therefore, the minimum value of the  $EWV$  in the presence of Gaussian noise is  $\frac{40}{N} \sigma^2$ . Relation (3.37) also tells us that, ideally, when the modulation scheme can provide access with equal uncertainties to the Stokes parameters  $S_1$ ,  $S_2$ , and  $S_3$ , these uncertainties are three times higher for  $S_1$ ,  $S_2$ , and  $S_3$  than for  $S_0$ . Knowing the intensity value and noise variance can give us a clear idea about the achievable precision of the Stokes parameters.

On the other hand, if a non-additive Poisson noise perturbs the system, then the vector  $\vec{\Delta}_I$  is no longer of covariance  $\sigma^2 \cdot \mathbb{1}$ . Instead, its covariance will depend on the Stokes parameters. Therefore, the elements of the covariance matrix of  $\vec{S}$  are (Dai et al., 2018; Goudail, 2009):

$$(\mathbb{K}_{\vec{s}})_{ij} = \sum_{k=0}^3 S_k \sum_{n=0}^{N-1} W_{in}^\dagger W_{jn}^\dagger W_{nk} \quad , \quad i, j = 0, \dots, 3. \quad (3.38)$$

If  $W$  is an optimal matrix, then the diagonal elements of the covariance matrix converge towards:

$$\begin{cases} (\mathbb{K}_{\vec{s}})_{00} = \frac{2S_0}{N} \\ (\mathbb{K}_{\vec{s}})_{jj} = \frac{6S_0}{N} \end{cases}, \quad j = 1, 2, 3 \quad (3.39)$$

Therefore, the minimum value of the  $EWV$  in the presence of Poissonian noise is  $\frac{20S_0}{N}$ . As expected, the variations of the Stokes parameters in the presence of a non-additive noise are related to the intensity ( $S_0$ ). As with Gaussian noise, they are three times larger for  $S_1$ ,  $S_2$ , and  $S_3$  than for  $S_0$ , but the correlation term is now the intensity,  $S_0$ . On the other hand, both results demonstrate that increasing the number of measurements has, as a consequence, a decrease in uncertainty. The only condition is that the number of measurements should not be increased by reducing the optimal quality of the matrix  $W$ . This must remain an optimal matrix.

### THE CONDITION NUMBER

Another metric that can be used to assess the quality of a modulation scheme is represented by the condition number ( $\kappa$ ). This is an algebraic notion with a more subtle meaning. A brief mathematical description can prove very useful for understanding it (Belsley et al., 1980). The condition number applies to a system of linear equations of the type  $A\vec{x} = \vec{b}$ , where  $A$  is an invertible matrix,  $\vec{x}$  is the vector of unknowns, and  $\vec{b}$  represents the vector of the linear equations' solutions. For various reasons, such as noise, systemic problems, etc.,  $\vec{b}$  can record a  $\delta\vec{b}$  variation about the expected value. This will eventually translate into a variation of the determined solutions  $\delta\vec{x}$ . The same is true if matrix  $A$  undergoes a change  $\delta A$ . There may be situations when a slight variation of  $\delta\vec{b}$  or  $\delta A$  can lead to an explosion of  $\delta\vec{x}$ . In other words, returning to the studied polarimetric system, a small variation of the detected intensity or the modulation matrix can cause an extremely large error in the measured polarization. The extent of this phenomenon is determined exclusively by the matrix  $A$ . Thus, let us write the general system of linear equations:

$$A \cdot \vec{x} = \vec{b}, \quad (3.40)$$

and suppose that the matrix  $A$  does not undergo any changes now. There is only a change  $\delta\vec{b}$ , which triggers a variation  $\delta\vec{x}$  of the solution:

$$A \cdot (\vec{x} + \delta\vec{x}) = \vec{b} + \delta\vec{b}. \quad (3.41)$$

Multiplying at left by  $A^{-1}$  we obtain:

$$\vec{x} + \delta\vec{x} = A^{-1}\vec{b} + A^{-1}\delta\vec{b}. \quad (3.42)$$

Therefore, we can write:

$$\delta\vec{x} = A^{-1}\delta\vec{b}. \quad (3.43)$$

Taking the norm of this expression and using the property that tells us that  $\|AB\| \leq \|A\| \cdot \|B\|$ , true for any  $m \times n$  matrices, we obtain:

$$\|\vec{\delta x}\| \leq \|A^{-1}\| \cdot \|\vec{\delta b}\|. \quad (3.44)$$

Applying the norm to the Eq. (3.40):

$$\|\vec{b}\| \leq \|A\| \cdot \|\vec{x}\|. \quad (3.45)$$

In the end, by multiplying the relations (3.44) and (3.45) we obtain:

$$\frac{\|\vec{\delta x}\|}{\|\vec{x}\|} \leq \|A\| \cdot \|A^{-1}\| \cdot \frac{\|\vec{\delta b}\|}{\|\vec{b}\|}. \quad (3.46)$$

From here, we can define the condition number associated to the matrix  $A$ :

$$\kappa(A) = \|A\| \cdot \|A^{-1}\| \geq \frac{\left(\frac{\|\vec{\delta x}\|}{\|\vec{x}\|}\right)}{\left(\frac{\|\vec{\delta b}\|}{\|\vec{b}\|}\right)}. \quad (3.47)$$

Similarly, if we suppose that the cause of the variation of  $\vec{b}$  is a variation of  $A$ , we can quickly obtain:

$$\kappa(A) = \|A\| \cdot \|A^{-1}\| \geq \frac{\left(\frac{\|\vec{\delta x}\|}{\|\vec{x} + \vec{\delta x}\|}\right)}{\left(\frac{\|\delta A\|}{\|A\|}\right)}. \quad (3.48)$$

That means the condition number is the ratio between the relative error on the unknowns of the system and the relative error on solutions of the systems. Translated into the domain of polarimetry, where the place of the matrix  $A$  is taken by  $W$ , the condition number will represent the ratio between the relative error on the Stokes parameters and the relative variation of the intensity.

A high value of the condition number signifies that slight variations in the detected intensities are converted into significant variations of the retrieved Stokes parameters. While the equally weighted variance deals with noise propagation, the condition number only refers to the  $W$  matrix. Therefore, it can help assess the impact of the systematic errors.

Optimizing the modulation matrix means finding the form with the smallest  $\kappa$ .

Using the relations (3.47), (3.48), and (3.28) we have:

$$\kappa(W) = \|W\| \cdot \|W^\dagger\|. \quad (3.49)$$

Considering that the norm is the Frobenius norm, we can write:

$$\|W\| = \sqrt{\text{Tr}(WW^T)} = \sqrt{\text{Tr}(W^T W)}. \quad (3.50)$$

Based on (3.36) we have:

$$\|W\| = \sqrt{\text{Tr}(W^T W)} = \sqrt{\frac{N}{2}}, \quad (3.51)$$

and, from (3.33, 3.37):

$$\|W^\dagger\| = \sqrt{\text{Tr}((W^\dagger)^T W^\dagger)} = \sqrt{\text{Tr}[(W^T W)^{-1}]} = \sqrt{\frac{40}{N}}. \quad (3.52)$$

Therefore, based on (3.49), (3.51) and (3.52), the minimal value of the condition number, corresponding to an optimal modulation matrix is:

$$\kappa(W) = \sqrt{\frac{N}{2}} \cdot \sqrt{\frac{40}{N}} = \sqrt{20} \approx 4.472. \quad (3.53)$$

### 3.3. EXAMPLES OF INSTRUMENTS

As mentioned at the beginning of this work, two important directions have developed over time in polarization measurement methods. One of the directions, known under the name of temporal division, calls for a repetitive modification of the optical system to produce new configurations that generate the modulation matrix  $W$ . Each line of this matrix is produced at a specific moment in time so that in addition to the integration time of the polarimetric signal at the detector level, the instrument also requires time to pass from one configuration to another. This additional measurement delay is one of the main impediments of this method when it comes to its application to scenes with very fast polarimetric dynamics.

The second method, called aperture division, uses several optical channels with different polarimetric configurations simultaneously. The  $N$  measurements of the modulation scheme are performed simultaneously. The immediate advantage of this technique is that the possible delays generated by the preparation of a new configuration, faced by time division, are eliminated. A possible disadvantage is that the light flux is divided between several channels, which causes a decrease in the detected intensity at the level of each channel. Consequently, noise can become more problematic for this measurement method, especially in conditions where the integration time of the detector cannot be extended very much.

When dealing with stable polarimetric scenes, temporal division can be more robust than the aperture division method. In addition, the division of time remains open, in general, to other polarization determination procedures, such as the fit with a theoretical function or the isolation of specific frequencies associated with different types of polarization.

Both methods present an important series of advantages and disadvantages. The aspects that weigh the most in adopting one method or the other depend on the type and field of application. Otherwise, both methods can lead to the formation of optimal modulation schemes and can embrace the form of highly performing instruments. The main advantages and disadvantages of these methods, valid for any field of application, are summarized in Tables 3.1 and 3.2.

Most of the time, the advantages of the temporal method pale in comparison to the disadvantages when it comes to spatial applications. The risks of misalignment of optical

<b>Division of time</b>	
<b>Advantages</b>	<b>Disadvantages</b>
Tunable modulation schemes	Difficulties with very dynamic scenes
Low impact of noise	Risk related to misalignment
Can accept multiple demodulation procedures Rotating mechanism	Compute-intensive demodulation

Table 3.1: Main advantages and disadvantages of the division of time procedure

<b>Division of aperture</b>	
<b>Advantages</b>	<b>Disadvantages</b>
Can deal with very dynamic scenes	Higher impact of noise
Low risk of misalignment	Voluminous
Fast demodulation	Frozen modulation scheme

Table 3.2: Main advantages and disadvantages of the division of aperture procedure

components or the difficulties of monitoring scenes with rapidly changing polarization make this method one with limited applicability.

Due to the greater interest in the static aperture division method when it comes to space applications, we have chosen to present some examples of tools based on this approach in the following section. At the same time, based on the available data, the modulation schemes' efficiency, the equally weighted variances, and the condition number are computed and compared for these examples.

### 3.3.1. DOAP SPECTROPOLARIMETER

An excellent example of the division of aperture instrument for complete Stokes determination is the one proposed by (Compain and Drevillon, 1998) (see Fig. 3.1). This is one of the possible developments from a principle devised by Azzam in 1982 (Azzam, 1982). The advantage of the design (called DOAP) is that it can be easily tuned to achieve high efficiency in the modulation scheme. The working principle supposes the split of the incoming light into two directions with the help of an uncoated dielectric prism (see Fig. 3.3).

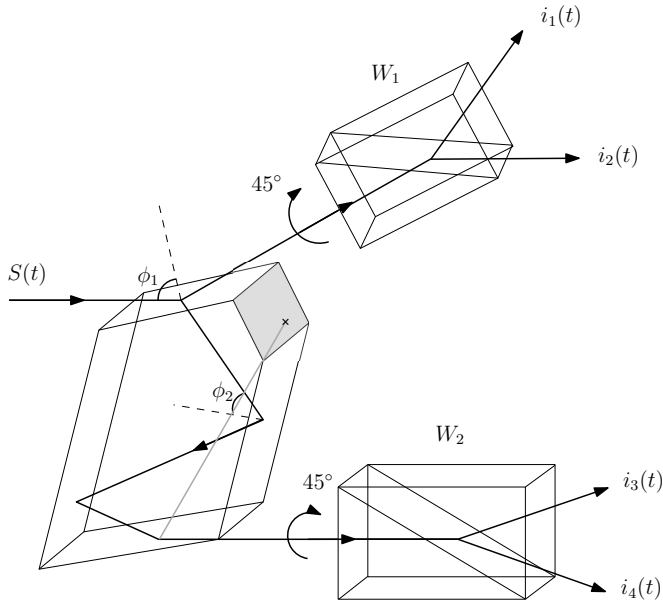


Figure 3.3: Experimental design of DOAP. Figure adapted after (Compain and Drevillon, 1998).

The two beams, reflected and transmitted, have a polarization depending on the angles of incidence  $\phi_1$  and  $\phi_2$  and on the refractive index of the prism. Further, these two beams pass through a Wollaston prism ( $W_1$  and  $W_2$ ), separating the incident polarization's orthogonal components. Four beams will arrive on the detectors, carrying the intensities  $i_1$ ,  $i_2$ ,  $i_3$  and  $i_4$ .

The modulation matrix ( $W$ ) associated with this method of determining polarization can be theoretically computed for various wavelengths with the help of the Fresnel terms for transmission and reflection.

For instance, according to (Compain and Drevillon, 1998), the theoretical value of  $W$  for  $\lambda = 458 \text{ nm}$  is :

$$W = \begin{pmatrix} 1 & -0.577 & 0.816 & 0 \\ 1 & -0.577 & -0.816 & 0 \\ 1 & 0.619 & -0.065 & 0.782 \\ 1 & 0.619 & 0.065 & -0.782 \end{pmatrix}. \quad (3.54)$$

Applying the relations (3.14) and (3.20), the efficiencies of this scheme can be easily computed:

$$\begin{cases} \xi_0 = 0.999 \\ \xi_1 = 0.598 \\ \xi_2 = 0.577 \\ \xi_3 = 0.512 \\ \xi_{tot} = \sqrt{\xi_1^2 + \xi_2^2 + \xi_3^2} = 0.997 \end{cases}. \quad (3.55)$$

Using the relation (3.49), the condition number of the matrix  $W$  can also be computed:

$$\kappa(W) = 4.4915. \quad (3.56)$$

It can be noticed that the values of the efficiencies are very close to the ideal ones ( $1/\sqrt{3} \approx 0.5774$ ). However, a slight difference exists between the three parameters, translated into the fact that the uncertainty on  $S_1$  will be the smallest, while that on the circular polarization will be the highest. On the other hand, the value of the condition number, which is also slightly different from the optimal one (4.472), is another hint that the  $W$  matrix is not optimal. The conditions for a  $W$  matrix to be optimal are expressed by the relations (3.18) and (3.20). In the case studied here, we can find that the product  $W^T W$  is:

$$W^T W = 4 \begin{pmatrix} 1 & 0.021 & 0 & 0 \\ 0.021 & 0.358 & 0 & 0 \\ 0 & 0 & 0.335 & -0.0254 \\ 0 & 0 & -0.0254 & 0.3058 \end{pmatrix}. \quad (3.57)$$

This matrix differs from the form obtained when  $W$  is optimal. In conclusion, we can say that the polarimeter model presented here is very close to an ideal one, ensuring an almost equal uncertainty on Stokes parameters. However, it is expected to work better to determine the linear polarization.

### 3.3.2. SFSIP IMAGING SPECTROPOLARIMETER

Another example of a division aperture instrument is the one proposed by (Mu et al., 2015). The snapshot full-Stokes imaging polarimeter (*SFSIP*), tested with a 480 nm bandpass filter ( $FWHM = 10$  nm), also reaches a very high modulation efficiency and, through its geometry, can be considered a precursor of our project. The instrument uses an array of Wollaston prisms,  $WP_1$ ,  $WP_2$ , and  $WP_3$  (see Fig. 3.4). The last one is coupled with a quarter-wave plate (*QWP*) situated in front. The orientation of the fast axes is indicated in Fig. 3.4. The three different compounds are followed by a lens array that projects six images of the object, each providing different polarimetric information.

Thus, the first Wollaston prism from the top will split the received beam into two beams carrying orthogonal polarizations (horizontal and vertical). The second Wollaston prism, from the middle, has the optical axes oriented at  $45^\circ$  and  $135^\circ$ , which will split the received light into two beams of orthogonal polarizations. We obtain information about  $45^\circ$  and  $135^\circ$  of linear polarization this time. Ultimately, the last compound of *QWP*+Wollaston will split the light according to the circular polarization. The emerging beams will be linearly polarized in orthogonal planes. However, their intensities will be related to the circular component of the incoming light. Therefore, in the end, on the detector, we will obtain 6 regions carrying information about linear ( $0^\circ$ ,  $90^\circ$ ,  $45^\circ$ ,  $135^\circ$ ) and circular (left and right) polarizations.

The ideal modulation matrix of this instrument is (Mu et al., 2015):



$$W = \begin{pmatrix} 1 & 1 & 0 & 0 \\ 1 & -1 & 0 & 0 \\ 1 & 0 & 1 & 0 \\ 1 & 0 & -1 & 0 \\ 1 & 0 & 0 & 1 \\ 1 & 0 & 0 & -1 \end{pmatrix}. \quad (3.58)$$

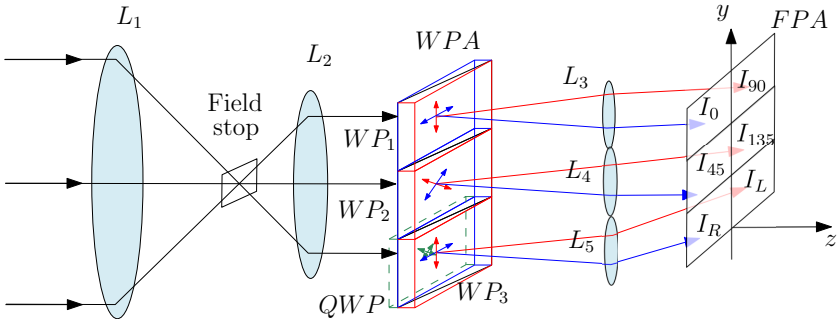


Figure 3.4: Design of the SFSIP imaging polarimeter. The part of the instrument responsible for the polarization measurement comprises three Wollaston prisms ( $WP_1$ ,  $WP_2$ ,  $WP_3$ ) and one QWP. The optical axes of each component are presented in blue and red. This instrument provides six images of the same object, each with a distinctive polarization: linear ( $0^\circ$ ,  $90^\circ$ ,  $45^\circ$ ,  $135^\circ$ ) degree and circular left and right. Figure adapted after (Mu et al., 2015)

The efficiencies, calculated with the relation 3.14 are:

$$\begin{cases} \xi_0 = 1 \\ \xi_1 = 0.5774 \\ \xi_2 = 0.5774 \\ \xi_3 = 0.5774 \\ \xi_{tot} = 1 \end{cases}. \quad (3.59)$$

These efficiencies are the highest achievable and correspond to an optimal modulation scheme. They show that equal uncertainties characterize the Stokes parameters. If we compute now the product  $W^T W$ , we obtain:

$$W^T W = 6 \begin{pmatrix} 1 & 0 & 0 & 0 \\ 0 & 0.333 & 0 & 0 \\ 0 & 0 & 0.333 & 0 \\ 0 & 0 & 0 & 0.333 \end{pmatrix}, \quad (3.60)$$

which proves that the  $W$  matrix is an optimal one. Also, the condition number for this case is  $\kappa(W) = 4.472$ , which is the smallest value achievable for a polarimeter. However, obtaining such a matrix in practice is almost impossible. The effect of the Wollaston prisms depends on the wavelength, and the extinction ratio is never zero. Thus, experimentally, the modulation matrix obtained in this case by the authors of the study was:

$$W = \frac{1}{2} \begin{pmatrix} 1.0846 & 0.9514 & -0.0040 & 0.0766 \\ 1.0778 & -0.9746 & -0.0098 & -0.0784 \\ 1.0910 & 0.0080 & 0.9558 & -0.0814 \\ 1.1052 & -0.0080 & -0.9624 & 0.0698 \\ 1.1596 & -0.0282 & 0.1122 & 0.8288 \\ 1.0510 & 0.0502 & -0.0940 & -0.8382 \end{pmatrix}. \quad (3.61)$$

Normalizing this matrix by 1.1596, we can compute the experimental efficiencies:

$$\begin{cases} \xi_0 = 0.9444 \\ \xi_1 = 0.4793 \\ \xi_2 = 0.4802 \\ \xi_3 = 0.4178 \\ \xi_{tot} = 0.7968 \end{cases}. \quad (3.62)$$

Therefore, we see that, in reality, the efficiencies are below the theoretical value, and equal uncertainties no longer characterize the retrieval of the Stokes parameters. The spectropolarimeter will perform the best for the measurement of the linear  $45^\circ$ ,  $135^\circ$  polarizations and the worst for the circular polarizations.

### 3.4. SPECTROPOLARIMETRY AND IMAGING SPECTROPOLARIMETRY

Measuring the polarization of light at different wavelengths can be of critical importance in a situation where the polarization is wavelength-dependent. We recall, for instance, that in the case of the Zeeman effect, the polarization was related to the spectral lines, which are only precise wavelength values. Also, in another field, such as climatology, detecting all polarization states at different wavelengths can drastically improve our knowledge of aerosols (Gassó and Knobelspiesse, 2022). This need is not manifested only in these two areas. Most of the time, as we will see in Chapter 8, the study of polarization from scattering requires a wider spectral coverage. This allows a much more precise identification of the sources of polarization. Going further and adding an imaging capability to a spectropolarimeter can increase the information obtained with such instruments. This feature would allow us to locate a scene's polarimetric characteristics precisely. Such property proves to be very important in domains that require precise identifications of the areas characterized by different polarimetric features. Medicine and defense are just two examples that can benefit from imaging spectropolarimetry. However, adding a spectral or spatial dimension to polarimetry complexifies the measurement of polarization even more. Most polarimetric measurements require a collimated beam passing at a precise angle through the modulating components. Because of this, these instruments are very limited in terms of field of view. In the same way, the polarizing elements used to modulate or analyze the polarization are spectrally dependent, and, therefore, ensuring good efficiency on a large waveband is also difficult.

Following the methods of polarimetry's division, imaging spectropolarimetry has evolved into a sequential approach and a snapshot approach (Hagen, 2012). Because we

are concerned here with the division of the aperture technique of polarimetry, snapshot imaging spectropolarimetry is the development that best suits our interests. A snapshot imaging spectropolarimeter is an instrument that simultaneously collects spatial, spectral, and polarimetric information in a single shot. Since spatial information is two-dimensional, all these data form a hypercube as a whole. An instantaneous spectropolarimeter can display such a hypercube layer by layer. The same scene (spatial coordinates  $(x, y)$ ) will be observed at different wavelengths, and for each "voxel", which is an elementary hypercube of information, spatial coordinates, spectral features, and polarimetric properties can be determined.

Snapshot imaging spectrometry is the basis of snapshot imaging spectropolarimetry. In most approaches, snapshot imaging spectrometry uses a diffractive element such as an optical prism, a grating, or a grism placed in the collimated part of the light stream. As we saw previously, the polarimeter also requires a collimated light. As a result, the best positioning of the polarimetric optics is right in front of the diffractive element in the same collimated region. The type of modulation required to extract the polarimetric information dictates the details of such an optical arrangement.

### 3.4.1. INTEGRAL FIELD SPECTROMETRY WITH LENSLET ARRAY (IFS-L)

For example, one of the methods used in imaging spectrometry is the Integral Field Spectrometry with Lenslet array (IFS-L) (Hagen, 2012; Hagen and Kudenov, 2013). The operating principle is presented in Fig. 3.5.

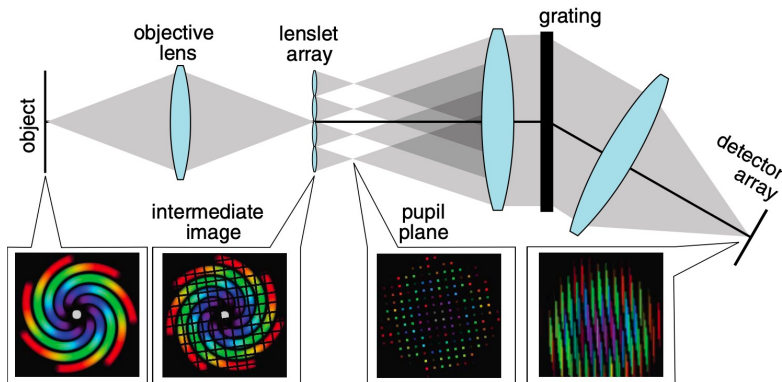


Figure 3.5: IFS-L principle. Source: (Hagen and Kudenov, 2013)

The light collected by an objective lens or a telescope is focused on a plane where a lenslet array is arranged. Each microlens will capture the light coming from different fields of view. A collimator placed after the microlens array leads to the collimation of the light coming from each field and to the image's magnification. The dispersion is subsequently applied in a direction dictated by the lenslet array's geometry to avoid the

images' superposition. Finally, the light is refocused on the detector.

The characteristic of such a design is that the lenslet array must lead to a smaller f-number than the objective lens, which can result in difficulty in obtaining separate images in the detector plane. The compromise found in practice to solve this difficulty is using a pinhole mask in tandem with the lenslet array at the cost of the quantity of light transmitted (Sugai et al., 2009).

An example of an instrument that uses the IFS-L principle is LATIS (Dwight and Tkaczyk, 2017). This instrument, designed for fluorescence microscopy, allows almost instantaneous access to multiple spectral bands of a scene (hyperspectral datacubes or lambda stacks) through a tunable optical design.

The operating principle closely repeats the IFS-L scheme. The peculiarity of the design lies in the fact that the lenslet array, with a hexagonal structure, can be rotated to avoid overlapping the spectral dispersion. In addition, the spectral dispersion can be adjusted by changing the focal distance of the collimator and reimaging optics.

Figure 3.6 illustrates how one can obtain an extension of the spectral dispersion by changing the focal length of the re-imaging optics. However, this measure leads to overlapping images from different targeted fields in the first step. To correct this effect, a rotation of the lenslet array is necessary.

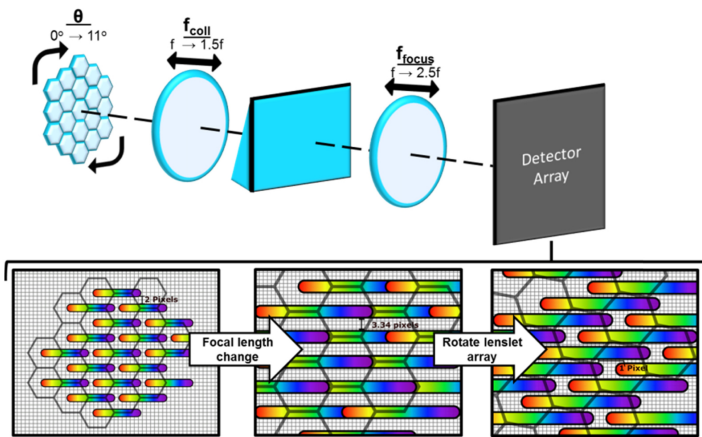


Figure 3.6: LATIS tunability. Source: (Dwight and Tkaczyk, 2017)

### 3.4.2. INTEGRAL FIELD SPECTROMETRY WITH SLICING MIRRORS (IFS-M)

Another approach for instant access to spatial and spectral information is the Integral Field Spectrometry with Slicing Mirrors (IFS-M) (Hagen, 2012). The technique, applied for example, in creating the ISS instrument (Gao et al., 2010), involves using an image slicer. This is a stack of micro-mirrors ( $16\text{ mm} \times 160\ \mu\text{m}$  in the case of ISS) with different tilt angles, which can reflect the various fields in different directions. The reflected light is later collected by a collimator that forms multiple pupils in the pupil plane. Furthermore, with the help of a beam expander, the stream of light is adjusted to the size of the detector. The magnified pupils are later dispersed using an optical prism. Finally, the different fields are imaged at the detector level using re-imaging lenses.

If IFS-L is much more adapted for high spatial resolution, IFS-M is a more suitable approach for applications requiring high spectral resolution. Overall, the latter technique has the advantage of a higher throughput but comes with more significant manufacturing difficulties.

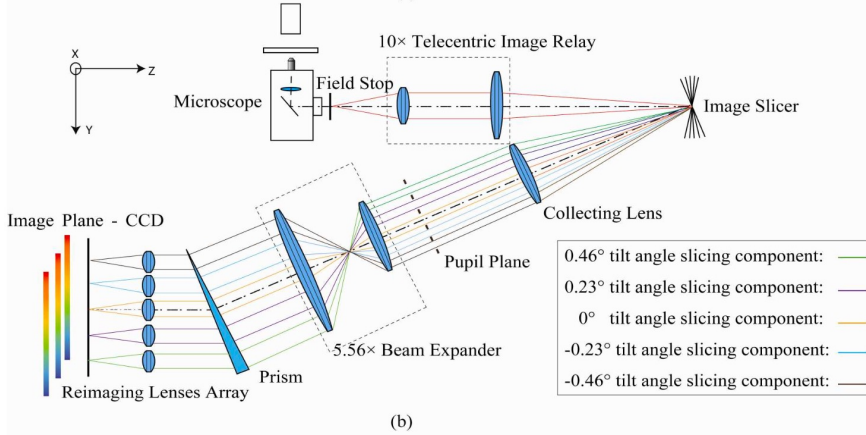


Figure 3.7: IFS-M optical design. Source: (Gao et al., 2010)

### 3.5. POLARIMETRY WITH METASURFACES

Metasurfaces can successfully replace classical optical elements to achieve both diffraction and determination of light polarization. Metasurfaces are diffractive optical elements smaller than the wavelength of light obtained by lithographic methods, whose geometric arrangement and size influence light diffraction and phase difference.

The main advantage of metasurfaces is compactness. They allow the creation of optical instruments in which the polarimetric and the diffractive elements are compressed into a single piece of a tiny size compared to the size of the classical elements. An example of an instrument that integrates a metasurface intended for imaging polarimetry is the one developed by (Li et al., 2023) and presented in Fig. 3.8. According to this scheme, the metasurface is placed at the entrance of the optical instrument. It is provided with orders of diffraction that act as analyzers for the different polarization states (Fig. 3.8, a, b). After the metasurface, the optical imaging part follows, which allows obtaining polarimetric images. Particular attention should be given to the control of the field of view ( $FoV$ ). Since the metasurface is characterized by its own diffraction angle, a  $FoV$  that is too large can lead to overlapping images in the detector's plane. This effect can be easily controlled with the help of a field stop. The example reproduced here allows the measurement of the entire Stokes vector on a narrow waveband. To cover a wider waveband, the design must be modified so that the spectral and polarimetric modulation do not overlap in the plane of the detector. Examples of instruments based on metasurfaces that allow obtaining spectropolarimetric images can already be found in the literature (Rubin et al., 2018, 2019, 2022).

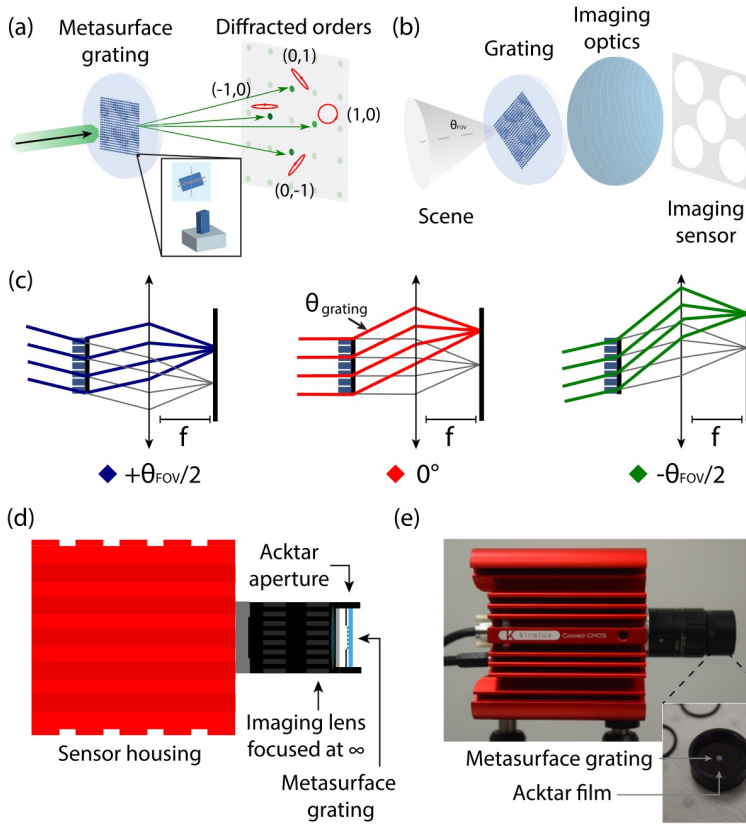


Figure 3.8: Schematic representation of an instrument that uses a metasurface to obtain polarimetric images. With the help of a metasurface grating (a), the light is deflected in four distinct directions depending on the type of polarization. Four distinct images with different polarimetric properties are obtained using imaging optics in the detector's plane. A fifth image, the central one, carries information about the light intensity. We notice from the panel d) how compact this instrument may become. Source: (Li et al., 2023)

Manufactured by a lithographic method, the metasurface from the experiment mentioned here uses a  $\text{TiO}_2$  substrate (Devlin et al., 2016). It consists of pillar-like dielectric elements, which act as tiny birefringent plates. The size of these pillars influences the variation of the light phase, while their geometric arrangement determines the position of the fast axis.

Metasurfaces demonstrate great versatility and allow the construction of highly compact instruments adapted for different observation conditions and applications. Certain limitations related to the precision of the manufacturing process continue to manifest themselves. Over time, they will probably become smaller, which is why metasurfaces represent a future field for spectropolarimetry and spectropolarimetry imaging.



# BIBLIOGRAPHY

- Azzam, R. (1982). Division-of-amplitude photopolarimeter (DOAP) for the simultaneous measurement of all four Stokes parameters of light. *Optica Acta: International Journal of Optics*, 29(5), 685–689. <https://doi.org/10.1080/713820903>
- Belsley, D. A., Kuh, E., & Welsch, R. E. (1980). *Regression diagnostics: Identifying influential data and sources of collinearity*. Wiley.
- Collett, E. (2005). *Field guide to polarization*. SPIE. <https://doi.org/10.1117/3.626141>
- Compain, E., & Drevillon, B. (1998). Broadband division-of-amplitude polarimeter based on uncoated prisms. *Applied Optics*, 37(25), 5938. <https://doi.org/10.1364/AO.37.005938>
- Dai, J., Goudail, F., Boffety, M., & Gao, J. (2018). Estimation precision of full polarimetric parameters in the presence of additive and poisson noise. *Optics Express*, 26(26), 34081. <https://doi.org/10.1364/OE.26.034081>
- del Toro Iniesta, J. C. (2003). *Introduction to spectropolarimetry*. Cambridge University Press.
- del Toro Iniesta, J. C., & Collados, M. (2000). Optimum modulation and demodulation matrices for solar polarimetry. *Applied Optics*, 39(10), 1637. <https://doi.org/10.1364/AO.39.001637>
- Devlin, R., Khorasaninejad, M., Chen, W., Oh, J., & Capasso, F. (2016). Broadband high efficiency dielectric metasurfaces for the visible spectrum. *Proceedings of the National Academy of Sciences*, 113(38), 10473–10478. <https://doi.org/10.1073/pnas.1611740113>
- Dong, J., & Zhou, H. (2020). Polarimeters from bulky optics to integrated optics: A review. *Optics Communications*, 465, 125598. <https://doi.org/10.1016/j.optcom.2020.125598>
- Dwight, J. G., & Tkaczyk, T. S. (2017). Lenslet array tunable snapshot imaging spectrometer (LATIS) for hyperspectral fluorescence microscopy. *Biomedical Optics Express*, 8(3), 1950. <https://doi.org/10.1364/BOE.8.001950>
- Foreman, M. R., & Goudail, F. (2019). On the equivalence of optimization metrics in stokes polarimetry. *Optical Engineering*, 58(8), 1. <https://doi.org/10.1117/1.OE.58.8.082410>
- Gao, L., Kester, R. T., Hagen, N., & Tkaczyk, T. S. (2010). Snapshot image mapping spectrometer (IMS) with high sampling density for hyperspectral microscopy. *Optics Express*, 18(14), 14330. <https://doi.org/10.1364/OE.18.014330>
- Gassó, S., & Knobelspiesse, K. D. (2022). Circular polarization in atmospheric aerosols. *Atmospheric Chemistry and Physics*, 22(20), 13581–13605. <https://doi.org/10.5194/acp-22-13581-2022>
- Goudail, F. (2009). Noise minimization and equalization for stokes polarimeters in the presence of signal-dependent poisson shot noise. *Optics Letters*, 34(5), 647. <https://doi.org/10.1364/OL.34.000647>



- Goudail, F. (2016). Equalized estimation of stokes parameters in the presence of poisson noise for any number of polarization analysis states. *Optics Letters*, 41(24), 5772. <https://doi.org/10.1364/OL.41.005772>
- Hagen, N. (2012). Snapshot advantage: A review of the light collection improvement for parallel high-dimensional measurement systems. *Optical Engineering*, 51(11), 111702. <https://doi.org/10.1117/1.OE.51.11.111702>
- Hagen, N., & Kudenov, M. W. (2013). Review of snapshot spectral imaging technologies. *Optical Engineering*, 52(9), 090901. <https://doi.org/10.1117/1.OE.52.9.090901>
- Li, L. W., Rubin, N. A., Juhl, M., Park, J.-S., & Capasso, F. (2023). Evaluation and characterization of imaging polarimetry through metasurface polarization gratings. *Applied Optics*, 62(7), 1704. <https://doi.org/10.1364/AO.480487>
- Mignani, R., Shearer, A., Słowikowska, A., & Zane, S. (Eds.). (2019). *Astronomical polarisation from the infrared to gamma rays* (Vol. 460). Springer International Publishing. <https://doi.org/10.1007/978-3-030-19715-5>
- Mu, T., Zhang, C., & Liang, R. (2015). Demonstration of a snapshot full-stokes division-of-aperture imaging polarimeter using wollaston prism array. *Journal of Optics*, 17(12), 125708. <https://doi.org/10.1088/2040-8978/17/12/125708>
- Rubin, N. A., Chevalier, P., Juhl, M., Tamagnone, M., Chipman, R., & Capasso, F. (2022). Imaging polarimetry through metasurface polarization gratings. *Opt. Express*, 30(6), 9389–9412. <https://doi.org/10.1364/OE.450941>
- Rubin, N. A., D'Aversa, G., Chevalier, P., Shi, Z., Chen, W. T., & Capasso, F. (2019). Matrix fourier optics enables a compact full-stokes polarization camera. *Science*, 365(6448), eaax1839. <https://doi.org/10.1126/science.aax1839>
- Rubin, N. A., Zaidi, A., Juhl, M., Li, R. P., Mueller, J. B., Devlin, R. C., Leósson, K., & Capasso, F. (2018). Polarization state generation and measurement with a single metasurface. *Optics Express*, 26(17), 21455. <https://doi.org/10.1364/OE.26.021455>
- Sugai, H., Hattori, T., Kawai, A., Ozaki, S., Hayashi, T., Ishigaki, T., Ishii, M., Ohtani, H., Shimono, A., Okita, Y., Matsubayashi, K., Kosugi, G., Sasaki, M., & Takeyama, N. (2009). The Kyoto Tridimensional Spectrograph II on Subaru and the University of Hawaii 88 in Telescopes. *Publications of the Astronomical Society of the Pacific*, 122(887), 103. <https://doi.org/10.1086/650397>
- Tyo, J. S., Goldstein, D. L., Chenault, D. B., & Shaw, J. A. (2006). Review of passive imaging polarimetry for remote sensing applications. *Applied Optics*, 45(22), 5453. <https://doi.org/10.1364/AO.45.005453>

# 4

## A NEW DESIGN OF SPECTROPOLARIMETER

*If you wish to make an apple pie from scratch, you must first invent the universe.*

Carl Sagan

### 4.1. THE STARTING POINT

Light polarization measurement technology is quite advanced today. Polarimetry, spectropolarimetry, and snapshot spectropolarimetry can be performed today using different approaches, depending on the applications for which these instruments are intended. Polarization measurement is a relative process: the accuracy of the instruments and the types of polarizations that can be measured depend on the intrinsic requirements of the application domains. Polarimetric remote sensing of clouds and aerosols thus requires measuring degrees of linear polarization starting from at least 0.5% (Dubovik et al., 2019; Waquet et al., 2009). Studying exoplanets requires instruments capable of detecting circular polarization up to  $10^{-7}$  (Kemp et al., 1971; Li et al., 2023). Such constraints dictate the optical design of these instruments.

When it comes to instruments designed to measure polarization in space, the accuracy exigencies are compounded by the considerable constraints of the operating environment. The instruments' mass, volume, or robustness thus play a crucial role. The history of this optics domain proves that gathering all these qualities in a single device remains challenging.

A promising direction for the development of spectropolarimetry was opened in 2012 (Sparks et al., 2012). Aiming at the development of a spectropolarimeter capable of detecting the entire Stokes vector, with a sensitivity of the order of  $10^{-4}$  for circular polarization so that biologically induced polarization becomes detectable in remote sensing, the authors of this study proposed a variety of concepts capable of satisfying most of these requirements.

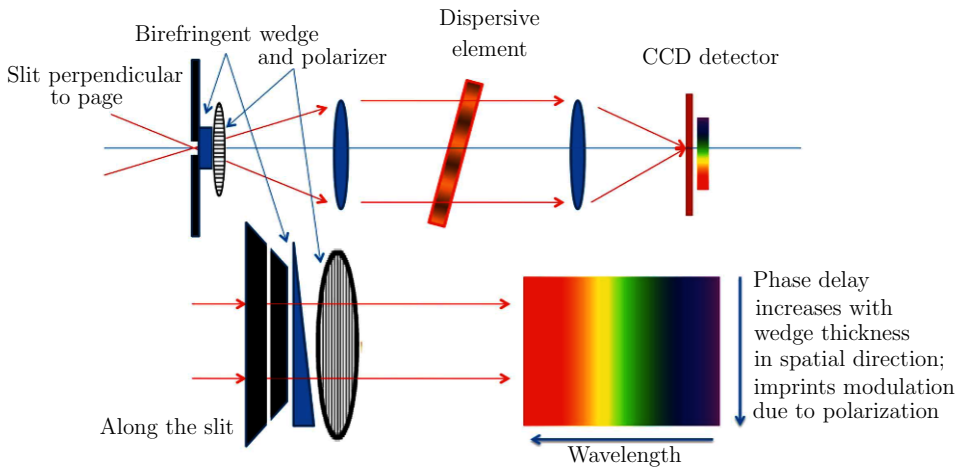


Figure 4.1: Concept of spectropolarimeter employing a birefringent wedge. Source: (Sparks et al., 2012)

The new approach uses a birefringent wedge, playing the role of a polarimetric modulator, followed by a linear polarizer and a dispersive element (see Fig. 4.1). The variable thickness of the birefringent wedge ensures a continuous variation of the phase difference between the orthogonal components of the light electric field in the direction of the slit. In contrast, the dispersive element ensures a spectral dispersion in a direction

perpendicular to the direction of the slit. The variation of the phase difference causes an incident light, characterized by a particular polarization, to undergo a continuous change of the state of polarization in the direction of the slit after passing through the birefringent wedge.

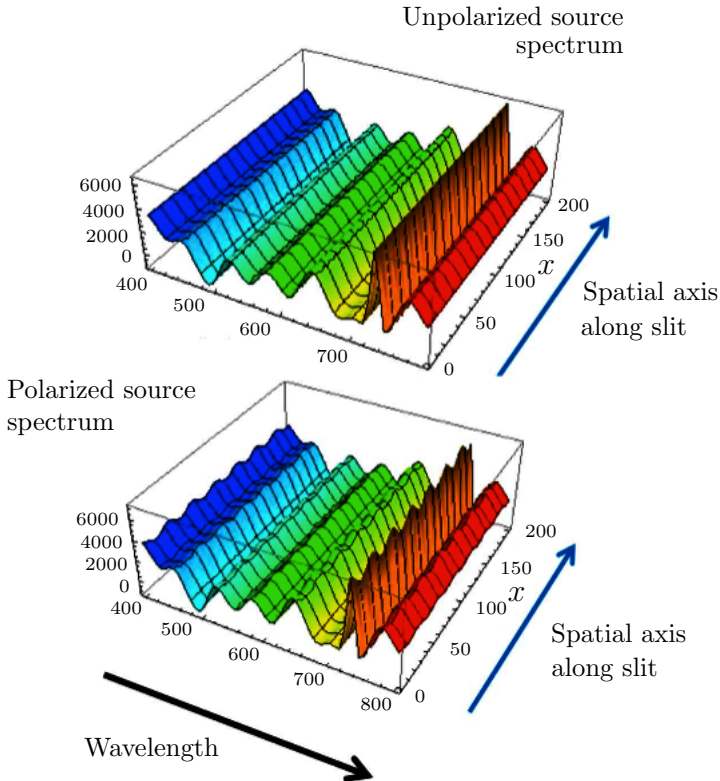


Figure 4.2: Hypothetical modulation produced by the wedge-spectropolarimeter. The units for the  $x$ -axis are  $\mu\text{m}$ , and for the wavelengths,  $\text{nm}$ . Source: (Sparks et al., 2012)

This variation of the polarization state in the vertical direction is transformed into an intensity variation with the help of the analyzer. Overall, in the plane of the detector, in the perpendicular direction of the slit, the spectral dispersion is obtained. Along the slit, the intensity variation caused by the change of the incident polarization by the wedge will be observed (see Fig. 4.2). No polarimetric modulation can be obtained if the incident light is not polarized.

This design is highly compact but does not allow for determining all polarization states, as we will see in what follows. To overcome this shortcoming, at least one more birefringent element must be added to the setup, with an optical axis different from the first one. In this sense, (Sparks et al., 2012) have proposed using a component similar to the one shown in Fig. 4.3. This design allows the complete determination of the Stokes vector over a spectral range that depends on the material used to manufacture

the prisms.

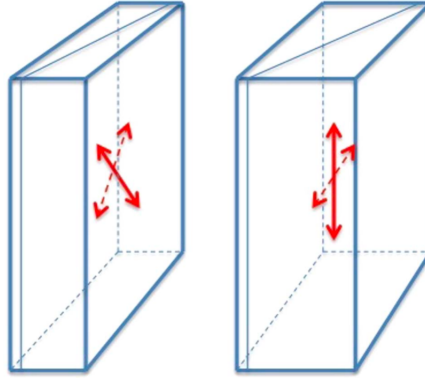


Figure 4.3: Structure proposed for full Stokes spectropolarimetry. The red arrows (continued and dashed) indicate the orientation of the fast axes for the birefringent wedges. Source: (Sparks et al., 2012)

A further step in exploiting this spectropolarimetric design idea was made by (Pertenais et al., 2015).

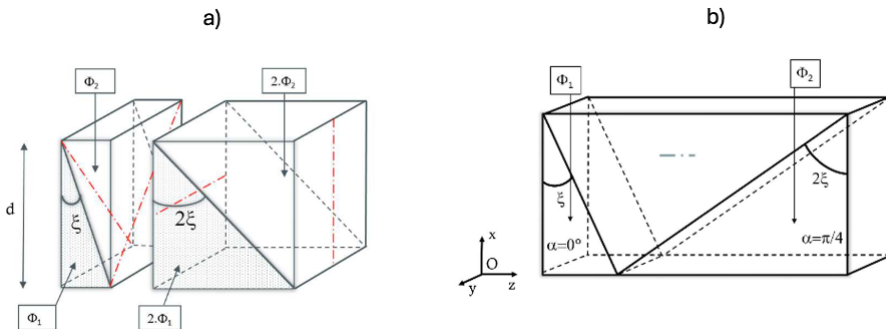


Figure 4.4: Types of modulators studied by Pertenais et al. The red dashed lines from figure a) indicate the orientation of the optical axes of the prisms. Source: (Pertenais et al., 2015)

The design from Fig. 4.4, a) uses four prisms glued two-by-two. The first two prisms from the left have an apex angle  $\xi$  and fast axes oriented at  $45^\circ$  and  $-45^\circ$  (the red dashed lines) with respect to the  $y$ -axis. The first wedge introduces a phase shift  $\phi_1$ , varying in the vertical direction, whereas the second wedge is characterized by a phase shift  $\phi_2$ . The following two wedges bonded together in a single prism, with the fast axes oriented at  $0^\circ$ , respectively  $90^\circ$ , are introducing a phase shift of  $2\phi_1$ , respectively  $2\phi_2$ .

In a second approach, Fig. 4.4, b), the authors proposed to replace the four prisms with a single block of three prisms optically glued together. The first wedge from the left of the new type of modulator has an apex angle  $\xi$ , and the fast axis is oriented here at  $\alpha = 0^\circ$  with respect to the  $y$ -axis. The middle prism has a fast axis along the  $z$ -axis, which is the direction of light propagation. In the third prism, the fast axis is placed at

$45^\circ$  with respect to the  $y$ -axis. The apex angle of this last wedge is  $2\xi$ . In this way, if the first prism determines a phase shift of  $\phi$ , the last prism will be characterized by a phase shift  $2\phi$ .

Both approaches proved extremely promising, ensuring a complete determination of the Stokes vector and satisfying the constraints related to mass, volume, and robustness imposed by the necessity of use in space. The type of modulator shown in Fig. 4.4 b) was identified by (Pertenis et al., 2015) as the most robust and most suitable for space applications. It has the smallest number of surfaces and can also ensure the minimization of the risks related to the misalignment of the optical components.

As a result, we focused our attention on this modulator model. Previous studies (Pertenis et al., 2014, 2015) have demonstrated its potential. The following sections will dissect this modulator concept in detail. We will closely see where the need for a triple structure comes from, how it acts on polarized light, and how it can facilitate polarization determination. In addition, for the first time, we will discuss the geometrical parameters of this instrument concept. We will see how its performance is influenced by the values these parameters can take, which are the most suitable geometries to be realized practically, and the polarimetric signal demodulation methods at hand. Furthermore, some hints for obtaining spectropolarimetric images will be proposed.

## 4.2. TOWARDS A COMPACT STRUCTURE

The crystal chosen to build the modulator, the critical component of the instrument studied here, was  $\text{MgF}_2$ . This salt has an excellent transmission between UV and IR, with more than 94% in the interval  $[0.2, 6]\mu\text{m}$ , at normal incidence. The birefringent property also spans the same broad spectrum, making the material a good choice for spectropolarimetric applications. In addition, it is less brittle than  $\text{CaF}_2$  and can be easily manufactured in different shapes and polished. Moreover, the behavior of the crystal with temperature or humidity is well studied, and comprehensive data is available (Tropf and Spie, 1995). Figure 4.5 displays the variation of the refractive index with the wavelength, in agreement with Dodge's study of  $\text{MgF}_2$  (Dodge, 1984).

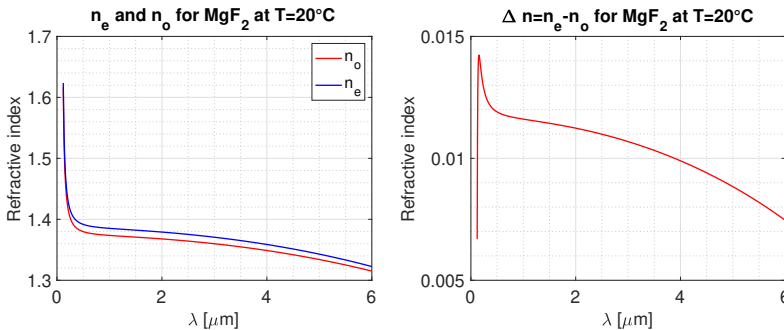


Figure 4.5: Birefringence of  $\text{MgF}_2$ . Used model: Dodge

The Sellmeier model devised by Dodge for the two indices of refraction is:

$$\begin{cases} n_o^2 - 1 = \frac{0.48755108\lambda^2}{\lambda^2 - 0.043384082} + \frac{0.39875031\lambda^2}{\lambda^2 - 0.094614422} + \frac{2.3120353\lambda^2}{\lambda^2 - 23.7936042} \\ n_e^2 - 1 = \frac{0.41344023\lambda^2}{\lambda^2 - 0.036842622} + \frac{0.50497499\lambda^2}{\lambda^2 - 0.090761622} + \frac{2.4904862\lambda^2}{\lambda^2 - 23.7719952} \end{cases} \quad (4.1)$$

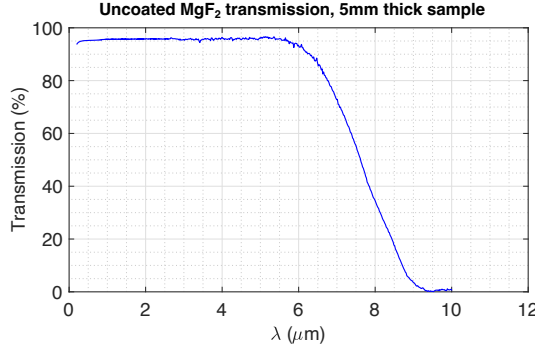


Figure 4.6: Transmission of MgF<sub>2</sub>, for normal incidence and 5 mm thick sample. Source of data: Thorlabs

This modulator in MgF<sub>2</sub> has three parts. These are three wedges from the same material, cut so that the fast axes are differently oriented in each of them. The reason for using wedges is that, in this way, the length of the optical path will vary inside each prism, and thus, the phase difference between the orthogonal components of the electric field of light will also vary.

Let us consider the simple example of a prism in MgF<sub>2</sub>, upon which the light, with a wavelength  $\lambda$ , arrives orthogonally from the left side (see Fig. 4.7) and for which the fast axis makes an arbitrary angle  $\rho$  with the  $x$ -direction. Suppose this optical wedge is followed by a linear polarizer, oriented at angle  $\theta$  to the same  $x$ -direction. In that case, the intensity detected at the position  $y$  in the vertical direction is:

$$I = \frac{1}{2} \left( S_0 + S_1 m(\rho, \theta, \phi(y, \lambda)) + S_2 n(\rho, \theta, \phi(y, \lambda)) + S_3 p(\rho, \theta, \phi(y, \lambda)) \right), \quad (4.2)$$

where  $m$ ,  $n$ , and  $p$  are modulation functions determined by the modulator's features and the analyzer's orientation, and  $S_i$ ,  $i = 0, 1, 2, 3$  are the Stokes parameters of the incoming light.

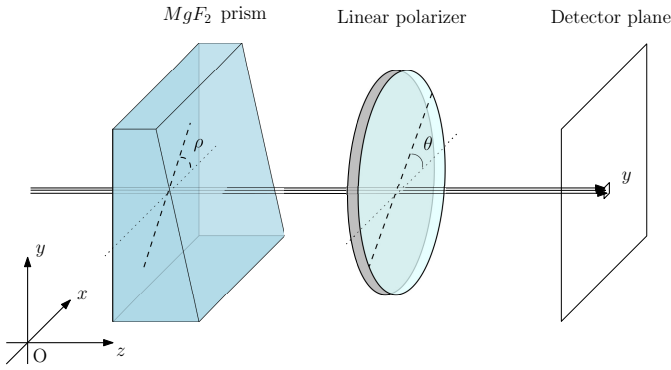


Figure 4.7: General schema of a polarimeter employing a single prisms in MgF<sub>2</sub> as modulator.

With the help of the Mueller calculus and ignoring the Fresnel terms, which are very small for normal and close to normal incidence, the functions  $m$ ,  $n$ ,  $p$  can be easily computed:

$$\begin{cases} m(\rho, \theta, \phi(y, \lambda)) = \cos(2\theta) \left( C^2 + S^2 \cos(\phi) \right) - CS \sin(2\theta) \left( \cos(\phi) - 1 \right) \\ n(\rho, \theta, \phi(y, \lambda)) = \sin(2\theta) \left( S^2 + C^2 \cos(\phi) \right) - CS \cos(2\theta) \left( \cos(\phi) - 1 \right) \\ p(\rho, \theta, \phi(y, \lambda)) = C \sin(2\theta) \sin(\phi) - \cos(2\theta) \sin(\phi) \end{cases}, \quad (4.3)$$

where  $C = \cos(2\rho)$ ,  $S = \sin(2\rho)$ , and  $\phi$  represents the phase difference between the orthogonal components of the electric field induced by the prism at the level  $y$ .

This phase difference is given by:

$$\phi(y, \lambda) = \frac{2\pi}{\lambda} \Delta n(\lambda) D(y), \quad (4.4)$$

where  $\lambda$  is the wavelength of the incoming light, and  $\Delta n(\lambda) = |n_o(\lambda) - n_e(\lambda)|$  is the birefringence of the prism.

The distance,  $D(y)$ , traveled by the light inside the prism at the level  $y$  can be easily computed using the notations from Fig. 4.8:

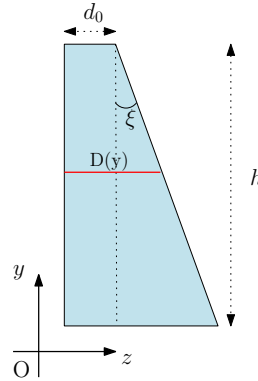


Figure 4.8: Geometry of the prism.

$$D(y) = d_0 + (h - y) \tan(\xi). \quad (4.5)$$

In this equation,  $h$  is the height of the wedge, and  $\xi$  is the apex angle, whereas  $d_0$  is an additional thickness that can be foreseen to strengthen the prism's body and facilitate the manipulation.

The advantage of such a design is that it ensures an almost complete modulation of the polarization. One can retrieve the incoming Stokes vector from a single shot with



enough readings or illuminated pixels in the vertical direction. Still, there is an indeterminate. When the incoming light is linearly polarized at the same angle as the fast axis orientation of the prism, or orthogonal to this, then there will be a single component of the electric field. No phase difference will be imposed between the field components for these cases. Consequently, the intensity of the light having these polarizations will be constant in the  $y$  direction. Because of this, such linear polarization states will remain indeterminate and indistinguishable from unpolarized light. A second prism (see Fig. 4.9) can be placed after the first to overcome the undetermination. If the fast axis of the second prism is differently oriented, then a modulation can also be obtained for the linear state that is parallel or perpendicular to the first axis. Various orientations of the fast axes for the two prisms can be chosen. As long as these two axes are neither parallel nor perpendicular to each other, a complete modulation of the polarization can be achieved. Such a modulator, followed by a linear analyzer, can serve as a full Stokes snapshot spectropolarimeter. The expression of the intensity in the detector plane can be computed using the Mueller calculus.

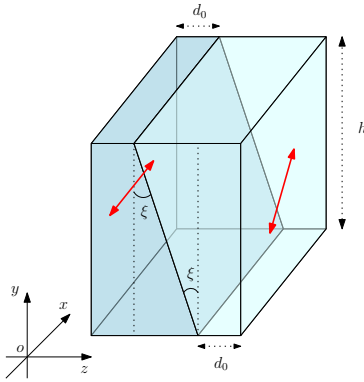


Figure 4.9: Hypothetical design that can solve the undetermination of the linear state. The orientation of the fast axes is represented in red.

As a simple illustration of what can be obtained with this configuration, one can imagine the situation of two prisms with the fast axes oriented at  $0^\circ$ , respectively  $45^\circ$ , and presenting the same apex angle. This would be a robust design with parallel faces. For this configuration, the phase difference determined by the first prism is:

$$\phi_1 = \frac{2\pi}{\lambda} \Delta n(\lambda) (d_0 + (h - y) \tan(\xi)), \quad (4.6)$$

whereas in the second prism is:

$$\phi_2 = \frac{2\pi}{\lambda} \Delta n(\lambda) (d_0 + y \tan(\xi)). \quad (4.7)$$

With the help of the Mueller calculus (Eq. 2.25), the Mueller matrices associated with the two prisms can be easily computed. Therefore, the first prism from the left, with a fast axis oriented along the  $x$ -axis, has the matrix:

$$M_1(\rho = 0) = \begin{pmatrix} 1 & 0 & 0 & 0 \\ 0 & 1 & 0 & 0 \\ 0 & 0 & c_1 & s_1 \\ 0 & 0 & -s_1 & c_1 \end{pmatrix} \quad (4.8)$$

where  $c_1 = \cos(\phi_1)$ ,  $s_1 = \sin(\phi_1)$ . We see now clearly that the first prism lets the incoming state of polarization  $\tilde{S}_{in} = (S_0, S_1, 0, 0)^T$  unaffected. Globally, its effect on the Stokes parameters can be summarized as follows:

$$\begin{cases} S_0 \rightarrow S_0 \\ S_1 \rightarrow S_1 \\ S_2 \rightarrow \begin{cases} S'_2 \\ S'_3 \end{cases} \\ S_3 \rightarrow \begin{cases} S'_2 \\ S'_3 \end{cases} \end{cases}, \quad (4.9)$$

where  $\vec{S}_{out} = (S'_0, S'_1, S'_2, S'_3)^T$  is the resulting Stokes vector, recorded on the exit face of the prism. In other words, the linear horizontal and vertical polarizations will pass unaffected through the prism. In contrast, the linear  $\pm 45^\circ$  and circular polarizations will be converted into one another in a certain amount, depending on the position on the vertical at which the light passes through the prism.

Using again the relation (2.25), the Mueller matrix of the second prism, having a fast axis oriented at  $45^\circ$  with respect to the  $x$ -axis, can be retrieved:

$$M_2(\rho = 45) = \begin{pmatrix} 1 & 0 & 0 & 0 \\ 0 & c_2 & 0 & -s_2 \\ 0 & 0 & 1 & 0 \\ 0 & s_2 & 0 & c_2 \end{pmatrix} \quad (4.10)$$

where  $c_2 = \cos(\phi_2)$ , and  $s_2 = \sin(\phi_2)$ . As is expected, the second prism lets unaffected state  $\pm 45^\circ$  while it converts the linear horizontal-vertical and circular polarizations into one another in a certain amount. The global transformation of an incoming Stokes vector after passing through this wedge is:

$$\begin{cases} S_0 \rightarrow S_0 \\ S_1 \rightarrow \begin{cases} S'_1 \\ S'_3 \end{cases} \\ S_2 \rightarrow S_2 \\ S_3 \rightarrow \begin{cases} S'_1 \\ S'_3 \end{cases} \end{cases}, \quad (4.11)$$

The compound represented in Fig. 4.9 has a total Mueller matrix  $M$ :

$$M = M_2(\rho = 45) \cdot M_1(\rho = 0) = \begin{pmatrix} 1 & 0 & 0 & 0 \\ 0 & c_2 & s_1 s_2 & -s_2 c_1 \\ 0 & 0 & c_1 & s_1 \\ 0 & s_2 & -s_1 c_2 & c_2 c_1 \end{pmatrix} \quad (4.12)$$

This result shows that any state of polarization arriving from the left side is converted into a new form of polarization by the block of two prisms. The type of the new polarization depends on the position in the vertical direction. If we look closely at the matrix (4.12), we notice that the transformations undergone by the Stokes parameters can be summarized like:

$$\left\{ \begin{array}{l} S_0 \rightarrow S_0 \\ S_1 \rightarrow \begin{cases} S'_1 \\ S'_3 \end{cases} \\ S_2 \rightarrow \begin{cases} S'_1 \\ S'_2 \\ S'_3 \end{cases} \\ S_3 \rightarrow \begin{cases} S'_1 \\ S'_2 \\ S'_3 \end{cases} \end{array} \right. , \quad (4.13)$$

4

The variation of the outgoing vector with the position  $y$  in the vertical direction can also be observed with the help of the Poincaré sphere. Figure 4.10 shows how, starting from the incoming vector  $\vec{S} = (1, 1/\sqrt{3}, 1/\sqrt{3}, 1/\sqrt{3})^T$  (the black dot), arbitrarily chosen, a series of completely new vectors (green dots) is obtained all around the sphere.

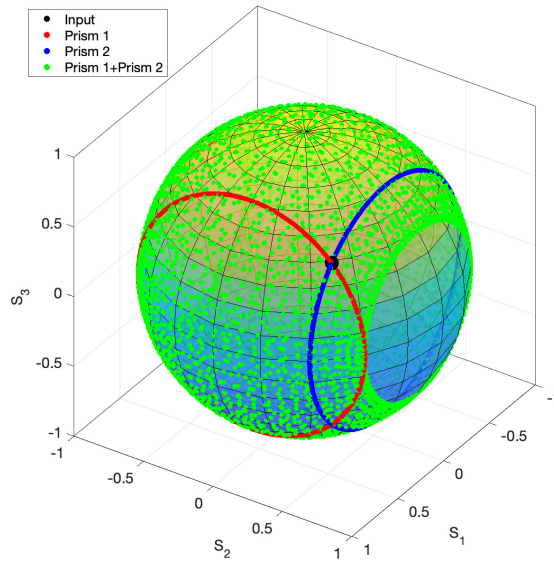


Figure 4.10: Poincaré representation of the outgoing states resulting after the passage of light characterized by the Stokes vector  $S = (1, 1/\sqrt{3}, 1/\sqrt{3}, 1/\sqrt{3})^T$  (the black dot) through the prism 1 (red dots), through the prism 2 (blue dots) and through the block formed by the two prisms (green dots).

If, after this block, we add a linear polarizer, with the transmission axis oriented at an angle  $\theta$  with respect to the same  $x$ -axis, then the resulting Muller matrix of the entire optical system is:

$$M = M_{LP(\theta)} \cdot M_2(\rho = 45) \cdot M_1(\rho = 0) = \frac{1}{2} \begin{pmatrix} 1 & cc_2 & cs_1s_2 + sc_1 & -cs_2c_1 + ss_1 \\ c & c^2c_2 & c^2s_1s_2 + c_1cs & -c^2s_2c_1 + s_1cs \\ s & c_2cs & css_1s_2 + s^2c_1 & -s_2c_1cs + s_1s^2 \\ 0 & 0 & 0 & 0 \end{pmatrix} \quad (4.14)$$

where  $c = \cos(2\theta)$ , and  $s = \sin(2\theta)$ . The Stokes vector resulting after the passage of light after this optical system is:

$$\begin{pmatrix} S'_0 \\ S'_1 \\ S'_2 \\ S'_3 \end{pmatrix} = (M_{LP(\theta)} \cdot M_2(\rho = 45) \cdot M_1(\rho = 0)) \cdot \begin{pmatrix} S_0 \\ S_1 \\ S_2 \\ S_3 \end{pmatrix} \quad (4.15)$$

Therefore, the intensity ( $I_{out}$ ) detected by an optical detector placed after the linear polarizer is represented by the first term of the resulting Stokes vector:

$$I_{out} = S'_0 = \frac{1}{2} (S_0 + S_1(cc_2) + S_2(cs_1s_2 + sc_1) + S_3(ss_1 - cs_2c_1)) \quad (4.16)$$

Consequently, the functions  $m$ ,  $n$ , and  $p$ , previously presented (Eq. (4.3)) become now:

$$\begin{cases} m(y, \theta, \phi_1, \phi_2) = cc_2 = \cos(2\theta) \cos(\phi_2) \\ n(y, \theta, \phi_1, \phi_2) = cs_1s_2 + sc_1 = \sin(2\theta) \cos(\phi_1) + \cos(2\theta) \sin(\phi_1) \sin(\phi_2) \\ p(y, \theta, \phi_1, \phi_2) = ss_1 - cs_2c_1 = \sin(2\theta) \sin(\phi_1) - \cos(2\theta) \cos(\phi_1) \sin(\phi_2) \end{cases} \quad (4.17)$$

The drawbacks of this design are mainly related to the deviation of light after the passage from the first into the second prism. Both ordinary and extraordinary vibrations from the first prism will be split into two new ordinary and extraordinary rays according to the orientation of the fast axis inside the second prism. The phenomenon will be more visible in the upper part, as the rays will travel longer in the second prism at this level. It is a design proposed in 2012 (Pertenaïs et al., 2015). The two prisms can be placed in an antiparallel configuration to compensate for this effect. A third prism can be inserted in the middle to ensure an almost constant index of refraction and keep the light on the z-axis (see Fig. 4.11). If the fast axis of this middle body is also oriented along z, then this prism will not affect the polarization of light. From a polarimetric point of view, it will be an inactive medium, serving only the purpose of keeping everything together in a compact structure. If the two active wedges have the apex angles  $\xi$  and  $\psi$ , then the phase difference induced by each of them will be:

$$\begin{cases} \phi_1 = \frac{2\pi}{\lambda} \Delta n(\lambda) (d_0 + (h - y) \tan(\xi)) \\ \phi_3 = \frac{2\pi}{\lambda} \Delta n(\lambda) (d_0 + (h - y) \tan(\psi)) \end{cases}, \quad (4.18)$$

where  $\phi_1$  is the phase difference determined by the first prism from the left, and  $\phi_3$  is the phase difference induced by the third prism. In the scenario when the fast axis from

the first prism is oriented at  $0^\circ$ , along the  $x$ -axis, while the third prism makes an angle of  $45^\circ$  with the same  $x$ -axis, in the  $xy$  plane, the modulation functions are provided by the relations (4.17), where  $\phi_2$  is replaced with  $\phi_3$ .

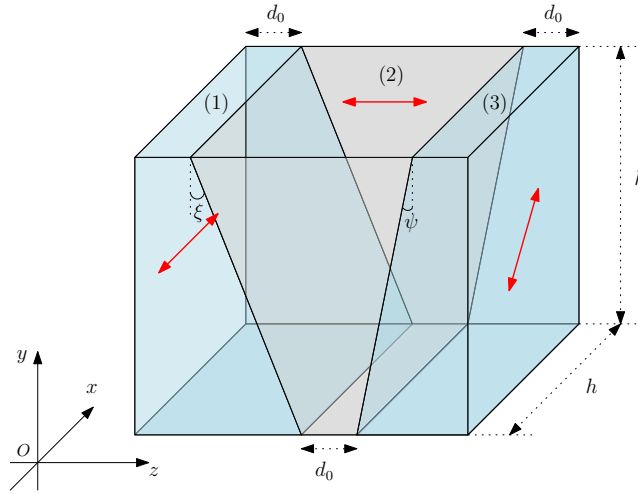


Figure 4.11: Modulator with triple prism structure. The orientations of the fast axes are marked in red.

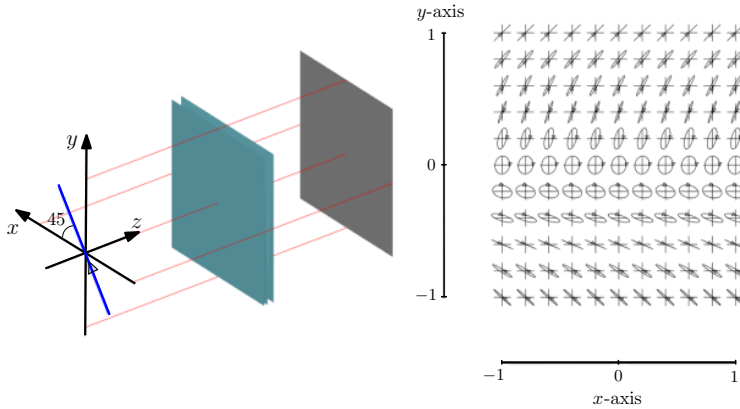


Figure 4.12: Code V representation of a  $45^\circ$  linear polarization passing through the modulator. No analyzer was considered for this simulation. We notice the continuous variation of the resulting polarization in the vertical direction. Because along the  $x$ -axis, there is no intensity modulation, the same state of polarization will emerge along the entire  $x$ -length of the prism.

### 4.3. THE WORKING PRINCIPLE

The working principle of a spectropolarimeter employing the above modulator is illustrated in Fig. 4.13 and 4.14.

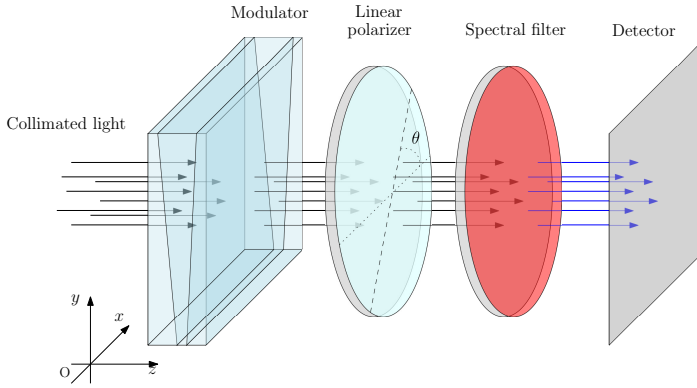


Figure 4.13: Schematic representation of the spectropolarimeter employing the triple prism modulator.

Therefore, the light arriving collimated from the left side passes through the modulator (the triple prism compound) and a linear polarizer before arriving on the detector (CCD). A spectral filter or a dispersive element should be introduced to select a particular wavelength between the linear polarizer and the CCD. The polarized (partially or entirely) light will be modulated in intensity in the vertical direction, whereas the optics will only attenuate the nonpolarized light. All polarization will generate a particular intensity pattern in the detector plane along the vertical. This pattern is related to the wavelength and the type of polarization. The ideal expression of the intensity detected by a pixel situated at the level  $y$ , at the wavelength  $\lambda$ , when the light carrying the state of polarization  $\vec{S} = (S_0, S_1, S_2, S_3)^T$  passes through the system is:

$$I(y, \theta, \phi_1, \phi_3) = \frac{1}{2} (S_0 + S_1 \cdot m(y, \theta, \phi_1, \phi_3) + S_2 \cdot n(y, \theta, \phi_1, \phi_3) + S_3 \cdot p(y, \theta, \phi_1, \phi_3)), \quad (4.19)$$

where the modulation functions  $m$ ,  $n$  and  $p$  are:

$$\begin{cases} m(y, \lambda, \theta) = \cos(2\theta) \cos(\phi_3) \\ n(y, \lambda, \theta) = \sin(2\theta) \cos(\phi_1) + \cos(2\theta) \sin(\phi_1) \sin(\phi_3) \\ p(y, \lambda, \theta) = \sin(2\theta) \sin(\phi_1) - \cos(2\theta) \cos(\phi_1) \sin(\phi_3) \end{cases}, \quad (4.20)$$

and the phase differences corresponding to the first ( $\phi_1$ ), respectively, the third prism ( $\phi_3$ ) are provided by Eq. (4.18).

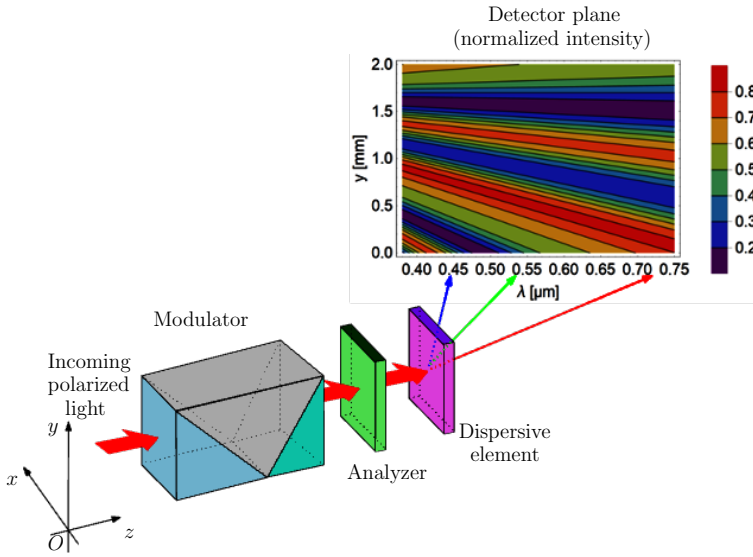


Figure 4.14: Illustration of the principle of functioning for the spectropolarimeter: the polarized light, coming collimated from the left side, passes through the modulator, the analyzer, and, then, a dispersive element (or a spectral filter). A distinctive intensity pattern in the vertical direction will characterize each wavelength. The prisms' apex angles and the modulator's size are exaggerated compared to the other instrument components.

We assumed in this expression that the light is perfectly collimated and orthogonal to the modulator. In addition, the impact of the Fresnel terms is neglected as the Mueller matrix corresponding to the transmitted beam is close to the unity matrix when the apex angles are very small. Using the relations (4.19) and (4.20), the intensity pattern can be simulated for any polarization and any wavelengths or conditions of observations.

Figure 4.15 displays the modulations obtained for the arbitrary state of polarization  $\vec{S} = (1, 0.3, 0.3, 0.3)^T$ , at two different wavelengths ( $0.5\mu m$ , respectively  $0.7\mu m$ ), and a signal-to-noise ratio ( $SNR$ ) of 50, when the analyzer has the transmission axis arbitrarily oriented at  $73^\circ$  to the  $x$ -axis. The normalized intensity displayed here corresponds to the modulation associated with the normalized Stokes vector.

The signal-to-noise ratio is defined as:

$$SNR = \frac{S_0}{Noise} \quad (4.21)$$

It can be noticed that increasing the wavelength spreads the pattern more. The phenomenon is due only to the fact that the birefringence of  $MgF_2$  decreases with wavelength.

The degree of polarization (see Eq. 2.10) is translated into the amplitude of the variation. Completely polarized light has a higher amplitude than partially polarized light (see Fig. 4.16).

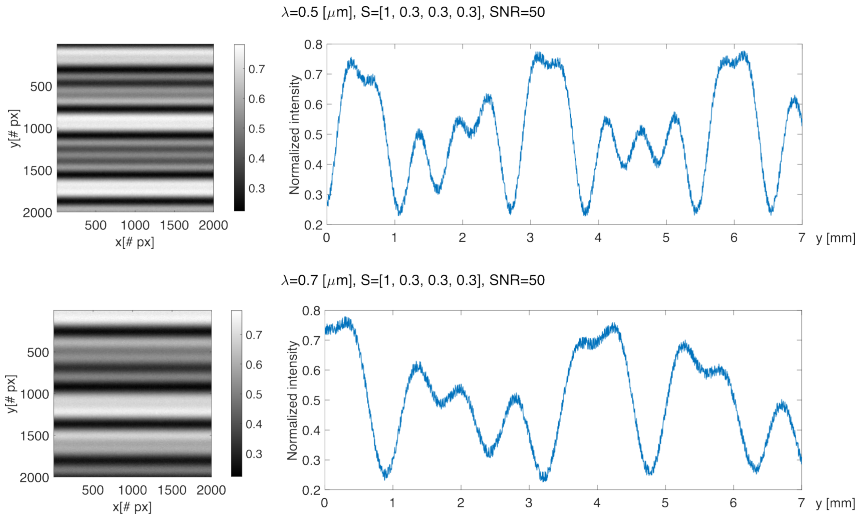


Figure 4.15: Simulated modulation for an incoming Stokes vector  $\vec{S} = (1, 0.3, 0.3, 0.3)^T$ , and two different wavelengths,  $\lambda = 0.5\mu\text{m}$ , and  $\lambda = 0.7\mu\text{m}$ . The 2D representations from the left simulate the image the detector displays, while the right plots present the intensity variation along a column of pixels.

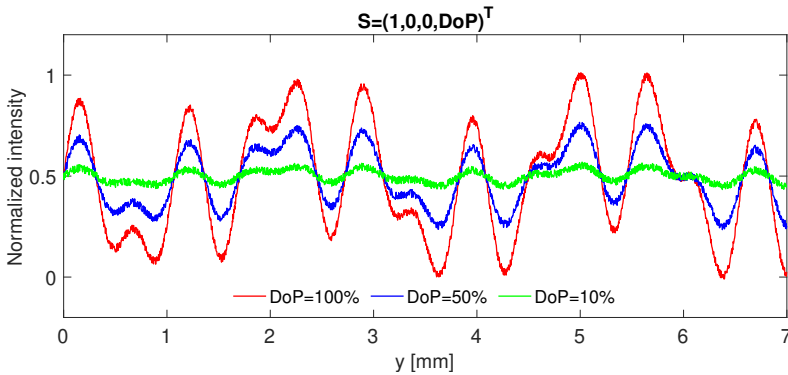


Figure 4.16: Smaller degrees of polarization (*DoP*) are translated into smaller modulation amplitudes.

Mitigating background noise and adjusting the integration time remain the best strategies to access the tiniest degrees of polarization. In addition, due to the redundancy on the horizontal, multiple lines of pixels can be used to access the state of polarization, decreasing the impact of noise in this way. A certain pattern characterizes each polarization passing through this type of modulator. As we can observe from Fig. 4.17, the shape of the variation changes from one polarization to another. Therefore, the Stokes parameters of the incoming light could be retrieved by fitting the detected intensity pattern with the theoretical function from Eq. (4.19).

Still, some fundamental questions should be answered before considering this concept of spectropolarimeter as a reliable and efficient approach for the snapshot mea-



surement of any polarization. These questions are:

- Does any polarization correspond to a unique pattern of intensity?
- What is the best choice for the modulator's apex angles?
- What is the best orientation of the analyzer?
- How could the observing conditions (spectral resolution, noise, temperature) impact the polarization retrieval?

All these questions will be answered in the next chapter.

4

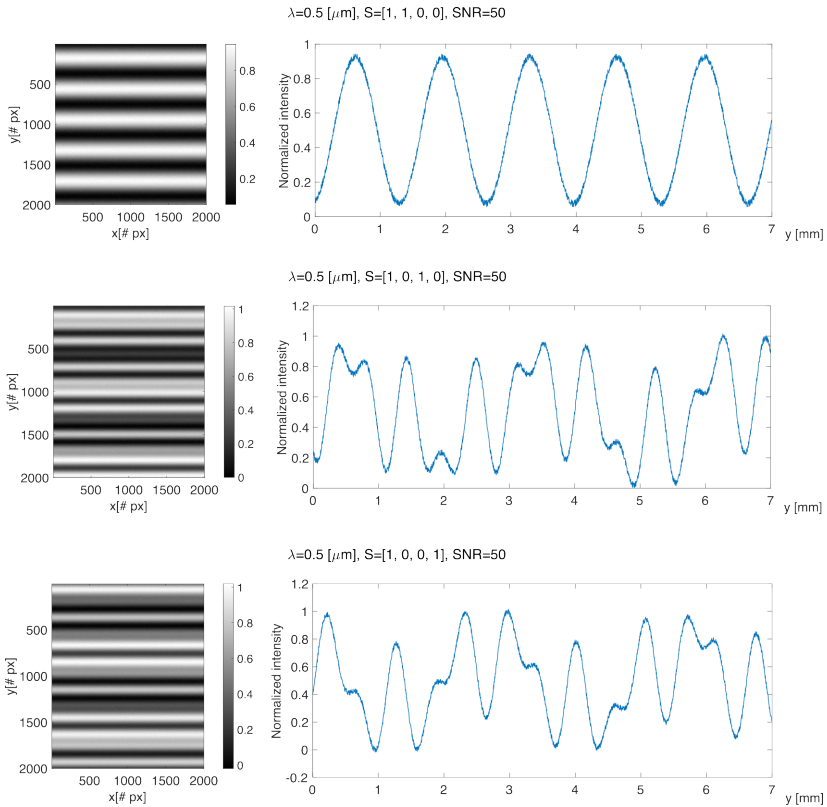


Figure 4.17: Simulated modulation for three different polarization states: linear horizontal polarization (top), linear 45° (middle), and circular right polarization (bottom).

#### 4.4. RETRIEVING THE POLARIZATION OF THE INCOMING LIGHT

Finding the Stokes vector of the incoming light means inferring the terms of this vector starting from the pattern of intensity in the detector plane. Two approaches are possible. The first, exploited mainly in the first part of this research, uses the fit of the modulation

function  $I(y, \theta, \phi_1, \phi_3)$  to the intensity data. The second approach uses the determination of a modulation matrix,  $W$ , and from here the inverse of  $W$ , called the instrumental matrix. Knowledge of the instrumental matrix makes retrieving incoming Stokes vectors through a simple matrix product possible (see Eq.(3.10)). At this point, a short clarification is necessary for these two methods.

Therefore, the first method, employing the fit, is an exquisite one, using the instrument's theoretical design. With the help of built-in algorithms from MATLAB or Python, the Stokes parameters can be quickly inferred (see Fig. 4.18). Still, there is a problem that this method should face before becoming applicable. It requires an exact knowledge of the modulator: fast axis orientations, apex angles, and birefringence, which can also be altered by humidity or temperature; all these parameters must be well determined. In addition, it is primarily applicable to the central field of view.

Any uncertainty we may have on these parameters is translated into errors. The impact can be considerable, even for tiny deviations.

- *Uncertainty on the apex angles*

Thus, starting from an arbitrary design of the modulator, in which the first apex angle is  $\xi = 2.2^\circ$  and the third angle is  $\psi = 3^\circ$ , Fig. 4.19 maps the relative error on the degree of polarization as a function of the uncertainty that we may have for these angles.

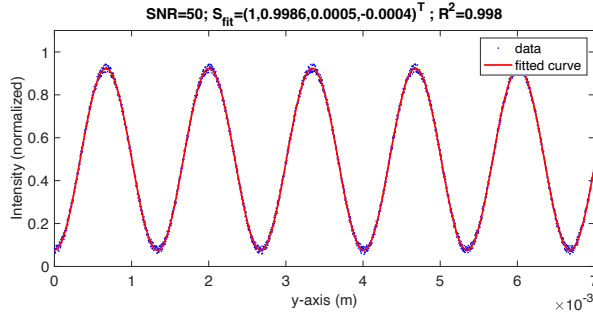
The formulas used to calculate this error are:

$$\left\{ \begin{array}{l} \Delta DoLP(\xi, \Delta\xi) = 100 \cdot \frac{|DoLP(\xi + \Delta\xi) - DoLP(\xi)|}{DoLP(\xi)} \\ \Delta DoLP(\psi, \Delta\psi) = 100 \cdot \frac{|DoLP(\psi + \Delta\psi) - DoLP(\psi)|}{DoLP(\psi)} \end{array} \right., \quad (4.22)$$

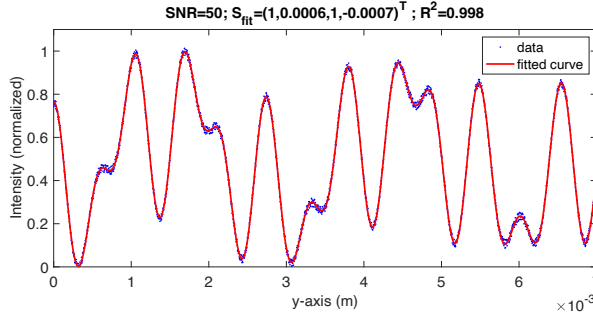
where  $\Delta\xi$  and  $\Delta\psi$  are the deviations of  $\xi$  and  $\psi$  from the considered values ( $\xi = 2.2^\circ$ ,  $\psi = 3^\circ$ ), and  $DoLP(\xi)$ ,  $DoLP(\psi)$  are the degrees of polarization retrieved when the apex angles correspond exactly to the reference values.

We notice how strong the impact of a small uncertainty can be. Thus, an error of the order of  $0.05^\circ$  degrees is translated in an error of the order of 10% on the degree of polarization. To stay below 5% with the error, we need a precision of approximately  $0.04^\circ$  degrees for the first angle and of approximately  $0.02^\circ$  for the second one. If the demodulation is very sensitive to the precision we can have on the apex angles, the situation is different in the case of the orientation of the fast axes (see Fig. 4.20).

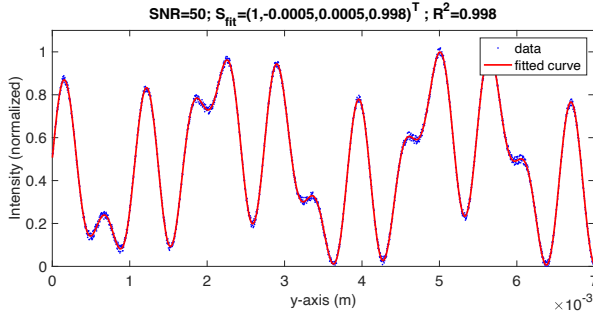
$$\vec{S}_{in} = \begin{pmatrix} 1 \\ 1 \\ 0 \\ 0 \end{pmatrix}$$



$$\vec{S}_{in} = \begin{pmatrix} 1 \\ 0 \\ 1 \\ 0 \end{pmatrix}$$



$$\vec{S}_{in} = \begin{pmatrix} 1 \\ 0 \\ 0 \\ 1 \end{pmatrix}$$



$$\vec{S}_{in} = \begin{pmatrix} 1 \\ 1/\sqrt{3} \\ 1/\sqrt{3} \\ 1/\sqrt{3} \end{pmatrix}$$

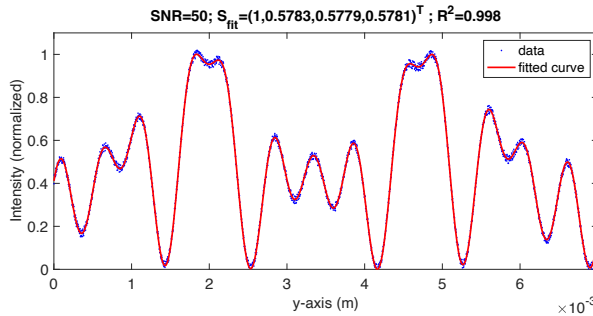


Figure 4.18: Examples of polarization retrieved with the fit procedure: a set of data corresponding to four incoming vectors ( $\vec{S}_{in}$ ) describing a totally polarized light is generated with the help of the function (4.19). Here, we used an arbitrary pixel size of  $3.5 \mu\text{m}$  and a wavelength of  $0.5 \mu\text{m}$ . We then apply an arbitrary level of noise to this data. Ultimately, we fit the distorted data with function (4.19) and recover the Stokes parameters ( $\vec{S}_{fit}$ ).

An error of approximately  $2^\circ$  on the orientation of the fast axes translates into an error of less than 1.8% on the determined degree of polarization.



Figure 4.19: Relative error on the degree of polarization (%) as a function of the uncertainty on the apex angles  $\xi$  and  $\psi$ .

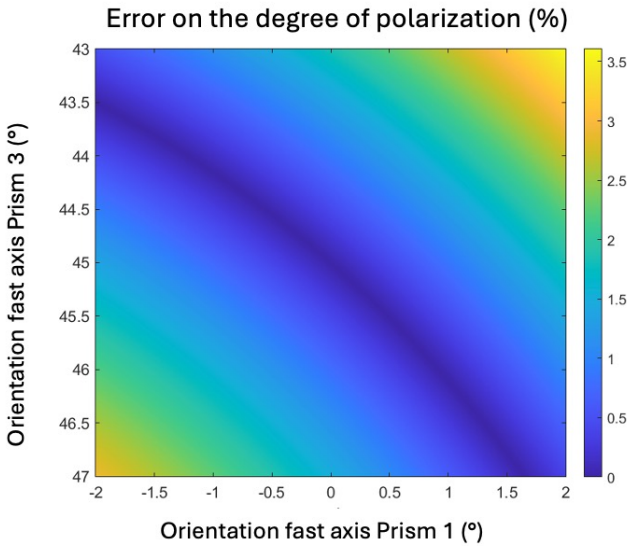


Figure 4.20: Relative error on the degree of polarization (%) as a function of the uncertainty on the orientation of the fast axes in the first and the third prism.

A similar formula with Eq. (4.22) was used to compute this error, and the only dif-

ference now comes from replacing the angles  $\xi$  and  $\psi$  with the orientations of the fast axes.

- *The field of view*

Another extremely sensitive parameter that must be considered in the analysis of the functioning of this instrument is the field of view (*FOV*). All previous simulations and illustrations were based on the hypothesis of a point source of polarized light that was perfectly collimated and had a normal incidence on the modulator. In other words, only the effect of the central field was monitored (the red field from Fig. 4.21). In reality, however, for an extended light source, the rays will be focused not on a point but on a surface (Petzval surface). As a result, the source of the collimator situated in front of the modulator will not be a point but an extended object. Consequently, the modulator will be crossed by the light coming from the central and off-axis fields. This overlap will propagate up to the level of the detector. This situation is intuitively represented in Fig. 4.22. Therefore, most pixels will be illuminated by a cone of light, the opening being determined by the *FOV* from which they receive the light.

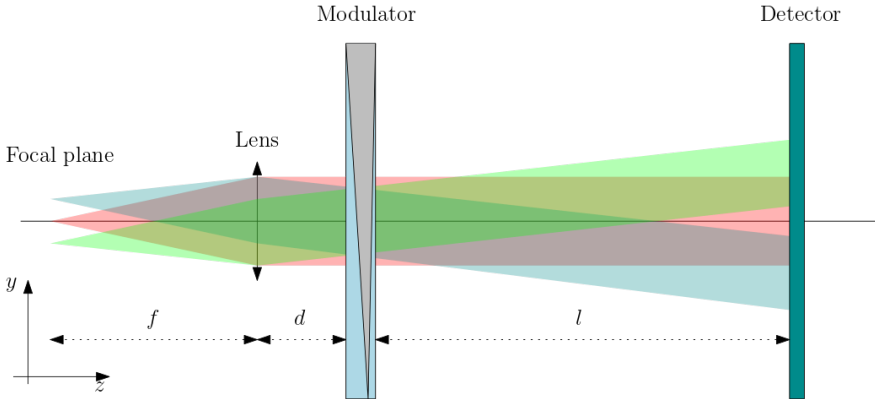


Figure 4.21: Schematic representation of the situation when *FOV* is different from zero. The light collected by the telescope (not presented here) converges in the focal plane. A collimator placed after the telescope's focal plane helps us collimate the light for the polarimetric part. Only the central field will have a normal incidence on the modulator. The rest of the fields will have an oblique incidence, depending on the focal length of the collimator and the image size from the focal plane.

Although this lighting cone is not necessarily symmetrical for all the pixels about the  $z$ -axis of the reference system, to simplify the simulations, we will place ourselves in this hypothesis (see Fig. 4.22). Therefore, the total intensity detected by a pixel with the extension  $\Delta y$  along the vertical direction is:

$$I_{out} = \int_{\Delta y_{i-1}}^{\Delta y_i} \int_{-\alpha}^{+\alpha} I(y, \alpha) dy d\alpha. \quad (4.23)$$

where  $I$  is the function from Eq. (4.19). This means that each pixel will receive light from the central field and the other fields located between 0 and the maximum angle  $\alpha = FOV/2$ . The difference between the rays belonging to the central field and the others

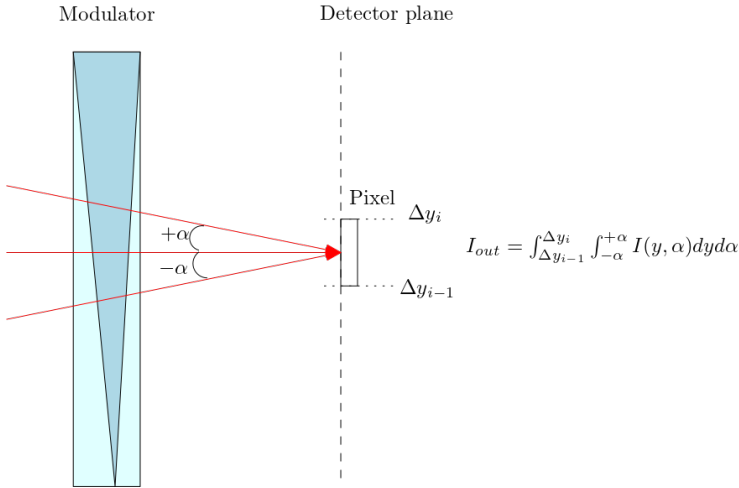


Figure 4.22: The *FOV* translated into the conditions of illumination of a pixel. The angle  $\alpha$  corresponds here to  $FOV/2$

lies, from a polarimetric point of view, in the fact that the off-axis rays will go through a different phase delay. It is not just a simple phenomenon of magnification. It is a phenomenon of superposition of modulations from various regions of the modulator.

The consequence of the existence of the  $FOV \neq 0$  is the reduction of the visibility of the intensity pattern. The difference between the minimum and maximum intensity values recorded along the vertical direction decreases as the field of view increases. The essential parameters that now intervene in forming the intensity pattern on the detector plane are the *FOV* (or  $\alpha$ ) and the distance between the detector and the modulator ( $l$ ). Thus, as the distance between the modulator and the detector increases, the projected size of the pixels in the modulator plane will also increase. The integration of the intensity modulation over an increasing distance results in a blurring of the intensity variations. In fact, when the light collected by a pixel is coming from a cone of light with an opening  $\alpha$ , the phase variation of the light collected by this pixel is no longer expressed by Eq. (4.18). The optical path traveled inside each of the prisms varies, which will affect the phase variation. The new expressions of the phase difference induced by the prisms 1 and 3 are:

$$\Delta\phi_1(y, \alpha) = \frac{2\pi}{\lambda} \Delta n(\lambda) \frac{1}{\cos(\alpha)} \left[ \frac{l + y \tan(\xi)}{1 - \tan(\alpha) \tan(\xi)} \right], \tag{4.24}$$

$$\Delta\phi_3(y, \alpha) = \frac{2\pi}{\lambda} \Delta n(\lambda) \frac{1}{\sin(\alpha) + \frac{\cos(\alpha)}{\tan(\psi)}} \left[ (3l + h(\tan(\xi) + \tan(\psi))) \tan(\alpha) + \frac{l + y \tan(\psi)}{\tan(\psi)} \right], \tag{4.25}$$

where  $\alpha$  is the angle of incidence, and  $l$  is the distance between the entry face of the modulator and the detector. The blurring of intensity can be observed in Fig. 4.23.

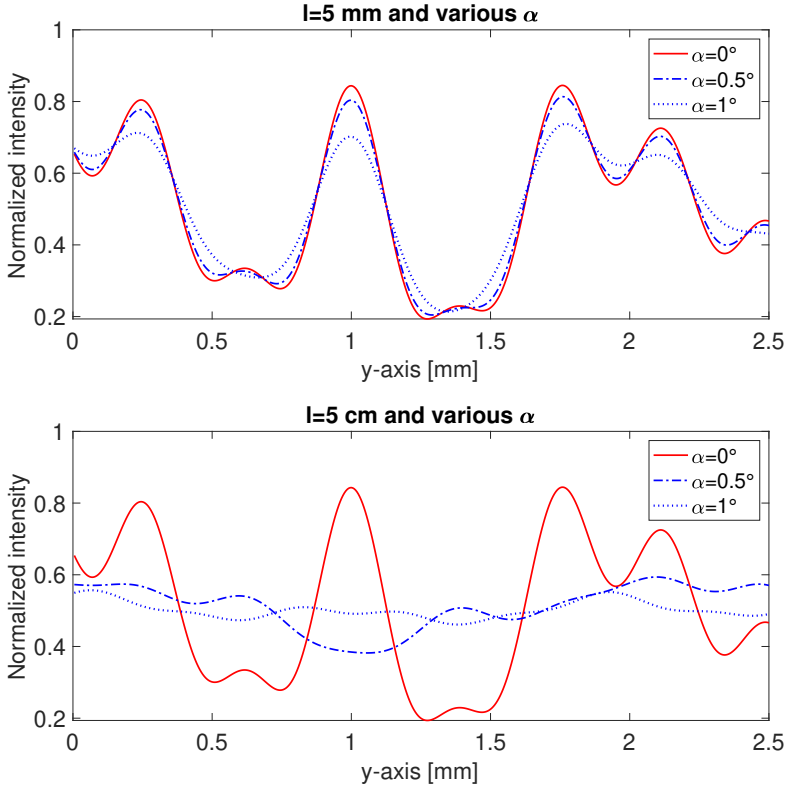


Figure 4.23: The effect of the field of view and the detector-modulator distance on the intensity pattern. The top plot shows the case of the gradual increase of  $\alpha$  from  $0^\circ$  to  $1^\circ$  for a modulator-detector distance of 5 mm. The second plot shows the same gradual increase of  $\alpha$ , when the detector is located at 5 cm from the modulator.

Thus, after correcting the expression of the phase difference in the three prisms of the modulator, to take into account an oblique incidence, we simulated the detected intensity for  $\alpha$  between  $0^\circ$  and  $1^\circ$ , and for two different distances modulator-detector ( $l$ ). In order to compute the intensity value, we used again a simplified model. The middle part of the modulator continues to have a negligible role in the signal modulation, and the Fresnel terms are ignored. Figure 4.24 details the case of a detector located at 5 mm or 5 cm away from the modulator. For a distance of 5 cm, we notice a strong "attenuation" of the pattern when  $\alpha$  increases.

The modification of the pattern of the intensity with the angle  $\alpha$  influences the error level in the determination of the Stokes parameters. To see this effect, a series of simulations were performed starting from an arbitrary input vector,  $\vec{S} = (1, 0.5, 0.5, 0.1)^T$ . The results are represented in Fig. 4.24.

The first plot from the top in Fig. 4.24 shows the intensity pattern corresponding to the central field. The second graph shows the effect of increasing  $\alpha$  from  $0^\circ$  to  $0.1^\circ$ ,

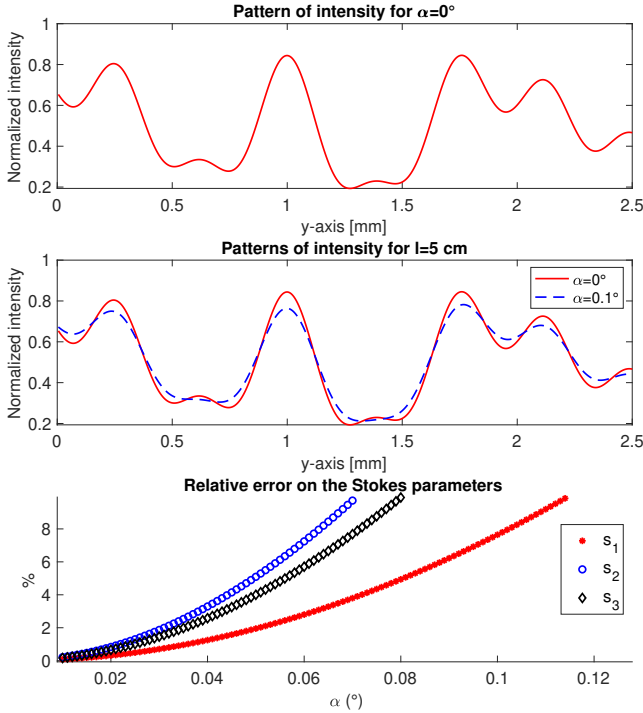


Figure 4.24: The effect of the field of view on the modulation quality.

under the conditions of a detector located 5 cm away from the modulator. Based on this pattern, the last graph shows the relative error in determining the Stokes parameters using the fit method when the field increases.

As explained above, the existence of an  $\alpha$  angle different from zero changes the intensity pattern. And this will translate into the demodulation quality. Determining the polarization is based on fitting the intensity function to the values in the detector plane, which calls only for the theoretical expression of the intensity corresponding to the central field. The extended function, which also considers the existence of a field of view, fails to produce a good fit.

Because of this constraint, the error in the polarization reconstruction will increase with the  $\alpha$  angle. For the values considered in this simulation, we note that an  $\alpha=0.05^\circ$  will cause an error of approximately 5% in determining parameters  $S_2$  and  $S_3$  and approximately 2% for  $S_1$ .

Creating an instrument in which the distance between the detector and the modulator is so small is, however, very difficult. Suppose we increase this distance up to, say, 10 cm (see Fig. 4.25). In that case, we notice that to stay within the limits of the same order of magnitude of the errors, we will have to decrease  $\alpha$  around  $0.03^\circ$ , a value con-



sistent with the values currently used in astronomy.

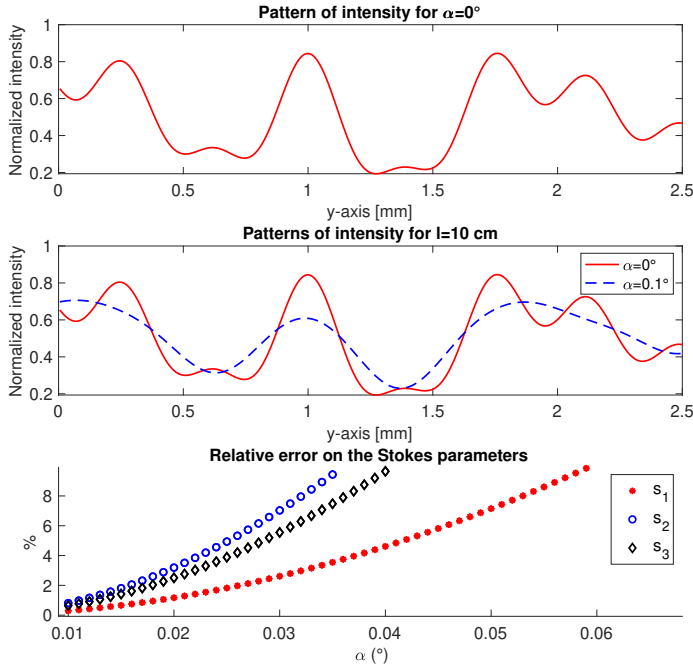


Figure 4.25: Same simulations as in Fig. 4.24, but for a detector situated at a distance of 10 cm to the entry face of the modulator.

Both simulations show that the field of view strongly affects the quality of the demodulation.

Thus, for a particular configuration of the optical system, which assumes a fixed distance between the modulator and the detector, the increase of the field of view results in a blurring of the intensity pattern and an increase in the error in determining the polarization (see Fig. 4.23). The contrast of the pattern was defined here as:

$$C = 100 \cdot \frac{I_{max} - I_{min}}{I_{max} + I_{min}}, \quad (4.26)$$

where  $I_{max}$  stands for the maximum value of the intensity detected, and  $I_{min}$  for the minimum value.

However, it should be emphasized that this is valid only in the case of demodulation based on the fit with the theoretical function. The main reason for the increase in error is not necessarily the decrease in the visibility of the pattern but the fact that the theoretical function no longer accurately describes the intensity variation at the detector level. As pointed out above, the reason behind this deviation is that only the function corresponding to the central field can be used for the fit.

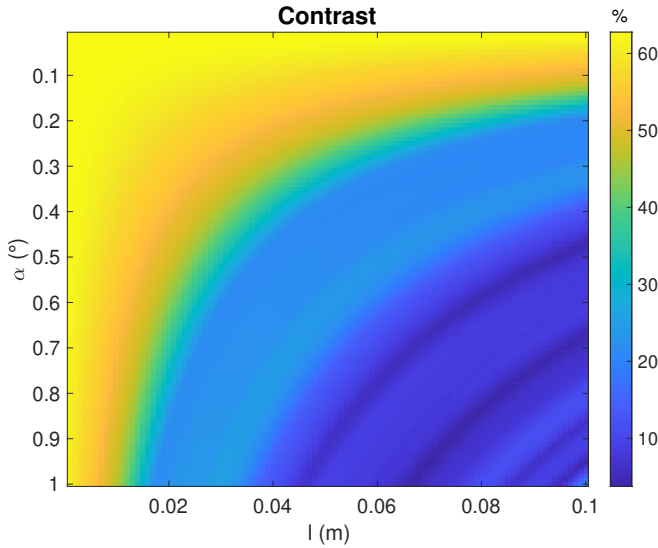


Figure 4.26: Contrast degradation as a function of  $\alpha$  and  $l$ .

If, instead, the demodulation is based on the determination of the instrumental matrix, then the field of view's effect is considered and included in the demodulation process. It no longer leads to an additional error. In the case of demodulation based on the instrumental matrix, the *SNR* value is the decisive factor, together with the degree of polarization. The latter plays an equally important role as the field of view, as it has the same effect on the intensity pattern.

The decrease in the degree of polarization of the incident light is also translated into a reduction in the visibility of the pattern. As an elementary rule, it can be noted that, at a constant *SNR*, the polarimetric sensitivity decreases by increasing the field of view so that only high degrees of polarization can be perceived. Reducing the field of view has the opposite effect: weaker degrees of polarization become accessible.

Based on the determination of the modulation matrix  $W$ , the second approach for the demodulation of the signal seems to cope much better with the errors and uncertainties related to the system parameters. Thus, instead of trying to assess the uncertainty of the main parameters of the optical system, this method uses the system's product as a whole. By this, it comprises the effect of the actual value of the main parameters. In this approach, the modulation matrix ( $W$ ) and the instrumental matrix ( $W^{-1}$ ) are, at first, determined experimentally for the required wavelength and optical setup. Then, the demodulation becomes possible from here, using the relation (3.13). The retrieval of the instrumental matrix is based on a calibration technique that uses a series of well-known polarization states as input and corresponding modulations (Boulbry et al., 2007). More details about this procedure are presented in the second part of this thesis. Instead of propagating errors on the system's parameters, this method propagates the uncertainty related to the input Stokes vector.

The two methods are not incompatible but complementary, and depending on the context, the more suitable one can be chosen. Thus, if the knowledge of the modulator can guarantee an error on the Stokes parameters below what we can achieve with a calibrated polarization state generator (PSG) in the second one, then there is no reason to choose the determination of the instrumental matrix. Due to the limited available time, in the current research, we have used the fit method of the theoretical function of the intensity (Eq. 4.19) to the simulated data in the theoretical exploration of the polarimeter. The second method was used for experimental validation. In the last part of this research, we will see that the second method can produce an excellent retrieval of the Stokes parameters even without a precise knowledge of the optical system.

- *Uncertainty on the temperature*

Just like the imprecision on the apex angles, the uncertainty on the temperature can also largely impact the use of the fit of the theoretical function to the experimental data to retrieve the polarization. The optical properties of the modulator vary depending on the temperature. Using the Sellmeier model, the variation of the birefringence of  $\text{MgF}_2$  with temperature can be determined, and thus, the impact of an inaccuracy on the temperature in determining the Stokes parameters can be simulated (Tropf and Spie, 1995). Figure 4.27 illustrates the error on the normalized parameters  $s_1$ ,  $s_2$ , and  $s_3$  for the temperature inaccuracy of up to  $1^\circ\text{C}$ .

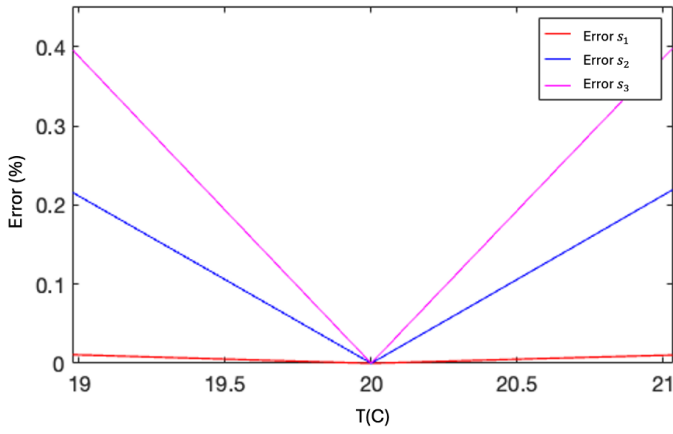


Figure 4.27: Relative error on the normalized Stokes parameters (%) as a function of the uncertainty on the temperature.

The formula used to compute this relative error is also similar to Eq. (4.22):

$$\Delta s_i(T, \Delta T) = 100 \cdot \frac{|s_i(T + \Delta T) - s_i(T)|}{s_i(T)}, \quad (4.27)$$

where  $s_i$  are normalized Stokes parameters ( $S_i/S_0$ , for  $i = 0, 1, 2, 3$ ),  $T$  is the reference temperature (here  $20^\circ\text{C}$ ), and  $\Delta T$  the deviation from this temperature.

Note that the most affected is the determination of the circular polarization, with an error of up to 0.4%, followed by the polarization at  $45^\circ$ . The effect on vertical or horizontal linear polarization is almost negligible.

## 4.5. SAMPLING CRITERIA

Patterns of modulation resembling those presented in Fig. 4.17 can be obtained for various geometrical configurations of the prisms. Considerable freedom exists for choosing the apex angles and the fast axes orientations for the two active wedges of the modulator. Still, the apex angles should stay at minimal values for a compact structure. This will also ensure the minimization of the effect of the split of rays and the impact of the Fresnel terms. If the choice of the fast axes orientation can be dictated by the simplicity of the model and the necessity to modulate the polarization that passes unaffected by the first prism, the reasoning for the apex angles is more complex. Therefore, it should be underlined that a larger apex angle has a faster variation of the phase in the vertical direction and an increase in the weight of the Fresnel terms for transmission and reflection. Because the phase affects the polarization modulation through the *cos* and *sin* functions, the Nyquist criteria should be fulfilled when sampling the signal in the detector plane. That means that the size of the pixels used to collect the signal is smaller than half of the shortest period of the variation of intensity in the vertical direction and that the signal is read on a distance at least equal to the largest period. Coming back to the example presented in Fig. 4.10, where the fast axes were oriented at  $0^\circ$ , respectively  $45^\circ$ , and the apexes were  $\xi$  and  $\psi$ , then the maximum dimension of a pixel ( $\Delta y_{max}$ ) and the minimum distance to be sampled ( $Y_{min}$ ) can be easily inferred using common trigonometric identities. Thus, if we consider, for simplicity, that the reference frame is pointing downwards with the  $y$ -axis, and the additional thickness,  $d_0$ , is zero, then we have the following criteria, separated by type of polarization:

- Horizontal or vertical incoming polarization:  $\vec{S}_{in} = (S_0, S_1, 0, 0)^T$

- Detected intensity:

$$I_{out}(y, \theta, \phi_1, \phi_2) = \frac{1}{2}(S_0 + S_1 \cdot m(y, \theta, \phi_1, \phi_2)) \quad (4.28)$$

- Maximum pixel size:

$$\Delta y_{max} = \frac{\lambda}{2\Delta n(\lambda) \tan(\psi)} \quad (4.29)$$

- Minimum sampling distance:

$$Y_{min} = 2 \cdot \Delta y_{max} \quad (4.30)$$

- $\pm 45^\circ$  linear polarization:  $\vec{S}_{in} = (S_0, 0, S_2, 0)^T$

- Detected intensity:

$$I_{out}(y, \theta, \phi_1, \phi_2) = \frac{1}{2}(S_0 + S_2 \cdot n(y, \theta, \phi_1, \phi_2)) \quad (4.31)$$

- Maximum pixel size:

$$\Delta y_{max} = \frac{\lambda}{2\Delta n(\lambda)(\tan(\xi) + \tan(\psi))} \quad (4.32)$$

- Minimum sampling distance:

$$Y_{min} = \frac{\lambda}{2\Delta n(\lambda)(\tan(\xi) - \tan(\psi))} \quad (4.33)$$

- Circular polarization:  $\vec{S}_{in} = (S_0, 0, 0, S_3)^T$

- Detected intensity:

$$I_{out}(y, \theta, \phi_1, \phi_2) = \frac{1}{2}(S_0 + S_3 \cdot p(y, \theta, \phi_1, \phi_2)) \quad (4.34)$$

- Maximum pixel size:

$$\Delta y_{max} = \frac{\lambda}{2\Delta n(\lambda)(\tan(\xi) + \tan(\psi))} \quad (4.35)$$

- Minimum sampling distance:

$$Y_{min} = \frac{\lambda}{2\Delta n(\lambda)(\tan(\xi) - \tan(\psi))} \quad (4.36)$$

Suppose we choose an arbitrary geometry, with the first apex angle of  $2.6^\circ$  and the second  $1.8^\circ$ . In that case, we notice that the camera's pixel size should be smaller than  $0.1 \text{ mm}$  to make observations at any wavelength. A condition that is easy to fulfill with most of the CCD cameras existing today. In addition, with a region of interest spanning at least  $4 \text{ mm}$  in the vertical direction, any polarimetric signal can be deciphered for any wavelength between  $0.12 \mu\text{m}$  and  $0.7 \mu\text{m}$ . Moreover, a geometry with apex angles of  $1.5^\circ$  and  $3^\circ$  can require an even smaller sampling distance, as shown in Fig. 4.28.

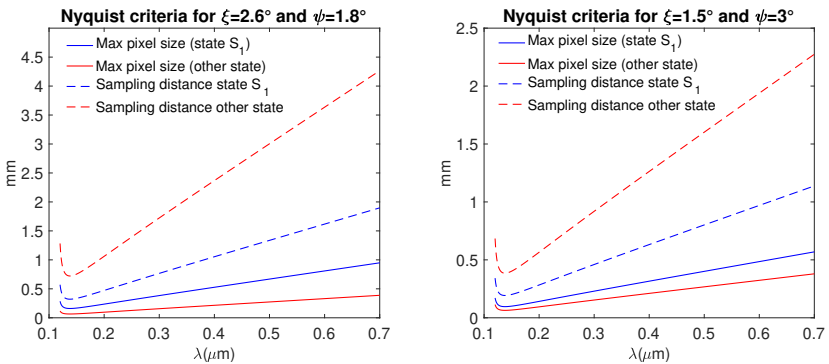


Figure 4.28: Sampling criteria for two possible modulator configurations.

However, the sampling distance should not be the only criterion for choosing an architecture of this type of modulator. As we proved in our previous research, which can be retrieved at the end of the next chapter, another concept should also be considered: the efficiency of the modulation scheme.

The functioning of the modulator supposes a collimated beam arriving orthogonal on the first prism. However, the spot size can contract or enlarge between this point and the detector, depending on the intermediary optics. The Nyquist criterion imposes the limits of this phenomenon of magnifications. Thus, when the spot contracts, we must pay attention that the smallest period of the signal is spread at the detector level on at least 2 pixels in the vertical direction. On the other hand, an enlargement of the image should comply with the necessity to cover, on the detector, at least the length of the longest signal period.

$$\left\{ \begin{array}{l} \text{Inferior limit: Magnification} = \frac{\text{Pixel size}}{\Delta y_{max}} \\ \text{Superior limit: Magnification} = \frac{\text{Detector size}}{\Delta Y_{min}} \end{array} \right. \quad (4.37)$$

The Fig. 4.29 presents the results for a modulator with the apex angles  $2.6^\circ$ ,  $1.8^\circ$ . The Nyquist criterion is not the only constraint of such design when discussing magnification. A magnification can result from the divergence or the convergence of the beam. However, in this case, this effect will be accompanied by a change in the phase difference of the orthogonal components of light reaching the detector. In other words, the detected modulation will be impacted, and the capacity of retrieving the polarization with the fit method will also be affected. We will discuss these aspects in more detail in Chapter 7.

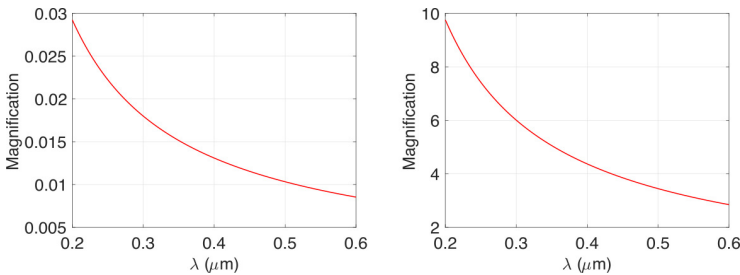


Figure 4.29: Magnification limits imposed by the Nyquist criterion. The inferior limit is presented on the left, and the superior limit is on the right. The system's magnification should stay between the two curves for correct signal sampling.

## 4.6. TOWARDS IMAGING SPECTROPOLARIMETRY

The design presented in the previous pages uses a point source of polarized light. A single central field is necessary to illustrate the functioning of the instrument. However, the modulator can also act on the off-axis fields and be used when extended objects are observed. As we saw, a limit for the field of view ( $FoV$ ) manifests as a limit that depends mainly on the signal's strength and the instrument's desired precision. Never-

theless, the fact that the modulator can also be used for the off-axis fields means that an imaging working mode is compatible with this concept. A possible implementation is presented in Figures 4.30 and 4.31. Figure 4.30 shows a possible development based on the technique of Integral Field Spectrometry with Microlens Array (*IFS-L*) (see Chapter 3). In contrast, Figure 4.31 extends the Integral Field Spectrometry with Slicing Mirrors (*IFS-M*).

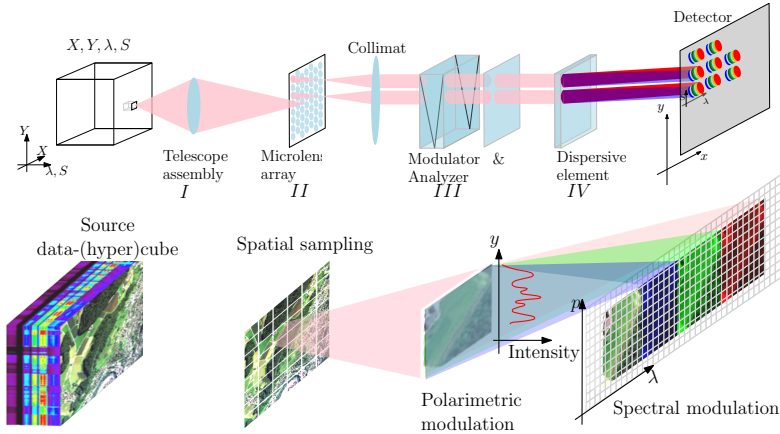


Figure 4.30: Possible design of a snapshot imaging spectropolarimeter based on the IFS-L method.

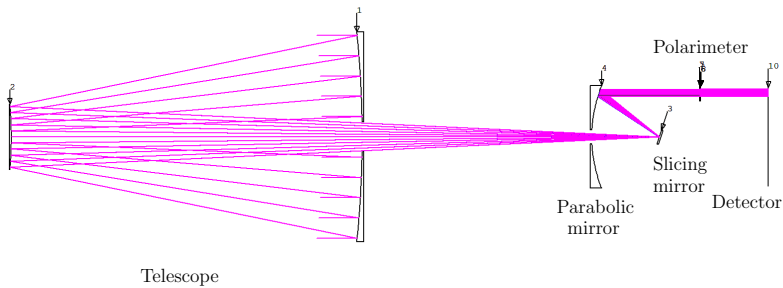


Figure 4.31: Possible design of a snapshot imaging spectropolarimeter based on the IFS-M method.

According to the IFS-L method, the light collected by a telescope assembly or an objective passes through a microlens array placed in the telescope's focal plane. Each field will be then collimated before arriving on the modulator with the help of a microlens array. After the analyzer, the light passes through a dispersive element. Then, using again a microlens array with cylindrical lenslets (not represented in Fig. 4.30), the various wavelengths could be spread along the  $x$ -axis. In contrast, the  $y$ -axis will conserve the modulation the polarimeter induces. Each voxel of data (hypercube of spectral, spatial, and polarimetric information) will pass then through a lenslet from the focal plane of the telescope, will be modulated in intensity by the polarimetric part, and, in the end, after passing through the dispersive element, will be imaged by a cylindrical lenslet. Each

cylindrical lenslet should span enough pixels in a vertical direction to ensure the sampling of the polarimetric modulation. This vertical distance will also give the lenslets the minimum vertical size. In addition, this will also fix the limits of the system's spatial resolution in the vertical direction. In the horizontal direction, a mask can be placed between the dispersive element and the cylindrical microlenses to avoid the overlap of the dispersed light.

Figure 4.31 shows a possible adaptation of the IFS-M (Gao et al., 2010; Hagen, 2012; Hagen and Kudenov, 2013) principle for snapshot imaging spectropolarimetry. In this approach, the light collected by the telescope (1) is reflected by the stack of slicing mirrors to a parabolic mirror (4). The latter allows the collimation of the separated fields with the help of slicing mirrors and placing a polarimeter, respectively, a dispersive element in front of the detector. With cylindrical lenses, re-imaging optics can focus the light in one direction and keep the modulation induced by the modulator in the other direction.





# BIBLIOGRAPHY

- Boulbry, B., Ramella-Roman, J. C., & Germer, T. A. (2007). Improved method for calibrating a stokes polarimeter. *Appl. Opt.*, 46(35), 8533. <https://doi.org/10.1364/AO.46.008533>
- Dodge, M. J. (1984). Refractive properties of magnesium fluoride. *Applied Optics*, 23(12), 1980–1985. <https://doi.org/10.1364/AO.23.001980>
- Dubovik, O., Li, Z., Mishchenko, M. I., & et al. (2019). Polarimetric remote sensing of atmospheric aerosols: Instruments, methodologies, results, and perspectives. *Journal of Quantitative Spectroscopy and Radiative Transfer*, 224, 474–511. <https://doi.org/10.1016/j.jqsrt.2018.11.024>
- Gao, L., Kester, R. T., Hagen, N., & Tkaczyk, T. S. (2010). Snapshot image mapping spectrometer (IMS) with high sampling density for hyperspectral microscopy. *Optics Express*, 18(14), 14330. <https://doi.org/10.1364/OE.18.014330>
- Hagen, N. (2012). Snapshot advantage: A review of the light collection improvement for parallel high-dimensional measurement systems. *Optical Engineering*, 51(11), 111702. <https://doi.org/10.1117/1.OE.51.11.111702>
- Hagen, N., & Kudenov, M. W. (2013). Review of snapshot spectral imaging technologies. *Optical Engineering*, 52(9), 090901. <https://doi.org/10.1117/1.OE.52.9.090901>
- Kemp, J., Wolstencroft, R., & Sweldun, J. (1971). Circular Polarization: Jupiter and Other Planets. *Nature*, (232), 165–168. <https://doi.org/10.1038/232165a0>
- Li, L. W., Rubin, N. A., Juhl, M., Park, J.-S., & Capasso, F. (2023). Evaluation and characterization of imaging polarimetry through metasurface polarization gratings. *Applied Optics*, 62(7), 1704. <https://doi.org/10.1364/AO.480487>
- Pertenais, M., Neiner, C., Bernardi, P., Reess, J.-M., & Petit, P. (2015). Static spectropolarimeter concept adapted to space conditions and wide spectrum constraints. *Applied Optics*, 54(24), 7377. <https://doi.org/10.1364/AO.54.007377>
- Pertenais, M., Neiner, C., Parès, L. P., Petit, P., Snik, F., & van Harten, G. (2014). UVMag: Space UV and visible spectropolarimetry. In T. Takahashi, J.-W. A. den Herder, & M. Bautz (Eds.), *Space telescopes and instrumentation 2014: Ultraviolet to gamma ray* (Vol. 9144). SPIE. <https://doi.org/10.1117/12.2060561>
- Sparks, W., Germer, T. A., MacKenty, J. W., & Snik, F. (2012). Compact and robust method for full stokes spectropolarimetry. *Applied Optics*, 51(22), 5495. <https://doi.org/10.1364/AO.51.005495>
- Tropf, W. J., & Spie, M. (1995). Temperature-dependent refractive index models for BaF<sub>2</sub>, CaF<sub>2</sub>, MgF<sub>2</sub>, SrF<sub>2</sub>, LiF, NaF, KCl, ZnS, and ZnSe. *Optical Engineering*, 34(5), 1369–1373. <https://doi.org/10.1117/12.201666>
- Waquet, F., Cairns, B., Knobelspiesse, K., Chowdhary, J., Travis, L. D., Mishchenko, M. I., & Schmid, B. (2009). Polarimetric remote sensing of aerosols over land. *Journal of Geophysical Research: Atmospheres*, 114. <https://doi.org/10.1029/2008JD010619>



# 5

## THE UNIQUENESS OF THE SOLUTION AND THE BEHAVIOR IN NOISY CONDITIONS

*To be prepared is half the victory*

M. de Cervantes Saavedra, 1615

To be able to measure any polarization with an instrument employing the modulator presented here means, at first, to prove the uniqueness of the modulation. We have to show that each state of polarization corresponds to a unique intensity pattern.

Looking closely at the model of the instrument presented in the previous Chapter (see Fig. 4.13), we notice that the continuous variation in the vertical direction of the phase difference induced by the prisms of the modulator can be translated into a continuous variation of the Mueller matrix of the modulator in the same direction.

At each level  $y$  in the vertical direction, we will have a certain value of the phase differences  $\phi_1(y)$  and  $\phi_3(y)$ , and, accordingly, a specific Mueller matrix  $M(y)$  of the compound formed by the modulator and the analyzer.

An incoming state of polarization  $\vec{S}_{in} = (S_0, S_1, S_2, S_3)^T$ , homogeneous over the entire entry face of the instrument, will be converted, at any position  $y$  along the vertical, in a state  $\vec{S}_{out}(y) = (S'_0(y), S'_1(y), S'_2(y), S'_3(y))^T$ :

$$\vec{S}_{out}(y) = M(y) \cdot \vec{S}_{in}. \quad (5.1)$$

The intensity that can be detected at the level  $y$  by the pixel of a hypothetical detector is:

$$I_{out}(y) = (M_{00}(y) \quad M_{01}(y) \quad M_{02}(y) \quad M_{03}(y)) \cdot \vec{S}_{in}, \quad (5.2)$$

where  $M_{ij}(y)$ , ( $i, j = 0, 1, 2, 3$ ), are the terms of the first line of the Mueller matrix  $M(y)$ , and  $I_{out}$  is the first term of the Stokes vector  $\vec{S}_{out}$ . We adopt the notation with  $I_{out}$  to simplify the reading.

The values taken by the  $I_{out}$  in the vertical direction follow a specific pattern as a function of the incoming polarization.

Considering that we have  $N$  readings of the intensity in the vertical direction, corresponding to different values of  $y$  we can transform the previous equation into a system of equations:

$$\begin{pmatrix} I_{out}(y_0) \\ I_{out}(y_1) \\ I_{out}(y_2) \\ \vdots \\ I_{out}(y_{N-1}) \end{pmatrix} = \begin{pmatrix} M_{00}(y_0) & M_{01}(y_0) & M_{02}(y_0) & M_{03}(y_0) \\ M_{00}(y_1) & M_{01}(y_1) & M_{02}(y_1) & M_{03}(y_1) \\ M_{00}(y_2) & M_{01}(y_2) & M_{02}(y_2) & M_{03}(y_2) \\ \vdots & \vdots & \vdots & \vdots \\ M_{00}(y_{N-1}) & M_{01}(y_{N-1}) & M_{02}(y_{N-1}) & M_{03}(y_{N-1}) \end{pmatrix} \cdot \vec{S}_{in}, \quad (5.3)$$

where each line  $M_{ij}(y_k)$ , ( $i, j = 0, 1, 2, 3$ ,  $k = 0, \dots, N-1$ ) is the first line of the Mueller matrix associated to the optical compound at the position  $y_k$  in the vertical direction.

In a contracted vectorial form, we saw (Eq. 3.10) that this system can be written as:

$$\vec{I} = W \cdot \vec{S}_{in}, \quad (5.4)$$

where  $\vec{I}$  is the vector of the intensity readings and  $W$  is the modulation matrix of the instrument.

For the case of the model of the instrument studied, the theoretical expression of the intensity is provided by the Eq. (4.19), reproduced here by considering only the dependency on  $y$ :

$$I_{out}(y) = \frac{1}{2}(S_0 + S_1 m(y) + S_2 n(y) + S_3 p(y)), \quad (5.5)$$

where the functions  $m(y)$ ,  $n(y)$  and  $p(y)$  are provided by Eq. 4.20. The modulation matrix  $W$  of the optical system can then be written in terms of the functions  $m$ ,  $n$ , and  $p$ :

$$W = \begin{pmatrix} 1 & m(y_0) & n(y_0) & p(y_0) \\ 1 & m(y_1) & n(y_1) & p(y_1) \\ 1 & m(y_2) & n(y_2) & p(y_2) \\ \cdot & \cdot & \cdot & \cdot \\ \cdot & \cdot & \cdot & \cdot \\ 1 & m(y_{N-1}) & n(y_{N-1}) & p(y_{N-1}) \end{pmatrix} \quad (5.6)$$

Using these notations, the question is whether the previous system of equations admits a single solution for the vector  $\vec{S}$ .

Several methods can be used to answer this question. It can be demonstrated, for instance, the independence of the functions  $m$ ,  $n$ , and  $p$  responsible for polarization modulation. This method was explored closely in our previous research (Vasilescu et al., 2020), and its demonstration is reproduced at the end of this chapter. A second method that can be used, equivalent to the first, is based on the orthogonality of the functions  $m$ ,  $n$ ,  $p$ . We presented this method at the International Conference in Space Optics - ICSO 2020 (Vasilescu et al., 2021). Despite being comparable to the first method, it comes with the advantage that it is much easier to adapt to the different characteristics of the optical system: the size of pixels, the wavelength, or the number of pixels can be much more easily considered. Finally, a numerical method can also be applied. This involves the calculation of the rank of the modulation matrix,  $W$ . Unlike the first two methods, the latter has the advantage of considering the actual optical system. After experimental determination, the technique can be applied directly to the modulation matrix.

Another important concept that must be discussed is the efficiency of the modulation scheme, as defined in Chapter 3. This concept opens the door to finding the best geometry of the modulator and a suitable analyzer orientation. A general presentation of this notion can be retrieved in one of our previous papers (Vasilescu et al., 2020).

The additional investigation of the efficiency conducted in (Vasilescu et al., 2021) establishes a clear relationship between the orthogonality of the functions  $m$ ,  $n$ ,  $p$  and the efficiency of the modulation scheme for the studied spectropolarimeter. Also, this study identifies the modulator + analyzer system configurations with the highest efficiency. This is an essential step towards the experimental implementation of the spectropolarimeter studied here. Thus, based on this analysis, we can identify which is the best orientation of the analyzer or which apex angles should have prisms 1 and 3 of the modulator.

## 5.1. THE UNIQUENESS OF THE SOLUTION: THE RANK OF THE MODULATION MATRIX

Let us consider an arbitrary system of linear equations:

$$A\vec{x} = \vec{B}, \quad (5.7)$$

where  $A$  is a  $n \times m$  matrix,  $\vec{x}$  is the vector of the unknowns ( $m \times 1$ ) and  $\vec{B}$  is the vector of solutions ( $n \times 1$ ).

Then, this system has a unique solution if

$$\text{rank}(A) = \text{rank}(A|B) = \text{number of rows in } \vec{x}. \quad (5.8)$$

The rank of a matrix is defined as the maximum number of linearly independent rows. The matrix  $(A|B)$  is called the augmented matrix and is formed by adding at the end of the columns of  $A$  the column of  $\vec{B}$ .

If the vector  $B$  is equal to 0, then the system  $A\vec{x} = 0$  will have a unique solution, the trivial solution  $x = 0$ , if and only if  $\text{rank}(A) = \text{number of rows in } \vec{x}$ .

Coming back to our model of spectropolarimeter, let us consider again the intensity pattern detected by a column of  $N$  pixels (see Eq. 5.3) when a state of polarization  $\vec{S}_{in}^A = (S_0^A, S_1^A, S_2^A, S_3^A)^T$  enters the system. The vectorial system (5.4) becomes:

$$\vec{I} = W \cdot \vec{S}_{in}^A \quad (5.9)$$

Suppose now that there exists a second state of polarization,  $\vec{S}_{in}^B = (S_0^B, S_1^B, S_2^B, S_3^B)^T$ , different from  $\vec{S}_{in}^A$ , but generating the same pattern of intensity,  $\vec{I}$ . We can write then:

$$\vec{I} = W \cdot \vec{S}_{in}^B. \quad (5.10)$$

Subtracting Eq. (5.9) from Eq. (5.8):

$$\vec{0} = W \cdot \Delta\vec{S}_{in}, \quad (5.11)$$

where

$$\Delta\vec{S}_{in} = \vec{S}_{in}^A - \vec{S}_{in}^B. \quad (5.12)$$

This way, the question about the uniqueness of the intensity pattern is reduced to the question of the uniqueness of the solution of the system (5.11).

A trivial solution of this system is  $\Delta\vec{S}_{in} = 0$ . According to the definition, if  $\text{rank}(W)=4$ , then  $\Delta\vec{S}_{in} = 0$  is the only solution of this system. In addition, the rank of these matrices is four if the lines of  $W$  are linearly independent.

However, the lines of the matrix  $W$  depend on many parameters. The positions  $y$ , the pixel size over which the signal is integrated, the wavelength, and the spectral resolution are just a few factors that can be considered in the computation of this matrix.

One possibility for answering the question is to use the numerical approach.

Simulations can be performed for different pixel size values, wavelength, spectral resolution, etc. In our case, all these simulations revealed that, for an ideal instrument where the noise can be ignored, the rank of the matrix  $W$  is four.

Nevertheless, in the case of a real optical system, the polarimetric parameters and noise can generate numerical combinations that can decrease the rank of the  $W$  matrix. Besides the fact that this will affect the uniqueness of the modulation scheme, a rank lower than four will also mean that this concept of an instrument cannot be used for full Stokes polarimetry. For this reason, a practical realization of this spectropolarimeter must comprise a prior check of the rank of  $W$  to guarantee the uniqueness of the solution.

The argument behind the retrieved result is that the columns of the  $W$  matrix are linearly independent. The leading cause of this is that the components of the polarimeter differently impact the incoming polarization states. Therefore, an incoming  $S_1$  state is modulated only by Prism 3, a state  $S_2$  is impacted only by Prism 1, and  $S_3$  or any other combination is affected by Prism 1 and 3 (see Fig. 4.11).

## 5.2. THE UNIQUENESS OF THE SOLUTION: THE WRONSKIAN OF THE MODULATION FUNCTIONS

When the terms of the matrix  $W$  are seen as continuous functions, then the problem of the linear independence of the columns of  $W$  becomes the problem of linear independence of the functions  $m$ ,  $n$ , and  $p$ .

A different mathematical apparatus must be used in this situation. Thus, to answer the question of uniqueness, we used the Wronskian notion in our research, which allows, just like the orthogonality, to assess linear independence. The following pages detail the method based on the computation of the Wronskian, as it was published in the Journal of Astronomical Telescopes, Instruments, and Systems (Vasilescu et al., 2020). In addition, the instrument's behavior in noisy conditions also received special attention. Considering the situation of the additive noise, independent of the signal, the uncertainties on Stokes parameters are computed for different configurations of the modulator. Based on this, the efficiency of the modulation scheme (see Chapter 3) was established for the same series of configurations. In the end, we proved that the modulation scheme's total efficiency (see Eq. 3.14) is close to the maximum value, and a large series of configurations (apex angles and orientations of the analyzer) exist where the efficiencies corresponding to the Stokes parameters are also close to the optimum.



# Journal of Astronomical Telescopes, Instruments, and Systems

AstronomicalTelescopes.SPIEDigitalLibrary.org

## **Solution uniqueness and noise impact in a static spectropolarimeter based on birefringent prisms for full Stokes parameter retrieval**

Bogdan Vasilescu  
Yaël Nazè  
Jérôme Loicq

Bogdan Vasilescu, Yaël Nazè, Jérôme Loicq, "Solution uniqueness and noise impact in a static spectropolarimeter based on birefringent prisms for full Stokes parameter retrieval," *J. Astron. Telesc. Instrum. Syst.* **6**(2), 028001 (2020), doi: 10.1117/1.JATIS.6.2.028001

**SPIE.**

# Solution uniqueness and noise impact in a static spectropolarimeter based on birefringent prisms for full Stokes parameter retrieval

Bogdan Vasilescu,<sup>a,\*</sup> Yaël Nazè,<sup>b</sup> and Jérôme Loicq<sup>a</sup>

<sup>a</sup>Université de Liège, Centre Spatial de Liège, Liège, Belgium

<sup>b</sup>Université de Liège, Liège, Belgium

**Abstract** An innovative model of a static spectropolarimeter able to cover the entire Stokes vector is discussed. The optical layout is based on a birefringent modulator formed by two anti-parallel prisms stuck together with the help of an intermediary part of the same material. This optical model has the advantage of being extremely compact. It avoids any movable parts or rotating components. By its architecture, the device induces a complete modulation on the vertical direction of any incoming polarized light, facilitating the determination of the entire Stokes vector through a single measurement. Because the modulation is also wavelength-dependent, spectral dependencies of the polarization states can be derived. The behavior of the model was first investigated in noise-free conditions. The existence of a unique solution was proven in the absence of noise and for any Stokes vector configuration. Under noisy conditions, the uncertainty on the Stokes parameters and the efficiency of the modulation scheme were evaluated as a function of the analyzer's angle and for two different configurations of the modulator. The simulations show that an almost ideal efficiency is reachable, qualifying the concept for the high-precision measurement of the polarization. © 2020 Society of Photo-Optical Instrumentation Engineers (SPIE) [DOI: [10.1117/1.JATIS.6.2.028001](https://doi.org/10.1117/1.JATIS.6.2.028001)]

**Keywords:** optics; polarimetry; spectropolarimetry; birefringence; modulation scheme; efficiency of modulation.

Paper 19129 received Dec. 19, 2019; accepted for publication Apr. 7, 2020; published online Apr. 23, 2020.

## 1 Introduction

The study of the polarization of light is an excellent way to get information about remote objects. Measuring this property leads to gathering essential information about the environment and the optical sources. In astronomy, for instance, with the help of the Zeeman or Hanle effect, the polarization becomes the best method to determine the magnetic field of stars.<sup>1,2</sup> Moreover, during the last years, polarimetry has also been found to be a possible interesting tool for the detection and study of exoplanets.<sup>3-5</sup>

With scattering theories, the polarization also brings information about the size, the shape, and the distribution of scattering particles, helping to characterize the surface or the atmosphere of astronomical bodies.<sup>1,2,5</sup> Combining polarization with spectral properties, the collected data become even more important for the description of the medium. Moreover, the applicability of the polarization goes far beyond astronomy. Chemistry, biology, and medicine are also making extensive use of this technique. Generally, the instruments used for polarization determination are based on a modulator (which can be a polarizer, a phase shifter, or a rotator) and a polarizer (analyzer). The role of the modulator is to convert any incoming state of polarization into a predetermined type of polarization, which will then be studied with the help of the analyzer. Because most of the detectors (such as CCD, CMOS, etc.) are only sensitive to light intensity, the structure of the polarimeter must convert the parameters relative to the polarization of light (Stokes parameters) onto a level of detected intensity.<sup>6,7</sup>

---

\*Address all correspondence to Bogdan Vasilescu, E-mail: [bvasilescu@uliege.be](mailto:bvasilescu@uliege.be)

It can be proven that the measured intensity depends both on the phase difference induced by the modulator and on the orientation of the analyzer.<sup>8</sup> In the past, two significant families of measurement techniques have been developed to evaluate the polarization states of light: one using rotating components and another using amplitude division.

In the first case, by varying the relative position of the analyzer and the modulator, a sequential (or temporal) modulation of the measured intensity is obtained. At least, four different configurations are required to determine all four Stokes parameters describing the polarization of the light. The second technique, which is static, is based on the use of birefringent elements such as Wollaston prisms, Babinet compensators, and Glan–Foucault prisms. In this way, precise modulations of the light intensity can be obtained at different positions in space with regard to the optical path of the incoming ray.

Thereby, the determination of the polarization can follow either a discrete method, either a continuous one, according to the number of modulations received by the outgoing intensity of light, and used to compute the incoming polarization. Most of the time, both measurement procedures occupy a relatively large volume and make use of complex mechanisms. The considerable dimensions and the need for rotating parts are the most significant drawbacks for the space usage of these classical types of polarimeters. Indeed, they directly impact the cost, the design, and the safety of space missions.

In this context, the methodology proposed by Sparks<sup>9</sup> and further developed by Pertenais et al.<sup>10</sup> for single-shot full Stokes polarimetry has the advantage of being extremely compact and robust, without any moving components.

The originality of this concept, hereafter referred to as STAS (static spectropolarimeter), is based on the modulation of the incoming signal due to the chromatic birefringence of the modulator  $\Delta n(\lambda)$  combined with a specific geometry of the device.<sup>10,11</sup> Any incoming polarization state will acquire a continuous modulation depending simultaneously on the wavelength and the position. The concept can be used on a large wavelength range by choosing an appropriate material for the modulator. For instance, the use of magnesium fluoride ( $\text{MgF}_2$ ) gives access to the entire spectrum between 0.12 and 7  $\mu\text{m}$ ,<sup>12,13</sup> whereas with calcium fluoride the working window is even larger, from 0.13 to 9.7  $\mu\text{m}$ .<sup>14,15</sup> Because of the wavelength dependence of the modulation characterizing the received intensity, the instrument can be converted into a spectropolarimeter only by placing a spectrometer after the analyzer.

The key part of the design is the modulator, formed by two antiparallel birefringent uniaxial wedges, with fast axes oriented at 45 deg one about another (see Fig. 1). By continuously varying the phase difference between the orthogonal components of light, the first wedge will modulate along the vertical direction any incoming state of polarization, except the  $Q$  state. This one will pass unaffected because the optical axis is oriented along the  $x$  direction (see Fig. 1). A second birefringent wedge, having the fast axis at 45 deg with respect to  $x$  direction will drastically simplify the computations and will lift the  $Q$  state degeneracy.

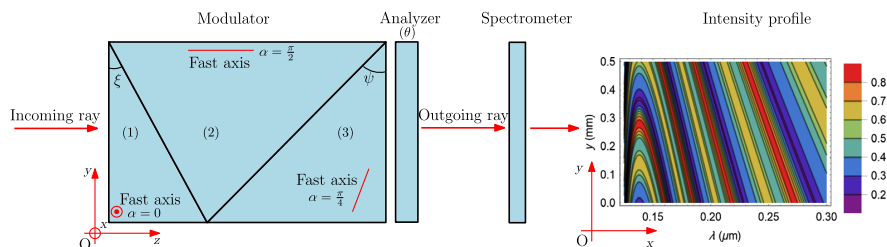


**Fig. 1** The incoming light arriving from the left-hand side is collimated and perpendicular to the surface of the instrument, the ( $xy$  plane). After passing through the polarimeter, the emerging light has an intensity modulated along the vertical direction (along the  $y$  axis). The spectrometer then leads to a wavelength dispersion along the horizontal direction ( $x$  axis). The observed intensity profile represented here corresponds to an arbitrary state of polarization  $\mathbf{S} = [1, 0.4, 0.3, 0.5]^T$  and to a modulator build in  $\text{MgF}_2$ , with the apex angles  $\xi = 1.5$  deg and  $\psi = 3$  deg. The orientation of the analyzer was  $\theta = 90$  deg. Additionally, it was considered that the entire incoming beam is identically polarized, being characterized by a single polarization state, i.e., the vector  $\mathbf{S}$ .

In this paper, we discuss three questions on this new concept of a spectropolarimeter. First, the uniqueness of the solution: we demonstrate in Sec. 3 that in the ideal conditions of the absence of noise, any pattern of the intensity from the detector plane is associated with a single state of polarization.

The second question concerns the quality of the measurement under noisy circumstances. What is the precision of this instrument when the noise is present? The answer to this question is detailed in Sec. 4.

The third question is related to the efficiency of the modulation scheme, as it was defined by del Toro Iniesta.<sup>8</sup> We study it in Sec. 5 for different orientations of the analyzer, different apex angles, and various modulation schemes. Answering this question allows us to compare the model with other existing instruments and to find an optimal architecture.

## 2 Static Spectropolarimeter Concept

The key part of STAS is the modulator based on three birefringent uniaxial elements made of the same material (Fig. 1). Two antiparallel wedges [parts (1) and (3) in Fig. 1] of very small apex angles  $\xi$  and  $\psi$  are optically glued together with the help of a third piece placed in between [element (2)]. The fast axis has a specific orientation in each component of the modulator: parallel to the  $x$  axis in the first wedge, parallel to  $z$  axis in the middle part and at 45 deg with regard to  $x$  axis [in the  $(xy)$  plane] in the last wedge.<sup>9,10,16</sup>

In addition to the modulator, the polarimeter needs a linear polarizer (or analyzer), oriented at an angle  $\theta$  about the  $x$  axis, in the plane  $(xy)$ . After the passage through the polarimeter, the light is spectrally dispersed by the spectrometer over the  $x$  axis.

### 2.1 Working Principle

The description of the polarization is performed with the Stokes formalism. According to this, the information about polarization is encoded into the Stokes vector:

$$\mathbf{S} = \begin{bmatrix} I \\ Q \\ U \\ V \end{bmatrix}. \tag{1}$$

Its components have the dimension of intensity and are associated with specific types of polarization of the incident light.<sup>7</sup>  $I$  represents the total intensity,  $Q$  is the linear horizontal or vertical polarization, and  $U$  is the linear polarization at 45 deg or 135 deg, whereas  $V$  is the circular left or right polarization:

$$\begin{cases} I = E_{0x}^2 + E_{0y}^2 \\ Q = E_{0x}^2 - E_{0y}^2 \\ U = 2E_{0x}E_{0y} \cos \epsilon \\ V = 2E_{0x}E_{0y} \sin \epsilon \end{cases}. \tag{2}$$

Under this notation,  $E_{0x}$  and  $E_{0y}$  are the amplitudes associated with the orthogonal components of the electric field of light, and  $\epsilon$  is the phase difference between these components. Another useful notion is the degree of polarization:

$$p = \frac{\sqrt{Q^2 + U^2 + V^2}}{I}, \quad 0 \leq p \leq 1, \tag{3}$$

with  $p = 1$  in the case of the totally polarized light and  $p = 0$  for the nonpolarized light. In a more detailed definition, the degree of linear polarization is given by  $p_{\text{lin}} = \sqrt{Q^2 + U^2}/I$  while the degree of circular polarization is  $p_{\text{circ}} = V/I$ .

To deal with the passage through an optical element like the modulator or the analyzer, the Mueller calculus is used. Principles of this state that to any polarizing element one may associate a Mueller matrix  $\mathbf{M}$ ,  $4 \times 4$ , such as

$$\mathbf{S}_{\text{out}} = \mathbf{M} \cdot \mathbf{S}_{\text{in}}, \tag{4}$$

where  $\mathbf{S}_{\text{out}}$  is the Stokes vector of the outgoing polarization, after its travel through the instrument, and  $\mathbf{S}_{\text{in}}$  is the incoming polarization. Every subelement of the optical assembly is represented by its Mueller matrix, giving the combination:

$$\mathbf{M} = \mathbf{M}_n \cdot \mathbf{M}_{n-1} \cdot \dots \cdot \mathbf{M}_1, \tag{5}$$

where  $\mathbf{M}_n$  is the last element crossed by light.

Based on this formalism, we analyze in this section each component of the modulator, emphasizing the need for a triple structure.

### 2.2 Single Wedge and Analyzer

Being composed of a birefringent uniaxial material with the fast axis oriented along the  $x$  axis, the first element acts as a variable waveplate (see Fig. 2).

Indeed, because the distance travelled by the light inside the wedge decreases upward, the phase difference ( $\Delta\phi_1$ ) varies linearly with  $y$  following the relation:

$$\Delta\phi_1 = \frac{2\pi}{\lambda} \Delta n(\lambda)(h - y) \tan \xi, \tag{6}$$

where  $\lambda$  is the wavelength of the incoming light,  $\Delta n(\lambda) = |n_o(\lambda) - n_e(\lambda)|$  is the absolute value of the difference between the ordinary and the extraordinary indices of refraction of the element (1),  $h$  is the height of the wedge,  $y$  is the position on the vertical axis of the incidence point for the incoming ray, and  $\xi$  is the apex angle. Due to this geometry, periodically, at certain levels along the  $y$  axis, the phase difference will embrace particular values such as  $\frac{\pi}{2}$ ,  $\pi$ , or  $2\pi$ . At these precise positions, the wedge will behave like a quarter-wave plate, half-wave plate, and full-wave plate, respectively. Because of this, any incoming homogeneous state of polarization, described by

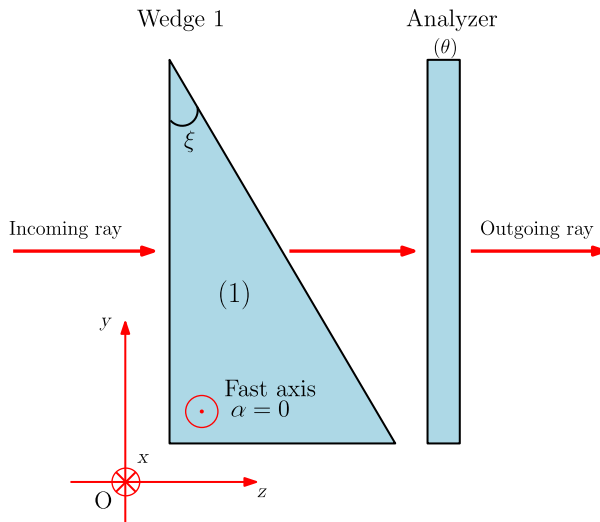


**Fig. 2** General representation of the first block, (1), followed by an analyzer. The fast axis of the element (1) is oriented along the  $x$  axis. The analyzer, which is a linear polarizer, has its optical axis oriented at an angle  $\theta$  with respect to the same  $x$  direction, in the  $(xy)$  plane.

Eq. (2), will see its  $U$  and  $V$  parameters varying along the vertical. Given the orientation of the fast axis in the first wedge, the  $Q$  term cannot be affected by this polarizing element. Any incoming linear polarization, horizontal or vertical, is passing through the system without changes. A comprehensive representation of the transformations endured by light travelling through the instrument is obtained via the Mueller calculus. The general Mueller matrix of a rotated waveplate [with a rotation angle  $\alpha$  with regard to the  $x$  axis, in the  $(xy)$  plane] is given by<sup>7</sup>

$$\mathbf{M} = \begin{bmatrix} 1 & 0 & 0 & 0 \\ 0 & c^2 + s^2 \cos \Delta\phi & (1 - \cos \Delta\phi)cs & s \sin \Delta\phi \\ 0 & (1 - \cos \Delta\phi)cs & s^2 + c^2 \cos \Delta\phi & -c \sin \Delta\phi \\ 0 & -s \sin \Delta\phi & c \sin \Delta\phi & \cos \Delta\phi \end{bmatrix}, \quad (7)$$

where  $c = \cos 2\alpha$ ,  $s = \sin 2\alpha$ , and  $\Delta\phi$  is the phase difference induced by the birefringent medium between the ordinary and the extraordinary rays. Because in the present case  $c = 1$ ,  $s = 0$ , the corresponding Mueller matrix can be easily computed. The Mueller matrix of an analyzer oriented at an angle  $\theta$  is given by<sup>7</sup>

$$\mathbf{M}_A(\theta) = \frac{1}{2} \begin{pmatrix} 1 & c & s & 0 \\ c & c^2 & cs & 0 \\ s & cs & s^2 & 0 \\ 0 & 0 & 0 & 0 \end{pmatrix}, \quad (8)$$

in which the notation  $c = \cos 2\theta$ ,  $s = \sin 2\theta$  was again adopted for  $\theta$  the angle between the optical axis of the polarizer and the positive  $x$  axis, in the  $(xy)$  plane.

Using Eqs. (7) and (8) and the general rules for the Mueller calculus [Eqs. (4) and (5)], we find the outgoing Stokes vector  $\mathbf{S}_{\text{out}}$  corresponding to an incoming polarization  $\mathbf{S}_{\text{in}} = [I_{\text{in}}, Q_{\text{in}}, U_{\text{in}}, V_{\text{in}}]^T$ :

$$\mathbf{S}_{\text{out}}(\theta, y, \lambda) = \frac{1}{2} \begin{pmatrix} I_{\text{in}} + Q_{\text{in}}c + U_{\text{in}}s \cos \Delta\phi_1 - V_{\text{in}}s \sin \Delta\phi_1 \\ cI_{\text{in}} + Q_{\text{in}}c^2 + U_{\text{in}}cs \cos \Delta\phi_1 - V_{\text{in}}cs \sin \Delta\phi_1 \\ I_{\text{in}}s + Q_{\text{in}}cs + U_{\text{in}}s^2 \cos \Delta\phi_1 - V_{\text{in}}s^2 \sin \Delta\phi_1 \\ 0 \end{pmatrix}. \quad (9)$$

This vector depends on the orientation of the analyzer through  $c = \cos 2\theta$  and  $s = \sin 2\theta$ , on the position on the vertical direction of the incidence point of the incoming ray ( $y$ ) and of the wavelength of this ray ( $\lambda$ ). For a static design, the angle  $\theta$  is fixed. The first term of the vector is the outgoing intensity, which can be measured by a detector. In the present case, we have

$$I_{\text{out}}(\theta, y, \lambda) = \frac{1}{2}(I_{\text{in}} + Q_{\text{in}}c + U_{\text{in}}s \cos \Delta\phi_1 - V_{\text{in}}s \sin \Delta\phi_1). \quad (10)$$

Taking measurements of the intensity at different positions along the  $y$  axis and at a given wavelength, one finds different values, because of the phase difference variation ( $\Delta\phi_1$ ). Nevertheless, no matter the number of equations that are obtained for different values of the phase, the  $I_{\text{in}}$  and  $Q_{\text{in}}$  terms cannot be determined from this configuration of the polarimeter. In any system of equations that is build, the columns corresponding to  $I_{\text{in}}$  and  $Q_{\text{in}}$  are just multiple of one another. The only solution to this problem is to insert a second wedge between the first one and the analyzer. If the fast axis of this second birefringent element is oriented in a different way with respect to the first, then the  $Q$  state will also acquire a modulation, and the systems of equations that can be build to express the outgoing intensity become entirely determined.

### 2.3 Compound Structure

The best architecture able to ensure a full modulation of the Stokes parameters then has the form presented in Fig. 1. A second wedge [element (3) in Fig. 1] of apex angle  $\psi$  and antiparallel to the first one is added along the light path. In order to ensure the stiffness of the compound and

a homogeneous index of refraction so that the deviation of light to be minimized, an intermediary element [labeled with (2) in Fig. 1] is placed in between. This middle part of the polarimeter plays no role in the modulation of light. Indeed, since the fast axis lies along the  $z$  axis ( $\alpha = \frac{\pi}{2}$ ), the ordinary and extraordinary rays are traveling at the same speed along the  $z$  axis, and because of this, the phase difference is constant for any position along the vertical axis. The Mueller matrix of the element (2) is then the identity matrix, 1. Considering that the element (3) has a fast axis oriented at an angle  $\alpha = \frac{\pi}{4}$  with respect to the  $x$  axis in the  $(xy)$  plane, the phase difference acquired here is  $\Delta\phi_3 = \frac{2\pi}{\lambda} \Delta n(\lambda)(h-y) \tan \psi$ , and then, with the help of the Eqs. (7) and (8), the Mueller matrix of the entire birefringent block can be calculated. The reason for choosing  $\alpha = \frac{\pi}{4}$  is mostly related to simplification of computations, this value ensuring an elegant form for the Muller matrix of the element (3). Multiplying this matrix with the Stokes vector of the incoming light,  $\mathbf{S}_{in} = [I_{in}, Q_{in}, U_{in}, V_{in}]^T$ , the outgoing Stokes vector can be obtained

$$\mathbf{S}_{out}(\theta, y, \lambda) = \frac{1}{2} \begin{bmatrix} I_{in} + Q_{in}cc_3 + U_{in}(sc_1 + cs_1s_3) + V_{in}(cc_1s_3 - ss_1) \\ I_{in}c + Q_{in}c^2c_3 + U_{in}(csc_1 + c^2s_1s_3) + V_{in}(c^2c_1s_3 - csc_1) \\ I_{in}s + Q_{in}csc_3 + U_{in}(s^2c_1 + csc_1s_3) + V_{in}(csc_1s_3 - s^2s_1) \\ 0 \end{bmatrix}, \quad (11)$$

where the following contracted notations were used

$$\begin{aligned} c &= \cos 2\theta & s &= \sin 2\theta \\ c_1 &= \cos \Delta\phi_1 & s_1 &= \sin \Delta\phi_1 \\ c_3 &= \cos \Delta\phi_3 & s_3 &= \sin \Delta\phi_3. \end{aligned}$$

The terms  $c$  and  $s$  are constants as they describe the orientation of the analyzer, which is considered fixed. However, the terms  $c_1, s_1$  and  $c_3, s_3$  are variables, depending simultaneously on the vertical position and on the wavelength. The intensity measured by a detector placed after this polarimeter is given by the first element of the vector [Eq. (11)]:

$$I_{out}(\theta, y, \lambda) = \frac{1}{2} [I_{in} + Q_{in}cc_3 + U_{in}(sc_1 + cs_1s_3) + V_{in}(cc_1s_3 - ss_1)]. \quad (12)$$

In order to simplify further calculations, an even more contracted form of the outgoing intensity can be employed:

$$I_{out}(\theta, y, \lambda) = \frac{1}{2} [I_{in} + Q_{in} \cdot m(\theta, y, \lambda) + U_{in} \cdot n(\theta, y, \lambda) + V_{in} \cdot p(\theta, y, \lambda)], \quad (13)$$

where

$$\begin{cases} m(\theta, y, \lambda) = \cos(2\theta) \cos \Delta\phi_3 \\ n(\theta, y, \lambda) = \sin(2\theta) \cos \Delta\phi_1 + \cos(2\theta) \sin \Delta\phi_1 \sin \Delta\phi_3. \\ p(\theta, y, \lambda) = \cos(2\theta) \cos \Delta\phi_1 \sin \Delta\phi_3 - \sin(2\theta) \sin \Delta\phi_1 \end{cases} \quad (14)$$

The new architecture of the polarimeter ensures the modulation of the  $Q$  parameter, with the help of the term  $\cos \Delta\phi_3$  from the  $m(\theta, y, \lambda)$  function. Reading the intensity at different vertical positions, a given wavelength (i.e., at a given horizontal position) and with a fixed orientation of the analyzer, a system of equations can be built

$$\begin{cases} I_{\text{out}}(y_1) = \frac{1}{2}[I_{\text{in}} + Q_{\text{in}} \cdot m(y_1) + U_{\text{in}} \cdot n(y_1) + V_{\text{in}} \cdot p(y_1)] \\ I_{\text{out}}(y_2) = \frac{1}{2}[I_{\text{in}} + Q_{\text{in}} \cdot m(y_2) + U_{\text{in}} \cdot n(y_2) + V_{\text{in}} \cdot p(y_2)] \\ I_{\text{out}}(y_3) = \frac{1}{2}[I_{\text{in}} + Q_{\text{in}} \cdot m(y_3) + U_{\text{in}} \cdot n(y_3) + V_{\text{in}} \cdot p(y_3)] \\ I_{\text{out}}(y_4) = \frac{1}{2}[I_{\text{in}} + Q_{\text{in}} \cdot m(y_4) + U_{\text{in}} \cdot n(y_4) + V_{\text{in}} \cdot p(y_4)] \\ \vdots \\ \vdots \end{cases} \quad (15)$$

This system allows us to determine the polarization state of the incoming light and represents the modulation scheme of the polarimeter. However, given the complexity of the functions  $m$ ,  $n$ , and  $p$  and the arbitrary number of equations, the uniqueness of the solution for the system [Eq. (15)] has to be proven.

### 3 Uniqueness of the Solution

To validate this configuration, the ability of the STAS to distinguish different incoming polarization states must be demonstrated. In other words, we have to prove that any incoming Stokes vector gives rise to a unique intensity profile. We use a “reductio ad absurdum” method: let us suppose that, for at least one wavelength, there exist two incoming Stokes vectors  $\mathbf{S}_{\text{in}1}$  and  $\mathbf{S}_{\text{in}2}$  providing the same intensity pattern  $I_{\text{out}}$  on the detector plane

$$\begin{cases} \mathbf{S}_{\text{in}1} \neq \mathbf{S}_{\text{in}2} \\ I_{\text{out}1}(y) = I_{\text{out}2}(y), \text{ for at least one } \lambda \text{ and } \forall y, \end{cases} \quad (16)$$

where  $\mathbf{S}_{\text{in}1} = [I_1, Q_1, U_1, V_1]^T$  and  $\mathbf{S}_{\text{in}2} = [I_2, Q_2, U_2, V_2]^T$ , whereas  $I_{\text{out}1}(y)$  and  $I_{\text{out}2}(y)$  are the received intensities for a given wavelength [Eq. (13)]. Therefore:

$$\begin{cases} I_{\text{out}1}(y) = \frac{1}{2}[I_1 + Q_1 \cdot m(y) + U_1 \cdot n(y) + V_1 \cdot p(y)] \\ I_{\text{out}2}(y) = \frac{1}{2}[I_2 + Q_2 \cdot m(y) + U_2 \cdot n(y) + V_2 \cdot p(y)] \end{cases} \quad (17)$$

where  $m(y)$ ,  $n(y)$ ,  $p(y)$  are the functions defined in Eq. (14) for the considered wavelength, and driven only by the instrumental parameters.

Combining Eqs. (16) and (17), we then find that

$$\Delta I + \Delta Q \cdot m(y) + \Delta U \cdot n(y) + \Delta V \cdot p(y) = 0, \quad \text{for at least one } \lambda \text{ and } \forall y, \quad (18)$$

where  $\Delta I = I_2 - I_1$ ,  $\Delta Q = Q_2 - Q_1$ ,  $\Delta U = U_2 - U_1$ , and  $\Delta V = V_2 - V_1$ .

A combination  $(\Delta I, \Delta Q, \Delta U, \Delta V)$  different from  $(0, 0, 0, 0)$  satisfying this last relation for any value of  $y$  and for at least one wavelength exists only if the functions  $[1, m(y, \lambda), n(y, \lambda), p(y, \lambda)]$  are linearly dependent. To test this hypothesis, the mathematical theorem of the Wronskian is used.<sup>17,18</sup> According to this, if for a set of functions  $f_i(y)$ ,  $i = 1, 2, \dots, n$  which are  $n - 1$  times differentiable on an interval  $[a, b]$ , we have

$$\mathbf{W}[f_1(y), f_2(y), f_3(y), \dots, f_n(y)] = \begin{vmatrix} f_1(y) & f_2(y) & f_3(y) & \dots & f_n(y) \\ \frac{df_1(y)}{dy} & \frac{df_2(y)}{dy} & \frac{df_3(y)}{dy} & \dots & \frac{df_n(y)}{dy} \\ \frac{d^2f_1(y)}{dy^2} & \frac{d^2f_2(y)}{dy^2} & \frac{d^2f_3(y)}{dy^2} & \dots & \frac{d^2f_n(y)}{dy^2} \\ \dots & \dots & \dots & \dots & \dots \\ \frac{d^{n-1}f_1(y)}{dy^{n-1}} & \frac{d^{n-1}f_2(y)}{dy^{n-1}} & \frac{d^{n-1}f_3(y)}{dy^{n-1}} & \dots & \frac{d^{n-1}f_n(y)}{dy^{n-1}} \end{vmatrix} = 0 \quad (19)$$

$$\forall y \in [a, b],$$

then the functions are linearly dependent. Thus if there exists  $y \in [a, b]$  such as  $\mathbf{W}[f_1(y), f_2(y), \dots] \neq 0$ , then the functions are independent.<sup>17,18</sup> In the present case, for any given  $\lambda$ , the Wronskian can be expressed as



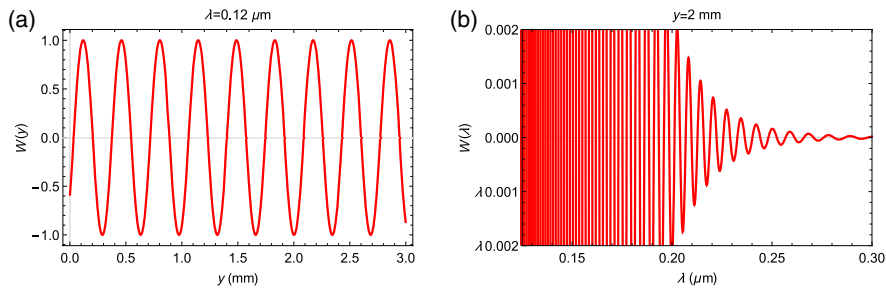


**Fig. 3** Variation of the normalized Wronskian determinant. The behavior with respect to (a)  $y$  is shown for  $\lambda = 0.12 \mu\text{m}$  and (b)  $y = 2 \text{ mm}$ . To simplify the computation of  $W[1, m(\lambda), n(\lambda), p(\lambda)]$ , a constant birefringence of the medium was assumed, of  $\Delta n = 0.0132$ , corresponding to the mean value of the birefringence of  $\text{MgF}_2$  between  $0.12$  and  $0.4 \mu\text{m}$ . For the legibility of the graphic, only the UV part of the spectrum was represented here. Also for the simplicity of computation, the orientation of the analyzer was chosen to be  $\theta = 90 \text{ deg}$ .

$$\mathbf{W}[1, m(y), n(y), p(y)] = \begin{vmatrix} 1 & m(y) & n(y) & p(y) \\ 0 & \frac{dm(y)}{dy} & \frac{dn(y)}{dy} & \frac{dp(y)}{dy} \\ 0 & \frac{d^2m(y)}{dy^2} & \frac{d^2n(y)}{dy^2} & \frac{d^2p(y)}{dy^2} \\ 0 & \frac{d^3m(y)}{dy^3} & \frac{d^3n(y)}{dy^3} & \frac{d^3p(y)}{dy^3} \end{vmatrix} \quad \forall y \in [0, h], \quad (20)$$

where  $h$  is the height of the instrument. Meanwhile, in order to eliminate the possibility to obtain  $\mathbf{W}[1, m(y), n(y), p(y)] = 0$  because of the inappropriate choice of the wavelength, the determinant  $\mathbf{W}[1, m(\lambda), n(\lambda), p(\lambda)] \forall \lambda$  must also be calculated for an arbitrary value of  $y$ . Both determinants are plotted with regard to  $y$  and  $\lambda$  (Fig. 3). Because the functions  $m(y, \lambda)$ ,  $n(y, \lambda)$ , and  $p(y, \lambda)$  depend on the parameters of the system, a structure on  $\text{MgF}_2$ , with apex angles  $\xi = 1.5 \text{ deg}$ ,  $\psi = 3 \text{ deg}$  was chosen for computation, according to the classical design of the instrument.<sup>10</sup>

Figure 3 shows that both the determinant computed for any value of  $y$  at a given wavelength and the determinant calculated for any value of  $\lambda$  at an arbitrary  $y$  are not constantly zero over the definition interval.

As a consequence, we may infer that the functions  $[1, m(y), n(y), p(y)]$  are linearly independent over the entire range of  $y$  and for any given  $\lambda$ . The only combination  $\Delta I, \Delta Q, \Delta U, \Delta V$  able to satisfy Eq. (18) is  $(0, 0, 0, 0)$ . As a consequence, the two incoming Stokes vectors must be equal ( $\mathbf{S}_{\text{in1}} = \mathbf{S}_{\text{in2}}$ ) fact which contradicts the hypothesis [Eq. (16)].

In conclusion, for each incoming, Stokes vector will correspond a different pattern of the intensity on the detector plane. Subsequently, it will be impossible to obtain the same output from two different incoming polarizations. Nevertheless, the use of a different material, a different configuration, or a particular binning procedure will require all the time the computation of this test for the uniqueness of the solution.

#### 4 Impact of Noise

As a matter of fact, the measurements realized with a real device will be impacted by noise. The sources of noise are diverse, including many effects as photon counting, detector readout, and dark current. The previous derivation giving the uniqueness of the solution was performed in an ideal case exempt of noise. The question then is: how do noise perturbations in the signal impact the quality of results and the inversion process? In this paper, we will consider that the difference between the measured intensity and the theoretically predicted value will be mainly generated by the photon noise. The corresponding distribution is Poissonian, but can be assimilated to a Gaussian distribution in the (usual) case of a large number of photons.<sup>19</sup> Hence, its effects

on the quality of the extraction of the Stokes parameters can then be easily statistically estimated.<sup>20,21</sup>

In order to evaluate the impact of noise on the Stokes parameters retrieval through the inversion process, a random value  $\sigma$  is applied on the output signal. The variation range of  $\sigma$  defines the level of noise. Through the triple prism modulator and the grating, the light intensity ( $y$  axis) at any wavelength ( $x$  axis) projected on the detector plane is

$$I_{\text{out}}^{\text{meas}}(y_j) = I_{\text{out}}^0(y_j) + \sigma(y_j), \tag{21}$$

where  $I_{\text{out}}^{\text{meas}}(y_j)$  is the noise impacted intensity at the position  $y_j$  on vertical,  $I_{\text{out}}^0(y_j)$  is the corresponding analytical signal [Eq. (13)], and  $\sigma(y_j)$  is the random noise on any elementary pixel.

Applying the least-squares fit method to Eq. (21), the uncertainties on the Stokes parameters can be computed.<sup>21</sup> This procedure provides information about the quality of the extraction of the Stokes parameters, for a given configuration of the system and of the modulation scheme. In order to compare between different configurations of the polarimeter (orientation of the analyzer and apex angles), the concept of efficiency of the modulation scheme, developed by del Toro Iniesta<sup>8,19,22</sup> and Collados<sup>23,24</sup> can be used. Both analyses are developed hereafter.

The function of merit of the fit is a chi-square function:

$$\begin{aligned} \chi^2(I, Q, U, V) &= \sum_{j=1}^N \left[ \frac{I_{\text{out}}^{\text{meas}}(y_j) - I_{\text{out}}^0(y_j)}{\sigma(y_j)} \right]^2 \\ &= \sum_{j=1}^N \left\{ \frac{I_{\text{out}}^{\text{meas}}(y_j) - \frac{1}{2}[I + Qm(y_j) + Un(y_j) + Vp(y_j)]}{\sigma(y_j)} \right\}^2. \end{aligned} \tag{22}$$

Minimizing this function with respect to  $I, Q, U, V$  parameters ( $\frac{\partial \chi^2}{\partial S_i} = 0, S_i = I, Q, U, V$ ) provides the variances on the Stokes parameters. The partial derivatives yield immediately:

$$\frac{1}{2} \sum_{j=1}^N \underbrace{\begin{bmatrix} \frac{1}{\sigma^2(y_j)} & \frac{m(y_j)}{\sigma^2(y_j)} & \frac{n(y_j)}{\sigma^2(y_j)} & \frac{p(y_j)}{\sigma^2(y_j)} \\ \frac{m(y_j)}{\sigma^2(y_j)} & \frac{m^2(y_j)}{\sigma^2(y_j)} & \frac{m(y_j)n(y_j)}{\sigma^2(y_j)} & \frac{m(y_j)p(y_j)}{\sigma^2(y_j)} \\ \frac{n(y_j)}{\sigma^2(y_j)} & \frac{n(y_j)m(y_j)}{\sigma^2(y_j)} & \frac{n^2(y_j)}{\sigma^2(y_j)} & \frac{n(y_j)p(y_j)}{\sigma^2(y_j)} \\ \frac{p(y_j)}{\sigma^2(y_j)} & \frac{p(y_j)m(y_j)}{\sigma^2(y_j)} & \frac{p(y_j)n(y_j)}{\sigma^2(y_j)} & \frac{p^2(y_j)}{\sigma^2(y_j)} \end{bmatrix}}_{\mathbf{B}} \underbrace{\begin{pmatrix} I \\ Q \\ U \\ V \end{pmatrix}}_{\mathbf{S}} = \sum_{j=1}^N \underbrace{\begin{bmatrix} \frac{I_{\text{out}}^{\text{meas}}(y_j)}{\sigma^2(y_j)} \\ \frac{I_{\text{out}}^{\text{meas}}(y_j)m(y_j)}{\sigma^2(y_j)} \\ \frac{I_{\text{out}}^{\text{meas}}(y_j)n(y_j)}{\sigma^2(y_j)} \\ \frac{I_{\text{out}}^{\text{meas}}(y_j)p(y_j)}{\sigma^2(y_j)} \end{bmatrix}}_{\mathbf{R}}. \tag{23}$$

Using the contracted notation, this last system can be expressed as

$$\mathbf{B} \cdot \mathbf{S} = \mathbf{R}. \tag{24}$$

According to the least-squares fit method,<sup>21</sup> the variances corresponding to  $I, Q, U,$  and  $V$  are given by the diagonal elements of the matrix  $\mathbf{B}^{-1}$ :

$$\begin{cases} \sigma_1^2 = \sigma^2(I) = \mathbf{B}_{11}^{-1} \\ \sigma_2^2 = \sigma^2(Q) = \mathbf{B}_{22}^{-1} \\ \sigma_3^2 = \sigma^2(U) = \mathbf{B}_{33}^{-1} \\ \sigma_4^2 = \sigma^2(V) = \mathbf{B}_{44}^{-1} \end{cases}. \tag{25}$$

To compute the elements of the matrix  $\mathbf{B}$ , we will suppose that the noise  $\sigma(y_j)$  is the same all along the vertical axis [ $\sigma(y_j) = \sigma$ ]. Also we will consider that the uncertainty on the Stokes parameters is constant over the beam area.<sup>9</sup> This assumption is the natural consequence of the collimation of beam after the telescope assembly. Variations along the  $x$  and  $y$  axes could appear due to possible instrumental artifacts, and the calibration of the instrument would imply the knowledge of these variations and the correction. However, this topic is set aside from this paper.

The span of the summation from the system [Eq. (23)]  $N$  is driven by the Shannon–Nyquist theorem applied to the signal from Eq. (13) at a given wavelength. According to this theorem, the minimum sampling frequency should be at least twice the highest frequency contained in the signal or the Nyquist frequency. In terms of periods, measured along the  $y$  axis, we need to have

$$Y_s \leq \frac{Y_{\min}}{2}, \tag{26}$$

where  $Y_s$  is the sampling period and  $Y_{\min}$  is the shortest period from the signal, corresponding to the Nyquist frequency.

Simultaneously, the sampling must cover at least the longest period of the signal ( $Y_{\max}$ ). The value of  $Y_{\min}$  thus provides information about the maximum size of a pixel (PS),  $PS \leq Y_{\min}/2$ , whereas  $Y_{\max}$  represents the minimum height of the wedges and the detector. Using the Fourier transform, the frequencies from the signal provided by Eq. (13) can be found for any value of the wavelength and any architecture of the modulator. Figure 4 presents the dependency on the wavelength of the ratio  $Y_{\min}/2$  and of the minimum height of the wedges  $Y_{\max}$  for a modulator in  $MgF_2$ , with apex angles  $(\xi, \psi) = (1.5 \text{ deg}, 3 \text{ deg})$ .

To sample the signal at any wavelength in the transmission band of  $MgF_2$ , the size of the pixels must be smaller than the minimum of the curve from Fig. 4. This minimum occurs around  $\lambda = 0.14 \mu\text{m}$  and depends on the value of the apex angles. Therefore, for  $(\xi, \psi) = (1.5 \text{ deg}, 3 \text{ deg})$ , the pixels must be smaller than  $64.5 \mu\text{m}$ , whereas for  $(\xi, \psi) = (3 \text{ deg}, 1.8 \text{ deg})$  the value should be less than  $59.3 \mu\text{m}$ .

The minimal height of the wedges (and of the detector), which can be inferred from the  $Y_{\max}$  variation, depends on the chosen waveband and the apex angles.

For instance, in order to cover the spectral band  $0.12$  to  $0.3 \mu\text{m}$ , the prisms (and the detector) must be at least  $0.9 \text{ mm}$  high, whereas covering the entire transmission window of  $MgF_2$  will require at least  $4.6 \text{ cm}$ , in the case of the first geometry,  $(\xi, \psi) = (1.5 \text{ deg}, 3 \text{ deg})$ . For the second geometry,  $(\xi, \psi) = (3 \text{ deg}, 1.8 \text{ deg})$ , the minimum height is of about  $1.14 \text{ mm}$  at  $\lambda = 0.3 \mu\text{m}$  and  $5.5 \text{ cm}$  at  $7 \mu\text{m}$ .

As long as  $Y_{\min}/2 \geq 2 \text{ PS}$ , multiple equations [Eq. (13)] can be used to cover a  $Y_{\min}/2$  distance [see Fig. 5]. This will increase the precision of the interpolation. Overall, for a detector of height  $h = N_{\text{px}} \cdot \text{PS} \geq Y_{\max}(\lambda)$ , where  $N_{\text{px}}$  is the total number of pixels from a column of the detector, a number of  $N = N_{\text{px}}/n$  equations can be associated, where  $n = 1, 2, \dots$  represents the number of pixels used to build a single equation [Eq. (13)]. If  $n = 1$  brings the highest precision, a value bigger than 1 may significantly reduce the computation time.

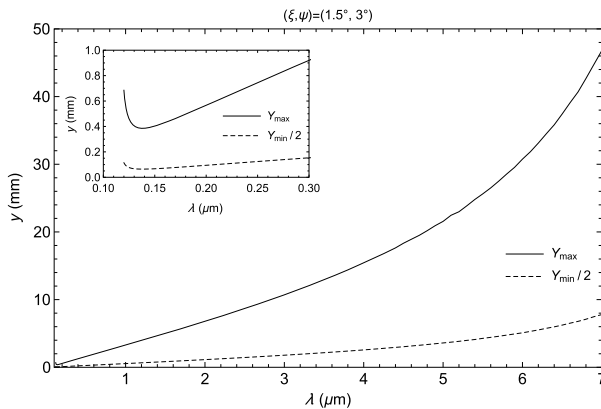


**Fig. 4** Variation with the wavelength of the ratio  $Y_{\min}/2$  corresponding to the maximum pixel size, and of the minimal height of the wedges  $Y_{\max}$  for a modulator in  $MgF_2$ , with the apex angles  $(\xi, \psi) = (1.5 \text{ deg}, 3 \text{ deg})$ . The covered spectral band ( $0.12$  to  $7 \mu\text{m}$ ) corresponds to the entire transmission window of  $MgF_2$ . The small graphic from top-left presents a zoom on the region  $0.12$  to  $0.3 \mu\text{m}$ , where the minima of the curves are located.

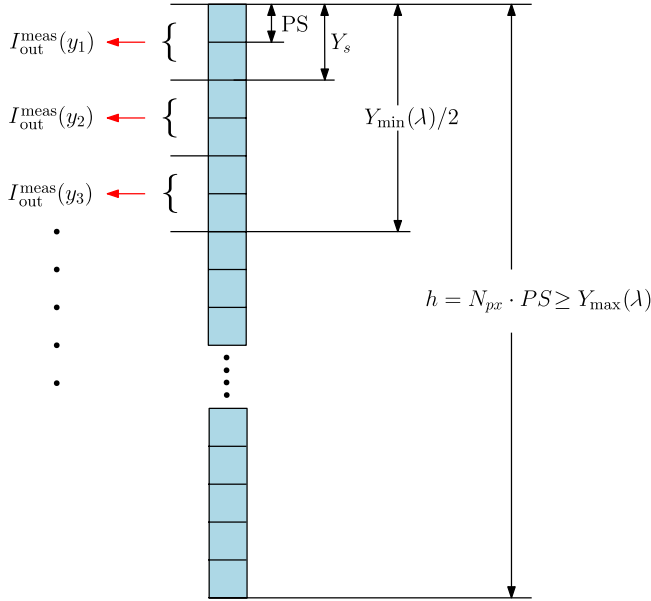


**Fig. 5** Each measurement of the intensity  $I_{out}^{meas}(y_j)$  corresponds to a number of  $n$  pixels, with  $n \cdot PS \leq Y_{min}/2$ , where  $Y_{min}$  is the minimum sampling distance resulting from the Nyquist theorem, and  $PS$  is the size of a pixel. In practice, the  $Y_{min}/2$  of the structure presented above, based on  $MgF_2$ , is around  $59.4 \mu m$  for a modulator with apex angles  $(\xi, \psi) = (3 \text{ deg}, 1.8 \text{ deg})$  and about  $64.5 \mu m$  for  $(\xi, \psi) = (1.5 \text{ deg}, 3 \text{ deg})$ . Considering the particular case of the UV domain, these values are above the common pixel sizes used in this range, situated between  $10$  and  $25 \mu m$ . This allows the combination of multiple number of pixels in the construction of the modulation scheme. In this figure, the situation having  $n = 2$  was depicted.

No matter the value of  $n$ , Eq. (21) and all the relations resulting from it must be integrated on the considered number of pixels  $n$ .

Assuming that the uncertainty affecting the detected intensity is the same along a column of the detector,<sup>9</sup>  $\sigma(y_j) = \sigma$ , then the matrix  $\mathbf{B}$  can be written as

$$\mathbf{B} = \frac{1}{2} \frac{1}{\sigma^2} \sum_{j=1}^N \underbrace{\begin{bmatrix} 1 & m(y_j) & n(y_j) & p(y_j) \\ m(y_j) & m^2(y_j) & m(y_j)n(y_j) & m(y_j)p(y_j) \\ n(y_j) & n(y_j)m(y_j) & n^2(y_j) & n(y_j)p(y_j) \\ p(y_j) & p(y_j)m(y_j) & p(y_j)n(y_j) & p^2(y_j) \end{bmatrix}}_{\mathbf{C}} \quad (27)$$

Therefore, we have directly

$$\mathbf{B}^{-1} = 2\sigma^2 \mathbf{C}^{-1} \quad (28)$$

and from Eqs. (25) and (28)

$$\sigma_i = \sigma \sqrt{2C_{ii}^{-1}}, \quad (29)$$

where  $C_{ii}^{-1}$  are the diagonal elements of the matrix  $\mathbf{C}^{-1}$ , and  $i = 1, 2, 3, 4$ , corresponding to  $I, Q, U, V$  parameters.

The ratios  $\sigma_i/\sigma$  can be then plotted for different configurations of the modulator and various orientations of the analyzer. For instance, with a sampling distance of  $10 \mu m$  (corresponding to

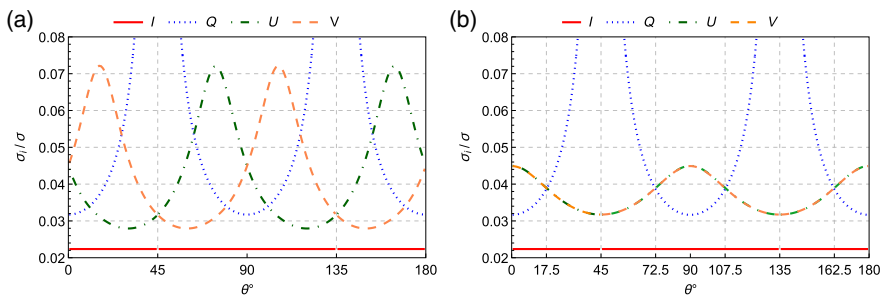


**Fig. 6** Variation of the ratio  $\sigma_i/\sigma$ , between the uncertainty on the Stokes parameters and the uncertainty on the measured intensity, as a function of the orientation of the analyzer (the angle  $\theta$ ). (a) The “classical” case of a modulator,<sup>10</sup> with apex angles  $\xi = 1.5$  deg and  $\psi = 3$  deg and (b) a new geometry having  $\xi = 3$  deg,  $\psi = 1.8$  deg was considered. A uniform uncertainty along the  $y$  axis, on a wavelength of  $0.125 \mu\text{m}$ , is assumed for the detected intensity and the Stokes parameters. The particular case of an  $\text{MgF}_2$  medium was considered.

**Table 1** Minimal and maximal values of uncertainties on Stokes parameters.

	$(\xi, \psi) = (1.5 \text{ deg}, 3 \text{ deg})$		$(\xi, \psi) = (3 \text{ deg}, 1.8 \text{ deg})$	
	Min	Max	Min	Max
$\sigma_I$	$\frac{1}{\sqrt{N}}$		$\frac{1}{\sqrt{N}}$	
$\sigma_Q$	$\frac{1.45}{\sqrt{N}}$	$\infty$	$\frac{1.45}{\sqrt{N}}$	$\infty$
$\sigma_{U,V}$	$\frac{1.27}{\sqrt{N}}$	$\frac{3.27}{\sqrt{N}}$	$\frac{1.45}{\sqrt{N}}$	$\frac{2}{\sqrt{N}}$

the approximate size of a pixel) and a column of  $N = 2000$  pixels, the variations from Fig. 6 can be obtained for two different configurations of a modulator in  $\text{MgF}_2$ .

As it was expected, the  $I$  uncertainty is independent of the orientation of the analyzer, whereas the rest of the Stokes parameters are closely related to this angle. Thereby, for two specific analyzer orientations, 45 deg and 135 deg, the  $\mathbf{B}$  matrix is no longer invertible because all the terms containing the  $m(y)$  function are zero, as it can be noticed from Eqs. (13) and (14). This leads to an indetermination of the  $Q$  parameter.

Apart from the orientation of the analyzer, the general geometry of the modulator also plays an important role in the spectropolarimeter performances. Figure 6 presents the results for two different configurations. Each of them is associated with a different couple  $(\xi, \psi)$  representing the apex angles of the modulator (see Fig. 1). At left, the “classical” case<sup>10</sup> of a modulator with  $(\xi, \psi) = (1.5 \text{ deg}, 3 \text{ deg})$  was plotted, whereas at right a case having  $(\xi, \psi) = (3 \text{ deg}, 1.8 \text{ deg})$  was considered. We notice, in the second configuration, that similar values of the uncertainty on  $Q$ ,  $U$  and  $V$  parameters can be obtained for orientations of the analyzer at 17.5 deg and 72.5 deg, 107.5 deg and 162.5 deg, respectively. In contrast, the first scenario has no intersection points for all the three parameters. The couples  $(\xi, \psi)$  able to minimize the uncertainties on the Stokes parameters can be derived through the study of the efficiency of the modulation scheme. The minimal and the maximal values of the ratio  $\sigma_i/\sigma$  corresponding to the studied cases are presented in Table 1.

Despite the periodical variation, the average level of this ratio remains close to the ideal one,<sup>9</sup>  $1/\sqrt{N}$ , in both cases (the red horizontal lines in Fig. 6).

## 5 Efficiency of the Modulation

Because the working principle of this spectropolarimeter is based on the continuous phase variation of the outgoing rays on the vertical direction, theoretically an infinite number of equations

[Eq. (15)] can be built on the  $y$  axis to help retrieve the incoming polarization. Practically, a limited number must be used, given the finite height of a detector and the pixel size. The questions about the appropriate number of equations, the best integration distance, and the best geometry of the modulator can be answered with the help of the concept of efficiency of the modulation scheme, as it was defined by del Toro Iniesta<sup>8,22</sup> and Collados.<sup>23,24</sup> Simultaneously, a comparison of this concept of spectropolarimeter with existing instruments can be inferred from the computation of the efficiency.

The system [Eq. (15)], describing the modulation scheme of the spectropolarimeter, can be rewritten under a matrix form as

$$\underbrace{\begin{bmatrix} I_{\text{out}}(y_1) \\ I_{\text{out}}(y_2) \\ \dots \\ I_{\text{out}}(y_N) \end{bmatrix}}_{\mathbf{I}_{\text{out}}} = \frac{1}{2} \underbrace{\begin{bmatrix} 1 & m(y_1) & n(y_1) & p(y_1) \\ 1 & m(y_2) & n(y_2) & p(y_2) \\ \dots & \dots & \dots & \dots \\ 1 & m(y_N) & n(y_N) & p(y_N) \end{bmatrix}}_{\mathbf{O}} \cdot \underbrace{\begin{pmatrix} I_{\text{in}} \\ Q_{\text{in}} \\ U_{\text{in}} \\ V_{\text{in}} \end{pmatrix}}_{\mathbf{S}_{\text{in}}}, \quad (30)$$

or

$$\mathbf{I}_{\text{out}} = \mathbf{O} \cdot \mathbf{S}_{\text{in}}, \quad (31)$$

where  $\mathbf{O}$  is the modulation matrix. Therefore

$$\mathbf{S}_{\text{in}} = \mathbf{O}^{-1} \cdot \mathbf{I}_{\text{out}}, \quad (32)$$

where  $\mathbf{O}^{-1}$  is the demodulation matrix (also written as  $\mathbf{D}$ ).

As described in Sec. 4 (Fig. 4), the detector plane is subdivided into  $N$  integration intervals, leading to  $N$  equations in the modulation scheme. If  $N > 4$ , then the matrix  $\mathbf{O}$  is no longer easily invertible, and a pseudoinverse matrix must be used.<sup>8,19</sup>

$$\mathbf{D} = (\mathbf{O}^T \mathbf{O})^{-1} \mathbf{O}^T. \quad (33)$$

This works as a left-inverse matrix ( $\mathbf{D} \cdot \mathbf{O} = 1$ ). The notion of the efficiency of the modulation as presented by del Toro Iniesta<sup>8</sup> can be then introduced

$$\epsilon_i = \left( N \sum_{j=1}^N \mathbf{D}_{ij}^2 \right)^{-\frac{1}{2}} \quad i = 1, 2, 3, 4, \quad (34)$$

where  $i$  corresponds to each of the Stokes parameters. The four terms vector  $\epsilon_i$  provides simultaneously information about the “quality” of the extraction of the Stokes parameters and the modulation scheme (the matrix  $\mathbf{O}$ ). The total efficiency of the modulation scheme is defined by

$$\epsilon = \sqrt{\epsilon_2^2 + \epsilon_3^2 + \epsilon_4^2}. \quad (35)$$

The maximum reachable efficiency is 1 and is given by the configuration  $\epsilon_i = \frac{1}{\sqrt{3}}$  for  $i = 2, 3, 4$ .

The concept of efficiency is also closely related to the uncertainty on the Stokes parameters. Indeed, from Eq. (32), we have that

$$\mathbf{S}_{\text{in}}(i) = \sum_{j=1}^N \mathbf{D}_{ij} \mathbf{I}_{\text{out}}(j) \quad i = 1, 2, 3, 4. \quad (36)$$

Applying the propagation of errors, we obtain

$$\sigma_i^2 = \sigma^2 \sum_{j=1}^N \mathbf{D}_{ij}^2, \quad (37)$$

where  $\sigma_i$  is the uncertainty characterizing each of the Stokes parameters, and  $\sigma$  is the error related to each of the values  $I_{\text{out}}(y_j)$ , supposed to be the same for all the vertical pixels (or pixel compounds, if several are grouped). Combined to Eq. (34), this yields

$$\frac{\sigma_i}{\sigma} = \frac{1}{\epsilon_i \sqrt{N}}. \tag{38}$$

Therefore, the efficiency of the extraction of the Stokes parameters is nothing else but the inverse of the corresponding uncertainty. Any variation of the efficiency is then translated into a variation of the uncertainty. Higher is the efficiency for a parameter, lower is the uncertainty characterizing it and the more it constitutes a better choice for the modulation matrix. However, finding the best modulation matrix is not straightforward.

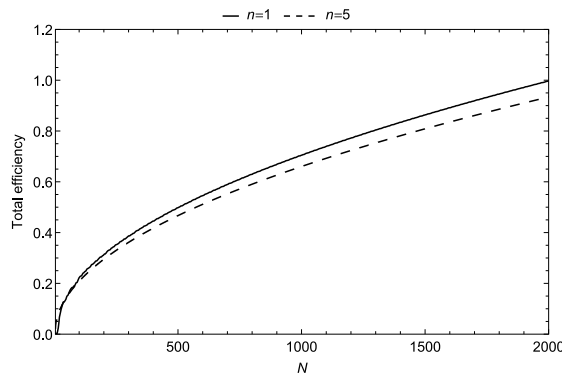
An essential role in the optimization of the modulation scheme is played by the number of equations  $N$  and by the number of pixels  $n$  used for each equation of the system [Eq. (15)]. This aspect can be easily proved by observing the evolution of the total efficiency as a function of  $N$ , for different values of  $n$  (Fig. 7).

A small integration step ensures a quicker retrieval of the highest efficiency, lowering the computation time.

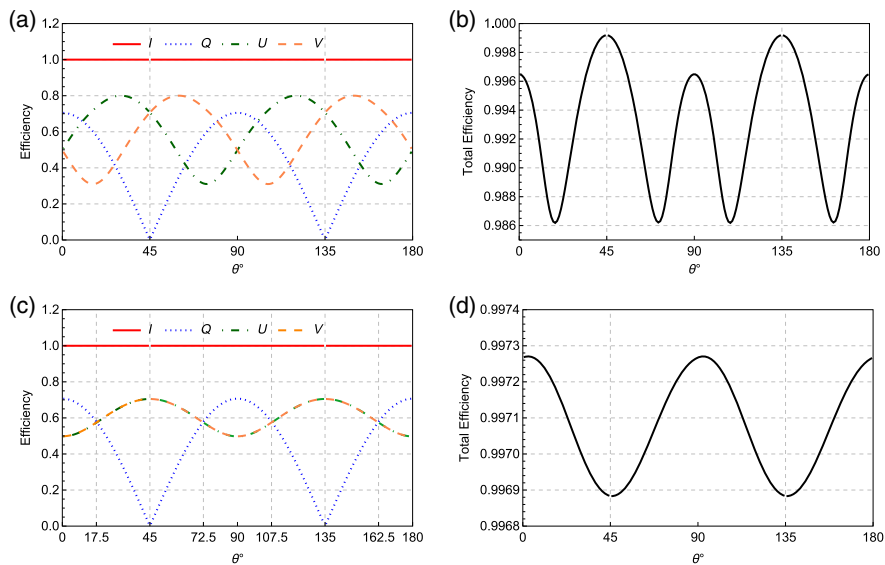
The impact of the orientation of the analyzer on the quality of the extraction of the Stokes parameters, already observed in the case of the uncertainty, can be retrieved as well in the case of the efficiency.

Figure 8 shows the variation of the efficiency for each Stokes parameters with the orientation of the analyzer for a modulation scheme, in which 2000 integration intervals were considered with a pixel size  $\Delta y = 10 \mu\text{m}$ . In order to illustrate the impact of the apex angles, two configurations are presented:  $(\xi, \psi) = (1.5 \text{ deg}, 3 \text{ deg})$ , and  $(\xi, \psi) = (3 \text{ deg}, 1.8 \text{ deg})$ . Overall, the total efficiency of the system is around 0.99. This value is above classical cases such as ZIMPOL—Zurich Imaging Polarimeter (0.72), ASP—Advanced Stokes Polarimeter (0.88), or TIP—Tenerife Infrared Polarimeter (0.92)<sup>8,24</sup> and proves that the studied model can be an important candidate at least for the astronomical observation. Also for a modulator with the apex angles  $(\xi, \psi) = (3 \text{ deg}, 1.8 \text{ deg})$ , it can be noticed that orientations of the analyzer at 17.5 deg, 72.5 deg, 107.5 deg, or 162.5 deg the efficiency of  $Q$ ,  $U$  and  $V$  is around 0.574, very close to the ideal value of  $\frac{1}{\sqrt{3}} = 0.577$ .

In order to keep a high level of the efficiency and thus a low level of the uncertainty, the couple  $(\xi, \psi)$  must be chosen so that the two angles are not multiple one of another (Fig. 9):



**Fig. 7** Variation of the total efficiency for a modulator in  $\text{MgF}_2$  with  $(\xi, \psi) = (3 \text{ deg}, 1.8 \text{ deg})$  and  $\theta = 72.5 \text{ deg}$  with respect to the number of equations from the modulation scheme and for two choices of pixel compounding,  $n$ . The continuous line corresponds to an integration pixel by pixel ( $n = 1$ ,  $N_{\text{px}} = N$ ) and the dashed line to an integration on compounds of five pixels ( $n = 5$ ,  $N_{\text{px}} = 5N$ ). The size of a pixel was considered here as being around  $10 \mu\text{m}$  and the wavelength  $\lambda = 0.125 \mu\text{m}$ .



**Fig. 8** Efficiency of the extraction for each of the Stokes parameters and total efficiency as a function of the orientation of the analyzer  $\theta$  for two combinations of the apex angles  $(\xi, \psi)$ . For  $\xi = 1.5$  deg and  $\psi = 3$  deg, (a), (b) the variations of the efficiencies of the extraction of  $Q$ ,  $U$ , and  $V$  are following different patterns. There is no common maximum. Nevertheless, a (c), (d) different combination of the apex angles permits to have the same efficiency for  $U$  and  $V$ . Because the  $Q$  term is modulated only by the function  $m[\theta, \Delta\phi_3(\psi)]$ , varying the couple  $(\xi, \psi)$  does not impact the corresponding efficiency. The particular case of  $\lambda = 0.125 \mu\text{m}$ ,  $N = 2000$ , and  $\Delta n(\lambda)$  corresponding to  $\text{MgF}_2$  was considered.

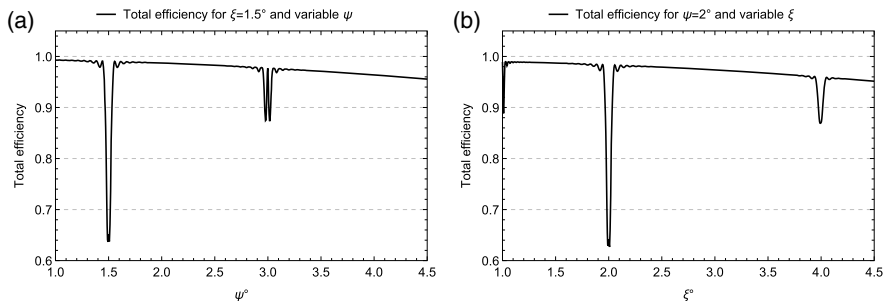


**Fig. 9** The variation of the efficiency of the modulation scheme as a function of the apex angles. (a) For a fixed value of  $\xi = 1.5$  deg, the angle  $\psi$  varies between 1 deg and 4.5 deg. It is noticeable the drop of the efficiency for  $\psi = 1.5$  deg and around 3 deg. (b)  $\psi = 2$  deg and  $\xi$  varies between 1 deg and 4.5 deg. Again, drops of the efficiency are observed at  $\xi = k\psi$ ,  $k = 1, 2$ .

$$\begin{cases} \text{a) for a given } \xi: \psi \neq k\xi, k = 1, 2, \dots \forall \xi \\ \text{b) for a given } \psi: \xi \neq k\psi, k = 1, 2, \dots \forall \psi \end{cases} \quad (39)$$

Indeed, if the values of  $\xi$  and  $\psi$  are multiple one of another, then the nondiagonal terms of the matrix  $A = O^T O$  are maximized, and because of this the  $O$  matrix is not an optimal matrix of the modulation.<sup>8</sup> Again, just like in the case of the variation with the orientation of the analyzer (Fig. 8), the concept of efficiency is a good method to assess the best geometry of the modulator.



## 6 Conclusions

This mostly theoretical description of the STAS concept has shown that in ideal conditions, exempted of noise, such a device does not interfere with the polarization states: it is impossible to obtain the same pattern of intensity from different states of polarization.

Nevertheless, when the noise is added to the nominal signal, the determination of any incoming polarization is accompanied by uncertainty. By mapping the uncertainty on the Stokes parameters with respect to the orientation of the analyzer, it has been shown that angles like 45 deg and 135 deg should be avoided as they are erasing any information about the  $Q$  parameter of the incoming light. Apart from the orientation of the analyzer, the couple of angles  $(\xi, \psi)$  also plays an important role in the precision of measurements. Therefore, a geometry with  $(\xi, \psi) = (3 \text{ deg}, 1.8 \text{ deg})$  can provide equal values of the uncertainties on the Stokes parameters for orientations of the analyzer at 17.5 deg, 72.5 deg, 107.5 deg, 162.5 deg. The level of uncertainty corresponding to these positions is 1.73 times higher than in the ideal case of a polarimeter, but it represents a compromise in which all Stokes parameters are determined with similar low errors (choosing other angles may improve the situation for one parameter, but degrade it for another).

Because this type of spectropolarimeter is based on the continuous variation of the phase on the vertical direction, multiple modulation schemes can be imagined. One of the best criteria to choose among them is the efficiency of the extraction of the Stokes parameters. In this paper, we investigated the dependency of the efficiency on the orientation of the analyzer and on the geometry of the modulator. Maxima of the total efficiency of about 0.99 are attainable, situating this concept of spectropolarimeter above classical examples such as ZIMPOL, ASP, or TIP. The impact of the apex angles on the efficiency has also proved that configurations of the type  $\xi = k\psi$  or  $\psi = k\xi$ , where  $k = 1, 2, 3, \dots$  must be avoided.

## Acknowledgments

The first author acknowledges the support of the STAR Institute and the Centre Spatial de Liège.

## References

1. A. Morozhenko and A. Vid'machenko, *Polarimetry and Physics of Solar System Bodies*, Springer Science, pp. 369–384 (2005).
2. J.-L. Leroy, *La polarisation de la lumière et l'observation astronomique*, Editions des archives contemporaines, Paris (2001).
3. J. Bailey, L. Kedziora-Chudczer, and K. Bott, "Polarized radiative transfer in planetary atmospheres and the polarization of exoplanets," *Mon. Not. R. Astron. Soc.* **480**(2), 1613–1625 (2018).
4. L. C. G. Rossi and D. M. Stam, "Circular polarization signals of cloudy (exo)planets," *Astron. Astrophys.* **616**, A117 (2018).
5. L. Kolokolova, J. Hough, and A. C. Levasseur-Regourd, *Polarimetry of Stars and Planetary Systems*, Cambridge University Press, Cambridge (2015).
6. D. H. Goldstein, *Polarized Light*, CRC Press, Taylor & Francis Group, Boca Raton (2011).
7. E. Collett, *Field Guide to Polarization*, SPIE Press, Bellingham, Washington (2005).
8. J. C. del Toro Iniesta, *Introduction to Spectropolarimetry*, Cambridge University Press, Cambridge (2003).
9. W. Sparks et al., "Compact and robust method for full Stokes spectropolarimetry," *Appl. Opt.* **51**, 5495–5511 (2012).
10. M. Pertenais et al., "Static spectropolarimeter concept adapted to space conditions and wide spectrum constraints," *Appl. Opt.* **54**, 7377–7386 (2015).
11. M. Pertenais et al., "UVMag: space UV and visible spectropolarimetry," *Proc. SPIE* **9144**, 1017–1025 (2014).
12. M. J. Dodge, "Refractive properties of magnesium fluoride," *Appl. Opt.* **23**, 1980–1985 (1984).
13. H. H. Li, "Refractive index of alkaline earth halides and its wavelength and temperature derivatives," *J. Phys. Chem. Ref. Data* **9**, 161–290 (1980).

14. I. H. Malitson, "A redetermination of some optical properties of calcium fluoride," *Appl. Opt.* **2**, 1103–1107 (1963).
15. M. Daimond and A. Masumura, "High-accuracy measurements of the refractive index and its temperature coefficient of calcium fluoride in a wide wavelength range from 138 to 2326 nm," *Appl. Opt.* **41**(25), 5275–5281 (2002).
16. M. Pertenais, "Spectropolarimétrie stellaire UV et visible depuis l'espace," PhD thesis, Université Toulouse III—Paul Sabatier (2016).
17. E. W. Weisstein, "Wronskian," <http://mathworld.wolfram.com/Wronskian.html> (accessed 2019-20-05).
18. B. Borden, *Essential Mathematics for the Physical Sciences*, vol. I, Morgan & Claypool Publishers, San Rafael, California (2017).
19. C. U. Keller and F. Snik, "Polarimetry from the ground up," in *Solar Polarization*, R. S. V. Berdyugina and K. N. Nagendra, Eds., ASP Conference Series, vol. 405, pp. 371–382, Astronomical Society of the Pacific, San Francisco (2009).
20. D. A. Clarke, *Polarized Light and Optical Measurement*, International Series of Monographs in Natural Philosophy, vol. 35, Pergamon, Oxford (1971).
21. P. R. Bevington, *Data Reduction and Error Analysis for the Physical Sciences*, 3rd ed., McGraw-Hill Higher Education, Boston (2003).
22. J. C. del Toro Iniesta and V. M. Pillet, "Assessing the behavior of modern solar magnetographs and spectropolarimeters," *Astrophys. J. Suppl. Ser.* **201**, 22 (2012).
23. J. C. del Toro Iniesta and M. Collados, "Optimum modulation and demodulation matrices for solar polarimetry," *Appl. Opt.* **39**, 1637–1642 (2000).
24. M. Collados, "High resolution spectropolarimetry and magnetography," in *3rd Advances in Solar Physics Euroconference: Magnetic Fields and Oscillations*, B. Schmieder, A. Hofmann, and J. Staude, Eds., ASP Conference Series, vol. 184, 3–22, Astronomical Society of the Pacific (1999).

**Bogdan Vasilescu** received his BS degree in physics and his MS degree in space sciences from the University of Liège in 2016 and 2019, respectively. He is a PhD student at the Centre Spatial de Liège of the University of Liège. His current research is related to the development of a static imaging spectropolarimeter able to cover any type of polarization.

Biographies of the other authors are not available.

### 5.3. THE ORTHOGONALITY OF THE MODULATION FUNCTIONS

As mentioned before, another possible approach for proving the uniqueness of the solution is based on the orthogonality of the functions  $m$ ,  $n$ , and  $p$ , which determine the variation of the intensity in the detector plane (Vasilescu et al., 2021).

Theoretically, two functions  $f(x)$  and  $g(x)$  are orthogonal on the interval  $[a, b]$  if

$$\langle f, g \rangle = \int_a^b \overline{f(x)}g(x)dx = 0, \quad (5.13)$$

where  $\overline{f(x)}$  is the conjugate of  $f(x)$ . If the modulation functions  $(1, m(y), n(y), p(y))$  are orthogonal, then they form a basis, and the decomposition of a Stokes vector  $\vec{S}$  into this basis is unique.

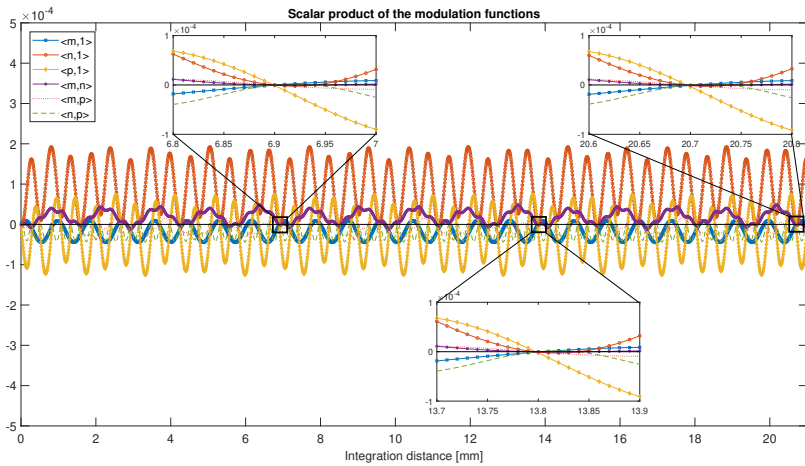


Figure 5.1: Variation of the scalar product of the modulation functions  $(1, m(y), n(y), p(y))$ , with the integration distance. It can be noticed that for integration over  $[0, 6.9]mm$ ,  $[0, 13.8]mm$ ,  $[0, 20.7]mm$ , for arbitrary angles  $\theta = 50.6^\circ$ ,  $\xi = 2.6^\circ$ ,  $\psi = 1.6^\circ$ , and  $\lambda = 0.3\mu m$ , the scalar product is zero (zoomed regions aside the main graphic). Source:(Vasilescu et al., 2021)

Computing the scalar product of the modulation functions for various integration distances corresponding to the hypothetical sampling distances, we get the results from Fig. 5.1. For each couple, this scalar product is very close to zero and passes through zero when the integration distance corresponds to the longest period of the product of two functions from the scalar product. Therefore, the functions are orthogonal over these distances, and the decomposition of the Stokes vectors is unique in the basis formed by these functions.

Aside from the unicity of the modulation scheme, efficiency also plays a crucial role in assessing the performance of the spectropolarimeter concept. As we saw in the previous section, in our case, the efficiency is driven by four parameters: the angles  $\xi$  and  $\psi$  of the modulator, the angle  $\theta$  of the analyzer, and the number of pixels.

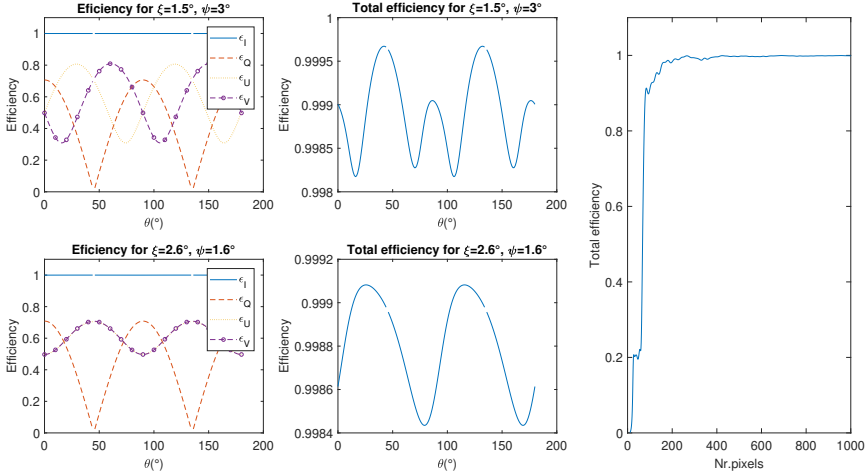


Figure 5.2: Efficiency of the modulation scheme and total efficiency as a function of the orientation of the analyzer ( $\theta$ ), for two couples  $(\xi, \psi)$ :  $(1.5^\circ, 3^\circ)$  and  $(2.6^\circ, 1.6^\circ)$ . The total efficiency as a function of the number of pixels is also plotted (right). The variations with  $\theta$  are considered for the case of 1000 pixels of  $10\mu\text{m}$  dimension. The efficiency as a function of number of pixels is observed for the scenario  $\xi = 2.6^\circ$ ,  $\psi = 1.6^\circ$ ,  $\theta = 30^\circ$ , and  $\lambda = 0.3\mu\text{m}$ . Source: (Vasilescu et al., 2021)

Analyzing the efficiencies of the polarimeter as a function of these parameters, recommendations for the best geometry, the analyzer's orientation, or the detector's dimension can be inferred.

Concerning the number of pixels required to reach a maximum efficiency, this is influenced, as we saw before, by the wavelength. The reason behind this dependency lies in the fact that the wavelength directly impacts the period of the signal. Therefore, working at  $\lambda = 0.125\mu\text{m}$  requires more than 2000 pixels to reach the maximum of total efficiency, while for  $\lambda = 0.3\mu\text{m}$  100 pixels are enough (see Fig. 5.2). Figure 5.2 also shows that the orientation of the analyzer does not impact the total efficiency. On the contrary, the efficiency corresponding to the Stokes parameters shows a strong dependency on the analyzer orientation and the geometry of the prisms. Concerning the apex angles  $\xi$  and  $\psi$ , values like  $(2.6^\circ, 1.6^\circ)$ , ensure equal efficiency in the determination of  $S_2$  and  $S_3$ . Simulations conducted for values of  $\xi$  and  $\psi$  between  $1^\circ$  and  $4^\circ$  show that for  $\xi = \psi$  an important drop of efficiency is observed (Fig. 5.3). Values of the type  $\xi = 2\psi$  or  $\psi = 2\xi$  are also characterized by a certain drop of efficiency, the effect being more important when the apex angle of the second wedge is bigger than the first,  $\psi > \xi$ . The reason for this efficiency drop is the fact that the scalar product of the modulation functions is no longer zero if  $\xi = \psi$  or  $\psi = 2\xi$ . The same situation can be pointed out for  $\xi = 2\psi$ . Consequently, the modulation functions are no longer orthogonal in these cases. Therefore, the uniqueness of the solution is not verified for this configuration of the modulator, and the uncertainty characterizing the Stokes parameters is maximal. Because of this, the geometry of the modulator should have:

$$\begin{cases} \psi \neq k \cdot \xi, \\ \xi \neq k \cdot \psi \end{cases} \quad k = 1, 2, \dots \tag{5.14}$$

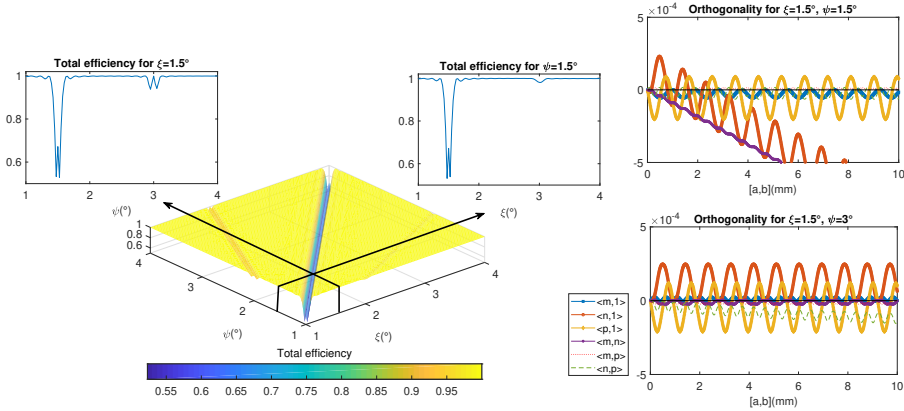


Figure 5.3: Total efficiency as a function of  $\xi$  and  $\psi$  angles of the modulator. The contour plot shows that equal values,  $\xi = \psi$ , or situations of the type  $\xi = 2\psi$ , respectively  $\psi = 2\xi$ , should be avoided as they generate a drop in efficiency. The particular cases of  $\xi = 1.5^\circ$  and  $\psi = 1.5^\circ$  are detailed. At right, the scalar product of the modulation functions for the particular cases  $\xi = \psi = 1.5^\circ$ , and  $\psi = 2\xi = 3^\circ$  is represented. It is noticeable the high slope of  $\langle m, n \rangle$  and  $\langle n, 1 \rangle$  in the case  $\xi = \psi = 1.5^\circ$ , characterized also by a huge drop of efficiency, and the smaller deviation of  $\langle n, p \rangle$  when  $\xi = 1.5^\circ, \psi = 3^\circ$ , corresponding also to a local minimum of efficiency. Source:(Vasilescu et al., 2021)

### 5.4. CONCLUSION

We have seen in this chapter that several methods are at hand to prove the uniqueness of the solution for this spectropolarimeter concept. Some are more computationally intensive and difficult to interpret, while others are more suited to experimental implementations. However, the bottom line is that a unique solution theoretically characterizes this spectropolarimeter concept. Each input polarization state corresponds to a distinctive intensity pattern in the detector plane. To assess the "quality" of Stokes parameter extraction, we investigated here the efficiencies associated with the modulation scheme. We have seen how these efficiencies are affected by the system's main parameters: the analyzer's orientation, the apex angles, and the number of pixels. Thus, we pointed out that two analyzer orientations ( $45^\circ$  and  $135^\circ$ ) should be avoided to allow full Stokes retrieval. In addition, specific apex angle values must also be avoided for modulator fabrication. These are the situations where the angles are equal or entire multiples of each other.

Theoretically, this spectropolarimeter concept proves its ability to find any polarization state unambiguously. However, deviations from ideal conditions must be anticipated when dealing with a real instrument using this modulation method. The next chapter shows how the instrument will work in this case. The modulation scheme will be analyzed from the perspective of condition number and equally weighted variance.

## BIBLIOGRAPHY

- Vasilescu, B., Nazè, Y., & Loicq, J. (2020). Solution uniqueness and noise impact in a static spectropolarimeter based on birefringent prisms for full stokes parameter retrieval. *Journal of Astronomical Telescopes, Instruments, and Systems*, 6(2), 1. <https://doi.org/10.1117/1.JATIS.6.2.028001>
- Vasilescu, B., Nazé, Y., Rauw, G., Kintziger, C., & Loicq, J. (2021, June 11). Development of a space spectropolarimeter for full stokes parameters retrieval. In Z. Sodnik, B. Cugny, & N. Karafolas (Eds.), *International conference on space optics — ICSO 2020* (p. 89). SPIE. <https://doi.org/10.1117/12.2599427>



# 6

## THE ANALYSIS OF THE MODULATION SCHEME

*If God hadn't rested on Sunday, He would have had time to finish the world.*

Gabriel Garcia Marquez



The previous chapters demonstrated that the modulator concept proposed here is very promising: it is theoretically characterized by the uniqueness of the solution, and among the countless ways in which it can be configured, some geometries ensure an almost ideal efficiency of the modulation scheme. This characteristic allows us to hope for obtaining minimal and equal uncertainties for all Stokes parameters under noise conditions.

The different configurations in which such a polarimeter can be built are translated, among others, into different modulation schemes. The modulation scheme acts as the coefficients of a system of equations meant to help recover the polarization. It allows us to convert intensity readings from the detector into Stokes parameter values. But also, they act like a filter.

The intensity values recovered from the detector are influenced by noise. In addition, the light reaching the detector passes through optical elements that may deviate slightly from the theoretical description. A "good" modulation matrix can help us alleviate these problems. Instead of turning small variations in intensity and optical properties into large uncertainties on the Stokes parameters, they can help us to restrain these uncertainties.

In the third Chapter, we saw that we have at hand two figures of merit to monitor these aspects for a modulation matrix: the condition number ( $CN$ ) and the equally weighted variance ( $EWV$ ). If the modulation efficiency, studied in the previous chapter, indicates how much the four Stokes parameters can be affected by Gaussian noise,  $CN$  and  $EWV$  allow us to extend the analysis to other types of noise and the propagation of different errors.

In a traditional instrument, the modulation matrix  $W$  has a generally fixed structure and depends on very few parameters. Thus, for instance, the number of pixels or their size plays an insignificant role in the case of a classical instrument. However, in our case, these parameters are defining and play a key role in establishing the modulation matrix and, implicitly, the quality of the instrument. The relation (4.19) shows us that the terms of this matrix depend on the vertical position of the projection of the pixels at the modulator level, the size of these pixels, the orientation of the analyzer, and the phase difference determined by prisms 1 and 3. Consequently, special attention was paid to analyzing the modulation matrices that can be obtained by varying these essential parameters of the system. The condition number and the equally weighted variance were used as metrics to determine the quality of the modulation matrices that can be obtained for various wavelengths, pixel sizes and number of pixels. The results, published in *Optics Express*<sup>1</sup>, are reproduced in the next pages. Overall, as in the case of the efficiency of the modulation scheme, the results of this study show that the concept advanced here exhibits an almost optimal behavior. For any wavelength and pixel size, there is a minimum number of pixels starting from which  $CN$  or  $EWV$  approaches the specific values of an optimal scheme. These new findings further strengthen our conviction that we are dealing with a method capable of generating multiple optimal polarization modulation schemes. However, it must be stressed that the variations of the  $W$  matrix considered here, which can influence our precision in determining the polarization, do not cover all

<sup>1</sup>Vasilescu, B., Piron, P., Loicq, J. (2023). "Performance analysis of a spectropolarimeter employing a continuous phase variation", *Optics Express*, 31(13), 21078

the possibilities. In reality, many more factors may come into play to differentiate the optical setup from the theoretical one. Temperature, humidity, or deviations from plans in the manufacturing process are just a few examples. For this reason, a realistic assessment of the instrument's quality can only be made after the experimental determination of the  $W$  matrix. This determination takes into account all the factors that can alter its shape.



# Performance analysis of a spectropolarimeter employing a continuous phase variation

BOGDAN VASILESCU,<sup>1,\*</sup>  PIERRE PIRON,<sup>1</sup> AND JÉRÔME LOICQ<sup>1,2</sup>

<sup>1</sup>Delft University of Technology, Kluyverweg 1, 2629 HS Delft, Netherlands

<sup>2</sup>University of Liège, Centre Spatial de Liège, Avenue du Pré Aily, 4031 Liège, Belgium

\*B.V.Mr.Vasilescu@tudelft.nl

**Abstract:** The light emitted or reflected by a medium can exhibit a certain degree of polarization. Most of the time, this feature brings valuable information about the environment. However, instruments able to accurately measure any type of polarization are hard to build and adapt to inauspicious environments, such as space. To overcome this problem, we presented recently a design for a compact and steady polarimeter, able to measure the entire Stokes vector in a single shot. The first simulations revealed a very high modulation efficiency of the instrumental matrix for this concept. However, the shape and the content of this matrix can change with the characteristics of the optical system, such as the pixel size, the wavelength or the number of pixels. To assess the quality of the instrumental matrices for different optical characteristics, we analyze here the propagation of errors, together with the impact of different types of noise. The results show that the instrumental matrices are converging towards an optimal shape. On this basis, the theoretical limits of sensitivity on the Stokes parameters are inferred.

© 2023 Optica Publishing Group under the terms of the [Optica Open Access Publishing Agreement](#)

## 1. Introduction

The understanding of reality can be hugely improved with the help of polarization. This property of light, referring to the orientation of the electric field, can be related to many characteristics of the environment. Therefore, with tremendous success, now we use polarization in astronomy [1–3], remote sensing [4], medicine, biology, chemistry, etc. [5–9].

However, despite the large number of applications, the measurement of polarization remains difficult. The main reason for this is the fact that the human eye and the optical detectors are not sensitive to the polarization of light. We need to use special instruments to measure it. These instruments are bulky, very sensitive to the measurement conditions, and only measure a limited set of polarization states.

In recent research, a new method for a non-imaging measurement of polarization was presented [10–12]. As a novelty, this method employs a new type of optical modulator. This component allows for overcoming most of the traditional problems related to polarization measurements. It gives the possibility to build an instrument compact, robust, and suitable even for use in harsh environments, like space. Moreover, it can measure any type of polarization through a single shot.

However, in contrast with the traditional way of measuring polarization, where a limited number of equations are used in the modulation schemes, the new instrument can employ much more equations. Therefore, the instrumental matrix can have a very large format. In addition, this matrix will depend on the geometry of the modulator or on the number of pixels, their size, and the used wavelength. Thus, finding an optimal form for these matrices is no longer easy.

Based on the previous results [10], a specific geometrical configuration can be chosen for the modulator to obtain the highest efficiency of the modulation scheme [13]. This way, only three variables are required in the analysis. The system's quality depends on the number of pixels, their size and the wavelength. Therefore, the theory of the impact of noise [14–17] can be used

for different configurations depending on these variables in order to assess the quality of the instrumental matrices that can be obtained.

This paper uses two main concepts to analyze these matrices: the condition number ( $CN$ ) and the equally weighted variance ( $EWV$ ). The  $CN$  provides information about how errors are propagated through the instrumental matrix. The  $EWV$  tells how the retrieved Stokes parameters are impacted by the type of noise. This way, we can see if the proposed instrument behaves or not like an optimal one.

The results of simulations show that, in certain conditions, the instrument is very close to an optimal one. No matter the wavelength, the matrices are converging towards an ideal form. In conclusion, the proposed design not only solves many practical difficulties related to the measurement of polarization, but also provides a very high degree of accuracy.

## 2. Measurement of polarization

The classical methods for the determination of polarization rely on Stokes formalism and on the Mueller calculus. The Stokes formalism is a straightforward mathematical description of polarization. At the basis is a vector with four parameters,  $\vec{S} = (S_0, S_1, S_2, S_3)^T$ , that can represent any type of polarization. Here  $S_0$  stands for the total intensity of light,  $S_1$  for the linear horizontal or vertical state of polarization,  $S_2$  for the linear  $45^\circ$  or  $135^\circ$  states, and  $S_3$  for the circular right or left polarization, while  $T$  denotes the transposition operator. Finding the four Stokes parameters requires at least four measurements under different configurations of the optical system. The Stokes vector is related to the structure of the system through the Mueller calculus. Therefore, the state of polarization,  $\vec{S}_{out} = (S_{out0}, S_{out1}, S_{out2}, S_{out3})^T$ , emerging from a system described by a  $4 \times 4$  Mueller matrix,  $M$ , is:

$$\vec{S}_{out} = M \cdot \vec{S}, \quad (1)$$

where  $\vec{S}$  is the incoming state of polarization. Given the fact that the detectors are sensitive only to the intensity of light, only the first term of the emerging vector,  $S_{out0}$ , must be taken into consideration for the measurement of polarization. Therefore, the detected intensity is:

$$S_{out0} = M_{00}S_0 + M_{01}S_1 + M_{02}S_2 + M_{03}S_3, \quad (2)$$

where  $(M_{00}, M_{01}, M_{02}, M_{03})$  are the terms of the first line of the Mueller matrix,  $M$ . When the configuration of the system changes, these terms may also change. To simplify the representation of a system that can embrace  $N$  configurations, it is useful then to change the notation from  $M$  into  $W$ , and from  $S_{out0}$  to  $I$ , so that:

$$\begin{cases} (M_{0i})_k = W_{ki+1} \\ (S_{out0})_k = I_k \end{cases} \quad \text{for } i = 0, \dots, 3; \quad k = 1, \dots, N, \quad (3)$$

where  $k$  is the index of the configuration. Consequently, the  $N$  equations that allow the measurement of polarization can be written in the following form [13,18]:

$$\begin{pmatrix} I_1 \\ I_2 \\ I_3 \\ \cdot \\ \cdot \\ I_N \end{pmatrix} = \begin{pmatrix} W_{11} & W_{12} & W_{13} & W_{14} \\ W_{21} & W_{22} & W_{23} & W_{24} \\ W_{31} & W_{32} & W_{33} & W_{34} \\ \cdot & \cdot & \cdot & \cdot \\ \cdot & \cdot & \cdot & \cdot \\ W_{N1} & W_{N2} & W_{N3} & W_{N4} \end{pmatrix} \cdot \begin{pmatrix} S_0 \\ S_1 \\ S_2 \\ S_3 \end{pmatrix}, \quad (4)$$

or, in a more contracted expression:

$$\vec{I} = W \cdot \vec{S}, \quad (5)$$

where  $\vec{I}$  is the vector of the detected intensities (i.e. number of photo-electrons),  $W$  is the instrumental matrix and  $\vec{S}$  is the incoming Stokes vector that must be measured.

If the transition from one configuration to another requires the move or the rotation of certain components of the instrument, then we are dealing with the sequential measurement of polarization. On the other hand, if the different configurations coexist, then we are speaking about the division of amplitude procedure.

If  $W$  is an invertible matrix, the Stokes vector is immediately accessible via

$$\vec{S} = W^{-1} \cdot \vec{I}. \quad (6)$$

Because noise is always present in this kind of measurement, increasing the number of lines of the system (Eq. (4)) may help mitigate the influence of spurious signals and enhance the precision of the polarization determination. However, if  $N > 4$ , then the  $W$  matrix is no longer invertible. The only possibility to solve the system (Eq. (5)) is to use the left-inverse matrix,  $W^\dagger$ :

$$\begin{cases} W^\dagger = (W^T W)^{-1} W^T \\ W^\dagger W = \mathbb{I}, \end{cases} \quad (7)$$

where  $T$  represents the matrix transposition. According to the theory [19], the left inverse matrix exists only if the rank of the matrix  $W(N \times 4)$  is equal to 4, when  $N \geq 4$ . Therefore, the use of the left-inverse matrix should be conditioned by the verification of this necessary and sufficient condition. Multiplying at left side the Eq. (5) with  $W^\dagger$ , we obtain

$$\vec{S} = W^\dagger \vec{I}. \quad (8)$$

### 3. Continuous phase variation spectropolarimeter concept

Most of the classical approaches to generate the  $W$  matrix are using the sequential method or the division of amplitude. Therefore, these kinds of instruments often are bulky, limited to certain types of polarization, or not suitable for harsh environments. In this context, we recently presented a new concept of spectropolarimeter able to solve most of these difficulties [10–12]. Using the division of amplitude method, the new instrument allows the full determination of the Stokes vector with a single measurement. Working with a collimated beam, this instrument is adapted for the non-imaging working mode.

The main part of the instrument, the modulator, is composed of three prisms in Magnesium Fluoride ( $\text{MgF}_2$ ), optically glued together and with the fast axis differently oriented in each wedge (see Fig. 1, (a, b)). Therefore, the first prism, (1), of apex angle  $\xi$ , has a fast axis oriented along the  $x$ -axis. In the middle part of the modulator, (2), the fast axis is oriented along the  $z$ -axis, while in the third wedge, (3), of apex angle  $\psi$ , the fast axis makes an angle of  $45^\circ$  with the  $x$ -axis, in the  $(xy)$ -plane. These particular orientations of the fast axes ensure a complete modulation along the vertical direction (i.e. the  $y$ -axis) of any incoming state of polarization arriving collimated from the left side of the instrument. Given the variation of the optical thickness along the vertical direction inside the modulator, the phase difference between the two orthogonal components of light varies continuously along the vertical direction. Therefore, a continuous variation of polarization is achieved along the vertical direction on the exit face of the modulator. Because the phase difference induced by the  $\text{MgF}_2$  prisms depends also on the birefringence of the material, the modulation of the signal is also spectrally dependent. By placing a linear polarizer after the modulator, with the transmission axis oriented at an angle  $\theta$  with respect to the horizontal direction, the variation of polarization along the vertical direction can be converted into an

intensity variation, as it is shown in Fig. 1(c). To avoid a high angular separation between the ordinary and extraordinary rays inside the modulator, small values of apex angles must be used. Therefore, the simulations conducted here rely on  $\xi = 2.6^\circ$  and  $\psi = 1.8^\circ$ , whereas the orientation of the analyzer was considered  $\theta = 72^\circ$ . These values were chosen also in order to ensure a very high efficiency of the modulation scheme [10,13].

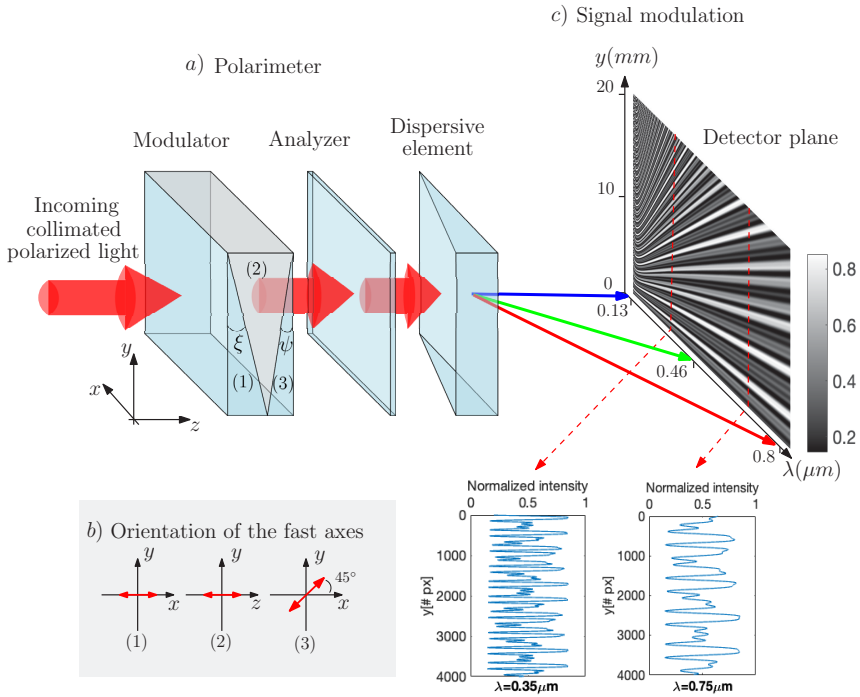


**Fig. 1.** The general principle of the spectropolarimeter: a) the polarized light arriving collimated from the left side passes through the modulator, the analyzer, and then is dispersed horizontally by a dispersive element. Each prism of the modulator has a particular orientation of the fast axis: along the  $x$  axis in (1), along  $z$  in (2), and at  $45^\circ$  in (3). The modulation of the signal obtained with this modulator is spectrally dependent (c). The period of the signal increases with the wavelength. In addition, each incoming state of polarization is characterized by a unique pattern of the intensity. An arbitrary state of polarization  $\vec{S} = [1, 0.5, 0.4, 0.3]$  was simulated here.

Since the modulation of the signal is spectrally dependent, due to the birefringence of the modulator, (see Fig. 1(c)), a dispersive element can be placed after the analyzer to disperse the light spectrally along the  $x$ -axis, orthogonal to the polarimetric modulation. For an incoming Stokes vector,  $\vec{S} = (S_0, S_1, S_2, S_3)^T$ , the intensity of light in the detector plane is described by the following equation:

$$I(\theta, y, \lambda) = \frac{1}{2} [S_0 + S_1 \cdot m(\theta, y, \lambda) + S_2 \cdot n(\theta, y, \lambda) + S_3 \cdot p(\theta, y, \lambda)] \quad (9)$$

where  $\theta$  is the angle of the linear analyzer with respect to the  $x$ -axis,  $y$  is the position in the vertical direction, and  $\lambda$  is the wavelength. The functions  $m, n, p$ , computed with the help of the

Mueller calculus, are given by:

$$\begin{cases} m(\theta, y, \lambda) = \cos(2\theta) \cos(\Delta\phi_3) \\ n(\theta, y, \lambda) = \sin(2\theta) \cos(\Delta\phi_1) + \cos(2\theta) \sin(\Delta\phi_1) \sin(\Delta\phi_3) \\ p(\theta, y, \lambda) = \sin(2\theta) \sin(\Delta\phi_1) - \cos(2\theta) \cos(\Delta\phi_1) \sin(\Delta\phi_3) \end{cases} \quad (10)$$

where  $\Delta\phi_1$  and  $\Delta\phi_3$  are the phase differences induced by the prisms (1) and (3):

$$\begin{cases} \Delta\phi_1 = \frac{2\pi}{\lambda} \Delta n(\lambda)(h - y) \tan(\xi) \\ \Delta\phi_3 = \frac{2\pi}{\lambda} \Delta n(\lambda)(h - y) \tan(\psi) \end{cases} \quad (11)$$

in which  $\Delta n(\lambda) = |n_o(\lambda) - n_e(\lambda)|$  is the absolute value of the difference between the ordinary and the extraordinary indices of refraction, also called the birefringence of the medium, while  $h$  is the height of the modulator.

Discretizing in the vertical direction the height of the ensemble formed by the modulator and the analyzer into  $N_t$  pixels of the same size as the detector pixels,  $\Delta y$ , then each small part of this ensemble will act as a polarimeter with a different configuration. Consequently, a column of  $N_t$  pixels from the detector plane will record the signal coming from  $N_t$  different polarimeters disposed on the same vertical. For a precise wavelength and orientation of the analyzer, the intensity measured by the illuminated pixels is:

$$\underbrace{\begin{pmatrix} I_1 \\ I_2 \\ \cdot \\ \cdot \\ I_N \\ \cdot \\ \cdot \\ \underbrace{I_{N_t}}_{\vec{i}} \end{pmatrix}}_{\vec{i}} = \frac{1}{2} \underbrace{\begin{pmatrix} \int_0^{\Delta y} dy & \int_0^{\Delta y} m(y)dy & \int_0^{\Delta y} n(y)dy & \int_0^{\Delta y} p(y)dy \\ \int_{\Delta y}^{2\Delta y} dy & \int_{\Delta y}^{2\Delta y} m(y)dy & \int_{\Delta y}^{2\Delta y} n(y)dy & \int_{\Delta y}^{2\Delta y} p(y)dy \\ \cdot & \cdot & \cdot & \cdot \\ \cdot & \cdot & \cdot & \cdot \\ \int_{(N-1)\Delta y}^{N\Delta y} dy & \int_{(N-1)\Delta y}^{N\Delta y} m(y)dy & \int_{(N-1)\Delta y}^{N\Delta y} n(y)dy & \int_{(N-1)\Delta y}^{N\Delta y} p(y)dy \\ \cdot & \cdot & \cdot & \cdot \\ \cdot & \cdot & \cdot & \cdot \\ \int_{(N_t-1)\Delta y}^{N_t\Delta y} dy & \int_{(N_t-1)\Delta y}^{N_t\Delta y} m(y)dy & \int_{(N_t-1)\Delta y}^{N_t\Delta y} n(y)dy & \int_{(N_t-1)\Delta y}^{N_t\Delta y} p(y)dy \end{pmatrix}}_W \cdot \underbrace{\begin{pmatrix} S_0 \\ S_1 \\ S_2 \\ S_3 \\ \vec{s} \end{pmatrix}}_{\vec{s}} \quad (12)$$

In the following discussions, the number of lines of the instrumental matrix,  $N$ , will always satisfy the relation  $N \leq N_t$ , where  $N_t = h/\Delta y$  is the total number of pixels from a column of the detector. The number of pixels  $N$  used in the construction of the  $W$  matrix can take any value between 4 and  $N_t$ . Therefore, using different values of  $N$  will not change the received flux per pixel. In addition, the size of the pixel,  $\Delta y$ , will be taken into account by considering the integrated value of the functions  $m$ ,  $n$ , and  $p$  over the pixel size (see Eq. (12)). When  $N > 4$ ,  $W$  is no longer invertible. However, working with  $N > 4$  may help to mitigate the impact of the noise if the  $W$  matrix is well-conditioned and close to an optimal one. Therefore, the objective of the current research is to show that the  $W$  matrices are converging toward optimal forms for certain couples of the number of pixels,  $N$ , and their size,  $\Delta y$ .

#### 4. Tools for the analysis of the instrumental matrix

From the Eqs. (10), (11) and (12) we see that, for a given configuration of the polarimeter (i.e. the angles  $\xi$ ,  $\psi$  and  $\theta$ , and the height,  $h$ ), and a given wavelength, the elements of the matrix  $W$ , as well as its dimension and other properties are determined by the number of pixels,  $N$ , their

size,  $\Delta y$ , and their location in the vertical direction. Therefore, the size of the matrix can span between  $4 \times 4$  and  $4 \times N$ . To see if these matrices  $W$ , that can be formed, are suitable or not for the retrieval of polarization, we need to assess their "quality". The best "instruments" for this are the condition number and the equally weighted variance [15,20–22]. Both will be analyzed hereafter. The advantage of the condition number is the fact that allows us to observe if the inverse of the  $W$  matrix can be computed with accuracy. On the other hand, the equally weighted variance tells us how the retrieval of the Stokes vector is impacted by different types of noise when a certain  $W$  matrix is used.

Both concepts, along with the demodulation of the signal, based on Eqs. (6) and (7), are relying on the possibility to compute the inverse of the instrumental matrix,  $W$ . As was underlined before, this happens only if the rank of  $W$  is 4, for any  $N \geq 4$  and for any  $\lambda$ . To have a rank equal to 4, the columns of  $W$  should be linearly independent. In addition, more than 4 rows should also be linearly independent. Our previous paper [10], proved that the functions  $m, n$  and  $p$  are linearly independent. Therefore, the columns of  $W$  are also linearly independent. A quick inspection of the Poincaré sphere (see Fig. (2)), where  $m, n, p$  are represented on a sphere of radius 1, reveals also that the points  $(m(y_i), n(y_i), p(y_i))$ ,  $(i = 1 \dots N)$  are covering the entire sphere, for any value of  $\lambda$ . Therefore, the rank of  $W$  is 4 and the necessary and sufficient condition for  $W$  to have a left-inverse is satisfied. Furthermore, an arbitrary example can be chosen to verify the demodulation procedure based on Eq. (8). Therefore, by considering an incoming normalized Stokes vector  $\vec{s} = (1, 1/\sqrt{3}, 1/\sqrt{3}, 1/\sqrt{3})^T$ , this procedure was applied to retrieve the polarization, ignoring, at this moment, any other sources of errors. The results (see Fig. (3)) show that for  $N > 6$ , the relative error on the normalized Stokes parameters is of the order of  $6.5 \cdot 10^{-12}$ . For  $N = 4$ , the highest error is observed on  $s_1$  parameter (approximately  $5.4 \cdot 10^{-8}$ ).

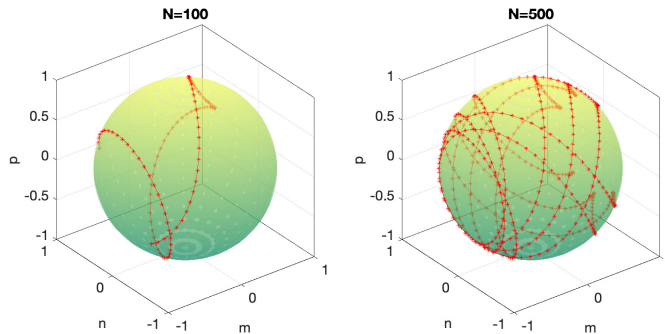


**Fig. 2.** Poincaré representation of the points  $(m(y_i), n(y_i), p(y_i))$ ,  $(i = 1, \dots, N)$  on a sphere of radius 1, for two values of  $N$ . For these simulations, the size of the pixel was considered to be  $\Delta y = 10 \mu\text{m}$  and the wavelength  $\lambda = 0.35 \mu\text{m}$ .

#### 4.1. Condition number

The condition number provides simultaneously information about how well-conditioned the  $W$  matrix is for inversion and how sensitive the system is to changes. Therefore, a small  $CN$  indicates a well-conditioned matrix. Small changes in the vector  $\vec{I}$ , due to noise, and in the matrix  $W$ , due to integration over pixel size, are converted into small variations of the computed Stokes vector  $\vec{S}$  with respect to the real incoming state of polarization,  $\vec{S}$ . Meanwhile, for an ill-conditioned  $W$  matrix, (large  $CN$ ), small changes of  $\vec{I}$  and  $W$  generate large changes in the computed state of polarization,  $\vec{S}$  [23]. The smallest value of  $CN$  is 1 and it corresponds to a unitary matrix, while the highest value is infinity, corresponding to non-invertible matrices. In



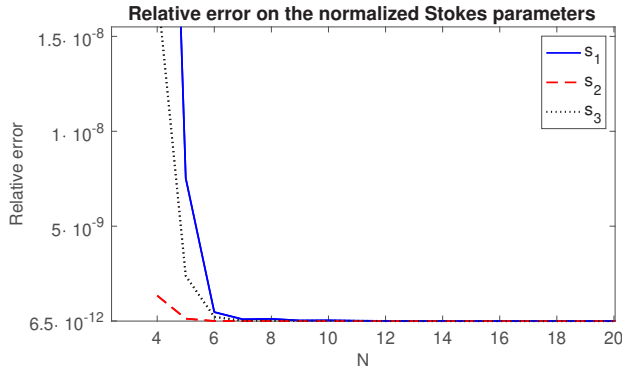


**Fig. 3.** Relative error on the normalized Stokes parameters as a function of the number of pixels,  $N$ . For these simulations, the size of the pixel was considered to be  $\Delta y = 10\mu m$ , the wavelength,  $\lambda = 0.35\mu m$ , whereas the incoming normalized polarization was arbitrarily chosen as  $\vec{s} = (1, 1/\sqrt{3}, 1/\sqrt{3}, 1/\sqrt{3})^T$ .

the case of a polarimeter, where  $W$  is no longer a square matrix, the  $CN$  is defined as [15,22]:

$$\begin{cases} CN(W) = \|W^\dagger\| \|W\| \\ \|W\| = \sqrt{\text{Tr}(W^T W)} \end{cases}, \tag{13}$$

where  $\text{Tr}$  is the trace operator. In [22] it was proved that the minimum condition number computed with this formula for an optimal  $W$  matrix is  $\sqrt{20}$ .

#### 4.2. Equally weighted variance

The error on Stokes parameters has two main sources: the algorithm of computation, through the matrix  $W$ , and the noise. To mitigate the impact of  $W$ , the best strategy is to search for the matrices with the smallest condition number. On the other hand, to assess the impact of noise, the concept of equally weighted variance ( $EWV$ ) can be used [15,20–22]. When the noise is present in the optical system, Eq. (5) must be adjusted:

$$\vec{I} = W\vec{S} + \vec{B}, \tag{14}$$

where  $\vec{B}$  is the noise vector. This noise can be related to the electronics of the instrument, speaking in this case about the Gaussian additive white noise (AWN), or to the number of the received photons, referred to as non-additive Poisson shot noise (PSN). Multiplying at left side with  $W^\dagger$ , the previous relation became:

$$\widehat{S} = \vec{S} + W^\dagger \vec{B}, \tag{15}$$

where  $\widehat{S} = W^\dagger \vec{I}$  is the corrupted Stokes vector. Because in our case  $W$  can embrace various forms, the purpose is then to see how the precision of the Stokes parameters is impacted by these forms when the different types of noise are present (see Fig. (4)). We can assess this impact with the help of the equally weighted variance. From its definition [20,21,24], the  $EWV$  is nothing else but the sum of the variances on the Stokes parameters of the vector  $\widehat{S}$ ,

$$EWV(W) = \sum_{k=0}^3 \text{var}(\widehat{S}_k) = \text{Tr}[\Gamma^{\widehat{S}}], \tag{16}$$

where  $\Gamma^{\widehat{S}}$  is the covariance matrix of  $\widehat{S}$ .

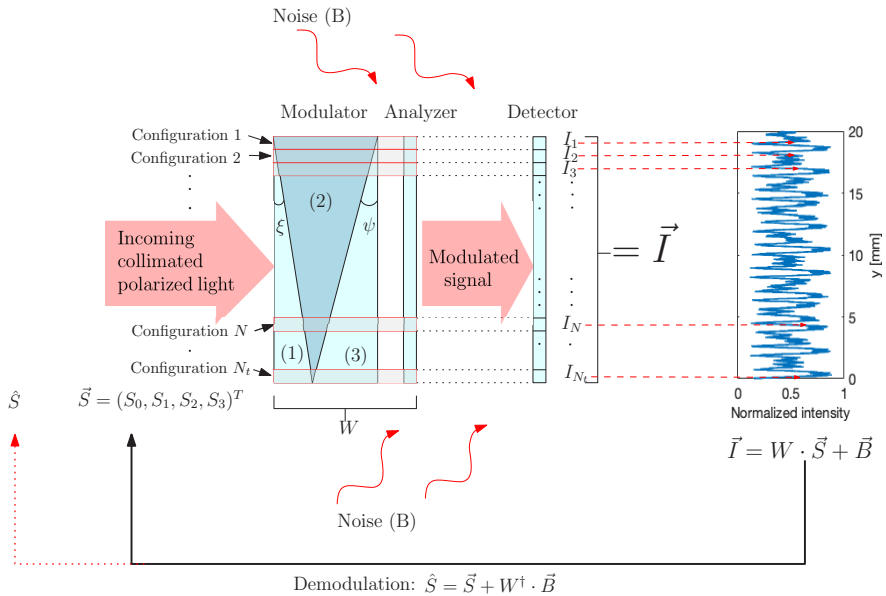


**Fig. 4.** Schematic representation of the working principle of the polarimeter in the presence of noise, for a single wavelength. The vertical modulation of the signal ( $\vec{I}$ ), obtained over a column of pixels, is corrupted by the noise  $\vec{B}$ . Consequently, the measured state of polarization is  $\hat{S}$  instead of  $\vec{S}$ . An optimal modulation matrix  $W$  allows the minimization of the difference between  $\hat{S}$  and  $\vec{S}$ .

Therefore, the imprecision on the Stokes parameters and on the degree of polarization can be directly accessed. In the case of a Gaussian white noise of standard deviation  $\sigma$ ,  $EWV$  becomes

$$EWV(W) = \sigma^2 \text{Tr} [(W^T W)^{-1}], \quad (17)$$

and the minimal values of  $EWV(W)$  correspond to optimal  $W$  matrices [25]. Previous studies [21,22] have shown that, in the presence of Gaussian noise, for the minimal values of  $EWV(W)$ ,  $\Gamma^{\vec{S}}$  has the form

$$\Gamma^{\vec{S}} = \sigma^2 (W^T W)^{-1} = \frac{4}{N} \sigma^2 \begin{pmatrix} 1 & 0 & 0 & 0 \\ 0 & 3 & 0 & 0 \\ 0 & 0 & 3 & 0 \\ 0 & 0 & 0 & 3 \end{pmatrix}, \quad (18)$$

where  $N$  is the total number of lines of the matrix  $W$ . For this value of  $\Gamma^{\vec{S}}$ , the  $EWV$  is  $40\sigma^2/N$ .

In the presence of a Poisson, non-additive noise, the expression of the covariance matrix is different as it depends on the intensity, and therefore on the Stokes parameters. In this case, the matrix is given by [14,21]:

$$\Gamma_{ij}^{\vec{S}} = \sum_{k=0}^3 S_k \sum_{n=1}^N W_{in}^\dagger W_{jn}^\dagger W_{nk} \quad \text{for } i, j = 0, \dots, 3. \quad (19)$$

For a design characterized by an optimal modulation scheme, the variances of the Stokes parameters, corresponding to the diagonal terms of the matrix (19) are [21]:

$$\begin{cases} \Gamma_{0,0}^{\bar{S}} = \frac{2S_0}{N} \\ \Gamma_{j,j}^{\bar{S}} = \frac{6S_0}{N}, j = 1, 2, 3 \end{cases} \quad (20)$$

whereas the covariance between  $S_0$  and the rest of the terms is no longer zero. Following Eqs. (13), and (20), the minimum value of the  $EWV$  is  $20S_0/N$ .

### 5. Optical system analysis

The two concepts previously introduced, for  $CN$  and  $EWV$ , are hereafter explored while applied to our spectropolarimeter. To simplify the analysis, the structural parameters of the polarimeter are considered fixed. Therefore, the analyzer is oriented at the angle  $\theta = 72^\circ$ , while the prisms of the modulator, built in  $MgF_2$ , have the apex angles  $\xi = 2.6^\circ$ , and  $\psi = 1.8^\circ$ . The only parameters driving the shape of the  $W$  matrix for a given wavelength,  $\lambda$ , are in this case the pixel size,  $\Delta y$ , and the number of lines,  $N$ , corresponding also to the number of pixels in the vertical direction. As was underlined before, a change in the size or number of pixels is not accompanied here by a variation of the flux. The limits of variation for  $\Delta y$  and  $N$  are imposed by the size of the modulator, which is here  $2cm \times 2cm$ . Consequently, the questions that we try to answer here are how many pixels we need to build an optimal modulation matrix and what is the suitable dimension of these pixels.

#### 5.1. Condition number

Using the Eq. (13), the  $CN$  was computed for various pixel sizes,  $\Delta y$ , and number of lines,  $N$ , of the matrix  $W$ . Precise values of the wavelength were arbitrarily chosen within the transmission range of  $MgF_2$ . Therefore, the Fig. (5)-left was plotted for  $\lambda = 0.35\mu m$ , and it shows that  $\Delta y$  and  $N$  are inversely correlated. An increase of the size of pixel corresponds to a decrease of the number of lines,  $N$ , required to obtain the same value of the  $CN$ . In addition, it is noticeable that the smallest value of  $CN$  is situated between 5 and  $\sqrt{20}$ , and is reachable for almost any value of the pixel size. This tendency is visible in the Fig. (5)-right. Here, the level of  $CN$  was

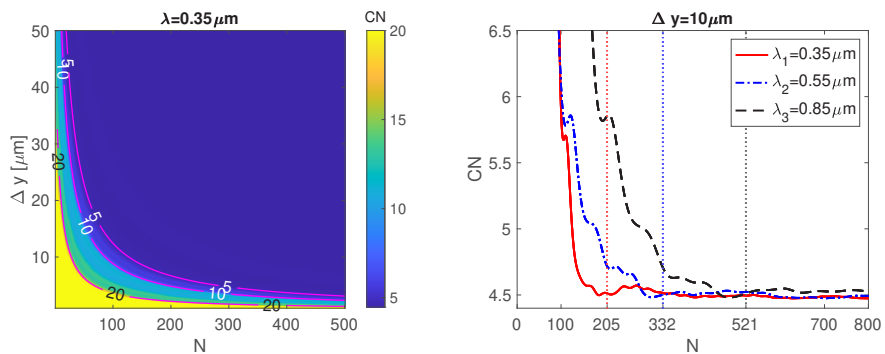


**Fig. 5.** Left:  $CN$  as a function of the pixel size,  $\Delta y$ , and number of lines,  $N$ , of the matrix  $W$ . For this example, an arbitrary wavelength  $\lambda = 0.35\mu m$  was considered. Level lines corresponding to  $CN = 20, 10$  and  $5$  were also plotted. Right:  $CN$  as a function of the number of lines,  $N$ , for a pixel size  $\Delta y = 10\mu m$  and three wavelengths. The dotted vertical lines correspond to  $\tau_{max}(\lambda_1)$ ,  $\tau_{max}(\lambda_2)$ , and  $\tau_{max}(\lambda_3)$  respectively.

monitored with respect to the value of  $N$  for three different wavelengths. The plot shows that for any wavelength, the  $CN$  converges similarly towards the optimal value of  $\sqrt{20}$ . The only impact of the wavelength is to shift the position of the minimum from where the convergence manifests. Approximately, the convergence occurs after the number of pixels,  $N$ , covers along the  $y$ -axis a distance equal to the largest period of the functions  $m, n, p$ . From Eq. (10) it can be easily shown that this period is:

$$\tau_{max}(\lambda) = \frac{\lambda}{\Delta n(\lambda) \cdot (\tan(\xi) - \tan(\psi))}. \quad (21)$$

## 6. Equally weighted variance (EWW)

As it was already proved, the notions of condition number and equally weighted variance are closely related [15]. However, the  $CN$  only provides information about the propagation of errors through the  $W$  matrix. It gives no hint about the level of errors on the Stokes parameters when the noise affects the measurements. For this, the  $EWW$  should be studied. This is based on the covariance matrix of the retrieved Stokes vector (see Eq. (16)). Therefore, it can provide information about the variances of the Stokes parameters and about the correlation existing between them.

### 6.1. Gaussian noise

When the system is subject to the Gaussian noise, the covariance matrix of the Stokes parameters,  $\Gamma^{\hat{S}}$ , is provided by Eq. (17). In the case of an optimal polarimeter, characterized by an equal impact of the noise on the Stokes parameters, the covariance matrix embraces the form from Eq. (18). Therefore, for such a polarimeter, the variances on  $S_1, S_2$ , and  $S_3$  are three times higher than for the intensity term,  $S_0$ . Because the rest of the matrix is zero, the presence of this noise brings no correlation between the Stokes parameters. Varying one of them will not affect the others.

As we saw in the study of  $CN$ , by changing the number of pixels,  $N$ , or the size of the pixels on the  $y$  direction,  $\Delta y$ , the shape and the "quality" of  $W$  can be changed. Thus, by increasing  $N$ , we noticed that  $CN$  converged towards the optimal value of  $\sqrt{20}$ . Conducting the same type of simulation for the covariance matrix, we want to see now if this trend can be retrieved again.

To simplify the comparison between the results for our instrument and an optimal case, described by the Eq. (18), we have monitored the evolution of the terms of the matrix  $G$ , defined by

$$G = \Gamma^{\hat{S}} \cdot \frac{N}{4\sigma^2}, \quad (22)$$

which is a normalized form of the covariance matrix. Therefore, if the modulation provided by the presented spectropolarimeter converges toward an optimal one, then we should also have:

$$G \xrightarrow{N} \begin{pmatrix} 1 & 0 & 0 & 0 \\ 0 & 3 & 0 & 0 \\ 0 & 0 & 3 & 0 \\ 0 & 0 & 0 & 3 \end{pmatrix}. \quad (23)$$

The upper graph from the Fig. (6) shows that the diagonal terms of the matrix  $G$  are converging, with the number of lines  $N$ , towards the values 1 and 3. This convergence occurs approximately after  $N = 200$ . Concerning the rest of the matrix, given the symmetry, only the lower terms are presented in Fig. (6)-bottom. The plots suggest a convergence towards zero. However, for this

trend to manifests, a higher value of  $N$  is required. Approximately, this value should satisfy the relation:

$$N \cdot \Delta y > 10 \cdot \tau_{max}(\lambda). \tag{24}$$

In conclusion, we can say that Eq. (24) is verified for instrumental matrices with a large number of lines. In this case, in the presence of Gauss noise, the studied model of spectropolarimeter behaves like an almost optimal one. By reducing  $N$ , the correlation between the Stokes parameters starts to increase. The most affected couples are  $(S_1, S_2)$  and  $(S_1, S_3)$ . Therefore, despite the fact that such modulation of the intensity allows the retrieval of the polarization state with a number of pixels covering the largest period,  $\tau_{max}(\lambda)$ , using a larger number proves to be better in the presence of Gauss noise.

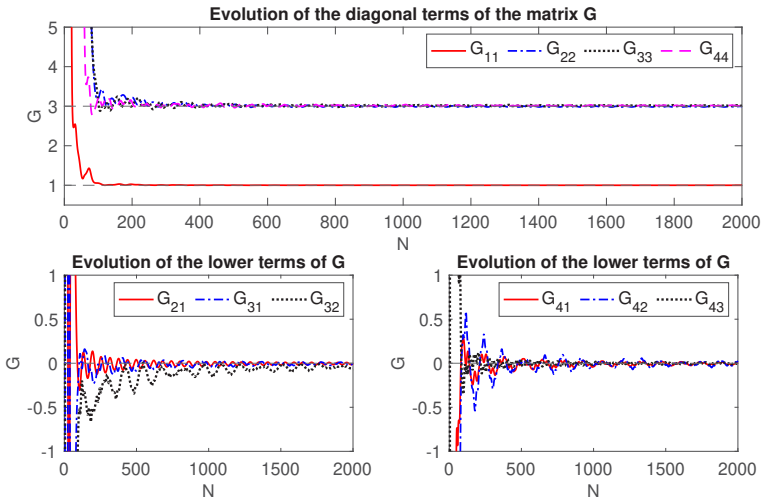


**Fig. 6.** Gaussian noise: evolution of the terms of the matrix  $G$  with the number of lines of the instrumental matrix  $W$ . An arbitrary value of the pixel size,  $\Delta y = 15 \mu m$ , was used for this simulation. The wavelength was set to  $0.35 \mu m$ . To point out the trend of the  $G$  terms, the maximum value of  $N$  was fixed now to 2000.

Concerning the value of the  $EWV$ , from the Eqs. (16), (17) and (23)) and from the results presented in Fig. (6), we may infer also that:

$$EWV(W(N)) = \frac{40\sigma^2}{N}, \tag{25}$$

for  $N \cdot \Delta y > \tau_{max}(\lambda)$ . Therefore, the equally weighted variance also converges towards the optimal value. This trend can be observed in Fig. (7) -left, where  $EWV$  was plotted with respect to  $N$  for an arbitrary pixel size of  $15 \mu m$  and  $\lambda = 0.35 \mu m$ . The convergence manifests in this case quicker than for the  $G$  terms because  $N$  is considered in the final expression of the  $EWV$ .

### 6.2. Poisson noise

The non-additive noise is dependent on the level of intensity. For our polarimeter, this level varies from one pixel to another, in the vertical direction, following a sinusoidal shape (see Fig. (1)). Therefore, the noise will vary also in the vertical direction, distorting differently the pattern of intensity from one pixel to another. To assume the impact of this non-additive contribution, the

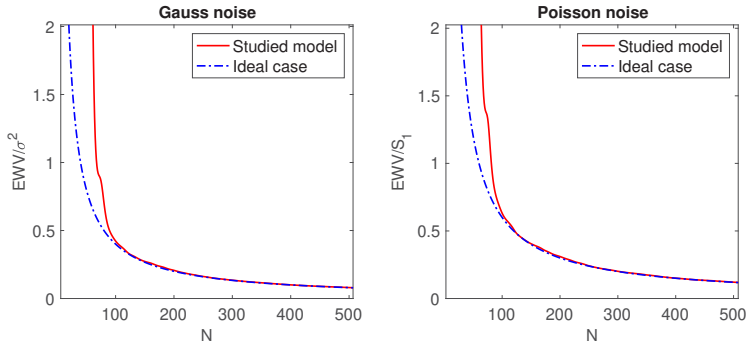


**Fig. 7.** EWW as a function of the number of lines of the matrix  $W$ , for  $\Delta y = 15\mu\text{m}$ , and  $\lambda = 0.35\mu\text{m}$ , in the presence of Gaussian noise (left), and Poisson noise (right). The plotted values were normalized by  $\sigma$ , supposed to be constant here, in the case of Gauss noise, and by  $S_0$ , for the Poisson noise.

relations (16) and (19) must be used. It can be noticed that the covariance matrix is different now from the case of the additive noise, as the terms of this matrix are related to the incoming state of polarization.

Using the same procedure as in the case of the Gaussian noise, we have computed the terms of the matrix  $G$ , where

$$G = \frac{N}{2S_0} \Gamma^{\vec{S}}, \tag{26}$$

for an arbitrary incoming Stokes vector  $\vec{S} = (3, 1.5, 1.4, 1.3)^T$ , as a function of the covered distance on the  $y$  direction. Because the obtained covariance matrix was proved to be symmetrical, again, only the lower part was presented in Fig. (8). The diagonal terms are showing strong convergence towards the optimal values (see Eq. (20)). However, the rest of the terms are no longer converging towards zero, as in the previous case. A certain trend or average value can be pointed out for each term of the covariance matrix, but the variation around these values is stronger than in the case of additive noise. Using again a large value of  $N$ , so that  $N \cdot \Delta y \geq 10 \cdot \tau_{max}$ , the covariance matrix becomes, approximately:

$$\Gamma^{\vec{S}} \rightarrow \frac{S_1}{N} \begin{pmatrix} 2 & 1 & 1 & 1 \\ 1 & 6 & 0 & 0 \\ 1 & 0 & 6 & 0 \\ 1 & 0 & 0 & 6 \end{pmatrix}. \tag{27}$$

Just like in the case of the additive noise, the variances on the Stokes parameters are three times higher than for the intensity term. However, the Stokes parameters are no longer uncorrelated now. Therefore, non-diagonal terms of the matrix  $\Gamma^{\vec{S}}$  are no longer zero. For small values of  $N$  (i.e.  $N \cdot \Delta y \leq 10 \cdot \tau_{max}(\lambda)$ ), there is also a small correlation between all the Stokes parameters. That means that a variation of one of the Stokes parameters will influence, most likely in a small amount, the value of all the others.

Concerning the equally weighted variance, Fig. (7)-right shows that for  $N \cdot \Delta y > \tau_{max}(\lambda)$  we have a superposition between the studied concept and the values corresponding to an optimal modulation scheme.

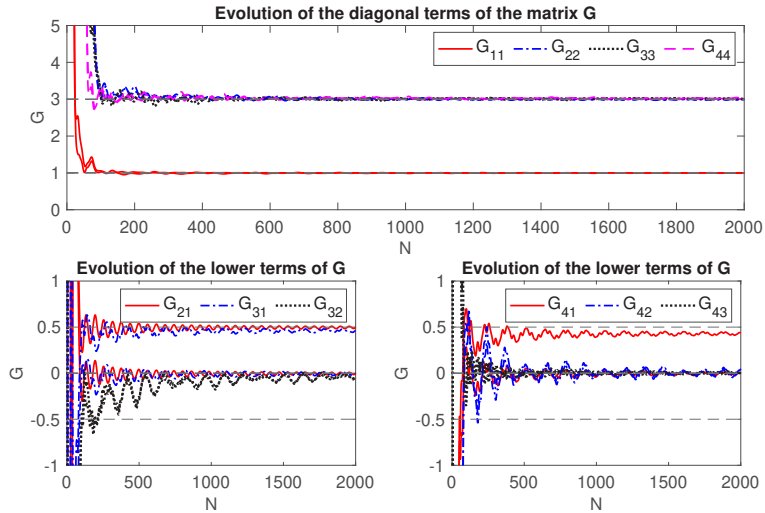


**Fig. 8.** Diagonal and upper right terms of the covariance matrix in the presence of Poisson noise. The lower-left part of the matrix is identical to the upper-right part, therefore the covariance matrix is diagonal. The simulations correspond to an arbitrary pixel size,  $\Delta y = 15\mu\text{m}$ , and to a wavelength  $\lambda = 0.35\mu\text{m}$ .

## 7. Conclusions

A new concept of spectropolarimeter based on a continuous phase variation was presented here and analyzed from the perspective of the instrumental matrix that is produced. In contrast with the 'traditional' instruments, employing limited and hardly tunable matrices, the instrument presented here allows the construction of various matrices. These matrices may vary in dimension and in the value of each line, according to the sizes of pixels used, and in the number of pixels chosen to extract the polarimetric information.

We have analyzed these matrices from the perspective of the condition number and the equally weighted variance. The condition number was used to assess the propagation of errors through the instrumental matrix. The equally weighted variance showed the impact of different types of noise on the determination of the Stokes vector.

The main parameters used to monitor different instrumental matrices were the number of lines,  $N$ , that corresponds also to the number of pixels used to read the signal on the vertical direction, and  $\Delta y$ , the size of the pixel.

For  $CN$ , the simulations showed that after a value of  $N$  verifying the relation  $N \cdot \Delta y = \tau_{\max}(\lambda)$ , we have a convergence towards the optimal value of  $\sqrt{20}$ . In other words, the signal must be read at least over the largest period to achieve this convergence.

Concerning the  $EWV$ , the study considered two cases: when the system is affected by the additive Gaussian noise and when it is affected by the non-additive Poisson noise. Because the computation of the  $EWV$  is based on the retrieval of the covariance matrix of the measured Stokes parameters, special attention was paid to the latter. Therefore, in the presence of the Gaussian noise, we discovered that the system converges towards an optimal behavior with the number of lines of the instrumental matrix. After approximately  $N \cdot \Delta y = 10 \cdot \tau_{\max}(\lambda)$ , the covariance matrix can be assimilated to the one corresponding to an optimal modulation scheme. However, when smallest values of  $N$  are used, a very small correlation between the Stokes parameters begins

to manifest. The couples  $(S_1, S_2)$  and  $(S_1, S_3)$  are the most affected. Overall, the covariance on  $(S_1, S_2, S_3)$  is three times higher than for the intensity,  $S_0$ . Searching in practice to improve the precision of the Stokes parameters beyond these limits will be impossible.

The system proves to be more sensitive in the presence of the Poisson noise. The covariance matrix also converges towards the optimal one in this case, but the variations around this limit value are higher. For short covered distances ( $N \cdot \Delta y < 10 \cdot \tau_{max}(\lambda)$ ) all the Stokes parameters prove to be correlated. A small variation of one of them affects all the rest. However, just like in the case of the additive noise, for  $N \cdot \Delta y > \tau_{max}(\lambda)$ , the covariance on  $(S_1, S_2, S_3)$  is three times higher than for the intensity,  $S_0$ . Because the covariance of the Stokes parameters follow closely the optimal scenario if  $N \cdot \Delta y > \tau_{max}(\lambda)$  for both types of noise, the equally weighted variance converges also towards the optimal value.

In conclusion, this study provided an evaluation of the modulation matrix that can be obtained with our instrument and of the error characterizing the Stokes parameters when the noise is present. We saw that, theoretically, the system can be very close to an optimal one and the limits of precision were inferred.

Still, in a realistic scenario, the modulation in intensity provided by the modulator may drastically differ from the theoretical pattern used during our analysis here. The misalignment of the prisms, of the orientations of the fast axis, or the presence of manufacturing errors related to the size of angles or to the flatness of surfaces may strongly impact the form of the matrix  $W$ . Because of this, the study presented here must be doubled by experimental validation. Therefore, laboratory implementation will represent the next step of this research.

**Disclosures.** The authors declare no conflicts of interest.

**Data availability.** Data underlying the results presented in this paper are not publicly available at this time but may be obtained from the authors upon reasonable request.

## References

1. J. Hough, "Polarimetry: a powerful diagnostic tool in astronomy," *Astron Geophys.* **47**(3), 3.31–3.35 (2006).
2. S. Trippie, "Polarization and polarimetry: a review," *J. The Korean Astron. Soc.* **47**(1), 15–39 (2014).
3. J. Trujillo Bueno, E. Landi Degl'Innocenti, and L. Belluzzi, "The physics and diagnostic potential of ultraviolet spectropolarimetry," *Space Sci. Rev.* **210**(1-4), 183–226 (2017).
4. O. Dubovik, Z. Li, and M. I. Mishchenko, *et al.*, "Polarimetric remote sensing of atmospheric aerosols: Instruments, methodologies, results, and perspectives," *J. Quant. Spectrosc. Radiat. Transf.* **224**, 474–511 (2019).
5. N. Ghosh, "Tissue polarimetry: concepts, challenges, applications, and outlook," *J. Biomed. Opt.* **16**(11), 110801 (2011).
6. D. Ivanov, V. Dremim, A. Bykov, E. Borisova, T. Genova, A. Popov, R. Ossikovski, T. Novikova, and I. Meglinski, "Colon cancer detection by using Poincaré sphere and 2d polarimetric mapping of *ex vivo* colon samples," *J. Biophotonics* **13**(8), 1 (2020).
7. S. L. Jacques, J. C. Ramella-Roman, and K. Lee, "Imaging skin pathology with polarized light," *J. Biomed. Opt.* **7**(3), 329 (2002).
8. L. Tchvialeva, G. Dhadwal, H. Lui, S. Kalia, H. Zeng, D. I. McLean, and T. K. Lee, "Polarization speckle imaging as a potential technique for *in vivo* skin cancer detection," *J. Biomed. Opt.* **18**(6), 061211 (2012).
9. T. Novikova, A. Pierangelo, A. De Martino, A. Benali, and P. Validire, "Polarimetric imaging for cancer diagnosis and staging," *Opt. Photonics News* **23**(10), 26 (2012).
10. B. Vasilescu, Y. Nazè, and J. Loicq, "Solution uniqueness and noise impact in a static spectropolarimeter based on birefringent prisms for full Stokes parameter retrieval," *J. Astron. Telesc. Instrum. Syst.* **6**(02), 1 (2020).
11. W. Sparks, T. A. Germer, J. MacKenty, and F. Snik, "Compact and robust method for full Stokes spectropolarimetry," *Appl. Opt.* **51**(22), 5495–5511 (2012).
12. M. Pertenais, C. Neiner, P. Bernardi, J.-M. Reess, and P. Petit, "Static spectropolarimeter concept adapted to space conditions and wide spectrum constraints," *Appl. Opt.* **54**(24), 7377–7386 (2015).
13. J. C. del Toro Iniesta and M. Collados, "Optimum modulation and demodulation matrices for solar polarimetry," *Appl. Opt.* **39**(10), 1637 (2000).
14. J. Dai, F. Goudail, M. Boffety, and J. Gao, "Estimation precision of full polarimetric parameters in the presence of additive and Poisson noise," *Opt. Express* **26**(26), 34081 (2018).
15. M. R. Foreman and F. Goudail, "On the equivalence of optimization metrics in Stokes polarimetry," *Opt. Eng.* **58**(08), 1 (2019).



16. D. S. Sabatke, A. M. Locke, M. R. Descour, W. C. Sweatt, J. P. Garcia, E. L. Dereniak, S. A. Kemme, and G. S. Phipps, "Figures of merit for complete Stokes polarimeter optimization," in *Proc. SPIE 4133 Polarization Analysis, Measurement, and Remote Sensing III*, 15 November (2000).
17. D. S. Sabatke, M. R. Descour, E. L. Dereniak, W. C. Sweatt, S. A. Kemme, and G. S. Phipps, "Optimization of retardance for a complete Stokes polarimeter," *Opt. Lett.* **25**(11), 802 (2000).
18. J. C. del Toro Iniesta, *Introduction to Spectropolarimetry* (Cambridge University, 2004).
19. J. Stoer and R. Bulirsch, *Introduction to Numerical Analysis*, vol. 12 of *Texts in Applied Mathematics* (Springer New York, 2002).
20. F. Goudail, "Noise minimization and equalization for Stokes polarimeters in the presence of signal-dependent Poisson shot noise," *Opt. Lett.* **34**(5), 647 (2009).
21. F. Goudail, "Equalized estimation of Stokes parameters in the presence of Poisson noise for any number of polarization analysis states," *Opt. Lett.* **41**(24), 5772 (2016).
22. M. R. Foreman, A. Favaro, and A. Aiello, "Optimal Frames for Polarization State Reconstruction," *Phys. Rev. Lett.* **115**(26), 263901 (2015).
23. E. Cheney and D. Kincaid, *Numerical Mathematics and Computing*, International student edition (Cengage Learning, 2007).
24. A. Bénére, F. Goudail, M. Alouini, and D. Dolfi, "Degree of polarization estimation in the presence of nonuniform illumination and additive Gaussian noise," *J. Opt. Soc. Am. A* **25**(4), 919 (2008).
25. A. Peinado, A. Lizana, J. Vidal, C. Lemmi, and J. Campos, "Optimization and performance criteria of a Stokes polarimeter based on two variable retarders," *Opt. Express* **18**(10), 9815 (2010).

# 7

## OPTIMAL CONFIGURATIONS

*Not everything that can be counted counts and not everything that counts can be counted*

Albert Einstein

We discovered in the previous chapters that the method proposed here for the retrieval of polarization can sometimes embrace forms close to the optimal one from the point of view of the modulation matrix,  $W$ . We also proposed using this modulation matrix to retrieve the polarization of light instead of fitting the theoretical function of the intensity to the experimental data. This approach copes much better with a complex design in which the various parameters are hard to retrieve. In the second part of this work, we will see the experimental advantage of using the modulation matrix. Until then, the question that still must be answered is: what are the best choices, from the point of view of the apex angles of the prisms and orientations of the analyzer, to build an instrument using this modulator?

In chapter 5, it was underlined that certain orientations of the analyzer should be avoided. The orientation at  $45^\circ$  and  $135^\circ$  is forbidden if we intend to measure the entire Stokes vector. In addition, certain values of the apex angles are also characterized by a drop in efficiency. The most profound loss of efficiency manifests for equal values of the apex angles.

This chapter is intended to provide a global image of the impact of these three parameters (the two apex angles and the orientation of the analyzer) on the efficiency of the modulation scheme. This way, we can identify the values that should be used to manufacture the modulator and assemble the polarimeter.

## 7.1. IDENTIFYING THE OPTIMAL CONFIGURATIONS

The angles  $\xi$  and  $\psi$  of the two active prisms of the modulator (see Fig. 7.1) should be kept as small as possible to avoid the increase of the Fresnel terms and the effect of the split of rays with orthogonal polarizations.

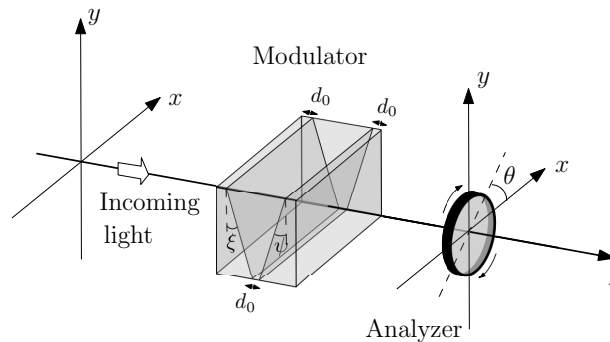


Figure 7.1: Optical setup composed of modulator and analyzer. The dimensions of the modulator are exaggerated to point out the angles  $\xi$  and  $\psi$ . The analyzer can be freely oriented, the transmission axis making an angle  $\theta$  with the  $x$ -axis.

Working with values below  $3^\circ$  for these angles ensures an angular separation of the rays emerging from the modulator below  $10^{-4}$  and a maximum separation of the emerging rays carrying orthogonal polarization states below  $1\mu\text{m}$  for a thickness on the edge  $d_0$  of about 0.5 mm. These values correspond to the scenario of the incoming light collimated and orthogonal to the entry face of the modulator. Therefore,  $3^\circ$  was established

as a superior limit of the apex angles for manufacturing the prisms.

Aside from the influence on the Fresnel terms and the split of rays, the angles of the two principal prisms of the modulator ( $\xi$ ,  $\psi$ ) also play an essential role in the quality of the modulation matrix (see Eq. (4.20), (5.6)) (Vasilescu et al., 2020). Alongside the two angles, the orientation of the analyzer,  $\theta$ , also strongly influences this matrix. We had already observed these effects in chapters 5 and 6 when we dealt with the efficiency of the modulation scheme, the condition number, and the equally weighted variance. Each of these figures of merit can be used to assess the modulation matrix as a function of these three angles ( $\xi$ ,  $\psi$ , and  $\theta$ ). We concentrated the attention here on the efficiency of the modulation scheme. We have tried to understand how this efficiency varies as a function of the three parameters. The purpose was to find in this way those values of the angles that lead to the highest efficiency and, consequently, allow the manufacturing of instruments with appropriate modulation schemes. Since we have three parameters that vary independently, building a global picture of efficiency can be challenging. To overcome this situation, we have conducted a series of simulations for various values of  $\theta$  and apex angles spanning the interval  $[1^\circ, 3^\circ]$ . Figure 7.2 reproduces some of the results obtained for three arbitrary orientations of the analyzer:  $10^\circ$ ,  $30^\circ$ , and  $60^\circ$ . The simulations revealed that the orientation of the analyzer has a limited impact on the system's total efficiency. The exceptions are, of course, observed when  $\theta$  is  $45^\circ$  or  $135^\circ$ . This quasi-constant behavior of the total efficiency to the orientation of the analyzer can be observed in Fig 7.2 (top). We notice here that the values of  $(\xi, \psi)$  characterized by the highest (or lowest) total efficiency are always almost identical. As it was proved before (see Chapter 5), values of the type  $\xi = \psi$ , or  $\psi = 2\xi$ , when  $\xi \leq 1.5^\circ$ , or  $\psi = 1/2\xi$ , when  $\xi \geq 2^\circ$  should be avoided, as they are characterized by a drop of efficiency for any orientation of the analyzer.

The detailed computation of the efficiencies for the Stokes parameters revealed in exchange that the orientation of the analyzer can play an essential role in the precision that we may have for each of the parameters. Therefore, in the same Figure 7.2, we observe that although the global behavior of the efficiency for each of the parameters follows the same pattern as the total efficiency, the maximum level is strongly affected by the orientation of the analyzer. Based on these observations, we can elaborate on a series of steps that can lead us to identify optimal configurations:

1. Choose an arbitrary orientation of the analyzer:  $\theta \neq (45^\circ, 135^\circ)$ .
2. Map the efficiencies as a function of the possible values of the apex angles:  $(\xi, \psi) \in [1^\circ, 3^\circ]$ .
3. Select a couple  $(\xi, \psi)$  from the region of maximum efficiency.
4. For the selected couple  $(\xi, \psi)$  verify the variation of efficiency with  $\theta$ , the orientation of the analyzer.
5. Point out configurations  $(\xi, \psi, \theta)$  with the highest efficiency.

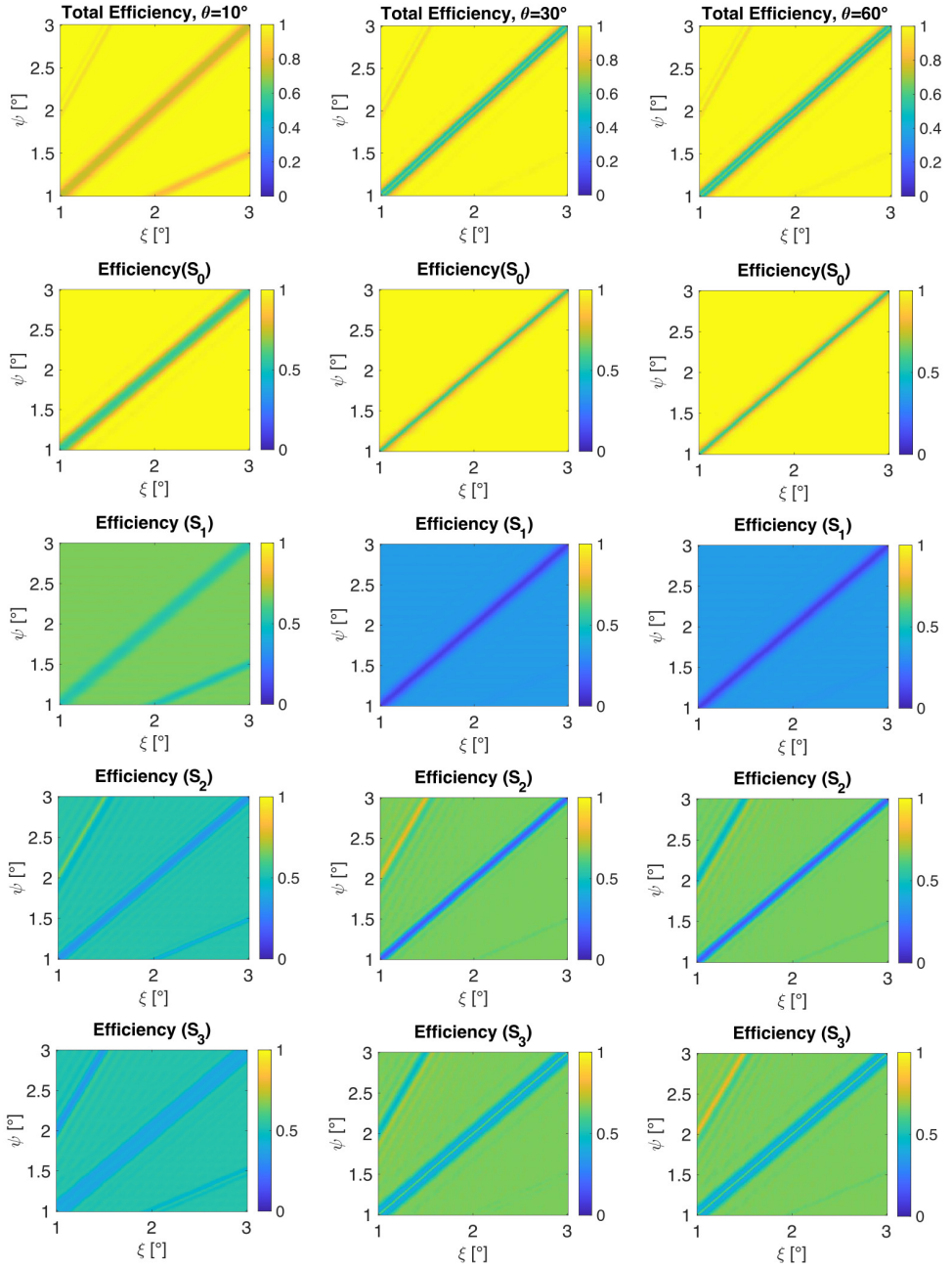


Figure 7.2: Efficiencies of the modulation scheme when the analyzer is oriented at  $10^\circ$ ,  $30^\circ$ , and  $60^\circ$ . The first three plots from the top display the total efficiency, whereas the following rows show the corresponding efficiencies for  $S_0$ ,  $S_1$ ,  $S_2$ , and  $S_3$  parameters.

An example of a couple of angles characterized by high efficiency is ( $\xi = 2.6^\circ$ ,  $\psi = 1.8^\circ$ ), pointed out with a red cross in Fig. 7.3 (left).

However, this is just a random example. Many others can be chosen from the regions of maximum efficiency. The maximum reachable efficiency corresponding to the Stokes parameters for such a couple will depend on the orientation of the analyzer. Figure 7.3 (right) shows the value of these efficiencies when the orientation of the analyzer varies between  $0^\circ$  and  $180^\circ$ .

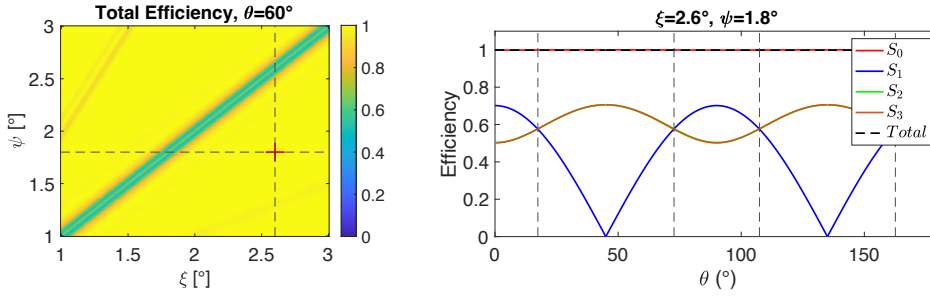


Figure 7.3: Efficiency on the Stokes parameters and total efficiency as a function of the orientation of the analyzer,  $\theta$ , for  $\xi = 2.6^\circ$ , and  $\psi = 1.8^\circ$ .

We discover again that  $45^\circ$  and  $135^\circ$  should be avoided because of the indetermination of  $S_1$  for these orientations. In addition, we find from Fig. 7.3 that, no matter the orientation of the analyzer,  $S_2$  and  $S_3$  will always be characterized by almost the same efficiencies. The points of intersections of the three curves, underlined with the help of the vertical dashed lines, are regions of equal efficiency. The values recorded here are approximately  $1/\sqrt{3}$ , the highest reachable value corresponding to optimal modulation schemes (del Toro Iniesta, 2003). These equal and maximum efficiencies are located at  $17.4^\circ$ ,  $73^\circ$ ,  $107.4^\circ$ , and  $162.6^\circ$ .

Figure 7.4 shows the values of efficiency corresponding to different pairs of angles  $\xi$  and  $\psi$ . We observe that as long as the values are chosen from the region of maximum total efficiency, the effect of the analyzer is the same. However, once we leave this area (see the case  $\xi = 1.3^\circ$  and  $\psi = 2.6^\circ$ ), the behavior of efficiency changes. We no longer have points of equal value.

In conclusion, this spectropolarimetry method is compatible with multiple optimal modulation schemes. The apex angles of prisms 1 and 3, which facilitate such schemes, are those characterized by the highest total efficiency, no matter the orientation of the analyzer. For a given total efficiency, with the help of the analyzer, we can, in the best scenario, find orientations that simultaneously maximize the precision of the extraction of all the Stokes parameters.

The same type of analysis as the previous one can be conducted using the modulation scheme's condition number ( $CN$ ) (Vasilescu et al., 2023). The results are similar in many aspects. Using this metric, we see again (Fig. 7.5) that a configuration with  $\xi = 2.6^\circ$ ,  $\psi = 1.8^\circ$ , and  $\theta = 73^\circ$  is characterized by a condition number close to the optimal value ( $\sqrt{20}$ ) (del Toro Iniesta and Collados, 2000).

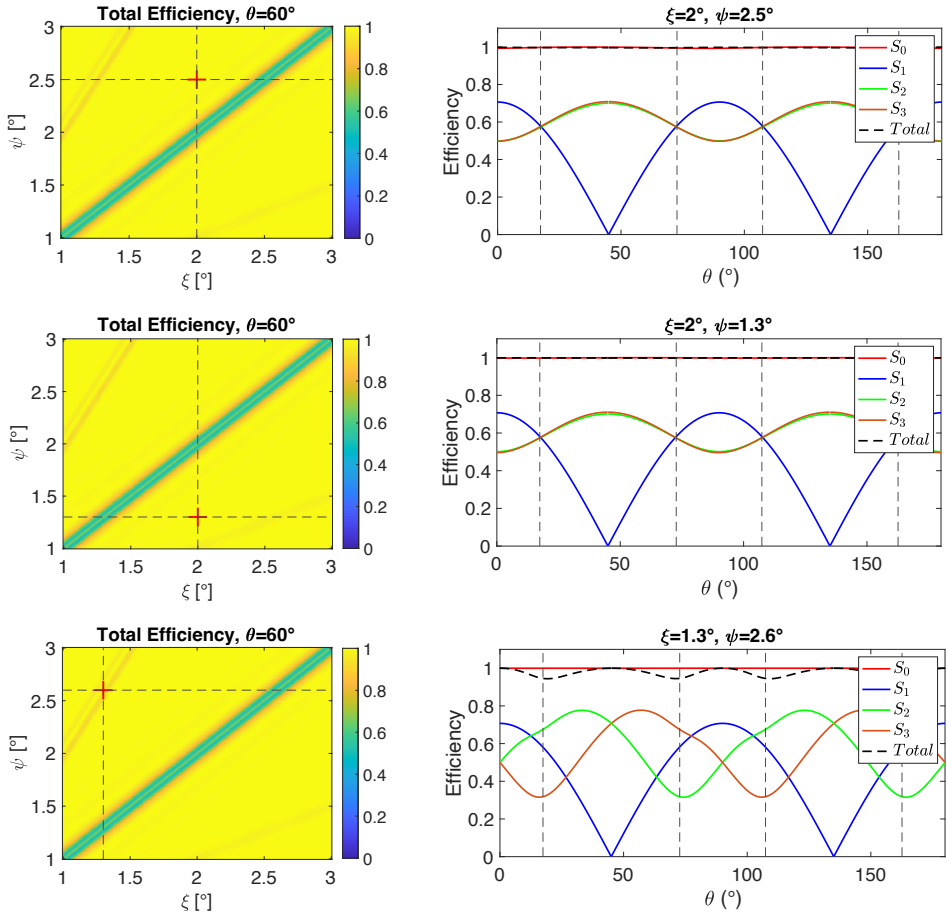


Figure 7.4: Efficiency on the Stokes parameters for three different pairs of angles  $\xi$  and  $\psi$ . The total efficiency was computed for an analyzer oriented at  $60^\circ$ .

7

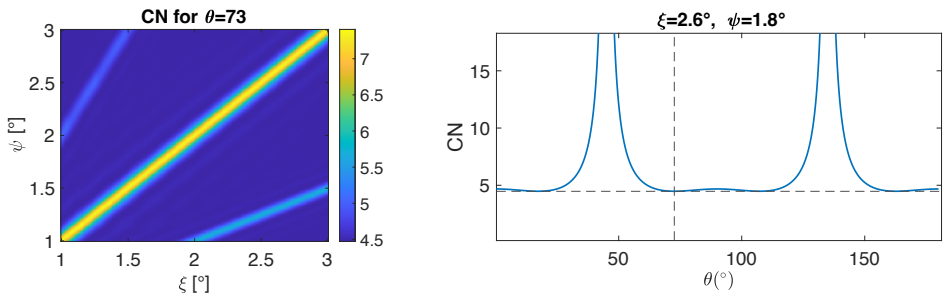


Figure 7.5: Condition number of the modulation scheme for different values of the apex angles (left), and for orientations of the analyzer between  $0^\circ$  and  $180^\circ$ . The vertical dashed line indicates the orientation of  $73^\circ$  of the analyzer, corresponding to a minimum of  $CN$ .

Based on this analysis, we chose for the fabrication of the modulator the values  $\xi = 2.6^\circ$  and  $\psi = 1.8^\circ$ . These angles generate one of the highest efficiencies when the analyzer is oriented at one of the four mentioned values. In addition, according to Fig. 7.2, this couple of angles is located in a region that allows large tolerances.

## 7.2. CONCLUSIONS

The spectropolarimetric method analyzed in this research can be implemented in various ways. The modulator, composed of three birefringent prisms, can present countless combinations of the apex angles, and the analyzer, also part of the polarimeter, can be turned freely in any position. However, we proved within this chapter that specific values of the apex angles and orientations of the analyzer should be avoided. Therefore, the analyzer should not be placed at  $45^\circ$  or  $135^\circ$ , and the apex angles should satisfy the following constraints:

- $\xi \leq 3^\circ$
- $\psi \leq 3^\circ$
- $\psi \neq \xi$
- $\psi \neq 2\xi$ , when  $\xi \leq 1.5^\circ$
- $\psi \neq \frac{1}{2}\xi$ , when  $\xi \geq 2^\circ$

Because the total efficiency was revealed to be less influenced by the orientation of the analyzer, the values of the apex angles for the manufacturing of the modulator should be chosen from the region of maximum total efficiency satisfying the previous conditions. Furthermore, the orientation of the analyzer should be searched afterward so that the efficiencies corresponding to the Stokes parameters can be maximized. We have chosen for the manufacturing of the modulator the values  $\xi = 2.6^\circ$  and  $\psi = 1.8^\circ$ . In addition, the analyzer's orientation of  $73^\circ$  was preferred during the experimental part.





# BIBLIOGRAPHY

- del Toro Iniesta, J. C. (2003). *Introduction to spectropolarimetry*. Cambridge University Press.
- del Toro Iniesta, J. C., & Collados, M. (2000). Optimum modulation and demodulation matrices for solar polarimetry. *Applied Optics*, 39(10), 1637. <https://doi.org/10.1364/AO.39.001637>
- Vasilescu, B., Nazè, Y., & Loicq, J. (2020). Solution uniqueness and noise impact in a static spectropolarimeter based on birefringent prisms for full stokes parameter retrieval. *Journal of Astronomical Telescopes, Instruments, and Systems*, 6(2), 1. <https://doi.org/10.1117/1.JATIS.6.2.028001>
- Vasilescu, B., Piron, P., & Loicq, J. (2023). Performance analysis of a spectropolarimeter employing a continuous phase variation. *Optics Express*, 31(13), 21078. <https://doi.org/10.1364/OE.487335>



# 8

## PRELIMINARY CONFIRMATION OF THE CONCEPT

*Whenever a theory appears to you as the only possible one, take this as a sign that you have neither understood the theory nor the problem which it was intended to solve.*

Karl Popper

The simulations carried out up to this point in our research were based on a MATLAB model of the polarimeter, which we built step by step according to the questions raised along the way. This model permanently used a series of approximations and neglected the impact of certain terms or phenomena, such as the Fresnel terms, the separation of rays when passing through prisms, or the effect of the intermediate prism on the modulation.

A more realistic check, which considers all these aspects ignored throughout our analyses, is a necessary step before the practical implementation of this concept.

We carried out this verification with TNO, with which we established a strong collaboration in order to implement our spectropolarimeter model in an instrument designed to detect the polarimetric signature of satellites in orbit around the Earth.

TNO noticed an important potential in the model we studied. The compactness of the model, its simplicity, and, above all, the ability to detect any polarization in a single shot with a reduced impact of noise and errors seemed to meet the criteria sought by TNO perfectly.

We then started a preliminary confirmation work of the spectropolarimeter. TNO built the same modulator design with OpticStudio (Zemax), an optical design and analysis software capable of working with polarimetric aspects. This software uses a sequential ray tracing model, meaning each light ray hits the pre-defined surfaces only once.

Many details can be verified through such a comparison. However, our main objective was to confirm the intensity modulation pattern for different types of polarization.

### 8.1. COMPATIBILITY OF THE MODELS

The first series of simulations considered a simple design composed of a point source, a collimator, followed by the modulator, a linear polarizer, and the detector, as we can see in Fig. 8.1.

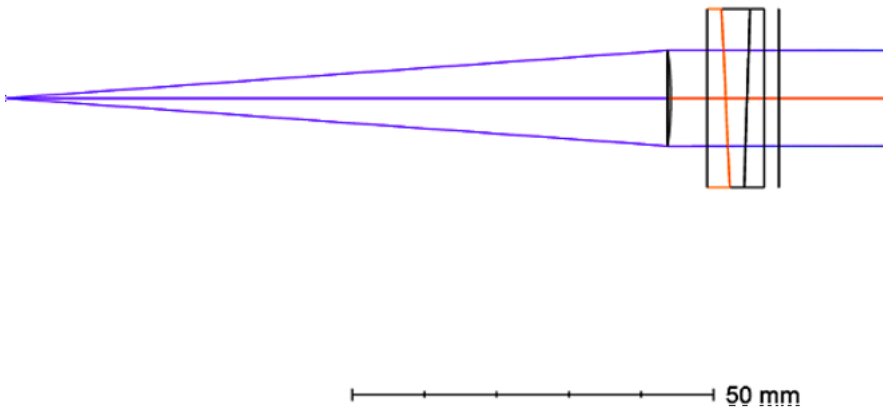


Figure 8.1: Instrument design for the check-up simulations. ©TNO

The purpose was to see if the same incoming polarization state corresponds to a similar intensity pattern in the detector plane when the same geometry is used to build the modulator, the analyzer has the same orientation, and the signal is sampled with the same pixel size.

Overall,  $10^8$  rays were generated in Zemax in a system with a numerical aperture  $NA = 0.07$ . The illuminated area at the level of the modulator was  $10 \times 10$  mm, and the detector had  $250 \times 250$  pixels.

Only the cases of total linear ( $0^\circ$ ,  $45^\circ$ ) and circular polarizations were investigated at this step, as the purpose was only to point out eventual fundamental differences. The central field was used for the simulations, and the arbitrary wavelength of  $0.35 \mu m$  was considered. The noise was ignored entirely in the Zemax construction, whereas in our model, an  $SNR = 1000$  was used to suppress the effect of noise (see Eq. (4.21)).

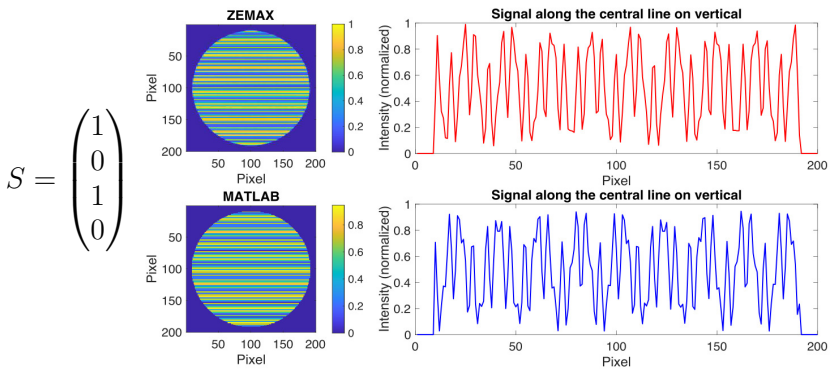
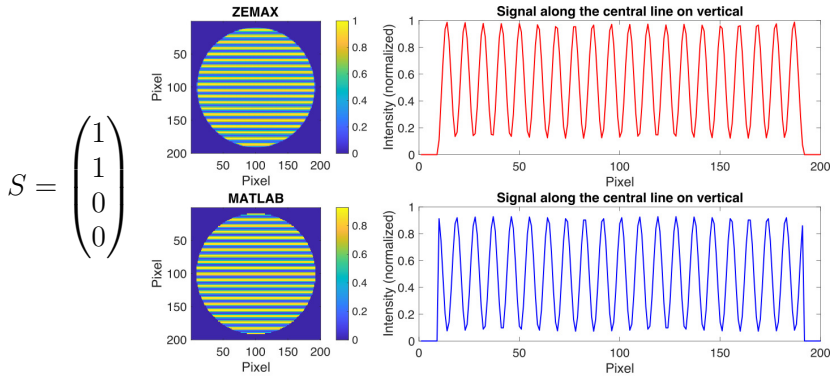
All three studied cases (linear  $0^\circ$ , linear  $45^\circ$ , and circular) show that a similar intensity pattern is obtained with both calculus instruments (see Fig. 8.2).

The slight differences manifested as small irregularities in the Zemax intensity profile are due to the limited number of rays and their distribution. In this simulation, Zemax generated approximately one ray/ $\mu m^2$ . We used a numerical integral over the pixel size ( $40 \times 40 \mu m$ ) to obtain the intensity value corresponding to a single pixel. Therefore, the signal read from a pixel in Zemax was obtained after a numerical integration of 40 values read along the vertical direction. On the contrary, the signal obtained with our model uses the definite integration of the functions  $m$ ,  $n$ , and  $p$  (see Eq. (4.20)) over the pixel height.

However, when studied in detail, the two simulations reveal the existence of other differences. These are related to the manifestation of a shift between the two intensity patterns. This fact is illustrated in Fig. 8.3, for two incoming polarizations, circular right and  $45^\circ$ , and it also manifests for other states. When superposing the two intensity profiles, we observe that in the same positions in the vertical direction, we record different intensity values. Keeping the pattern obtained with MATLAB fixed, we searched to see if a good match of the profiles could still be obtained by moving left or right the Zemax profile. This match is still possible and is periodic. It is enough to shift the Zemax pattern with several pixels left or right to have a good superposition of the two profiles.

For the two polarization states studied here, a shift of 47 pixels (for the circular state) and 56 pixels (for the linear state) was necessary to reduce, at minimum, the difference between the two patterns. We assume that the source of this difference is the deviation of rays due to the tilted surfaces inside the modulator. This effect was neglected in our model as it was proved to result in only a shift of the image and not an alteration of the modulation.

In conclusion, the Zemax check confirmed our MATLAB model. The same pattern of intensity was retrieved for the chosen sets of polarizations and the same parameters of the optical system. This confirmation supported the passage to the next step of our project: manufacturing the modulator and experimental implementation.



8

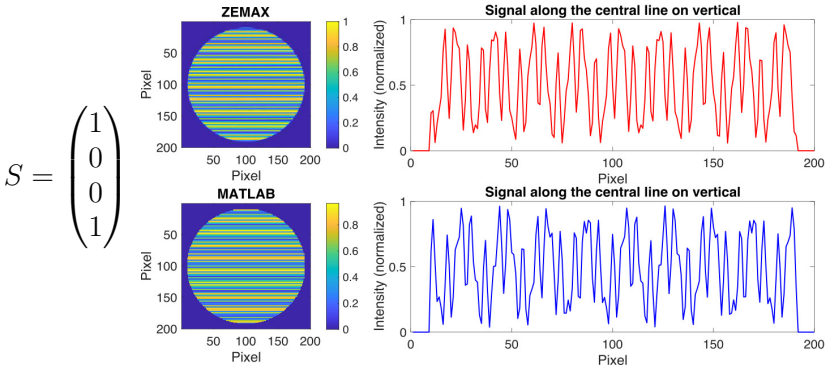


Figure 8.2: Intensity profiles obtained with Zemax and MATLAB for three different incoming Stokes vectors.

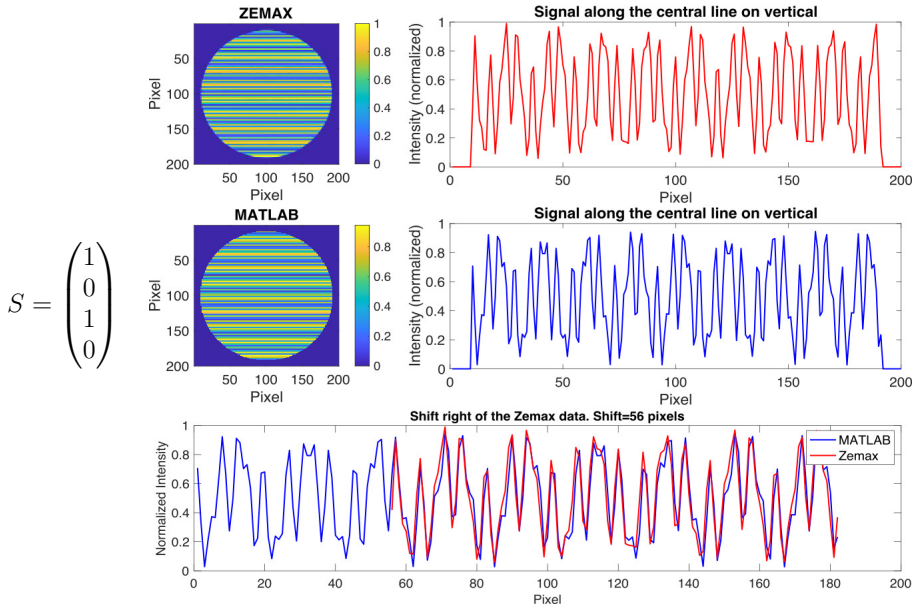
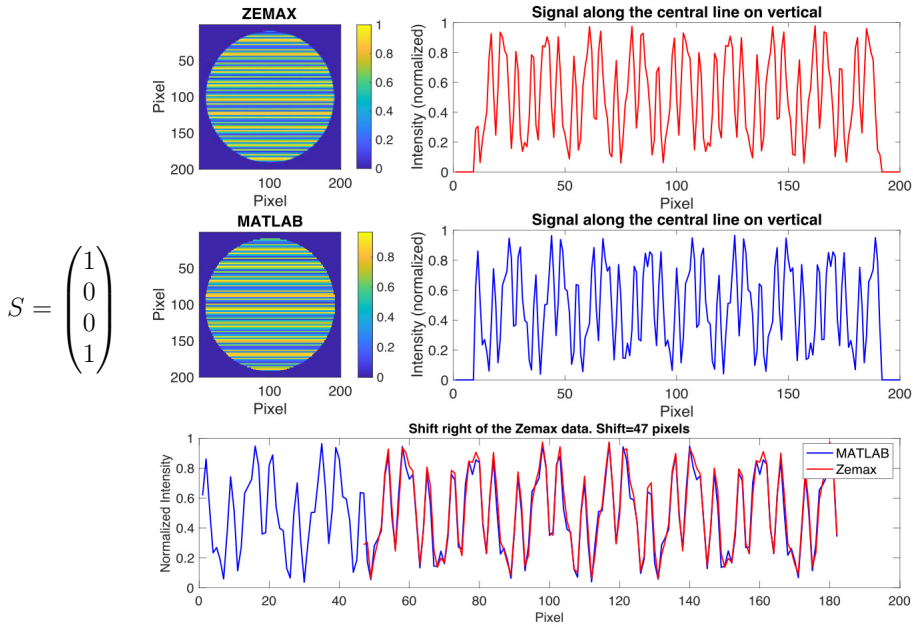


Figure 8.3: Intensity pattern obtained with Zemax and MATLAB for circular and linear polarization. Possible shifts that reduce the difference between the two intensity patterns are pointed out.



## 8.2. CASE STUDY: THE IDENTIFICATION OF SPACE OBJECTS

Spectropolarimetry is a good candidate for space object identification and characterization. Among these objects, the geostationary satellites are particularly interesting, both for space awareness programs and military applications (Bartels et al., 2022; Snel et al., 2023; Vasile et al., 2023). Theoretical and practical investigations have proved that, aside from a spectral fingerprint, the objects in orbit around the Earth are also characterized by a polarimetric signature, originating in the Fresnel reflection of light on their surface. Retrieving these spectral and polarimetric signatures increases the characterization's precision.

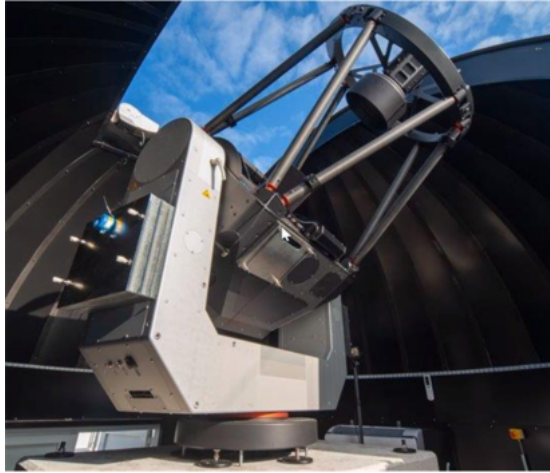


Figure 8.4: TNO's telescope from Amsterdam, of 80 cm diameter. ©TNO

### 8

The physical phenomenon underlying this application of spectropolarimetry is the multiple scattering of the light coming from the Sun by the covering material of the satellite. The light coming from the Sun is not polarized. However, the light reflected by satellites is polarized by a certain amount, depending on the phase angle, the wavelength, the material of the reflecting surface, and the number of reflections, following the Fresnel equations. Because multiple reflections could occur at the satellite level and between the satellite and the detector, the spectropolarimetric characterization and identification is mostly an empirical approach.

Figure 8.5 displays the simulated Stokes components for two types of alloys (aluminum + silicon (Al+Si), silicon + silicon (Si+ Si)) on a spectral band between 300 nm and 1000 nm. A double reflection was considered to obtain these results, with an incidence angle of  $50^\circ$ . Depending on the wavelength, we notice that the Al+Si compound may exhibit a degree of polarization between 11% and 41%, whereas Si+Si shows a degree of polarization between 18% and 56%. The possibility of discriminating between different types of polarization is of paramount importance. The polarimetric difference between the two alloys is that Al+Si reflects a stronger circular component, whereas Si+Si has a strong linear horizontal component.

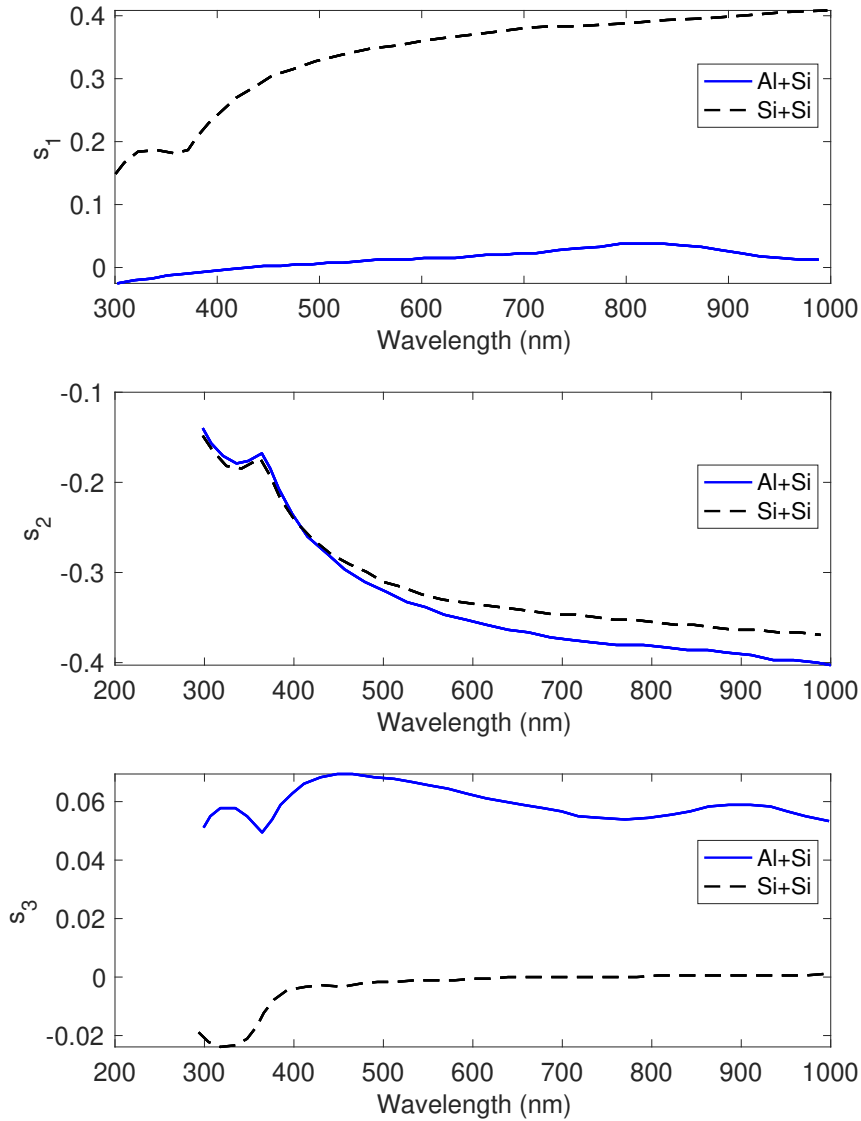


Figure 8.5: Spectropolarimetric fingerprint after double reflection for two types of alloys. The top plot displays the normalized  $s_1$  parameter of the Stokes vector. The middle plot refers to  $45^\circ$  and  $135^\circ$  polarization ( $s_2$ ), while the bottom plot shows the parameters of circular polarization ( $s_3$ ). Source of data: TNO

Considering that this polarization corresponds to a geostationary satellite, the flux

received by an 80 cm telescope on the ground (see Fig. 8.4) can be estimated. Figure 8.6 discloses this flux based on the presumption of a magnitude nine object. The curve was obtained by TNO with the help of Planck's radiation law and paying attention to the atmosphere's absorption. This curve suggests detecting 6 to 35 photons per second per nm. When using a spectral resolution of 50 nm and an integration time of 30 s, we have between 10000 and 50000 photons per spectral element.

Starting from the data presented in Fig. 8.5 and 8.6, we conducted a simulation to determine whether the instrument studied here can detect this target.

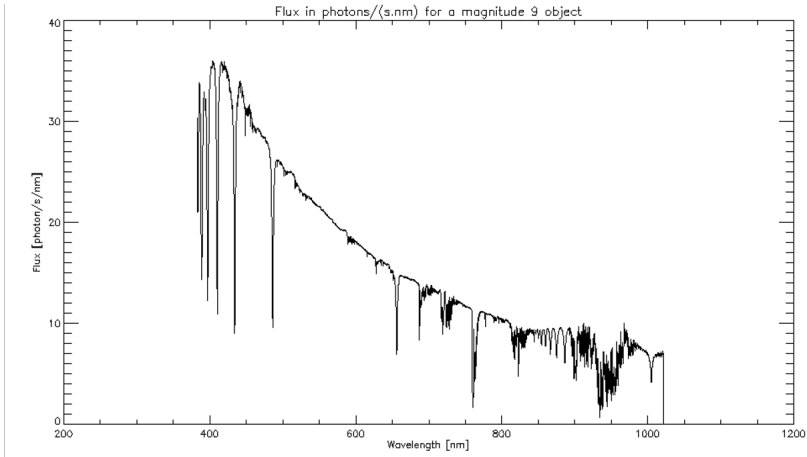


Figure 8.6: Flux of photons coming from a geostationary satellite. ©TNO

Therefore, based on the flux data and polarimetric expectations, we built a model of the point source target. We used the case of Al+ Si as input for the conceptual instrument (see Fig. 8.7 ), and we built the modulation of this signal for several configurations of the optical instrument. The spectropolarimetric data used in the exercise, extracted from the curves from Fig. 8.5, is presented in the following table (8.1).

Al+Si			
$\lambda(nm)$	$s_1$	$s_2$	$s_3$
425	0.00736	-0.2727	0.0677
475	0.01175	-0.3112	0.0688
525	0.01525	-0.3350	0.0668
575	0.0187	-0.3459	0.0639

Table 8.1: Approximated value of the Stokes parameters corresponding to Al+Si alloy.

The main parameters used to simulate the reception of this signal were the wavelength, the spectral resolution, the integration time, and SNR. The ability to retrieve such polarimetric features depends on the number of photons. Our concept of the instrument works based on the modulation in the vertical direction of light intensity. Therefore, if the number of photons is too low, the visibility of the modulation decreases, and conse-

quently, the error on the retrieved Stokes increases. We can observe this phenomenon in Fig. 8.8.

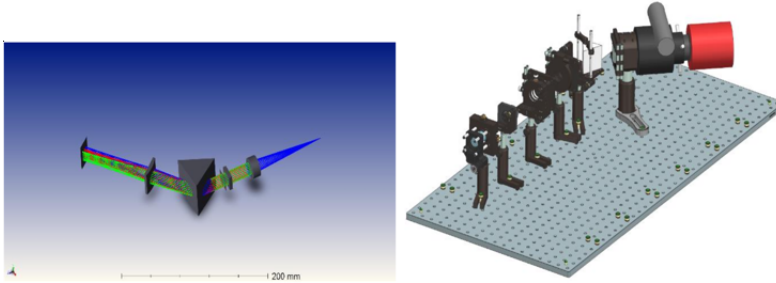


Figure 8.7: The instrument's optical design as TNO conceived it. The left image presents the Zemax construction, with the light coming from the right side, whereas the right panel shows the mechanical integration of the spectropolarimeter. Here, the light arrives from the left and passes first through a slit. Then, the light passes through a collimator, the modulator, and a linear polarizer (the analyzer). After the analyzer, the light is diffracted by a prism, and the different wavelengths are focused along the lines of the camera (the red cylinder) pixels with the help of a cylindrical lens. In the plane of the detector, the horizontal direction will give spectral information, whereas in the vertical direction, the modulation determined by the polarization should become accessible. ©TNO

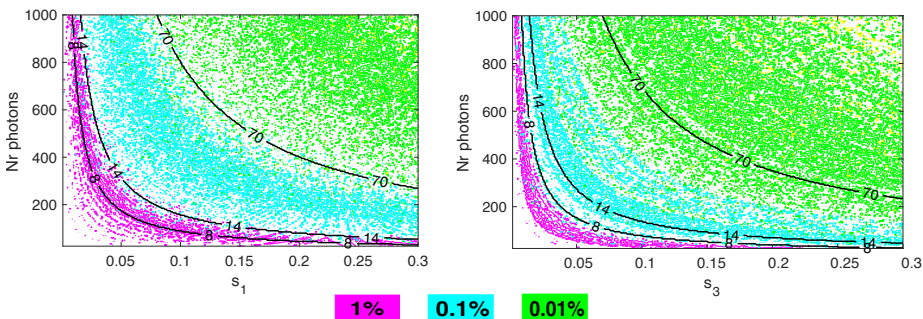


Figure 8.8: Errors on the Stokes parameters as a function of the number of photons per pixel. The black curves represent isocurves with the same  $\Delta n_{photons} = n_{max} - n_{min}$ , where  $n_{max}$  and  $n_{min}$  are maximum, respective minimum number of photons retrieved from the modulation of intensity. We observe how increasing  $\Delta n_{photons}$  decreases the error on the retrieved Stokes parameters. This simulation was conducted for a single wavelength,  $\lambda = 525nm$ . The results for  $s_2$  are very close to those for  $s_3$ .

For an arbitrary wavelength  $\lambda = 525 nm$ , we have mapped here the relative error on the Stokes parameters as a function of the number of photons received per spectral element, per pixel, and the polarization of the signal.

To achieve an error below 1% in determining the linear horizontal or vertical polarization coming from Al+ Si alloy, we must collect more than 1000 photons per pixel at an  $SNR = 100$ , and the integration time must be adjusted accordingly. The pixel size for these simulations was  $3.45\mu m$ , corresponding to the actual detector used in the experimental part of our research. Because most of the light reflected by Al+Si compounds carries 135° and circular polarization features, retrieving these polarization types will

require fewer photons. With only 100 photons, we can achieve an error below 1% this time.

As underlined before, the spectral resolution can also play an essential role in determining polarization. We took the same example of Al+Si reflection to understand the extent of this impact. Again, we considered that the pixel size is  $3.45\ \mu\text{m}$ , whereas the integration time could be adjusted between 1 s and 290 s.

We demodulated then the constructed signal built with an  $\text{SNR} = 100$  by considering various values of  $\Delta\lambda$  for a central wavelength between 400 and 800 nm. Several results are displayed in Fig. 8.9.

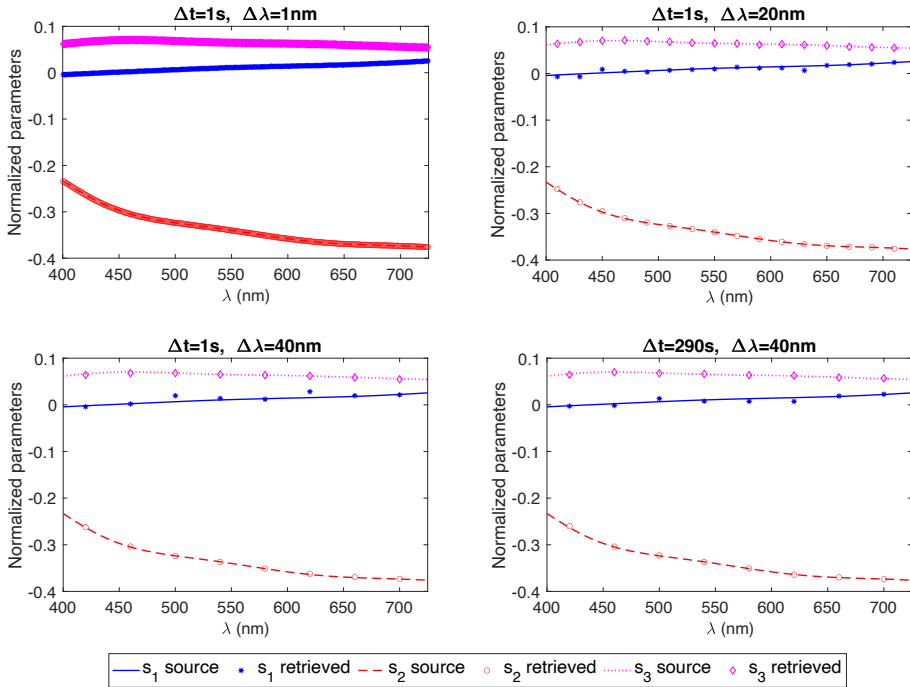


Figure 8.9: Simulation of the detected signal for various spectral resolutions and integration times. A constant  $\text{SNR}=100$  was considered.

Again, a relatively good assessment of the polarization of the observed target can be made. Our instrument could be capable of measuring the polarization of such a target. Of course, this is an ideal scenario. The errors of such measurements, or the polarimetric sensitivity of the instrument, will depend on the optical characteristics of the manufactured product.

### 8.3. CONCLUSIONS

We conducted a last investigation here to prepare for the manufacturing of the modulator and the laboratory verification of the studied polarimeter model. Together with TNO, who joined us in the efforts to transform this idea into an instrument, we compared the

results obtained with our mathematical model of spectropolarimeter with the results obtained by TNO with the same model built in Zemax. This comparison was restrained to the shape of the intensity pattern for different incoming polarizations. Overall, we obtained almost the same shapes for the considered polarizations.

Furthermore, with our model, we simulated detecting a polarimetric target (a satellite on a geostationary orbit) to see if such an instrument can answer the demands of TNO. Again, this model proved to be a good candidate for such a task. In the end, we can say that we have gathered enough proof to pass to the next stage of our investigation: the laboratory implementation.



## BIBLIOGRAPHY

- Bartels, N., Allenspacher, P., Hampf, D., Heidenreich, B., Keil, D., Schafer, E., & Riede, W. (2022). Space object identification via polarimetric satellite laser ranging. *Communications Engineering*, 1(1), 5. <https://doi.org/10.1038/s44172-022-00003-w>
- Snel, R. C., Vasilescu, B., Di Iorio, E., Piron, P., Loicq, J., Ferrario, I., & Silvestri, F. (2023, October 23). Spectropolarimetry for space object identification. In D. L. Hickman, H. Bürsing, O. Steinvall, & G. W. Kamerman (Eds.), *Electro-optical and infrared systems: Technology and applications XX* (p. 36). SPIE.
- Vasile, M., Walker, L., Campbell, A., Marto, S., Murray, P., Marshall, S., & Savitski, V. (2023, August 14). Space object identification and classification from hyperspectral material analysis. Retrieved September 22, 2023, from <http://arxiv.org/abs/2308.07481>





# II

## PART II



# 9

## INSTRUMENTAL SETUP AND FIRST LIGHT

*Chaos is merely order waiting to be deciphered.*

José Saramago

## 9.1. FABRICATION OF THE MODULATOR

The second part of this thesis is dedicated to the experimental validation of the modulator previously described. For this purpose, two specimens of the modulators were fabricated in  $\text{MgF}_2$  with the help of the Eksma Optics company and TNO (see Fig. 9.2, 9.3). In addition, the three prisms forming the modulator were purchased separately for a detailed study. The manufacturing requirements, together with the tolerances and schematics of the design, are presented in Table 9.1 and Fig. 9.1. The choices for the angles of the prisms, the orientation of the fast axis in each section, the dimensions, and the material were based on the previous analysis. The provided tolerances were carefully chosen to minimize the consequences of the misalignment or other fabrication defects. In addition, the thickness on the edge,  $d$ , was chosen to enhance the mechanical robustness and reduce the manipulation risks.

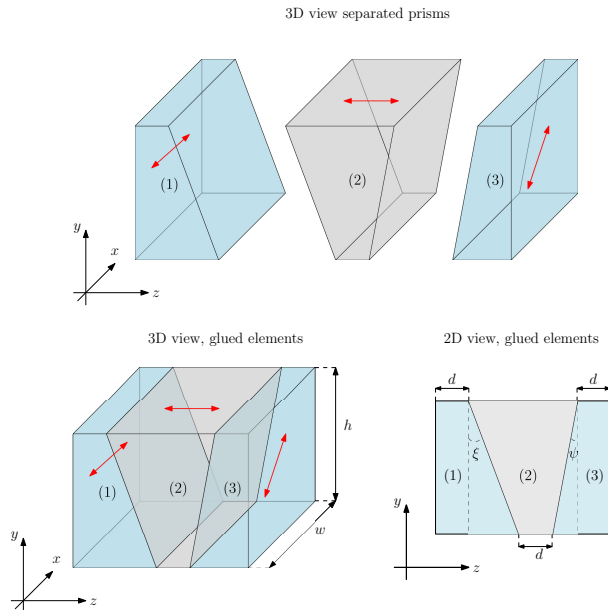


Figure 9.1: Modulator design for manufacturing. The double red arrows indicate the orientation of the optical axes in each component prism. Accepted dimensions and tolerances are shown in Tab. 9.1.

Fast-axis orientation ( $^\circ$ )	Sizes ( $mm$ )	Apex angle ( $^\circ$ )
Prism (1): along $x \pm 0.1^\circ$ in $(xy)$ plane	Thickness: $d = 1 \pm 0.5$	$\xi = 2.6^\circ \pm 0.2^\circ$
Prism (2): along $z \pm 0.1^\circ$ in $(xz)$ plane	Height: $h = 20 \pm 0.5$	
Prism (3): at $45 \pm 0.1^\circ$ in $(xy)$ plane	Width: $w = 20 \pm 0.5$	$\psi = 1.8^\circ \pm 0.2^\circ$

Table 9.1: Optical requirements addressed to the manufacturer for the fabrication of a modulator in  $\text{MgF}_2$ . The notations and orientations are those from Fig. 9.1.

The modulator manufactured by Eksma Optics is represented in Fig. 9.2 and 9.3.

Upon careful inspection of the images, one can notice the presence of the three prisms of the optical model, with the orientation of the optical axis of each component indicated in blue.

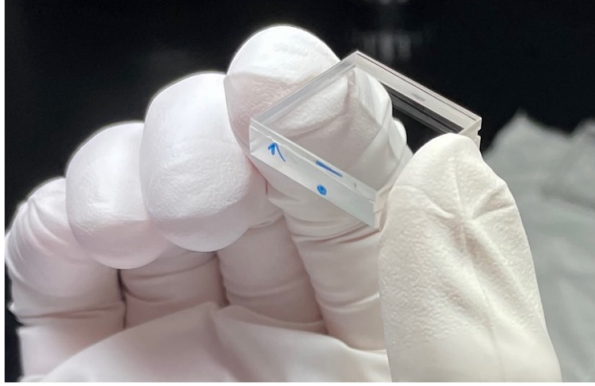


Figure 9.2: The modulator fabricated by Eksma Optics. The blue marks indicate the orientation of the fast axes inside each prism.

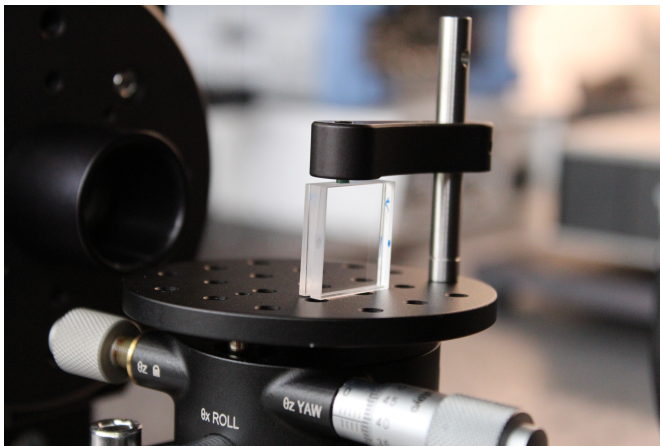


Figure 9.3: Detailed view of the modulator on the optical bench

As it can be observed from Fig. 9.2 and 9.3, the delivered specimens of the modulator present visible deviations from the requirements. The lateral faces of the prisms are not aligned in the same plane. The microscopic investigation highlights this (see Fig. 9.4).

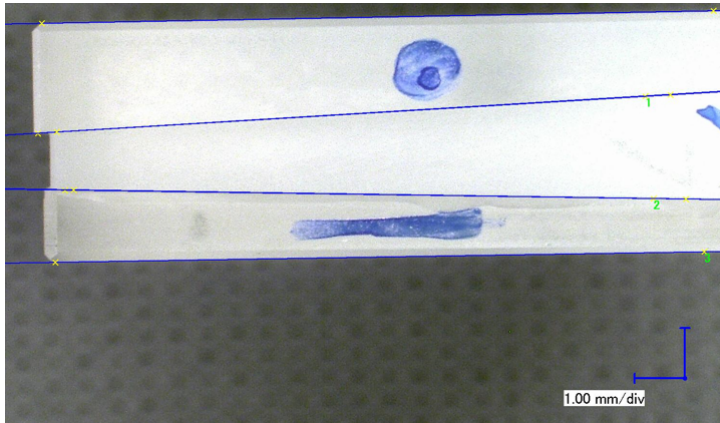


Figure 9.4: Microscopic view of the modulator. Source: TNO

However, the apex angles of the wedges correspond to the requirements. The measurements done with the help of the microscopic investigation shows the next set of values (Tab. 9.2):

Specimen 1			Specimen 2		
	$\xi$ (°)	$\psi$ (°)		$\xi$ (°)	$\psi$ (°)
Face 1	2.4	1.8	Face 1	2.5	1.7
Face 2	2.4	1.8	Face 2	2.6	1.7

Table 9.2: Measured apex angles for the two specimens of the modulator. The measurements were conducted on the face with the blue marks (see Fig. 9.4), and on the opposite face.

Consequently, the irregularities observed on the side faces are most likely due to a relative rotation of the prisms. This rotation may result in an angle between the fast axes of prisms (1) and (3) different from  $45^\circ$ . From the point of view of the modulation of the polarimetric signal, this is not a problem because the third prism should ensure a modulation of the linear horizontal and vertical polarization passing unaltered through prism 1. Or this modulation can happen for any orientation of the fast axis of the prism 3, which is different from  $0^\circ$ . However, the efficiency of the modulation scheme and the rest of the parameters of performance already computed will be affected. Another consequence of the prisms' relative rotation could be that the entry and exit faces are no longer parallel. This can lead to stronger internal reflections and a deviation of the rays from the  $z$ -axis.

Moreover, we conducted a preliminary check of the modulator before performing any precise optical setup alignment and proper components analysis. It was a raw experiment meant to provide a first confirmation or refutation of what was previously discussed in this thesis. A linearly polarized and collimated beam, with a wavelength of

535 nm, was projected through a modulator+linear polarizer assembly. According to the simulations presented in the previous chapters, this must generate a vertical modulation of the light, regardless of the incident linear polarization angle. Even though this first optical setup was quickly improvised, without proper alignment and measures to reduce the external noise, the intensity modulation was evident as the light of the day. It was a great confirmation of our theoretical endeavor (see Figures 9.5 - 9.9).

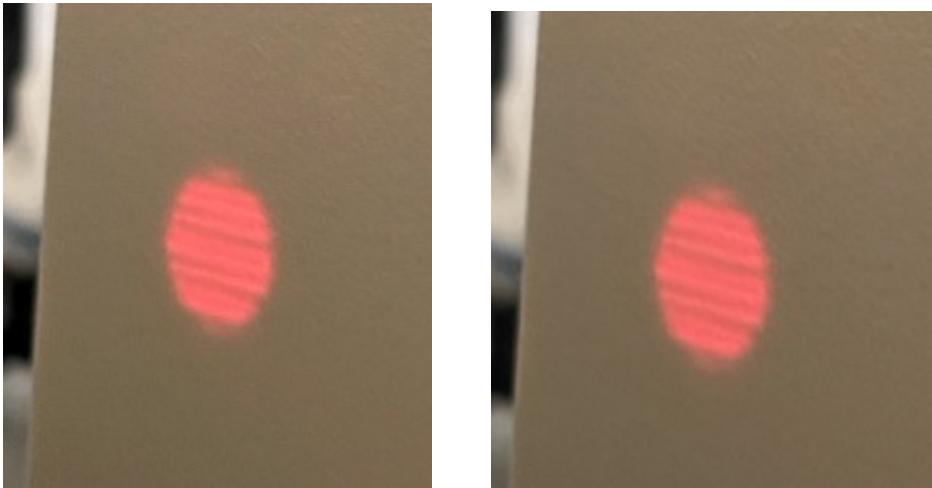


Figure 9.5: First light of our instrument. Light modulation in the vertical direction is visible on the screen for the two arbitrary states of linear polarization used as input.

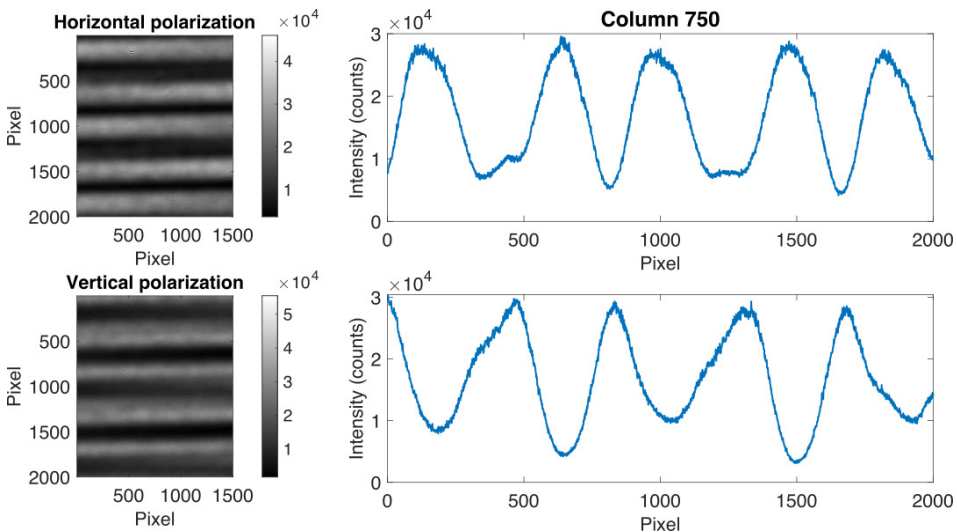


Figure 9.6: Examples of modulations obtained when the incoming light was linearly polarized horizontally (top) and vertically (bottom). On the right, the signal variation over a column of 2000 pixels is presented.



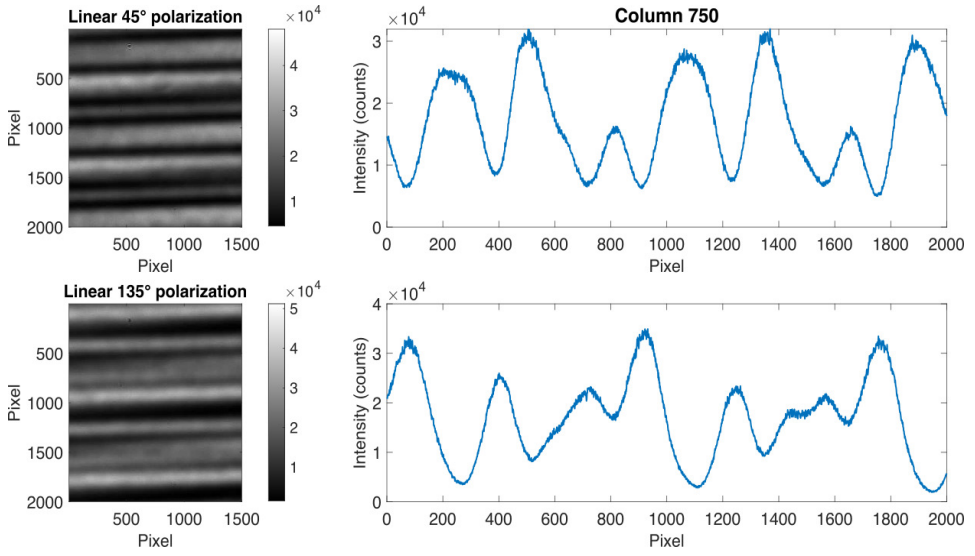


Figure 9.7: Examples of modulations obtained when the incoming light was linearly polarized at 45° (top) and 135° (bottom).

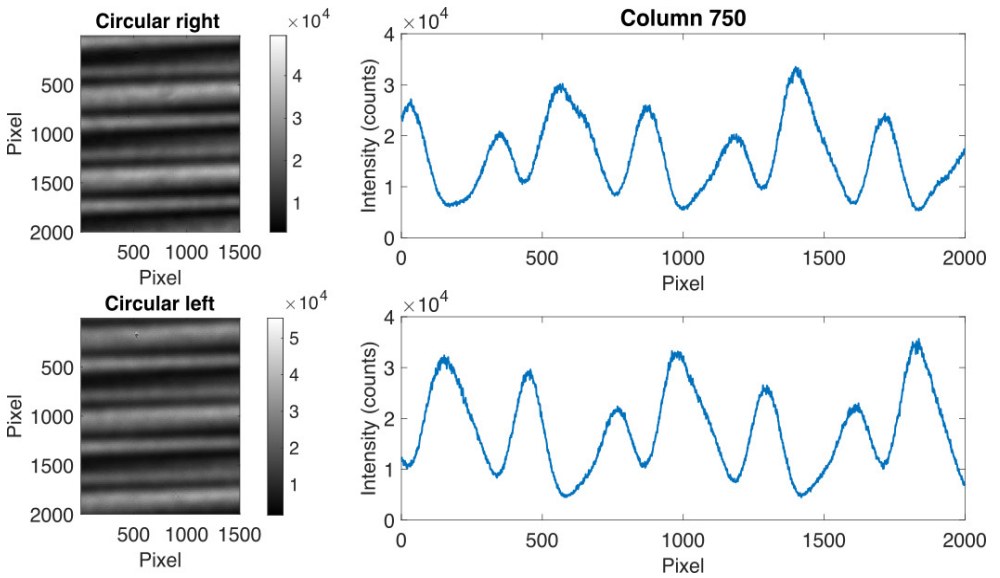


Figure 9.8: Examples of modulations obtained when the incoming light was circularly polarized.

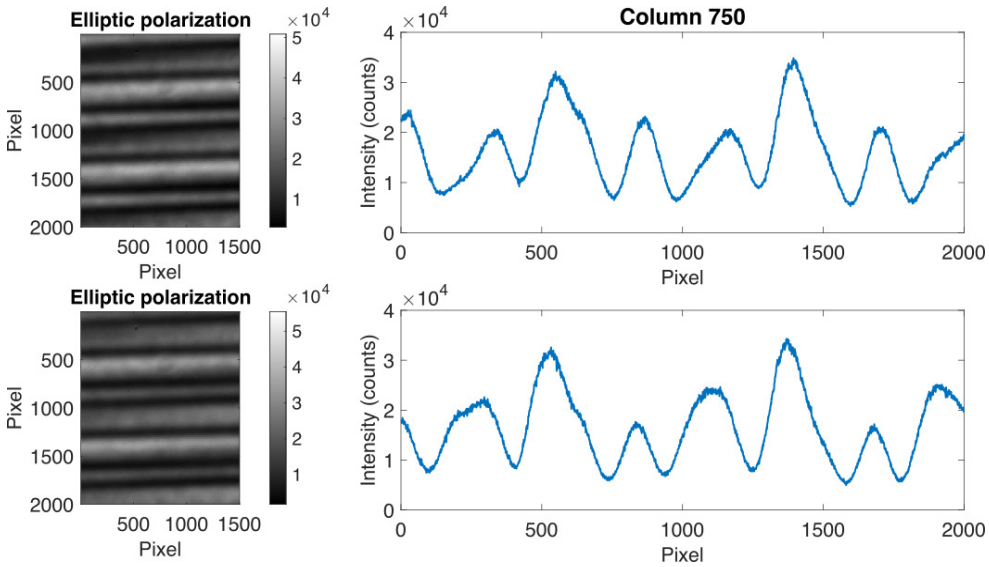


Figure 9.9: Examples of modulations obtained for two incoming elliptical polarization states.

This is an experimental validation of the spectropolarimeter model discussed in this thesis. These first images demonstrate a fundamental aspect of the discussed spectropolarimetric method: the existence of intensity modulation in the vertical direction of polarized light. It is an essential starting point for in-depth investigations of how this optical design works.

### 9.1.1. EXPERIMENTAL OBJECTIVES AND THE BASIC OPTICAL SETUP

The confirmation of the modulation's existence and the previous observations related to the misalignment of the prisms in the modulator component put us in front of several questions that must be answered to understand what is happening in this modulator and how it acts on light.

Certainly, we are dealing with a modulator that does not fully comply with the technical specifications only by considering what we can see directly. It continues to produce a predictable result to a reasonable extent. Still, the impact of deviations on the results will be difficult to quantify without a good knowledge of these deviations.

Because of this, the questions that must be answered next are:

1. What are the main characteristics (variation of the phase difference of the light and optical axis orientations) for the components of the modulator and the modulator as a whole?
2. Can we still use this modulator to measure the polarization of light as we theorized before?

We devised a two-stage work plan:

1. The first stage characterizes the prisms 1 and 3 and the modulator. This characterization, as we have already mentioned, refers to:
  - determining the phase difference induced in the vertical direction by each prism separately;
  - determining the orientation of the optical axis for each prism
  - highlighting the differences compared to the theoretical model
  - partial determination of the Mueller matrix corresponding to the modulator
2. Checking the possibility of demodulating the polarized signal:
  - determination of the optical system instrumental matrix;
  - generating test polarization states, recording the corresponding modulation, and testing the demodulation.

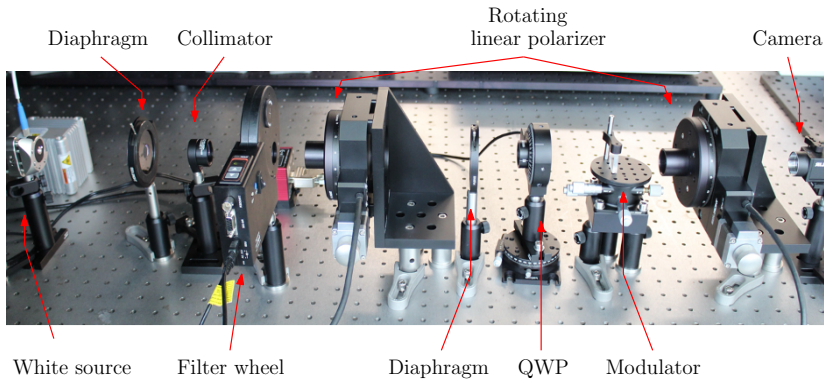


Figure 9.10: Optical setup used during the characterization procedures. The light, coming from the left side, passes through a diaphragm, a collimator, a filter located in a filter wheel, a linear polarizer located into a rotating mount, a diaphragm, a *QWP* (optional), the modulator, the analyzer (linear polarizer), and in the end reaches the camera.

We used a two-part optical set-up to perform all these practical investigations. The first part (see Fig. 9.10) contains the white light source, an aperture, a collimator, and a spectral filter. It is part of the optical configuration that remained almost unchanged during the post-alignment works. The only interventions concerned the replacement of the filter. The alignment of this front part of the set-up was mainly about positioning the collimator to get a collimated beam with a diameter of 2.54 cm. We obtained a divergence of approximately  $3 \cdot 10^{-5}^\circ$  for  $\lambda = 515.4$  nm and 633 nm. The divergence was estimated from the size of the spot at different distances. This value remains an approximation because of the diffraction effect around the edges caused by the aperture stop.

The second part of the instrument was generally composed of a linear polarizer (called hereafter  $LP_1$ ) followed by the modulator, analyzer (called hereafter  $LP_2$ ), and camera.

However, this part remained variable during the works. Depending on the type of investigation, various other components (*QWP*, *HWP*) were introduced or, possibly, extracted. The two linear polarizers used for almost all measurements were placed in rotating mounts, which were computer-controlled. These two polarizers' mounts were aligned with the first part of the optical set-up from the beginning.

Each stage of the experimental investigations involved using a particular optical setup. Sometimes, it was necessary to produce certain types of polarization, which necessitated the insertion of a *QWP* between the first linear polarizer and the modulator, and sometimes, the determination of some terms of the Mueller matrix required the introduction of other components between the modulator and the analyzer. All these changes will be described in detail in the following chapters as they will be required to determine the different parameters.

## 9.2. CHARACTERIZATION OF THE SOURCE

Before proceeding to the polarimetric characterization of the modulator and its components, we undertook a characterization of the light source from the point of view of stability and intrinsic polarization. This was followed by establishing a reference system by orienting the first linear polarizer with the help of a polarizing beamsplitter. It defined the horizontal and vertical of our optical system and helped us define a reference for the orientation of the various rotating components from the setup.

Concerning the intrinsic polarization of the source, the tests conducted by rotating linear polarizers in front of it (see Fig. 9.11) did not reveal the presence of a linear component.

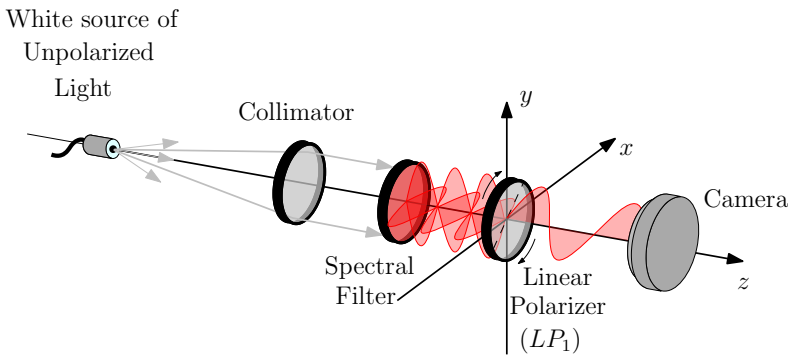


Figure 9.11: The optical setup used to check the linear polarization of the source: the unpolarized light coming from the left passes through a spectral filter and then a rotating linear polarizer before arriving on the detector.

Figure 9.12 a) shows the results obtained after turning two different linear polarizers ( $LP_1$  and  $LP_2$ ) between  $0^\circ$  and  $360^\circ$ , with a step of  $1^\circ$ . The transmission axis of  $LP_1$  was oriented, in the beginning, at  $0^\circ$  with respect to the  $x$ -axis of the reference system of the laboratory. In contrast, the transmission axis of  $LP_2$ , which was placed in the same mount after removing  $LP_1$ , was oriented at  $45^\circ$  at the beginning, even if the mount was again rotated between  $0^\circ$  and  $360^\circ$ . The global difference between the two variations ob-

tained for  $LP_1$  and  $LP_2$  is due to the inherent differences between the two optical components. However, the intensity variation follows the same pattern, independently of the orientation of the transmission axis. The misalignment of the optical components could explain the phenomenon. Over a complete polarizer rotation, in the case of  $LP_1$ , we detect a variation 0.45% around the mean, whereas, for  $LP_2$ , we have 0.8%.

Concerning the temporal stability of the source, the continuous measurement over four hours, with an integration time of 14 ms and a frequency rate of 1 Hz, shows a variation of  $\pm 0.17\%$  of the intensity (see Fig. 9.12). More technical details about the components of the optical setup can be retrieved in the Addendum of this thesis. The principal characteristics of the source and the alignment are presented in Tab. 9.3.

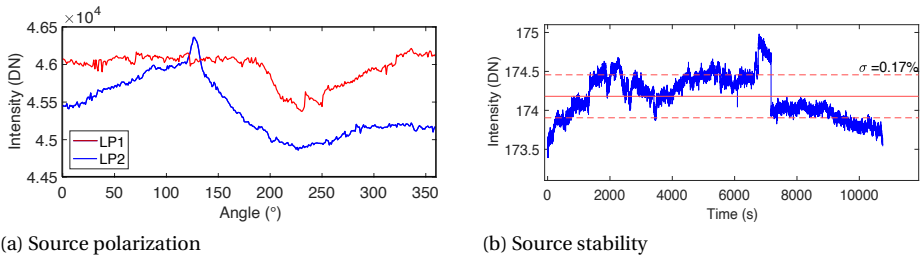


Figure 9.12: a) Rotating two linear polarizers ( $LP_1$  and  $LP_2$ ) in front of the source, in the same mount and one after the other shows that similar intensity variation is obtained for different orientations of the transmission axis. b) Variation of the mean signal for an area of  $1000 \times 1000$  pixels during 4 hours of observation. The intensity values were encoded on 8 Bits to reduce the total volume of data.

#### Source properties & alignment

Variation with $LP_{1,2}$	[0.45 0.8]%
Temporal variation	$\approx 0.17\%$
Beam divergence	$3 \cdot 10^{-5}^\circ$

Table 9.3: Main properties of the source: temporal stability, variation of the intensity with the position of  $LP_1$  and  $LP_2$ , and divergence of the collimated beam.

### 9.3. GENERAL PROCEDURE FOR THE POLARIMETRIC PART

All the measurements that involved a different setup of the polarimetric part of the instrument started with the orientation of the first linear polarizer ( $LP_1$ ) with the help of the polarizing beamsplitter. The reference frame for the polarization and the polarimetric components was thus established. The polarimetric part of the instrument used for this procedure contained only the polarizing beamsplitter,  $LP_1$ , and the camera (see Fig. 9.13).

The rotating mount of  $LP_1$  was rotated with a step of  $1^\circ$  between  $0^\circ$  and  $180^\circ$ . For each position, the value of the detected intensity was recorded. Applying Malus' law, this procedure allows establishing the orientation of the transmission axis of the linear polarizer with respect to the  $0^\circ$  position of the mount (see Fig. 9.14).

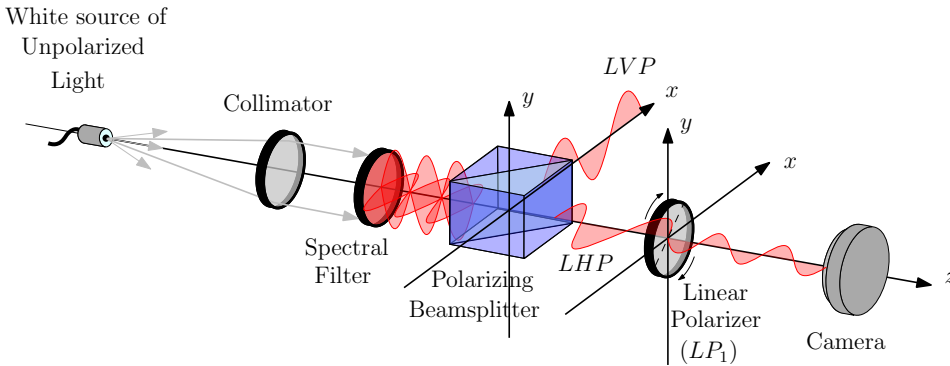


Figure 9.13: A general schema for the orientation of  $LP_1$ : the unpolarized light coming from the white source (left) passes through a collimator, a spectral filter, a polarizing beamsplitter, and the linear polarizer ( $LP_1$ ). In the end, the camera detects the light. The horizontal polarization exiting the beamsplitter defines the horizontal direction of the optical setup. All the linear polarizers coming after the beamsplitter are oriented according to this horizontal.

The average intensity value was used for this procedure, corresponding to a region of interest of  $1000 \times 1000$  pixels from the middle of the image. A dark value was subtracted from the intensity readings for each mount orientation. The dark was measured by obscuring the source with an opaque screen. The Malus' law, in this case, is:

$$I(\theta) = \frac{1}{2} \cos^2(\theta), \tag{9.1}$$

where  $\theta$  is the angle between the transmission axis of  $LP_1$  and the horizontal axis of the polarizing beamsplitter.

In general, a second set of measurements was performed after determining the maximum and minimum positions. This time, a step of  $0.05^\circ$  was used on an arbitrary interval around the maximum. An outcome example is displayed in Fig. 9.15.

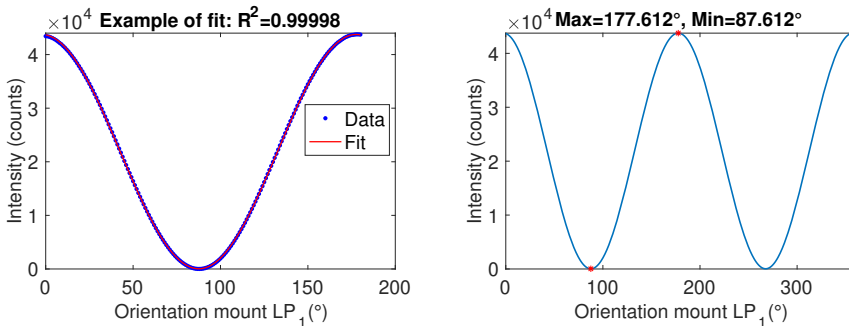


Figure 9.14: Malus' law applied to  $LP_1$  in relation to the polarizing beamsplitter. The graph on the right indicates the position obtained for the orientation of the mount, which corresponds to an optical axis of  $LP_1$  oriented along the  $x$ -axis (maximum) and along the  $y$ -axis (minimum).

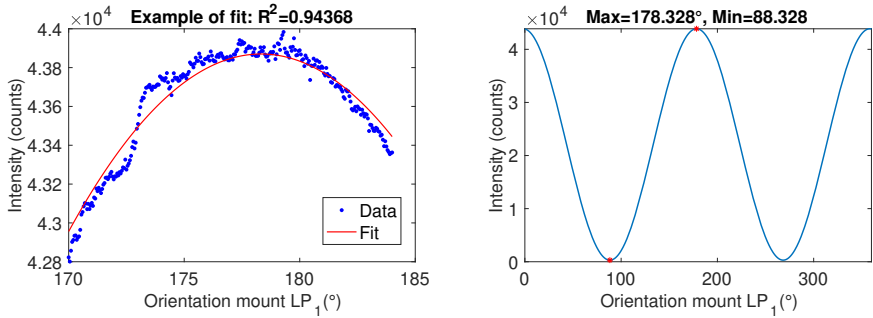


Figure 9.15: Malus' law applied to  $LP_1$  in relation to the polarizing beamsplitter. The step of rotation was decreased to  $0.05^\circ$ .

After establishing the horizontal corresponding to  $LP_1$ , the polarization beamsplitter is extracted from the setup, and  $LP_2$  is inserted into its rotating mount, located between  $LP_1$  and the camera. Again, Malus' law is used to determine the orientation of the  $LP_2$ 's optical axis relative to its own mount. For this,  $LP_1$  is positioned with the transmission axis along the horizontal, and the  $LP_2$  mount is rotated by a step of  $1^\circ$  between  $0^\circ$  and  $180^\circ$  (see Fig. 9.16).

The extinction ratio for the two polarizers, based on the average intensity corresponding to the region of interest, is presented in Tab. 9.4. This ratio, representing  $I_{min}/I_{max}$ , where  $I_{min}$  is the minimum of the obtained intensity and  $I_{max}$  the maximum of the intensity, was established for  $LP_1$  based on the polarization obtained with the polarizing beamsplitter, and for  $LP_2$ , based on the polarization obtained with  $LP_1$ .

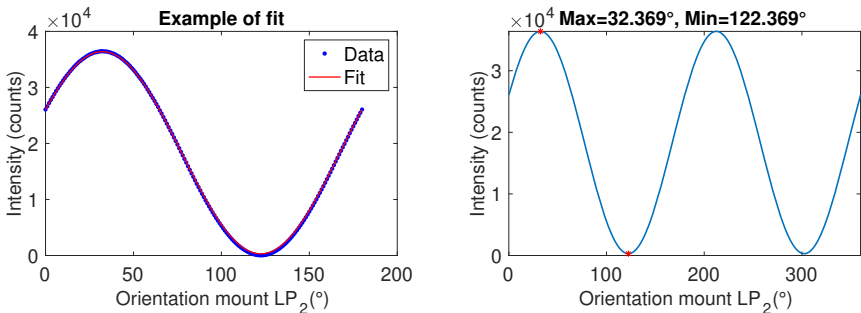


Figure 9.16: Intensity values obtained while rotating  $LP_2$  and maintaining  $LP_1$  with the transmission axis along the  $x$ -axis. The right image shows the positions of the mount  $LP_2$  for the maximum and minimum transmission.

The measurements conducted during this part have used, in general, a set of five frames for each value of the intensity. On the contrary, for the dark, a single frame was used. The integration time used for most of the measurements was 14 ms. This integration time is located in the middle of the detector's linearity curve for the considered optical setups. The encoding was, most often, on 16-bit.

Once the main properties of the source were established, the alignment completed, and the procedure for the orientation of the linear polarizers was defined, we passed to the next step: the characterization of the modulator.

Extinction ratio	
$LP_1$	$1.68 \cdot 10^{-4}$
$LP_2$	$9.77 \cdot 10^{-4}$

Table 9.4: Extinction ratio for the 2 linear polarizers

Measurements conditions	
Number of frames	5
Exposure time	14 ms
Encoding	16 bit

Table 9.5: Main settings used for the camera during the acquisition of images.

## 9.4. A STEP FORWARD: TNO'S IMPLEMENTATION OF THE CONCEPT

The auspicious results obtained from our simulations and from the crossed-check motivated TNO to construct an instrument employing the modulator presented here. We assisted this process in parallel with our research. The instrument was designed to be fitted on the 80 cm telescope from Amsterdam. The purpose of such an instrument is to help characterize the objects on a geostationary orbit around the Earth from a spectropolarimetric point of view. The nearly final form of this instrument is presented in Fig. 9.17 and follows closely the setup from Fig. 8.7.

The main components of this instrument are:

1. White source (integrating sphere)
2. Collimator
3. Modulator
4. Linear polarizer (analyzer)
5. Optical prism
6. Cylindrical lens
7. Camera

The integrating sphere is used here for characterization and calibration purposes, as it facilitates the depolarization of the source. Between the integrating sphere and the collimator, there is a pinhole that allows the passage of light. Instead of a filter wheel,



this instrument uses an optical prism. A cylindrical lens follows this. This way, the modulation corresponding to multiple wavelengths can be obtained simultaneously on the detector plane. This instrument is still in the construction phase. The characterization of the modulator to retrieve the main characteristics corresponding to this optical alignment is foreseen for the near future.

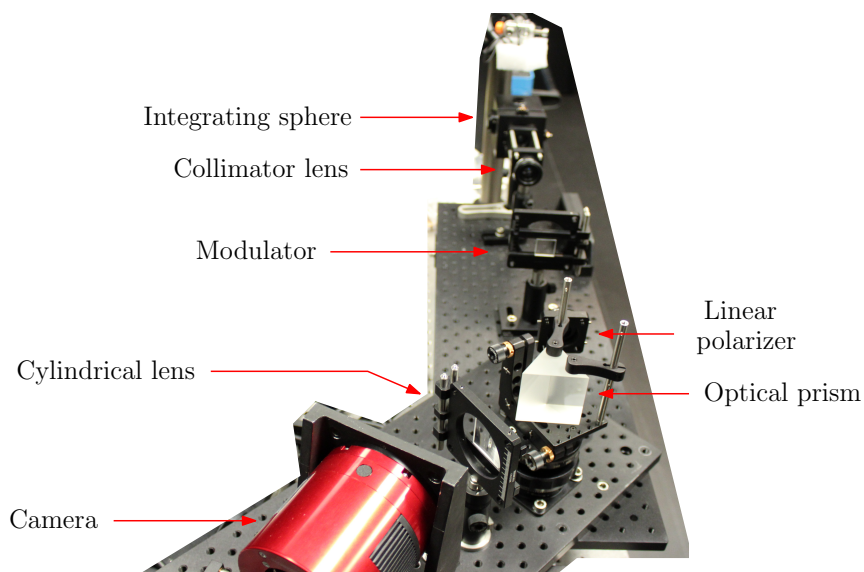


Figure 9.17: Instrument assembled by TNO and using the modulator studied here.

# 10

## CHARACTERIZATION OF THE MODULATOR

*Order and simplification are the first steps towards mastery of a subject.*

Thomas Man

We saw in the previous chapter that the manufactured modulator can produce a modulation in the intensity of the polarized light in the vertical direction. We do not know yet if this modulation corresponds to the theoretical expectations. However, we noticed some important deviations from the geometrical design. The three prisms were assembled with a slight rotation from one to the other so that the lateral faces are no longer in the same plane and the entry and exit surfaces are no longer parallel. Understanding these differences' implications and the manufactured modulator's properties is paramount. Only this will help us to understand what is happening with light inside the prisms, how the modulation is produced in reality, and if (and how) this optical component can measure polarization.

Two methods can be used to conduct this characterization. One method, called hereafter the fit of the intensity ratio method (Piron et al., 2018), tests the effect of the optical element on various linear polarizations in terms of diattenuation, polarizance, and rotation. Based on the results obtained for different positionings of the parallel and crossed polarizers used within the method, information about the orientation of the fast axis and the phase can be inferred. The limitations of this method are related to its assumptions: it considers that the analyzed component behaves like an ideal wave plate, as described by Eq. (2.25). Specifically, it assumes that the diattenuation and polarizance vectors are of norm zero or very close to zero. The method fails to produce a reliable result when these norms differ too much from zero. Another approach, which is more laborious, should be adopted then. It first consists of fully determining the Mueller matrix of the studied optical component. Applying the Mueller matrix decomposition (MMD) algorithm (Lu and Chipman, 1996), information about fast axis orientation and retardance can be retrieved with the help of the computed decomposition.

The theoretical description of these two methods is provided in the next sections.

### 10.1. METHOD 1: THE FIT OF THE INTENSITY RATIO

Any birefringent element acts as the basis transformation for an incoming Stokes vector. The associated Mueller matrix of this element is the transformation matrix that converts the incoming Stokes vector into the outgoing one. By illuminating the tested optical component with the linear polarization of various angles and measuring the intensities with an analyzer oriented along the direction of vibration of the incoming ray and in the orthogonal direction, we can assess the depolarization, the diattenuation and the rotation effect of the studied element. This is the principle of the fit method. Overall, it needs only two sets of measurements.

The general set-up employed to obtain the data is presented in Fig. 10.1. In this optical scheme, presenting two steps (A) and (B) in the Fig. 10.1, the light from a polychromatic source ( $PS$ ) passes through a collimator, a spectral filter, and then through a linear polarizer ( $LP$ ), with the transmission axis oriented along the  $x$ -axis (see the dashed line in the Fig. 10.1).

The linear polarization obtained with  $LP$  is then converted into a circular polarization with the help of a  $QWP$ , with the fast axis oriented at  $45^\circ$  in the  $xy$  plane. The purpose of the first linear polarizer and of the  $QWP$  is to minimize the effect of possible partial polarization of the source.

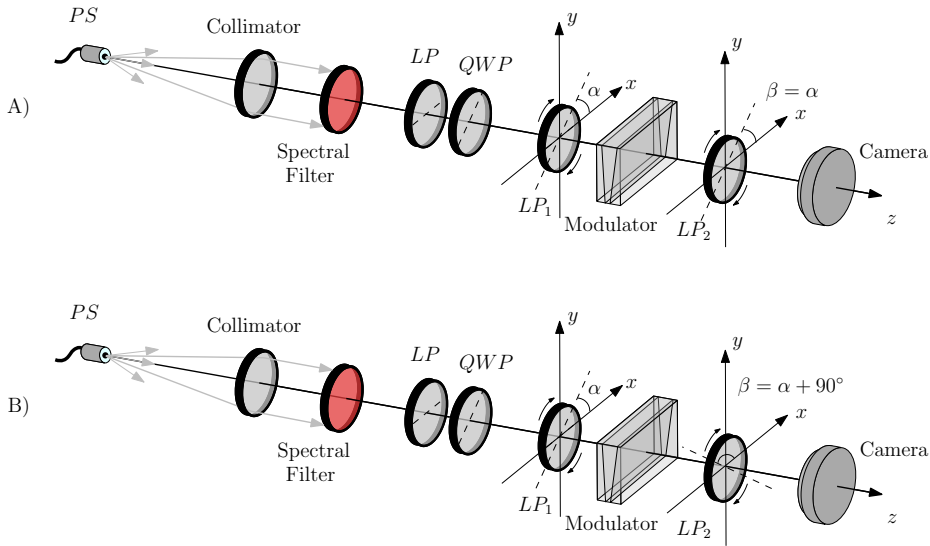


Figure 10.1: Optical setup conceived for characterizing the modulator. The unpolarized light, coming from a polychromatic source ( $PS$ ), passes at first through a collimator and a spectral filter. Then, circular polarization is obtained with the help of a linear polarizer ( $LP$ ) and a  $QWP$ . After the  $QWP$  follows a rotating linear polarizer ( $LP_1$ ), the modulator, and the second linear polarizer ( $LP_2$ ). In the end, the camera receives the light.  $LP_1$  and  $LP_2$  are placed in mounts that can be rotated synchronously. The first set of measurements (A) is conducted by turning  $LP_1$  and  $LP_2$  with parallel transmission axes. The second set (B) supposes that the transmission axes are orthogonal in permanence.

Placing then a linear polarizer of variable orientation ( $LP_1(\alpha)$ ), a constant linear polarization could be obtained for any orientation of the transmission axis.  $LP_1$  is followed along the stream of light by the birefringent element we want to characterize, then by a rotating analyzer ( $LP_2(\beta)$ ) and a detector. In Fig. 10.1, the modulator was drawn between the two rotating polarizers. However, any optical component can be placed instead of the modulator.

Before starting any measurements, the relative orientation of the linear polarizers is determined following the procedure explained in Chapter 9.3. This also helps establish the orientation of the transmission axes of  $LP_1$  and  $LP_2$  to the defined frame of the laboratory.

We start the first series of measurements by aligning  $LP_1$  and  $LP_2$  with the transmission axes parallel (Fig. 10.1, A). Then, we turn them synchronously, with a step of  $1^\circ$ . We took one intensity measurement for each  $\alpha$  between  $0^\circ$  and  $360^\circ$ .

The detected intensity for each  $\alpha$  will correspond to the first term of the outgoing Stokes vector,  $\vec{S}_{out}^{\parallel}(\alpha)$ :

$$\vec{S}_{out}^{\parallel}(\alpha) = M_{LP_2}(\beta = \alpha) \cdot M \cdot \vec{S}_{in}(\alpha), \quad (10.1)$$

where  $M_{LP_2}(\beta = \alpha)$  is the Mueller matrix of the polarizer  $LP_2$ ,  $\vec{S}_{in}(\alpha)$  is the incoming Stokes vector, whereas  $M$  is the Mueller matrix of the birefringent element that we want to study.

For the second set of measurements, at first, the linear polarizers  $LP_1$  and  $LP_2$  are positioned into a crossed configuration:  $\beta = \alpha + 90^\circ$  (Fig. 10.1, B)). Then, like before, the two linear polarizers are again rotated synchronously, with the angle  $\alpha$  taking the same values. The detected intensity for each value of  $\alpha$  is represented in this case by the first term of the Stokes vector  $\vec{S}_{out}^\perp(\alpha)$ :

$$\vec{S}_{out}^\perp(\alpha) = M_{LP_2}(\beta = \alpha + 90^\circ) \cdot M \cdot \vec{S}_{in}(\alpha). \quad (10.2)$$

Supposing that the Mueller matrix of the birefringent component could be assimilated to a waveplate with a fast axis oriented at an angle  $\theta$  to the  $x$ -axis, in  $xy$ -plane and characterized by a phase difference  $\phi$ , then, in the ideal scenario where no polarizance and no diattenuation are present, this matrix is:

$$M = \begin{pmatrix} 1 & 0 & 0 & 0 \\ 0 & C^2 + S^2 \cos(\phi) & CS(1 - \cos(\phi)) & -S \sin(\phi) \\ 0 & CS(1 - \cos(\phi)) & S^2 + C^2 \cos(\phi) & C \sin(\phi) \\ 0 & S \sin(\phi) & -C \sin(\phi) & \cos(\phi) \end{pmatrix}, \quad (10.3)$$

where  $C = \cos(2\theta)$ , and  $S = \sin(2\theta)$ .

Substituting the expression (10.3) into Eq. (10.1) and Eq. (10.2), we can then compute the ratio of the intensities measured for each value of the angle  $\alpha$  in the two scenarios:

$$R_f(\alpha) = \frac{I^\perp(\alpha)}{I^\parallel(\alpha)} = \frac{(\cos(\phi) - 1)(\cos(4(\alpha - \theta)) - 1)}{3 + \cos(\phi) - (\cos(\phi) - 1)\cos(4(\alpha - \theta))}. \quad (10.4)$$

Fitting the theoretical expression for  $R_f(\alpha)$  to the experimental data ensures the determination of the main parameters of the birefringent element that is characterized: the phase ( $\phi$ ), respectively the fast axis orientation ( $\theta$ ). It can be easily noticed from the expression of  $R_f(\alpha)$  that this method cannot be used for a full wave-plate, for which  $\phi = 2\pi$ .

When the approximation with the theoretical matrix is no longer valid, or the vector of diattenuation, respectively depolarization, is different from zero, the fit method cannot give us access directly to the fast axis orientation or the retardance of the element. In this less favorable scenario, the expression (10.3) must be replaced by a general, normalized Mueller matrix:

$$M = \begin{pmatrix} 1 & m_{01} & m_{02} & m_{03} \\ m_{10} & m_{11} & m_{12} & m_{13} \\ m_{20} & m_{21} & m_{22} & m_{23} \\ m_{30} & m_{31} & m_{32} & m_{33} \end{pmatrix} \quad (10.5)$$

Therefore, the expression of the ratio becomes:

$$R_f(\alpha) = \frac{1 - \cos(2\alpha) \cdot T_1 - \sin(2\alpha) \cdot T_2}{1 + \cos(2\alpha) \cdot T_1' + \sin(2\alpha) \cdot T_2'}, \quad (10.6)$$

where,

$$\begin{cases} T_1 = m_{11} \cos(2\alpha) - m_{01} + m_{10} + m_{21} \sin(2\alpha) \\ T_2 = m_{12} \cos(2\alpha) - m_{02} + m_{20} + m_{22} \sin(2\alpha) \\ T'_1 = m_{11} \cos(2\alpha) + m_{01} + m_{10} + m_{21} \sin(2\alpha) \\ T'_2 = m_{12} \cos(2\alpha) + m_{02} + m_{20} + m_{22} \sin(2\alpha) \end{cases} \quad (10.7)$$

Despite the large number of unknowns, this ratio can still be helpful. If the diattenuation terms ( $m_{01}$ ,  $m_{02}$ ) and the polarizance terms ( $m_{10}$ ,  $m_{20}$ ) are at first retrieved with the help of the procedure described in Chapter 2 (see Tab. 2.1), then the fit can still be applied for the inner terms ( $m_{11}$ ,  $m_{12}$ ,  $m_{21}$ ,  $m_{22}$ ) under the supposition that they will still be close to the expressions from Eq. (10.3). However, specific differences between these terms and their ideal form should be considered. Because of this, the fit method is susceptible to significant errors in this case.

## 10.2. METHOD 2: THE MUELLER MATRIX DECOMPOSITION

The fit method has limited applicability when the difference between the actual Mueller matrix and the theoretical one becomes hard to predict. In this case, retrieving only a part of the matrix is insufficient, and we cannot escape the Mueller matrix's full determination. Applying the polar decomposition to the measured matrix (Lu and Chipman, 1996; Manhas et al., 2006), the main parameters of the system, the retardance (linear and circular), the diattenuation, or the fast-axis orientation ( $\theta$ ), can be found. We need to use this decomposition because the information about the fast axis orientation or the retardance of the medium cannot be accessed directly from the values of the terms of the Mueller matrix. We do not know how these terms express these properties. We need the decomposition procedure of the Mueller matrix to isolate the effects of diattenuation, retardance, and polarization. According to this approach, a Mueller matrix ( $M$ , normalized) can be decomposed in the product of three matrices, corresponding to a diattenuator, a retarder, and a depolarizer:

$$M = M_{\Delta} \cdot M_R \cdot M_D, \quad (10.8)$$

where  $M_{\Delta}$  is the depolarizer,  $M_R$  is the retarder and  $M_D$  the diattenuator. This product is unique, except in the case of non-invertible Mueller matrices. The three terms of the previous product are expressed as:

$$M_{\Delta} = \begin{bmatrix} 1 & \vec{0}^T \\ \vec{P}_{\Delta} & m_{\Delta} \end{bmatrix}, \quad M_R = \begin{bmatrix} 1 & \vec{0}^T \\ \vec{0}^T & m_R \end{bmatrix}, \quad M_D = \begin{bmatrix} 1 & \vec{D}^T \\ \vec{D} & m_D \end{bmatrix}, \quad (10.9)$$

In this contracted form,  $\vec{P}_{\Delta}$  is a  $3 \times 1$  vector, related to the polarizance vector,  $\vec{P}$ , and  $\vec{D}$  is the diattenuation vector.  $m_{\Delta}$ ,  $m_R$  and  $m_D$  are  $3 \times 3$  matrices.

Using the notations from Eq. (10.5), the normalized polarizance and diattenuation vectors of the matrix  $M$  are:

$$\vec{P} = \begin{pmatrix} m_{10} \\ m_{20} \\ m_{30} \end{pmatrix}, \quad \vec{D} = \begin{pmatrix} m_{01} \\ m_{02} \\ m_{03} \end{pmatrix}, \quad (10.10)$$

whereas the norms are given by

$$P = \sqrt{m_{10}^2 + m_{20}^2 + m_{30}^3}, \quad D = \sqrt{m_{01}^2 + m_{02}^2 + m_{03}^3} \quad (10.11)$$

In the case of a depolarizing element (i.e,  $P \neq 0$ ), the computation of the matrices  $M_\Delta$ ,  $M_R$  and  $M_D$  follows the next algorithm (Lu and Chipman, 1996):

1. The submatrix  $m_D$  ( $3 \times 3$ ) is computed via:

$$m_D = \sqrt{1 - D^2} \cdot I + \frac{1 - \sqrt{1 - D^2}}{D^2} \cdot \vec{D} \vec{D}^T, \quad (10.12)$$

where  $I$  is the identity matrix ( $3 \times 3$ ). With the help of Eq. (10.12), (10.10), and (10.9), the  $M_D$  matrix can be calculated.

2. After computing  $M_D$  and  $M_D^{-1}$ , we multiply at right Eq. (10.8) with  $M_D^{-1}$ :

$$M_\Delta \cdot M_R = M \cdot M_D^{-1} = M'. \quad (10.13)$$

3. We compute  $m'$ , the submatrix of  $M'$ :

$$m' = m_\Delta m_R \quad (10.14)$$

4. It can be shown that:

$$m_\Delta^2 = m'(m')^T. \quad (10.15)$$

5. Using the Cayley-Hamilton theorem, we infer that:

$$m_\Delta = \pm \frac{(\sqrt{\lambda_1} + \sqrt{\lambda_2} + \sqrt{\lambda_3}) \cdot m'(m')^T + \sqrt{\lambda_1 \lambda_2 \lambda_3} \cdot I}{m'(m')^T + (\sqrt{\lambda_1 \lambda_2} + \sqrt{\lambda_2 \lambda_3} + \sqrt{\lambda_3 \lambda_1}) \cdot I}, \quad (10.16)$$

the sign of the expression corresponding to the sign of the determinant of  $m'$ .

6. By taking  $m$  as submatrix of  $M$ , then, according to Lu and Chipman, 1996 we have:

$$\vec{P}_\Delta = \frac{\vec{P} - m \vec{D}}{1 - D^2}. \quad (10.17)$$

7. Thus, with (10.9) and (10.17), the depolarization matrix,  $M_\Delta$ , can be retrieved. Furthermore, the net depolarization is provided by:

$$\Delta = 1 - \left( \frac{|\text{tr}(M_\Delta) - 1|}{3} \right). \quad (10.18)$$

8. Because  $M_D$ ,  $M'$  and  $M_\Delta$  are known,  $M_R$  can be computed now, based on (10.13):

$$M_R = M_\Delta^{-1} \cdot M'. \quad (10.19)$$

9. Therefore, the retardance can be accessed:

$$R = \cos^{-1} \left( \frac{\text{tr}(M_R)}{2} - 1 \right). \quad (10.20)$$

10. The linear ( $\phi$ ), respectively the circular retardance ( $\psi$ ) are provided by:

$$\phi = \cos^{-1} \left( \sqrt{(M_R(1,1) + M_R(2,2))^2 + (M_R(2,1) - M_R(1,2))^2} - 1 \right), \quad (10.21)$$

$$\psi = \tan^{-1} \left( \frac{M_R(2,1) - M_R(1,2)}{M_R(1,1) + M_R(2,2)} \right). \quad (10.22)$$

11. Because the total retardance matrix is nothing else but the combination of a linear retarder (of retardation  $\phi$  and fast-axis orientation  $\theta$  to the horizontal) and a circular retarder (of rotation  $\psi$ ) Ghosh et al., 2008 it follows that:

$$M_R = M_{LR} \cdot M_{rot}, \quad (10.23)$$

where  $M_{LR}$  is provided by (10.3), whereas

$$M_{rot} = \begin{pmatrix} 1 & 0 & 0 & 0 \\ 0 & \cos(2\psi) & \sin(2\psi) & 0 \\ 0 & -\sin(2\psi) & \cos(2\psi) & 0 \\ 0 & 0 & 0 & 1 \end{pmatrix}. \quad (10.24)$$

Multiplying at right with  $M_{rot}^{-1}$  the relation (10.23), it follows:

$$M_{LR} = M_R \cdot M_{rot}^{-1}. \quad (10.25)$$

12. Because the  $M_{LR}$  matrix can be also expressed as

$$M_{LR} = \begin{pmatrix} 1 & \vec{0}^T \\ \vec{0} & m_{LR} \end{pmatrix}, \quad (10.26)$$

then the elements of the linear retardance vector,  $\vec{LR} = [1, r_1, r_2, r_3]^T$  can be obtained:

$$r_i = \frac{1}{2} \sin(\phi) \cdot \sum_{j,k=1}^3 \epsilon_{ijk} m_{LR}(j, k), \quad (10.27)$$

where  $\epsilon_{ijk}$  is the Levi-Civita symbol.

13. Thus, the fast axis orientation to the  $x$ -axis can be obtained:

$$\theta = \frac{1}{2} \tan^{-1} \left( \frac{r_2}{r_1} \right). \quad (10.28)$$

The decomposition algorithm presented here is valid for a depolarizing and diattenuating medium. In the case of a perfect polarizer, certain modifications should be considered as it was proved before (Lu and Chipman, 1996). Overall, the decomposition



procedure is a lengthy activity. Many measurements and changes in the optical system are required to retrieve the complete Mueller matrix. Because of this, this procedure is prone to errors in alignment. On the other hand, the fit method is much faster and less exposed to alignment errors as it does not require any change of the optical system (aside from the rotation of the linear polarizers). As we saw, it is limited by the discrepancies between the analyzed waveplate and the ideal model or by the complexity of the model itself.

### 10.3. TEST OF THE METHOD 1

Before we try it, we cannot know if the fit of the intensity ratio is suitable for characterizing the prisms and the modulator. Only the fit quality that can be obtained can give us a clear indication in this sense. Until proven otherwise, this method has undoubted advantages over the complete determination of the Mueller matrix. For this reason, the first characterization tests were performed using the fit. However, the first step towards this application was testing the method on a "well-known" element. This helped us to verify its accuracy and to familiarize ourselves with the required manipulations. Thus, the fitting procedure was tested at first on a quarter waveplate (*QWP*,  $\phi = \pi/2$ ) with the optical axis oriented at  $0^\circ$  on the  $x$  axis. The detected signal from a random pixel for the two configurations, with aligned and crossed polarisers, is shown in Fig. 10.2.

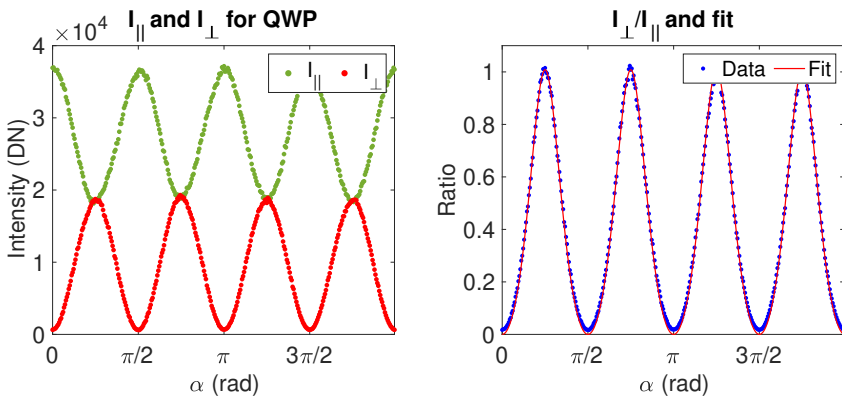


Figure 10.2: Left: detected intensity by a single, random pixel, while the angle  $\alpha$  varies between 0 and  $2\pi$ . The green dots represent the case when  $LP_1$  and  $LP_2$  are aligned, whereas the red dots correspond to the crossed orientation of the two linear polarizers. Right: the experimental ratio  $R_f(\alpha) = I_{\perp}(\alpha)/I_{||}(\alpha)$  for the selected pixel and the fit of the theoretical curve.

A Thorlabs spectral filter was used for this measurement, with the central wavelength (*CWL*) at 515.4 nm and full width at half maximum (*FWHM*) of 3 nm. The camera's exposure time was set to 14 ms, and for each value of the angle  $\alpha$ , a set of five images was collected in the aligned and crossed configuration of the linear polarizers. The rotation occurred between  $0^\circ$  and  $359^\circ$  with a step of  $1^\circ$ . Consequently, each dot from the plot below corresponds to the average value over the five measurements from which the corresponding dark value was extracted.

The pixel-by-pixel approach was favored here as the prisms and modulator characterization will require this procedure. Figure 10.3 shows that the experimental data can be fitted with the theoretical function  $R_f(\alpha)$ , derived from the Eq. (10.4) ensuring a very high quality of the fit for most of the pixels.

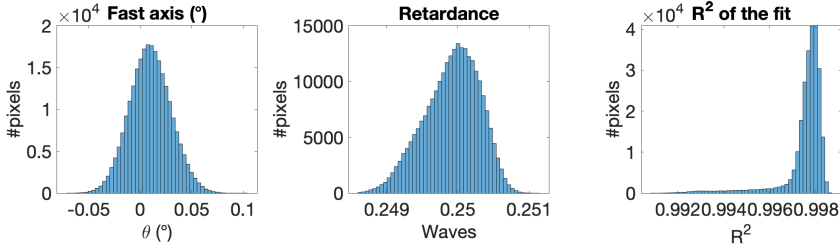


Figure 10.3: Results of the fit procedure applied to a well-known component, a zero-order achromatic QWP. The three histograms correspond to an arbitrary area of  $500 \times 500$  pixels.

The characteristics featured by the manufacturer of the QWP present a retardance of approximately 0.242 waves with an accuracy of  $\lambda/300$ . The fit results presented in Fig. 10.3 show a value of  $0.25 \pm 5 \cdot 10^{-4}$  waves. The difference between the two, of approximately 3.3%, comes mainly from the faults in the alignment of our optical set-up and the dust existing on the optical components.

In conclusion, it can be said that the method of the fit of the intensity ratio can be a robust procedure for characterizing the prisms and the modulator, at least as long as a good approximation of the Mueller terms can be made.

## 10.4. EXPERIMENTAL RESULTS FOR PRIMS 1

The critical components of the modulator are Prism 1 (input prism) and Prism 3 (output). They are responsible for the modulation of the polarized signal. As we saw before, each wedge was designed with specific characteristics to ensure the proper functioning of the modulator. A thorough characterization is then compulsory to see how much the manufacturer could handle the fabrication specifications. The results obtained for the QWP proved that, with our optical setup, we can successfully apply the fit method to a waveplate with properties close to the theoretical model. Considering this premise, we tried to apply the fit method to the first prism.

Just like for the QWP, the measurements were conducted with the spectral filter of 3 nm FWHM, and CWL 514 nm. The width of the filters has a substantial impact on the quality of the fit. This is because the experimental data corresponds to the integral of the expression (10.4) over the pixel size and the spectral resolution element. In contrast, the analytical expression corresponds to  $R_f(\alpha)$  before integration. Consequently, the integration intervals should be as small as possible to increase the quality of the fit.

The two prisms were reversed at  $90^\circ$ , around the z-axis in the experimental set-up. This positioning was necessary to secure the stability of the prisms on the optical mount. Because of this, the expected variation of phase induced by each prism should manifest in the horizontal direction, whereas the expected orientation of the fast axes should be

90° for prism 1, respectively 135° for the prism 3.

If, in the case of the QWP, the detected intensity in the parallel or orthogonal configuration of  $LP_1$  and  $LP_2$  was homogeneous across the detector for each value of the angle  $\alpha$ , in the case of prism 1, we noticed a variation of intensity along the horizontal direction. This indicates that the prism is, indeed, made of a birefringent element. The variation of the optical path of the light inside the prism along the  $x$  direction is thus translated into a variation of the phase and, finally, of the intensity.

The slight tilt to the left of the pattern from Fig. 10.4 results from positioning the prism into the mechanical mount.

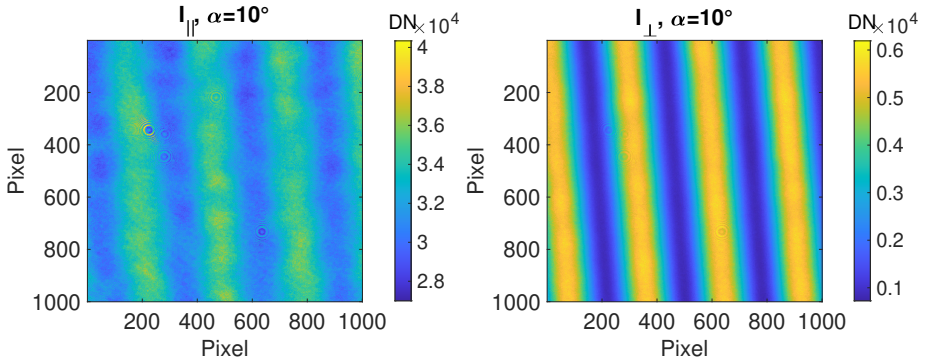


Figure 10.4: Intensity variation along the inclined face for prism 1 for the two relative orientations of  $LP_1$  and  $LP_2$ , when the angle  $\alpha = 10^\circ$ . An area of  $1000 \times 1000$  pixels from the middle of the illuminated region was used during the data analysis to reduce the processing time. The units of the detected intensity ( $DN$ ) are represented here by the number of detected photoelectrons per integration time.

Noticeably, the modulation undergone by light along the inclined face of the prism is more irregular at higher intensity values when  $LP_1$  and  $LP_2$  turn in parallel. The main reason is the Poisson noise that increases with the signal (see Fig. 10.5).

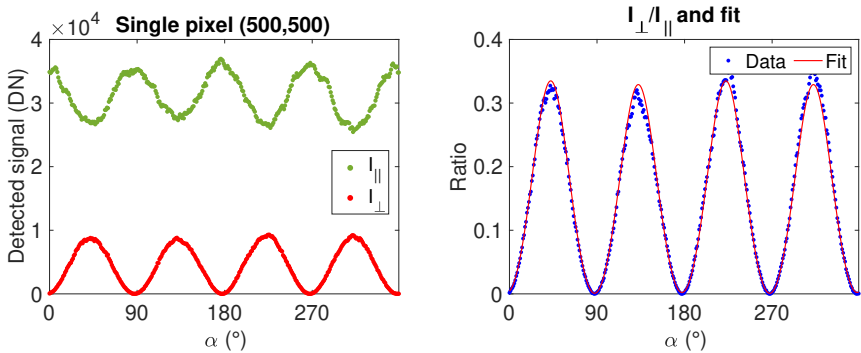


Figure 10.5: Left: example of the signal displayed by a random pixel when  $\alpha$  varies between  $0^\circ$  and  $359^\circ$ , with a step of  $1^\circ$ . At right: fit of the experimental ratio with the expression depending on  $m_{i,j}$ .

All attempts to fit a theoretical model to the experimental data, based on the expression (10.4), in which  $\phi$  and  $\theta$  were considered to vary from one pixel to another, have resulted in small values of  $R^2$ . In addition, the phase term could not be retrieved.

Therefore, a more generalist approach was favored. Instead of using the ideal expression of the Mueller matrix (10.3) and the corresponding formula for the ratio (10.4), the general expression from Eq. (10.6) was adopted. Therefore, the fit's objective was to retrieve the  $m_{i,j}$  terms ( $i, j = 0, 1, 2$ ) characterizing each pixel. This strategy allows a partial reconstruction of the Mueller matrix and the application of a second fit, using a different theoretical expression, only to those terms exhibiting the most critical impact of the phase variation.

Figure (10.6) shows that the terms corresponding to diattenuation and polarizance are quasi-constant and close to zero.

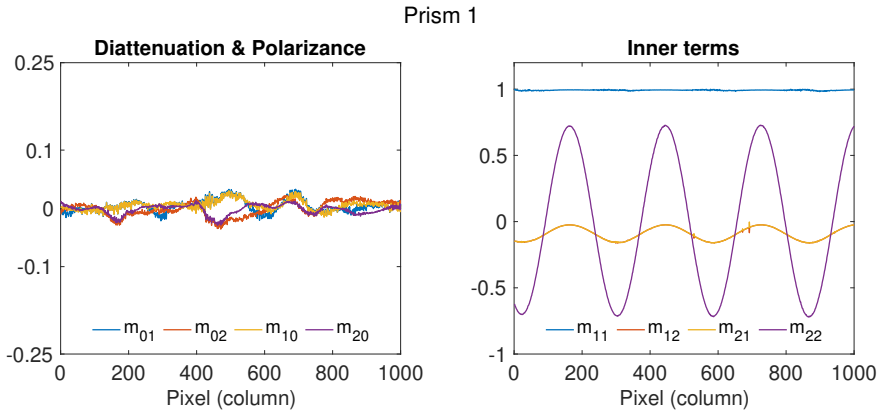


Figure 10.6: At left: terms from the diattenuation and polarizance vectors of the Mueller matrix corresponding to prism 1. The plotted values represent the average over columns of 1000 pixels. A slight and random deviation from zero is noticeable for all these terms. At right: a part of the inner terms of the Mueller matrix, averaged over each column of pixels. The modulation produced by the phase terms is noticeable here.

On the other hand, the inner terms  $m_{11}$ ,  $m_{12}$ ,  $m_{21}$ ,  $m_{22}$  display a strong impact of the phase, as it was expected (see Eq. (10.3)). In fact, if prism 1 was manufactured with the fast axis oriented horizontally (along the  $x$ -axis), then, in the setup described here, with prism 1 rotated around  $z$ -axis, the fast axis should be at  $\theta \approx 90^\circ$ . That means the inner terms are approximately:

$$\begin{cases} m_{11} = C^2 + S^2 \cos(\phi) \approx 1 \\ m_{12} = m_{21} = CS(1 - \cos(\phi)) \approx 0 \\ m_{22} = S^2 + C^2 \cos(\phi) \approx \cos(\phi) \end{cases} \quad (10.29)$$

These relations and Fig. (10.6) show that the experimental result is close to the anticipated value. However, a slight variation with respect to this is visible. Problems related to the misalignment of the optical components, with the internal reflections, scattering, or ignored Fresnel terms, can justify the deviation from the theoretical value. Nevertheless, if we assume that the prism has a homogeneous apex angle and is characterized by the

same orientation of the fast axis along an entire line of pixels, then the inner terms can be used to retrieve the main parameters of the prism for the considered line of pixels.

The best candidate to apply a second fit is  $m_{22}$ . Based on the previous observations, this term can be written as:

$$\begin{cases} m_{22} = corr + att \cdot (S^2 + C^2 \cos(\phi)) \\ \phi = c_0 + c_1 \cdot indx \end{cases}, \quad (10.30)$$

where  $cor$  is a correction term,  $att$  is an attenuation term, and  $c_0$  and  $c_1$  are the parameters describing the linear variation of the phase. To conduct the second fit, we consider  $indx$ , the index of the pixels, as a free parameter. The lower and upper bounds for the researched parameters are established as follows:

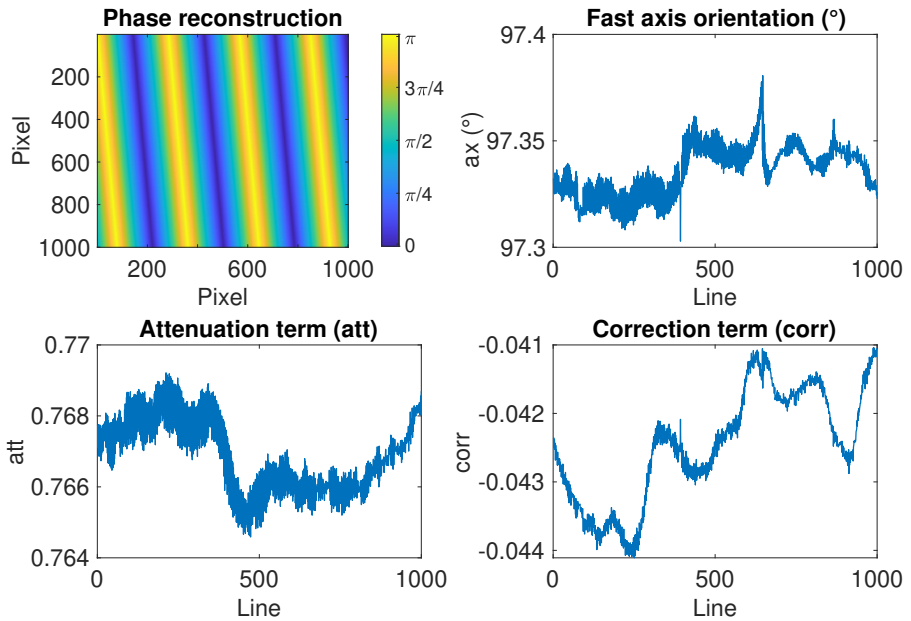


Figure 10.7: Main results of the second fit: phase variation across the region of interest, fast axis orientation, attenuation term, and correction term.

- $corr \in [-0.06, 0.06]$  : as suggested by diattenuation and polarizance terms;
- $att \in [0.75, 0.77]$ : resulting from the transmissivity of  $MgF_2$  and the corresponding Fresnel terms;
- $c_0 \in \frac{2\pi}{\lambda} \Delta n(\lambda) \cdot [d_0 - 0.5, d_0 + 0.5 + 0.98]$ , where  $d_0$  is the additional thickness of the plate (1 mm),  $\pm 0.5$  mm is the manufacturing tolerance and 0.98 mm is the maximum thickness of the plate in the limits of the provided tolerances;

- $c_1 \in \frac{2\pi}{\lambda} \Delta n(\lambda) \Delta p \cdot [\tan(2.6^\circ - 0.2^\circ), 1000 \tan(2.6^\circ + 0.2^\circ)]$ , where  $2.6^\circ \pm 0.2^\circ$  is the apex angle of the prism, and  $\Delta p = 3.45 \mu\text{m}$  is the size of a pixel.

The smooth variation of  $m_{22}$  dominated by the phase term ensures a precise determination of the phase variation across each detector line and the retrieval of the fast axis angle to the horizontal. The results for the first prism are displayed in Fig. (10.7).

The pronounced tilt retrieved for the fast axis agrees with the tilt of the wedge itself in the optical mount. In addition, the retrieved phase variation allows us to infer an apex angle for the first prism with an average value of  $2.53^\circ$ , which also follows the manufacturing requirements for the angle  $\xi$ .

## 10.5. EXPERIMENTAL RESULTS FOR PRIMS 3

The same procedures were also applied to the exit prism. Therefore, a fit was initially conducted for the experimental data corresponding to the ratio  $R_f(\alpha)$  with a general model of the Muller matrix of the prism. Again, this procedure allowed a determination of the terms  $m_{i,j}$ , ( $i, j = 0, 1, 2$ ) for each pixel. Further, the inner terms of the Mueller matrix were compared, and the term presenting the most substantial modulation was used as a basis for a second fit. The results for the two sets of terms show that this time,  $m_{11}$  is the best candidate for applying the second fit. This is in agreement with the theoretical expression of the inner terms. Because the fast axis is supposed to be oriented at approximately  $135^\circ$ , these terms become now:

$$\begin{cases} m_{11} = C^2 + S^2 \cos(\phi) \approx \cos(\phi) \\ m_{12} = m_{21} = CS(1 - \cos(\phi)) \approx 0 \\ m_{22} = S^2 + C^2 \cos(\phi) \approx 1 \end{cases} \quad (10.31)$$

Therefore,  $m_{11}$  was used for applying the second fit. The entry data was the index of pixels in the horizontal direction. Just like in the case of prism 1, the searched parameters were the correction (*corr*), the attenuation (*att*), and the coefficients of the phase,  $c_0$  and  $c_1$ , respectively. The lower and upper bounds of these parameters were the same as for prism 1, except for the  $c_1$  coefficient of the phase. This should be actualized with the angle of the wedge,  $\psi = 1.8^\circ \pm 0.2^\circ$ . The expression fitted to this data was:

$$\begin{cases} m_{11} = corr + att \cdot (C^2 + S^2 \cos(\phi)) \\ \phi = c_0 + c_1 \cdot indx \end{cases} \quad (10.32)$$

In the end, the second fit gave the possibility to retrieve the main parameters of this optical element, the phase, and the fast axis orientation. In this case, it should be stressed again that the second fit does not allow a determination pixel by pixel.

The retrieved parameters characterize an entire line of pixels, and the validity of the approach is based on the assumption of constant characteristics (fast axis orientation,  $c_0$ ,  $c_1$ , *att*, and *corr*) along a line of pixels. Of course, the hypothesis should also be verified horizontally, which means that the retrieved values for these parameters must prove a small dispersion from one line to another.

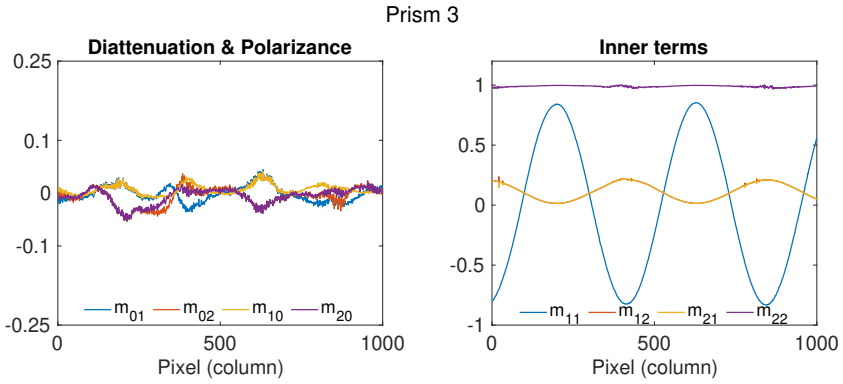


Figure 10.8: At left: terms from the diattenuation and polarizance vectors of the Mueller matrix corresponding to Prism 3, for an arbitrary line. At right: a part of the inner terms of the Mueller matrix.

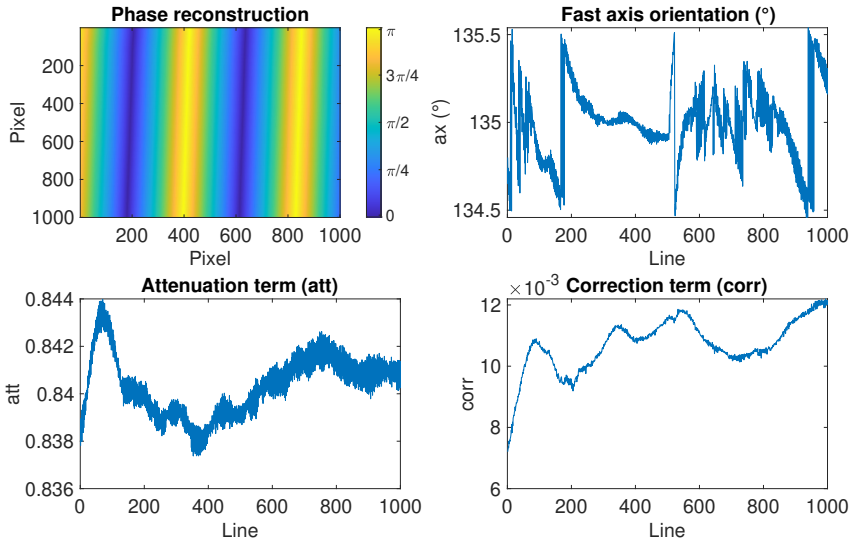


Figure 10.9: Main results of the second fit for prism 3: phase variation across the region of interest, fast axis orientation, attenuation term, and correction term.

Just like in the case of Prism 1, the applied method can receive further validation by computing the apex angle. According to the requirements, this angle should be  $1.8^\circ \pm 0.2^\circ$ . An average value of  $1.67^\circ$  is obtained from the reconstructed phase.

### 10.6. VERIFICATION OF THE RESULTS

Even though the fit method characterizes the prisms well, the results are still difficult to apply and reuse. Thus, the values retrieved for the phase and the fast axis, or, more

generally, for the  $m_{ij}$  terms, can be used to anticipate the modulation of a certain state of polarization passing through the prisms only if the entire optical system has a good alignment and the deviation of the exit rays is mitigated. Otherwise, it is possible that the computed  $m_{ij}$  terms do not correspond to the same position in the detector plane for different experiments. In this case, any attempt to anticipate an incoming state or to build a fit to find the incoming state of polarization fails.

The phenomenon is generated because the orthogonal components of the electric field of light are encountering two different indices of refraction inside the prisms. Therefore, on the exit face of prism 1, which is not perpendicular to the direction of propagation, the two light components will be refracted with a slight separation. The effect will become evident when the horizontal and vertical polarization patterns are compared. Things are the same for the third prism. The only difference is that the tilted surface is the entry surface of the prism. To observe the movement of the image,  $45^\circ$  and  $135^\circ$  linear polarizations should be compared. Consequently, the attempt to validate the results of characterizing the separated prisms should be considered cautiously.

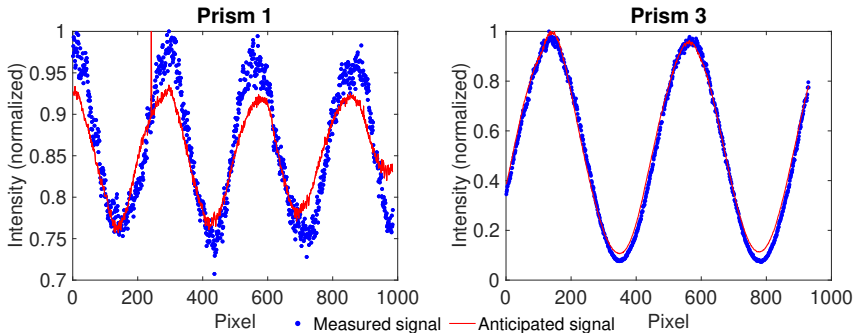


Figure 10.10: Left: Measured and anticipated signal (normalized) for the prism 1, for an incoming state of polarization  $(1, 0, 1, 0)^T$ , and analyzer oriented at an arbitrary angle of  $10^\circ$ . At right, for the same angle of the analyzer, a state  $(1, 1, 0, 0)$  is passing through prism 3.

Thus, Fig. 10.10 shows the measured and the anticipated signal when a certain polarization state passes through prism 1 and 3. For simplicity, a  $45^\circ$  linear polarization was used for prism 1, whereas for prism 3, a linear  $0^\circ$ . The analyzer was positioned at an arbitrary angle of  $10^\circ$  for both cases. For the incoming  $45^\circ$  linear polarization, the anticipated intensity in the detector plane was computed using:

$$I_{out}(\beta) = \frac{1}{2} S_0 \cdot M_{00} \left[ (1 + m_{02}) + (m_{10} + m_{12}) \cos(2\beta) + (m_{20} + m_{22}) \sin(2\beta) \right], \quad (10.33)$$

whereas for  $0^\circ$  it was used the formula:

$$I_{out}(\beta) = \frac{1}{2} S_0 \cdot M_{00} \left[ (1 + m_{01}) + (m_{10} + m_{11}) \cos(2\beta) + (m_{20} + m_{21}) \sin(2\beta) \right], \quad (10.34)$$

where  $S_0$  is the intensity of the incoming light,  $M_{00}$  is the transmission term of the Mueller matrix,  $\beta$  the orientation of the analyser, and  $m_{i,j}$  the normalized terms of the Mueller matrix previously computed. Figure 10.10 proves that a relatively good match of the



measured and anticipated signal can be obtained for prism 3. This is because prism 3 has a smaller apex angle and, therefore, a more negligible effect of deviation of the rays due to the refraction and birefringence. On the contrary, prism 1 has an apex angle almost double. The image shift is more pronounced when various polarizations pass through the prism. Consequently, the terms  $m_{ij}$  cannot accurately describe the intensity variation for any possible incoming polarization. They cannot be used successfully to retrieve the pattern of a specific incoming polarization.

### 10.7. TEST FOR THE MUELLER MATRIX DECOMPOSITION

Even though it can be extremely fast and simple, we have seen that the fit of the intensity ratio has limited applicability. To provide information about the analyzed optical element obliges us, in some cases, to a series of assumptions and approximations, which, in the end, require a laborious investigation. For this reason, we turned to the second characterization method: the decomposition of the Mueller matrix. To find the terms of the Mueller matrix, we used the procedure exposed in Chapter 3. As in the case of the fit of the intensity ratio method, we first tested this method of decomposing the Mueller matrix on a well-known element. We had at hand a Fresnel Rhomb, with the transmission axis oriented along the  $x$ -axis. This waveplate is equivalent to a quarter wave-plate oriented at  $0^\circ$ . That means the retardance is  $\frac{\pi}{2}$ , and the angle of the fast axis is  $0^\circ$ . The retrieved matrix for the Fresnel rhomb was:

$$M = \begin{pmatrix} 0.9134 & 0.0032 & 0.0068 & -0.0053 \\ -0.0028 & 0.9004 & 0.1241 & -0.1897 \\ 0.0095 & 0.0447 & -0.0404 & 0.8667 \\ -0.0092 & 0.2563 & -0.8690 & -0.0757 \end{pmatrix} \quad (10.35)$$

After applying the decomposition algorithm, the diattenuation ( $M_D$ ), the retardance ( $M_R$ ) and depolarization ( $M_\Delta$ ) matrices were obtained.

$$M_\Delta = \begin{pmatrix} 1 & 0 & 0 & 0 \\ -0.0088 & 1.0122 & -0.0790 & 0.0766 \\ 0.0161 & -0.0790 & 0.9480 & -0.0086 \\ -0.0045 & 0.0766 & 0.0086 & 0.9924 \end{pmatrix}, \quad (10.36)$$

$$M_R = \begin{pmatrix} 1 & 0 & 0 & 0 \\ 0 & 0.9686 & 0.2158 & -0.1230 \\ 0 & 0.1341 & -0.0377 & 0.9902 \\ 0 & -0.0106 & -0.9757 & -0.0654 \end{pmatrix}, \quad M_D = \begin{pmatrix} 0.9134 & 0.0032 & 0.0068 & -0.0053 \\ 0.0032 & 0.9133 & 0 & 0 \\ 0.0068 & 0 & 1.0130 & 0 \\ -0.0053 & 0 & 0 & 0.9133 \end{pmatrix}$$

Based on this decomposition, using the algorithm from Section 9.2, the following parameters were obtained for the Fresnel Rhomb:

Depolarization (dimensionless) = 0.0158	Circular retardance (rad) = 0.0811
Diattenuation (dimensionless) = 0.01	Total retardance (rad) = 0.52 $\pi$
Linear retardance (rad) = 1.6363	Fast axis angle (deg) = 3.64 $^\circ$

The results were impacted mainly by the misalignment of the quarter-wave plates used to generate the circular polarization and find the Mueller matrix's terms. Despite the minor differences in expected values, this preliminary test proves that the decomposition algorithm can be applied to retrieve the retardance and the fast axis orientation.

## 10.8. MUELLER MATRIX DECOMPOSITION: PRISM 1

Applying again the steps presented in Table 2.1 from Chapter 2, we measured the Mueller terms pixel by pixel for prism 1, rotated at  $90^\circ$  with respect to the  $x$ -axis. The results, covering a region of interest of  $1000 \times 1000$  pixels, are presented in Fig. 10.11 and 10.12.

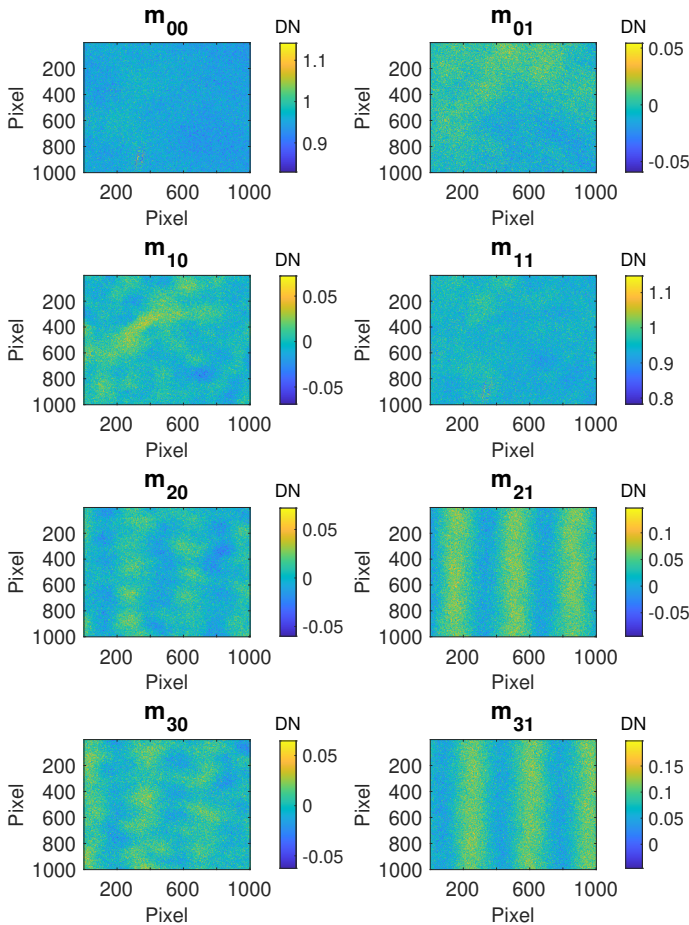


Figure 10.11: Mueller matrix terms for the prism 1, under illumination at  $633nm$ , and  $\Delta\lambda = 3nm$ .

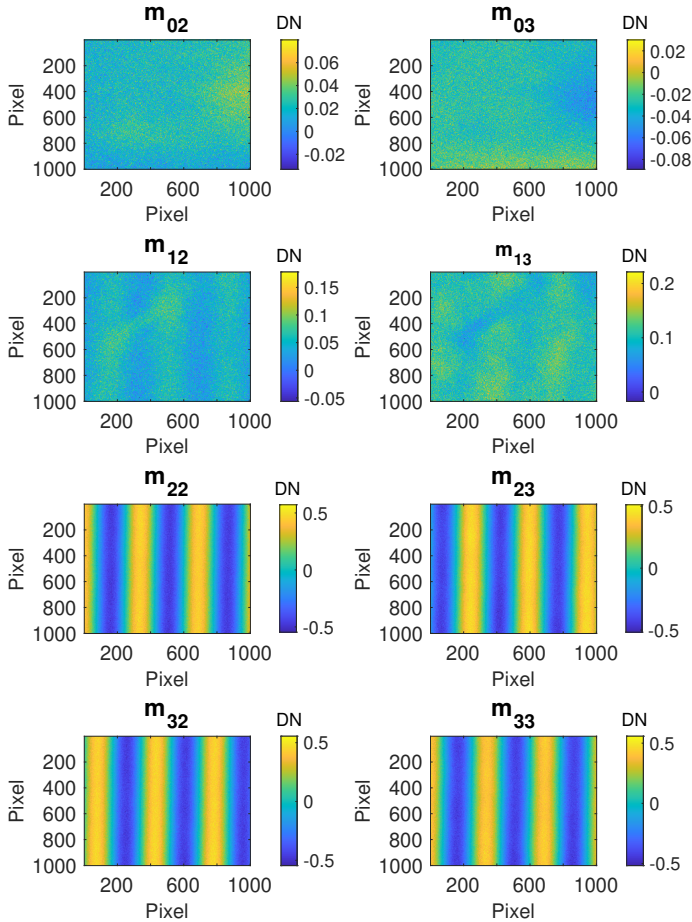


Figure 10.12: Second part of the Mueller matrix terms for the Prism 1.

The measurements were conducted with a narrow filter of 633 nm central wavelength and  $FWHM$  of 3 nm.

It should be stressed here that in its ideal form, the Mueller matrix of prism 1, rotated with the optical axis at  $90^\circ$ , as is the case in this measurement, should be (see Eq. (2.25)):

$$M = \begin{pmatrix} 1 & 0 & 0 & 0 \\ 0 & 1 & 0 & 0 \\ 0 & 0 & \cos(\phi) & -\sin(\phi) \\ 0 & 0 & \sin(\phi) & \cos(\phi) \end{pmatrix}. \quad (10.37)$$

Therefore, following the ideal expression, it is expected to obtain a strong modulation of the signal, determined by the variation of the phase difference  $\phi$ , for the terms  $m_{22}$ ,  $m_{23}$ ,  $m_{32}$ , and  $m_{33}$ . Figure 10.12 proves this strong modulation also manifests experimentally. However, we also notice a difference from the ideal scenario. The terms  $m_{20}$ ,  $m_{30}$ ,  $m_{21}$ ,  $m_{31}$ ,  $m_{12}$ , and  $m_{13}$ , measured experimentally, show the presence of a slight modulation, depending also on the phase, whereas, theoretically, they should be 0. The fact that  $m_{20}$  and  $m_{30}$  are slightly different from 0 proves that the prism alters all the incoming polarizations in small amounts. Ideally, according to the matrix (10.37), this prism should let the linear horizontal and vertical polarizations pass unaffected. The cause of this behavior will be investigated hereafter.

For the moment, it should also be stressed that  $m_{21}$ ,  $m_{31}$ ,  $m_{12}$ , and  $m_{13}$  are different from zero and display a slight modulation with the phase could be explained through an improper alignment of the prism. If the fast axis is not perfectly vertical, these terms will not cancel the phase terms from the Mueller matrix (see Eq. (2.25)).

Coming back to the "strange" behavior of the terms  $m_{20}$  and  $m_{30}$ , the prismatic shape or the fast axis's orientation cannot explain the presence of a modulation.

The most reasonable explanation of this deviation from the ideal case is based on the effect of the Fresnel terms for reflection and transmission. In Chapter 2 we saw that, at the passage from one medium to another, the light undergoes a change of path and a change in polarization, that depends on the angle of incidence.

Therefore, if the light arriving on the entry surface is not perfectly orthogonal on this face, it will undergo a slight linear polarization. The principle applies to the exit surface, too (see Eq. (2.30) and (2.31)).

If this situation occurs for the entry surface of our prism, and the Fresnel terms for transmission are not negligible, then this surface will act as a linear polarizer. Because of this, even the linear horizontal and vertical polarizations that should pass unaltered through prism 1 will be slightly modulated. In addition, even if the incoming light is unpolarized, a slight modulation of the intensity will occur, and it should be visible even without an analyzer. This phenomenon was observed experimentally.

Considering the Fresnel terms for transmission corresponding to the exit surface of the prism, their impact will be more limited. This surface will act as a weak linear polarization filter.

To obtain the full Mueller matrix of the prism, which also takes into consideration the Fresnel terms for transmission, it would be useful to note the following:

$$M_{F1} = \frac{1}{2} \begin{pmatrix} a_1 & b_1 & 0 & 0 \\ b_1 & a_1 & 0 & 0 \\ 0 & 0 & c_1 & 0 \\ 0 & 0 & 0 & c_1 \end{pmatrix}, \quad (10.38)$$

the Fresnel matrix for the transmission corresponding to the entry surface. In the same way, the matrix for the exit surface is:

$$M_{F2} = \frac{1}{2} \begin{pmatrix} a_2 & b_2 & 0 & 0 \\ b_2 & a_2 & 0 & 0 \\ 0 & 0 & c_2 & 0 \\ 0 & 0 & 0 & c_2 \end{pmatrix}. \quad (10.39)$$

In these expressions,  $a_1, b_1, c_1, a_2, b_2, c_2$  are the Fresnel terms for transmission (Collett, 2005).

In addition, the contracted representation of a general linear retarder can also be written as:

$$M = \begin{pmatrix} 1 & 0 & 0 & 0 \\ 0 & A & B & C \\ 0 & B & D & -E \\ 0 & -C & E & F \end{pmatrix}, \quad (10.40)$$

where

$$\begin{cases} A = \cos^2(2\theta) + \sin^2(2\theta) \cos(\phi) \\ B = \cos(2\theta) \sin(2\theta) (1 - \cos(\phi)) \\ C = \sin(2\theta) \sin(\phi) \\ D = \cos^2(2\theta) \cos(\phi) + \sin^2(2\theta) \\ E = \cos(2\theta) \sin(\phi) \\ F = \cos(\phi) \end{cases}, \quad (10.41)$$

in which  $\theta$  is the orientation of the fast axis, and  $\phi$  is the phase difference induced by the prism.

Consequently, the Mueller matrix (normalized) of a system composed of an entry Fresnel surface, an ideal modulator, and an exit Fresnel surface is:

$$M_{tot} = M_{F2} \cdot M \cdot M_{F1} = \frac{1}{4} \begin{pmatrix} m_{00} & m_{01} & m_{02} & m_{03} \\ m_{10} & m_{11} & m_{12} & m_{13} \\ m_{20} & m_{21} & m_{22} & m_{23} \\ m_{30} & m_{31} & m_{32} & m_{33} \end{pmatrix}. \quad (10.42)$$

In this expression, we have:

$$\begin{cases} m_{00} = a_2 a_1 + b_2 b_1 A \\ m_{01} = a_2 b_1 + b_2 a_1 A \\ m_{02} = b_2 c_1 B \\ m_{03} = b_2 c_1 C \\ m_{10} = b_2 a_1 + a_2 b_1 A \\ m_{11} = b_2 b_1 + a_2 a_1 A \\ m_{12} = a_2 c_1 B \\ m_{13} = a_2 c_1 C \end{cases}, \quad \begin{cases} m_{20} = c_2 b_1 B \\ m_{21} = c_2 a_1 B \\ m_{22} = c_2 c_1 D \\ m_{23} = -c_1 c_2 E \\ m_{30} = -c_2 b_1 C \\ m_{31} = -c_2 a_1 C \\ m_{32} = c_2 c_1 E \\ m_{33} = c_2 c_1 F \end{cases}. \quad (10.43)$$

In the situation when  $\theta$  is slightly different from  $90^\circ$ , the term  $B$  from (10.41) will vary as a function of  $\cos(\phi)$ . This variation, even very small, will become visible in  $m_{20}$ . In the same way, because the term  $C$  will vary as an attenuated  $\sin(\phi)$ ,  $m_{30}$  will be affected by the phase. This explains the observed variations of these terms from Fig. 10.11 and 10.12. On the other hand, for small deviations from  $90^\circ$ , the term  $A$  will be close to 1. In addition, because the terms  $b_1$  and  $b_2$  are also close to zero for small incidence angles,

it will result that  $m_{01}$ ,  $m_{02}$ , and  $m_{03}$  will be almost constant. This behavior was also observed experimentally.

After applying the fit for the intensity ratio, the prism was repositioned on the optical bench, and the complete Mueller matrix of the optical system was retrieved. This matrix refers to the Eq. (10.42) form, which is altered by the Fresnel terms, and not to the matrix (10.40) that remains to be determined. The displacement of the optical components was expected to generate slight variations in the results compared to the fit method. Indeed, small deviations were retrieved. Thus, the fast axis orientation was now approximately  $94^\circ$  (compared to  $97.34^\circ$  before), and the apex angle was  $2.65^\circ$  degrees, compared to  $2.53^\circ$ . Therefore, the two methods provide comparable results.

The fit for the intensity ratio approach or the decomposition of the Mueller matrix proved both reliable methods for characterizing the birefringent components of our modulator. The Mueller matrix decomposition is an almost exhaustive approach, but still, it is more prone to errors. Even in these conditions, the complete determination of the Mueller matrix of the system taught us an important lesson: the Fresnel terms should be addressed for such type of optical system. They are responsible for a slight effect of polarization that should be investigated before translating this method of spectropolarimetry into an accurate instrument.

#### ASSESSING THE FRESNEL MATRIX

The passage of light from one medium to another with an angle of incidence different from zero is accompanied by a linear polarization of the reflected and transmitted wave (see Chapter 2). This phenomenon is described by the Fresnel coefficients for reflection and transmission (Collett, 2005).

Overall, the Mueller matrix formulated with the help of the Fresnel coefficients corresponding to the interface is:

$$M_F = \frac{1}{2} \begin{pmatrix} \tau_s + \tau_p & \tau_s - \tau_p & 0 & 0 \\ \tau_s - \tau_p & \tau_s + \tau_p & 0 & 0 \\ 0 & 0 & 2\sqrt{\tau_s \tau_p} & 0 \\ 0 & 0 & 0 & 2\sqrt{\tau_s \tau_p} \end{pmatrix} \quad (10.44)$$

where the coefficients for transmission are provided by:

$$\begin{cases} \tau_s = \frac{\sin(2i) \sin(2r_s)}{\sin^2(\alpha_s^+)} \\ \tau_p = \frac{\sin(2i) \sin(2r_p)}{\sin^2(\alpha_p^+) \cos^2(\alpha_p^-)} \end{cases} \quad (10.45)$$

$s$  stays for the ray with the electric field perpendicular to the optical axis, and  $p$  for the ray with the electric field parallel to the optical axis.

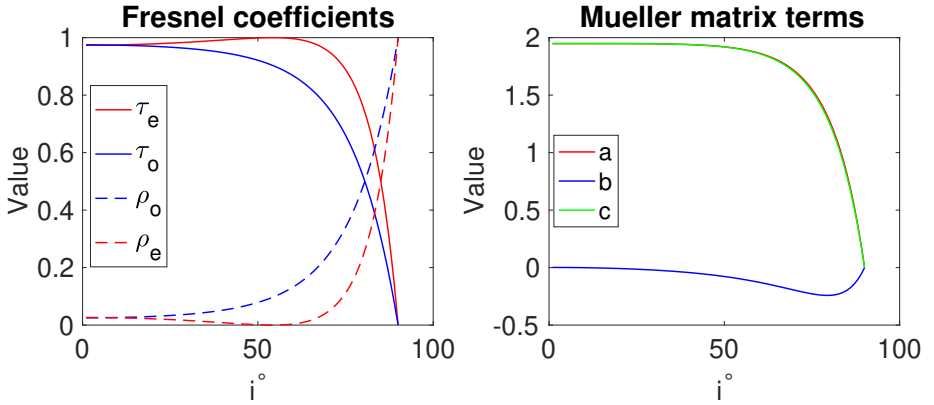


Figure 10.13: Left: Fresnel transmission coefficients for  $s$  and  $p$  polarization incident on the prism 1, for an angle of incidence  $i$ . At right, the variation of the terms of the matrix (10.38) with the angle of incidence.

In addition, we have:

$$\begin{cases} \alpha_{s,p}^+ = i + r_{s,p} \\ \alpha_{s,p}^- = i - r_{s,p} \end{cases}, \quad (10.46)$$

where  $i$  is the incidence angle and  $r_{s,p}$  is the refraction angle for the ordinary, respectively, extraordinary ray. Therefore, in the notation used in Eq. (10.44) we have:

$$\begin{cases} a = \tau_s + \tau_p \\ b = \tau_s - \tau_p \\ c = 2\sqrt{\tau_s \tau_p} \end{cases}. \quad (10.47)$$

For small values of the incidence angle ( $i < 5^\circ$ ), the Mueller matrix associated with the Fresnel terms is almost constant and close to the identity matrix. Because of this, the polarizance properties of the prism remain extremely weak. For instance, when  $i = 5^\circ$ , this matrix is:

$$M_F = \begin{pmatrix} 0.9742 & 4 \cdot 10^{-4} & 0 & 0 \\ 4 \cdot 10^{-4} & 0.9742 & 0 & 0 \\ 0 & 0 & 0.9742 & 0 \\ 0 & 0 & 0 & 0.9742 \end{pmatrix} \quad (10.48)$$

With this example, and based on the global variation described by Fig. 10.13 of the Fresnel matrix terms, we understand why the diattenuation terms of the total Mueller matrix are very close to zero, and the depolarization vector also shows a variation very close to zero.

## 10.9. CHARACTERIZATION OF THE MODULATOR

The characterization of the modulator as a whole is much more complex than that of the prisms. The number of parameters involved in the procedure is double if we ignore the effect of the middle prism. Because of this, evaluating the confidence limits for the

different terms becomes a very complex task, and the fit of the ratio of intensities fails to provide an accurate description. However, a more targeted approach can be used instead of quickly turning toward the full determination of the Mueller matrix of the modulator and then toward the decomposition of this matrix. We saw that the characteristics of the separated prisms are close to the manufacturing requirements. We may assume that the modulator is not far from the theoretical model. Under this hypothesis, the entry prism of the compound should have a fast axis that is horizontally oriented and the exit prism at  $45^\circ$ . Therefore, any incoming  $\pm S_1$  state arriving on the modulator will pass unaffected through the first prism, and it can be used to infer the phase difference determined by the third prism. Similarly, a polarization  $\pm S_2$  can help us understand the phase difference occurring in the first prism. In addition, in the ideal scenario when fast axes are close to the requirements, the complete Mueller matrix of the modulator is:

$$M = \begin{pmatrix} 1 & 0 & 0 & 0 \\ 0 & \cos(\phi_3) & \sin(\phi_1) \sin(\phi_3) & -\cos(\phi_1) \sin(\phi_3) \\ 0 & 0 & \cos(\phi_1) & \sin(\phi_1) \\ 0 & \sin(\phi_3) & -\sin(\phi_1) \cos(\phi_3) & \cos(\phi_1) \cos(\phi_3) \end{pmatrix}. \quad (10.49)$$

We should only try then to find  $M_{11}$  and  $M_{22}$  terms of the entire modulator's Mueller matrix to retrieve each component's phase variation. Therefore, according to Eq. 2.28, for an incoming  $\pm S_1$  state, observed with an analyzer oriented successively at  $0^\circ$  and  $90^\circ$ , we have:

$$\begin{cases} I^{S_1}(0) = \frac{1}{2} S_0 [(M_{00} + M_{10}) + (M_{01} + M_{11})] \\ I^{-S_1}(0) = \frac{1}{2} S_0 [(M_{00} + M_{10}) - (M_{01} + M_{11})] \\ I^{S_1}(90^\circ) = \frac{1}{2} S_0 [(M_{00} - M_{10}) + (M_{01} - M_{11})] \\ I^{-S_1}(90^\circ) = \frac{1}{2} S_0 [(M_{00} - M_{10}) - (M_{01} - M_{11})] \end{cases}. \quad (10.50)$$

In these relations, for instance,  $I^{S_1}(0)$  is the detected intensity when the incoming Stokes vector is  $\vec{S} = (S_0, S_1, 0, 0)$ , and the analyzer is oriented at  $0^\circ$ . In the same way, the term  $I^{-S_1}(0)$  corresponds to the Stokes vector  $\vec{S} = (S_0, -S_1, 0, 0)$  and the analyzer at  $0^\circ$ . In addition,  $I^{\pm S_1}(90^\circ)$  corresponds to the incoming vectors  $\vec{S} = (S_0, \pm S_1, 0, 0)$  and the analyzer oriented at  $90^\circ$ . From here, the normalised expression of  $m_{11}$ , corresponding to  $M_{11}/M_{00}$  can be retrieved:

$$m_{11} = \frac{1 - \Gamma_{11}}{1 + \Gamma_{11}}, \quad (10.51)$$

where

$$\Gamma_{11} = \frac{I^{S_1}(90^\circ) + I^{-S_1}(0)}{I^{-S_1}(90^\circ) + I^{S_1}(0)}. \quad (10.52)$$

A similar procedure can be applied for incoming state  $\vec{S} = (S_0, 0, \pm S_2, 0)$  in order to retrieve the  $m_{22}$  parameter. This time, the necessary orientations of the analyzer are  $45^\circ$  and  $135^\circ$ . Therefore, for this case, the ratio  $\Gamma_{22}$  is:

$$\Gamma_{22} = \frac{I^{S_2}(135^\circ) + I^{-S_2}(45^\circ)}{I^{-S_2}(135^\circ) + I^{S_2}(45^\circ)}. \quad (10.53)$$



Consequently, the term  $m_{22}$  is:

$$m_{22} = \frac{1 - \Gamma_{22}}{1 + \Gamma_{22}}. \quad (10.54)$$

The Figures 10.14 and 10.15 display the ratios corresponding to  $m_{11}$  and  $m_{22}$ , obtained over an area of  $2000 \times 2000$  pixels (left plot), and the variation of this ratio over a column of pixels (right plot).

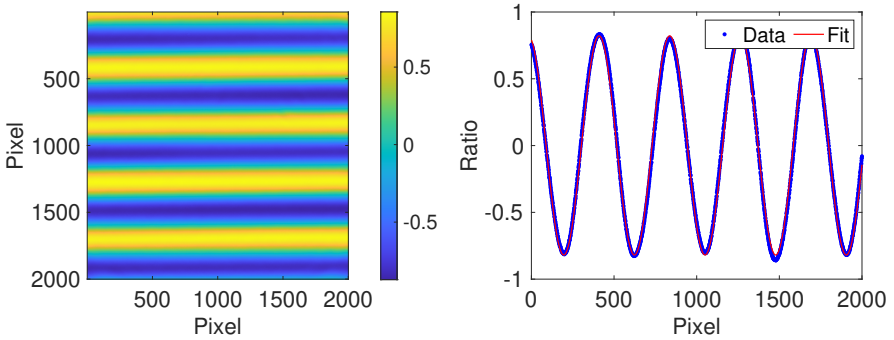


Figure 10.14: Left: the term  $m_{11}$  of the Mueller matrix of the modulator. At right, the fit of this term with the ideal expression is performed for an entire column of pixels. The name "Ratio", used for the ordinate axis in the right plot, refers to the generation of data for  $m_{11}$  with the help of the ratio (10.51).

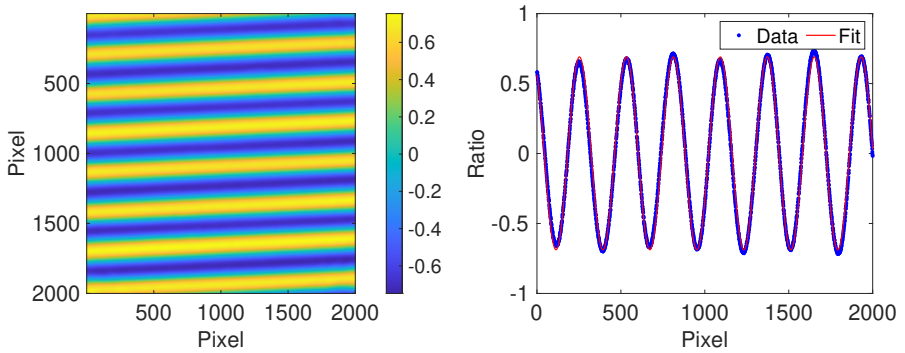


Figure 10.15: Left: the term  $m_{22}$  of the Mueller matrix of the modulator. At right, the fit of this term with the ideal expression is performed for an entire column of pixels. The name "Ratio", used for the ordinate axis in the right plot, refers to the generation of data for  $m_{22}$  with the help of the ratio (10.54).

Just like during the analysis of the separated prisms, we can assume that the terms  $m_{11}$  and  $m_{22}$  vary like:

$$\begin{cases} m_{11} = corr_{11} + att_{11} \cdot \cos(\phi_3) \\ m_{22} = corr_{22} + att_{22} \cdot \cos(\phi_1) \end{cases}. \quad (10.55)$$

Fitting these expressions to the experimental value of the corresponding relations (10.51, 10.54), the phase difference for prism 1 and 3 was reconstructed, pixel by pixel. To verify the results, the apex angles of the two prisms were inferred from the mathematical expression of the phase. The results are displayed in the Table 10.1. These results are consistent with the previous analysis of the separated prisms and also with the manufacturing specifications. However, this method does not provide a direct way to determine the fast axis orientation in each wedge. This information is lost in the complicated form of the *att* and *corr* terms.

	Modulator		Separated prisms	
	prism 1	prism 3	prism 1	prism 3
att	0.82	0.69	0.77	0.84
corr	$1.2 \cdot 10^{-3}$	$1.2 \cdot 10^{-3}$	-0.04	$1.1 \cdot 10^{-3}$
Apex	2.59°	1.70°	2.53°	1.67°

Table 10.1: Results extracted from the modulator analysis and from the separated prisms.

Another approach can be used to solve the problem. This is based on the measurement of the deviation from the ideal model. Therefore, we know that if the fast axis of the first prism is correctly oriented along the horizontal and in the third at 45°, then any incoming polarization  $\vec{S} = (S_0, \pm S_1, 0, 0)^T$  arriving collimated on the modulator will pass unaffected through the first prism (under the supposition that the Fresnel terms could be neglected). This state will receive a modulation only in the third prism. Therefore, if the first prism has a fast axis with a different orientation, then the only state that will pass unaffected will be, again, the linear state  $(S_0, S_1, S_2, 0)^T$  parallel with the real orientation of the fast axis. Thus, by varying the angle of the incoming linear polarization around the theoretical value of 0°, we can find the angle of polarization and, therefore, of the first fast axis that presents the smallest correction with respect to the theory. The same reasoning can be then applied to the third prism, through which a polarization  $\vec{S} = (S_0, 0, \pm S_2, 0)^T$  also passes unaffected.

Therefore, with the help of a series of linear polarizations, with angles close to 45°, we can also find the orientation of the third axis that minimizes the error. The measurements conducted on an interval of  $\pm 5^\circ$  around 0° and 45°, with a step of 0.1° show that the best fit of the ideal functions  $\cos(\phi_{1,3})$  is recorded for the first prism for an angle of 2.4°, and for the third prism at 48.7° (see Fig. 10.16).

That means, instead of having 45° between the first and the third axis, we have in reality 46.3°. The relative rotation with approximately 1.3° appears to happen around one of the edges. This rotation is also responsible for the tilt of the

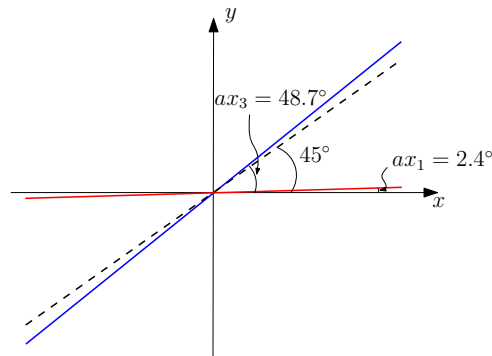


Figure 10.16: Fast axes orientation of the two main components of the modulator to the laboratory frame.

fringes visible in Fig. 10.15. Therefore, given this rotation, the rays passing through the modulator's right extremity are traveling a longer path inside the modulator than the rays from the left side. This results in an increasing deviation of the rays upward.

The phenomenon is only visible for the states different from  $(S_0, \pm S_1, 0, 0)^T$ . As we can see, this state passes unaltered through the first and second prisms. Therefore, it sees no rotation of the medium. On the contrary, the other linear states deviate upwards from the exit of the first prism. This deviation increases with the optical path. When the prisms are rotated, the entry and exit faces are no longer parallel, and then the light will travel different distances inside. These artifacts are a lesson learned about how detailed the manufacturing requirements for such a modulator should be.

# BIBLIOGRAPHY

- Collett, E. (2005). *Field guide to polarization*. SPIE. <https://doi.org/10.1117/3.626141>
- Ghosh, N., Wood, M. F. G., & Vitkin, I. A. (2008). Mueller matrix decomposition for extraction of individual polarization parameters from complex turbid media exhibiting multiple scattering, optical activity, and linear birefringence. *J. Biomed. Opt.*, 13(4), 044036. <https://doi.org/10.1117/1.2960934>
- Lu, S.-Y., & Chipman, R. A. (1996). Interpretation of Mueller matrices based on polar decomposition. *J. Opt. Soc. Am. A*, 13(5), 1106. <https://doi.org/10.1364/JOSAA.13.001106>
- Manhas, S., Swami, M. K., Buddhiwant, P., Ghosh, N., Gupta, P. K., & Singh, K. (2006). Mueller matrix approach for determination of optical rotation in chiral turbid media in backscattering geometry. *Opt. Express*, 14(1), 190–202. <https://doi.org/10.1364/OPEX.14.000190>
- Piron, P., Vargas Catalan, E., Absil, O., & Karlsson, M. (2018). Birefringence measurements of diamond space-variant subwavelength gratings. *Appl. Opt.*, 57(17), 4909. <https://doi.org/10.1364/AO.57.004909>



# 11

## INSTRUMENTAL MATRIX DETERMINATION

*The man with a new idea is a crank until the idea succeeds.*

Mark Twain

The modulator manufactured to test the method of polarization measurement studied within this thesis was close to the specifications. Still, unexpected manufacturing deviations were identified as a relative rotation between the component prisms. In addition, it was also revealed that the Fresnel terms, ignored in the theoretical modelization, should be considered for a more accurate description of the modulation of polarization. Because of these differences between the theoretical model of the modulator and the manufactured part, it becomes impossible to retrieve the polarization through a fit of the experimental data with the ideal function (4.19), which describes the variation of the intensity as a function of the Stokes parameters. The only solution for accessing the polarimetric information remains the determination of the modulation matrix  $W$  and, from here, of the demodulation (or instrumental) matrix,  $W^{-1}$  (see Chapter 3).

An arbitrary polarization state ( $\vec{S}_{in}$ ) that passes through an optical system consisting of the previously described modulator (of Mueller matrix  $M$ ) followed by a linear analyzer oriented at an angle  $\theta$ ,  $M_{LP2}$ , (see Fig. 11.1) is converted into the outgoing state  $\vec{S}_{out}$  following the classical relation:

$$\vec{S}_{out} = M_{LP2} \cdot M \cdot \vec{S}_{in}. \quad (11.1)$$

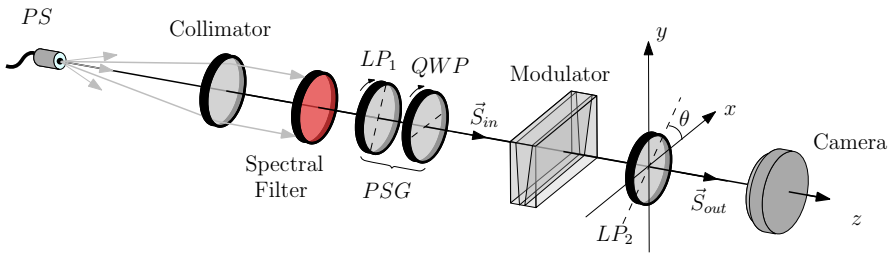


Figure 11.1: The light from a polychromatic source ( $PS$ ) first passes through a collimator and a spectral filter. A state  $\vec{S}_{in}$  is generated with the help of a polarization state generator ( $PSG$ ), composed from a linear polarizer ( $LP_1$ ) and a  $QWP$ .  $LP_1$  and  $QWP$  can be rotated to produce any desired polarization state. The light polarized by the  $PSG$  passes through the modulator  $M$  and the linear polarizer  $LP_2$ , oriented at an angle  $\theta$  to the  $x$ -axis. After  $LP_2$ , the state of polarization is  $\vec{S}_{out}$ . The camera detects the first term of the vector  $\vec{S}_{out}$ , representing light intensity.

The intensity detected after the passage of light through this optical system is represented by the first term of the outgoing Stokes vector,  $\vec{S}_{out}$ . If we call this term  $I_{out}$ , then we can write:

$$I_{out} = \vec{S}_{out}(1) = \left( M_{LP2} \cdot M \cdot \vec{S}_{in} \right) (1). \quad (11.2)$$

The previous chapter showed that the actual modulator differs from the theoretical model, and aberrations due to misalignment of the optical components are inherent. Because of this, it is expected that the phase will vary not only in the vertical direction but also very little in the horizontal direction. Therefore, each column of the detector should be characterized separately. Thus, for a column  $l$  of the detector, comprising  $n$  pixels, the intensity displayed by a pixel  $k$  is:

$$I_{out}^k = \frac{1}{2}(S_0 \cdot w_{00}^k + S_1 \cdot w_{01}^k + S_2 \cdot w_{02}^k + S_3 \cdot w_{03}^k), \quad (11.3)$$

where  $w_{0i}^k$ , ( $i = 0, 1, 2, 3$ ,  $k = 0 : n - 1$ ) are the elements of the first line of the matrix  $M_{LP2} \cdot M_M$ , characterizing the pixel ( $l, k$ ). Therefore, to the  $n$  pixels of the column  $l$  of the detector it can be associated the modulation matrix  $W^l$ :

$$W^l = \frac{1}{2} \begin{pmatrix} w_{00}^1 & w_{01}^1 & w_{02}^1 & w_{03}^1 \\ w_{00}^2 & w_{01}^2 & w_{02}^2 & w_{03}^2 \\ \dots & \dots & \dots & \dots \\ w_{00}^k & w_{01}^k & w_{02}^k & w_{03}^k \\ \dots & \dots & \dots & \dots \\ w_{00}^n & w_{01}^n & w_{02}^n & w_{03}^n \end{pmatrix}, \quad (11.4)$$

so that the intensity detected by each of these pixels from the line  $l$  can be expressed as:

$$\begin{pmatrix} I_1 \\ I_2 \\ \dots \\ I_n \end{pmatrix} = \frac{1}{2} \begin{pmatrix} w_{00}^1 & w_{01}^1 & w_{02}^1 & w_{03}^1 \\ w_{00}^2 & w_{01}^2 & w_{02}^2 & w_{03}^2 \\ \dots & \dots & \dots & \dots \\ w_{00}^k & w_{01}^k & w_{02}^k & w_{03}^k \\ \dots & \dots & \dots & \dots \\ w_{00}^n & w_{01}^n & w_{02}^n & w_{03}^n \end{pmatrix} \cdot \begin{pmatrix} S_0 \\ S_1 \\ S_2 \\ S_3 \end{pmatrix} \quad (11.5)$$

Thus, finding the incoming Stokes vector  $\vec{S}_{in}$  from the values of the intensity recorded along the line  $l$  of the detector,  $\vec{I}$ , seems to be trivial:

$$\vec{S}_{in} = (W^l)^{-1} \cdot \vec{I} \quad (11.6)$$

Unfortunately, as long as the actual instrument differs from the theoretical model, the modulation matrix  $W^l$  remains unknown, and the polarization cannot be retrieved. Also, for the same reason, the fit method, consisting of the fit of the retrieved experimental data with the function (4.19), cannot be successfully applied to find the polarization.

The only solution to this problem is trying to find  $W^l$  experimentally.

Two methods can be used to determine this matrix. One is based on the singular value decomposition of an intensity matrix obtained after measuring several well-known polarization states from the Poincaré sphere. The second is an iterative process considering the measurements conducted for only seven polarization states.

Both procedures are explained hereafter.

## 11.1. METHOD I: SINGULAR VALUE DECOMPOSITION

This method exploits the findings from (Boulbry et al., 2007), extending the principle from an instrument where the orientation of the analyzer varies to our instrument, where the phase varies.

Therefore, in its initial form, this method (Boulbry et al., 2007) considered the case of a polarimeter in which the modulation is obtained by changing the orientation of the analyzer. In our case, however, the polarizer is fixed, and the modulation results from the phase variation in the vertical direction. In other words, the difference between the



lines of the matrix  $W^l$  is determined by the phase difference of the light and not by the position of the analyzer.

By measuring  $P$  incoming states of polarization (well-known), chosen from the Poincaré sphere, then, for a column of pixels  $l$ , the previous relation (11.5) becomes:

$$\left\{ \begin{array}{l} \text{Measurement 1, incoming state } S_{in}^1 : \begin{pmatrix} I_1^1 \\ I_2^1 \\ \cdot \\ I_k^1 \\ \cdot \\ I_n^1 \end{pmatrix} = W^l \begin{pmatrix} S_0^1 \\ S_1^1 \\ S_2^1 \\ S_3^1 \end{pmatrix} \\ \text{Measurement 2, incoming state } S_{in}^2 : \begin{pmatrix} I_1^2 \\ I_2^2 \\ \cdot \\ I_k^2 \\ \cdot \\ I_n^2 \end{pmatrix} = W^l \begin{pmatrix} S_0^2 \\ S_1^2 \\ S_2^2 \\ S_3^2 \end{pmatrix} \\ \cdot \\ \cdot \\ \text{Measurement } P, \text{ incoming state } S_{in}^P : \begin{pmatrix} I_1^P \\ I_2^P \\ \cdot \\ I_k^P \\ \cdot \\ I_n^P \end{pmatrix} = W^l \begin{pmatrix} S_0^P \\ S_1^P \\ S_2^P \\ S_3^P \end{pmatrix} \end{array} \right. \quad (11.7)$$

We can write all these measurements in unique matrix form:

$$\begin{pmatrix} I_1^1 & I_1^2 & \dots & I_1^P \\ I_2^1 & I_2^2 & \dots & I_2^P \\ \dots & \dots & \dots & \dots \\ I_k^1 & I_k^2 & \dots & I_k^P \\ \dots & \dots & \dots & \dots \\ I_n^1 & I_n^2 & \dots & I_n^P \end{pmatrix} = \frac{1}{2} \begin{pmatrix} w_{00}^1 & w_{01}^1 & w_{02}^1 & w_{03}^1 \\ w_{00}^2 & w_{01}^2 & w_{02}^2 & w_{03}^2 \\ \dots & \dots & \dots & \dots \\ w_{00}^k & w_{01}^k & w_{02}^k & w_{03}^k \\ \dots & \dots & \dots & \dots \\ w_{00}^n & w_{01}^n & w_{02}^n & w_{03}^n \end{pmatrix} \cdot \begin{pmatrix} S_0^1 & S_0^2 & \dots & S_0^P \\ S_1^1 & S_1^2 & \dots & S_1^P \\ S_2^1 & S_2^2 & \dots & S_2^P \\ S_3^1 & S_3^2 & \dots & S_3^P \end{pmatrix} \quad (11.8)$$

This relation should be applied to all the detector lines using the measurements from the detector plane. Therefore, by ignoring the superscript  $l$ , we can write, in a very contracted form:

$$[I] = W \cdot [S], \quad (11.9)$$

where  $[I]$  is the  $(n \times P)$  matrix of intensity, and  $[S]$  the  $(4 \times P)$  matrix of the states of polarization used as input. It must be stressed that even if we ignore the superscript  $l$  in our notation, this relation continues to refer to a single line of pixels.

Because we search for the value of  $W^{-1}$ , which can give access to the determination of any incoming state of polarization  $\vec{S}$ , and the only known elements are now the measured intensity matrix  $[I]$  and the input states of polarization,  $[S]$ , we can write:

$$W^{-1} = [S] \cdot [I]^{-1}. \quad (11.10)$$

Here,  $[I]^{-1}$  is the right inverse matrix of  $[I]$ , and, generally, it can be computed via:

$$[I]^{-1} = [I]^\dagger = [I]^T \cdot ([I] \cdot [I]^T)^{-1}. \quad (11.11)$$

Theoretically, for our system (and not only (Boulbry et al., 2007)), the condition number of the product  $[I] \cdot [I]^T$  is infinite. Therefore, it cannot be inverted. It is expected that this product will also be ill-conditioned in practice. In this case, the singular value decomposition (SVD) could be used instead to retrieve  $[I]^{-1}$ . Using this method,  $[I]$  can be written as:

$$[I] = U \cdot D \cdot V^T. \quad (11.12)$$

In this formulation,  $U$  is built with the nonzero eigenvalues of  $[I]$ , noted here  $\sigma_i$ . The columns of  $U$  are given by:

$$u_i = \frac{1}{\sigma_i} [I] v_i, \quad (11.13)$$

where  $v_i$  is the eigenvector corresponding to  $\sigma_i$ .  $V$  is the matrix of the eigenvectors of  $[I]$ , and  $D = \text{diag}(\sigma_1, \sigma_2, \sigma_3, \sigma_4, \dots)$ . With this notation, the inverse of  $[I]$  becomes:

$$[I]^\dagger = V \cdot D^{-1} \cdot U^T = V \cdot \text{diag}\left(\frac{1}{\sigma_1}, \frac{1}{\sigma_2}, \dots, 0, \dots\right) \cdot U^T. \quad (11.14)$$

If the eigenvalues of the matrix  $[I]$  are equal to zero, we must carefully replace the expression  $1/\sigma_i$  with 0 in the matrix  $D^{-1}$ .

After obtaining the value  $[I]^\dagger$ , the instrumental matrix  $W^{-1}$  can be easily retrieved using Eq. (11.10) since the matrix  $[S]$  is already known.

## 11.2. ASSESSING THE INCOMING STOKES VECTORS

The challenge of this method for determining the instrumental matrix  $W^{-1}$  consists of correctly assessing the input Stokes vectors in the matrix  $[S]$ . Without a calibrated polarization state generator (PSG), these vectors must be obtained by combining polarizers and various waveplates. This fact can be the source of significant errors.

In addition, because every pixel counts in the characterization of the modulator, a lack of spatial homogeneity in the generated states of polarization across the illuminated area can also be a source of errors. To explain this phenomenon, we must return to equation (11.5). The vector  $\vec{S}_{in}$  characterizes the light entering the modulator at any point of the illuminated entry face. However, the vector  $\vec{I}$  contains the intensity detected by each

pixel of a column  $l$  of the detector. The homogeneity of the components of the polarization state generator, the detector, and the noise influences this vector. To completely avoid any problem related to spatial homogeneity of the incoming polarization, the procedure described in Eq. (11.5) must be applied pixel by pixel, this time by rotating the analyzer.

It is an approach that should be considered for future work. However, here, we have privileged a different approach. Instead of characterizing the modulator by pixels, we opted for line characterization. The difficulty of this approach is understanding how the system converts a supposed homogeneous incoming signal into an inhomogeneous detected signal. We use a rotating linear polarizer ( $LP_1$ ) and a quarter-wave plate ( $QWP$ ) to produce the required polarization states (see Fig. 11.2).

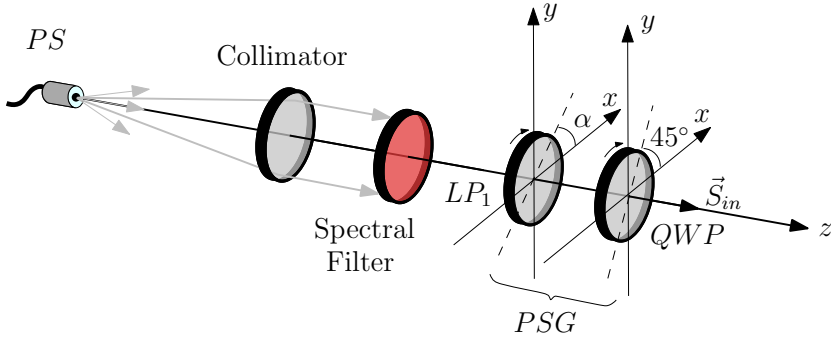


Figure 11.2: Working principle for the polarization state generator (PSG). By rotating the linear polarizer ( $LP_1$ ) in front of the  $QWP$  oriented at  $45^\circ$  to the  $x$ -axis, the states described by Eq. (11.16) are obtained. When the  $QWP$  is oriented at  $90^\circ$ , the states from Eq. (11.17) are generated.

Thus, if the  $QWP$  is oriented at  $45^\circ$  with respect to the horizontal, then by rotation  $LP_1$  we obtain the states of polarization:

$$\vec{S}(\alpha) = \frac{1}{2} S_0 \begin{pmatrix} 1 \\ 0 \\ \sin(2\alpha) \\ \cos(2\alpha) \end{pmatrix} \quad (11.15)$$

where  $\alpha$  is the orientation of the transmission axis of  $LP_1$  with respect to the horizontal (see Fig. 11.2). On the other hand, if the  $QWP$  is positioned with the fast axis at  $90^\circ$ , then we obtain the vectors:

$$\vec{S}(\alpha) = \frac{1}{2} S_0 \begin{pmatrix} 1 \\ \cos(2\alpha) \\ 0 \\ \sin(2\alpha) \end{pmatrix}. \quad (11.16)$$

In both cases,  $S_0$  is the term corresponding to the intensity of the incident light.

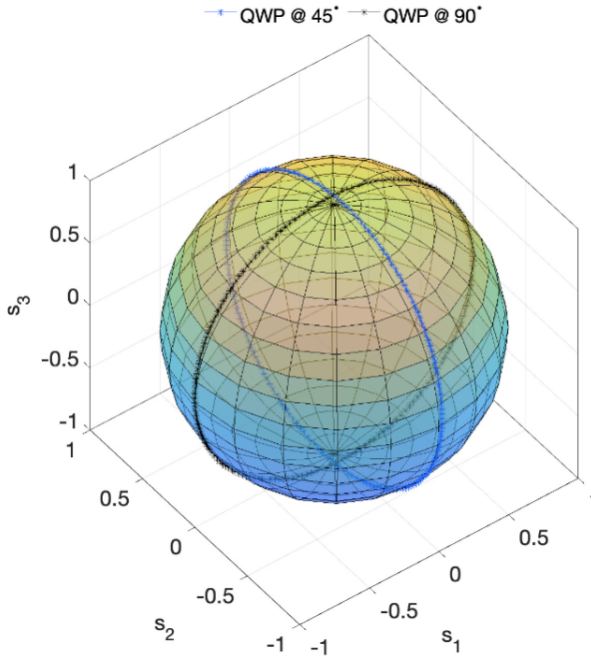


Figure 11.3: The average states of polarization used for the determination of the instrumental matrix of the modulator.

If we represent all these states on the Poincaré sphere, we obtain the result presented in Fig. 11.3. We have a complete encircling of the sphere.

However, the generated Stokes vectors can be different from the equations (11.15), (11.16). They can vary across the region of interest, from one pixel to another, complicating the instrumental matrix's measurement procedure. If we consider the spatial variation of the source only, which showed a standard deviation of 1.94%, then this distribution will characterize the  $S_0$  parameters of the Stokes vectors reaching each pixel. The rest of the parameters of the Stokes vectors will be affected by the properties and alignment of  $LP_1$  and  $QWP$ .

Thus, if we look at the  $QWP$ , we see that the actual physical properties of this component are slightly different from the theory. Therefore, at 515 nm, the  $QWP$  is not precisely a  $QWP$ , displaying a theoretical retardance of 0.242 waves, according to the datasheet, and a transmission of 96.64%. The Mueller matrix of the  $QWP$  must be adjusted to quantify the impact of these differences. In addition, the  $QWP$  should be oriented at  $45^\circ$  and  $90^\circ$  to produce the necessary polarization states, orientations that can only be obtained with approximate accuracy. All these deviations will have a direct impact on the generated Stokes vectors.

To characterize the  $QWP$  in the current  $PSG$ , we can use the procedure synthesized in Fig. 11.4.

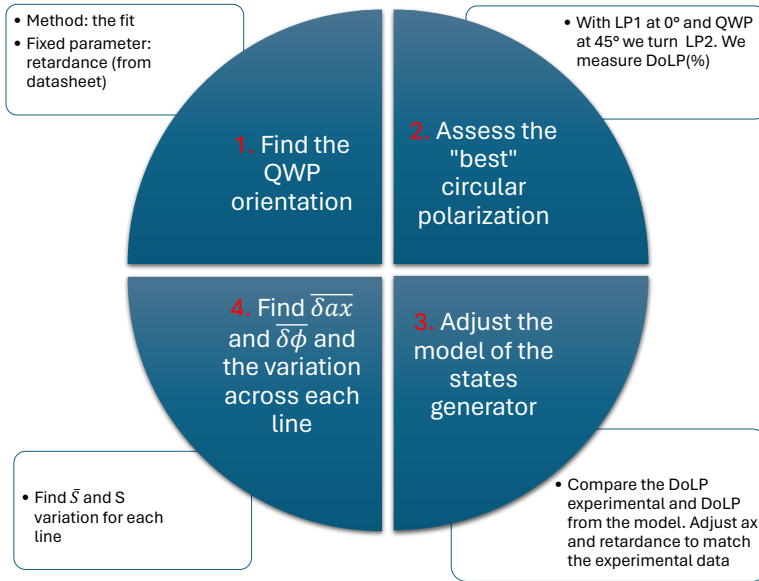


Figure 11.4: Generation of the incoming polarization states and assessment of errors

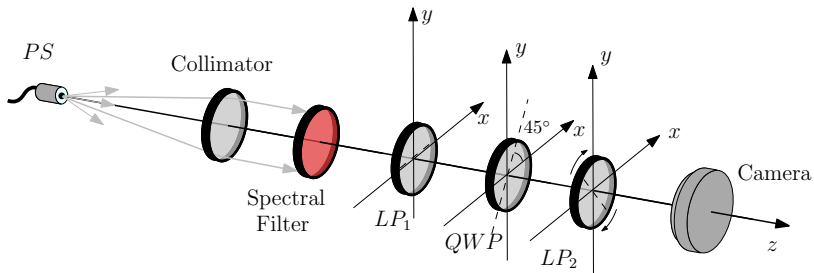


Figure 11.5: Check of the orientation of *QWP* with respect to *LP*<sub>1</sub>: the unpolarized light from the left side passes through *LP*<sub>1</sub> oriented at 0° and then through *QWP* with the fast axis at 45°; therefore, the polarization state after *QWP* should be circular. A rotation of *LP*<sub>2</sub> should not display a variation of the intensity with the position of its transmission axis.

At first, the fit procedure for the ratio of intensities (see Section 10.1) can be used to retrieve the orientation of the fast axis of *QWP* under the supposition that the birefringence of the plate corresponds to the datasheet. To verify the result, we can place the first linear polarizer (*LP*<sub>1</sub>) at 0°, the *QWP* at 45°, and then rotate the second linear polarizer (*LP*<sub>2</sub>) between 0° and 180° (see Fig. 11.5).

If the *QWP* is correctly oriented, and the birefringence corresponds exactly to the datasheet, we should obtain a maximal intensity variation with the angle of *LP*<sub>2</sub> of about

5%. The definition of variation corresponds, in this case, to the degree of linear polarization:

$$DoLP = 100 \frac{I_{max} - I_{min}}{I_{max} + I_{min}} \quad (11.17)$$

Having  $DoLP \neq 0$  means the system cannot produce a perfect circular polarization.

In practice, the retrieved variation of the intensity for this polarimetric configuration varies between 4% and 16% (see Fig. 11.6) across the region of interest.

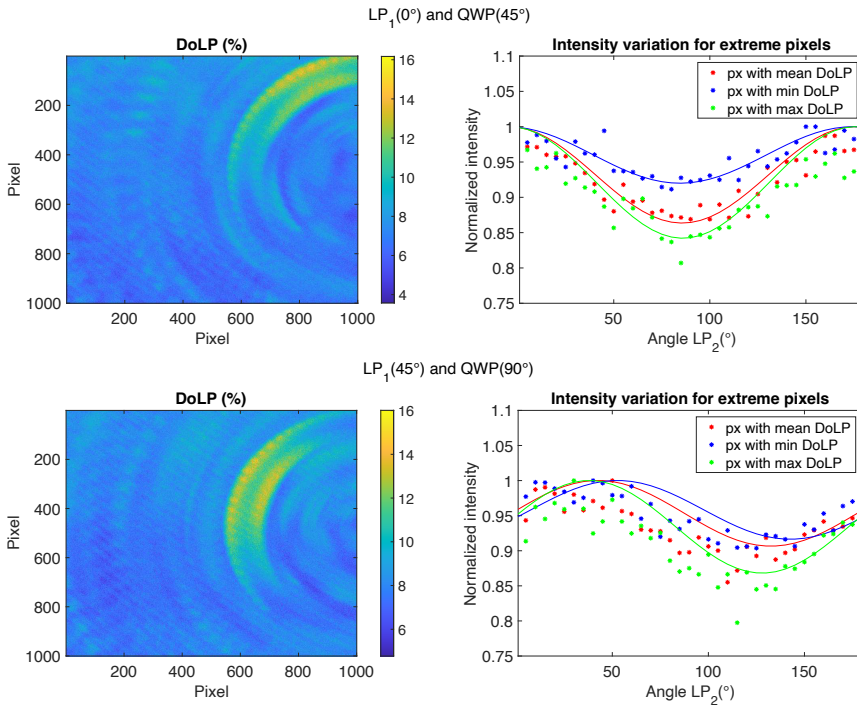


Figure 11.6: Degree of linear polarization ( $DoLP$ ) obtained with configurations of the  $PSG$  that should produce, theoretically, circular polarization. Ideally, the two configurations should be equivalent. In practice, we notice a slight difference between the two. This is due to a possible misalignment of the  $QWP$ . The right-side plots present the intensity variation while turning  $LP_2$  of the pixels that exhibit the maximum, average, and minimum  $DoLP$ . The continuous lines correspond to the theoretical model adjusted for the best fit.

In addition, even though a configuration  $LP_1(45^\circ)$  and  $QWP(90^\circ)$  should produce the same variation of intensity, we notice a difference between the two configurations, a difference which is caused by the misalignment of the setup. We will neglect the magnitude of the error due to this misalignment of the  $QWP$  for the moment. Instead, taking an arbitrary line of pixels (for instance, 200) that shows a relatively small average  $DoLP$ , we will try to adjust the theoretical model of the  $QWP$  so that the same  $DoLP$  is produced. We will look at the pixels close to the mean  $DoLP$ , those with maximum  $DoLP$ , and minimum  $DoLP$ . These three values will provide the mean values of the adjustments needed for the fast axis orientation and the retardance of the  $QWP$ . Ultimately,

with these adjustments, we can infer the possible values taken by the Stokes vectors created with  $LP_1$  and  $QWP$ .

As can be noticed in Fig. 11.6, the  $DoLP$  takes different values in the two cases studied ( $LP_1(0^\circ) + QWP(45^\circ)$ , and  $LP_1(45^\circ) + QWP(90^\circ)$ ), and the variation of intensity that allows the determination of this  $DoLP$  embrace distinct patterns in the two cases. In addition, adjusting the theoretical model for the best correspondence with the experimental data produces only an approximate result. This is because changing the fast axis and the retardance of the  $QWP$  are not enough to compensate for the variation in the intensity. These two parameters are insufficient to suppress the effects of the misalignment, dust, or other causes. However, by considering these variations of the  $DoLP$  across a single line of pixels, we can compute the approximate extreme values between which the generated Stokes vectors vary.

The results are presented in Fig. 11.7.

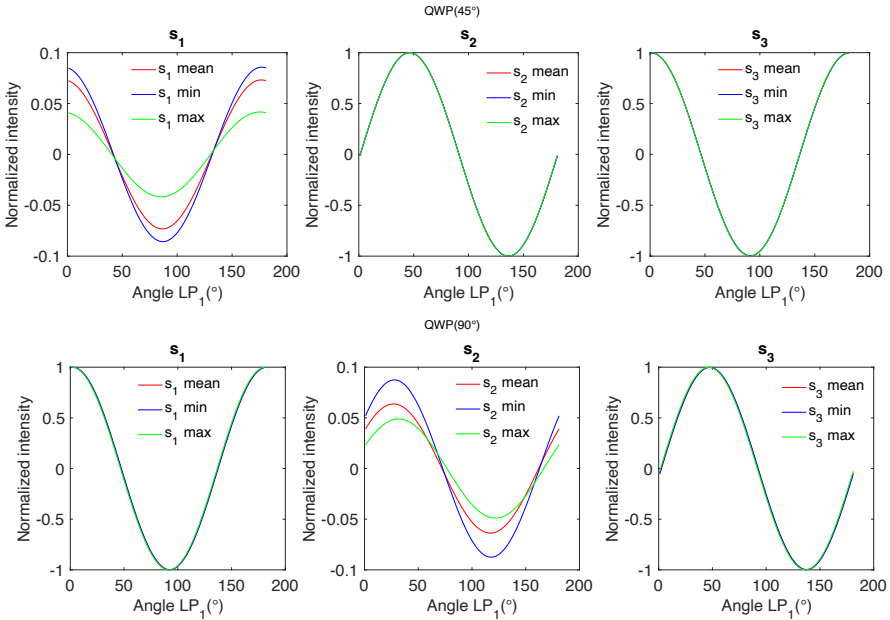


Figure 11.7: Possible values of the generated Stokes vectors as inferred from the variation of the  $DoLP$  across a single line of pixels.

We notice that with a rotating  $LP_1$  and a  $QWP$  oriented at  $45^\circ$ , the most impacted term is  $s_1$ , a term that should be zero. For the second configuration,  $s_2$  is the most impacted. Again, this is the case of the term that should be zero. A global view of this phenomenon is presented in Fig. 11.8, where the theoretical ideal value of the Stokes parameters is also plotted (the red curve) for each of the 360 vectors generated.

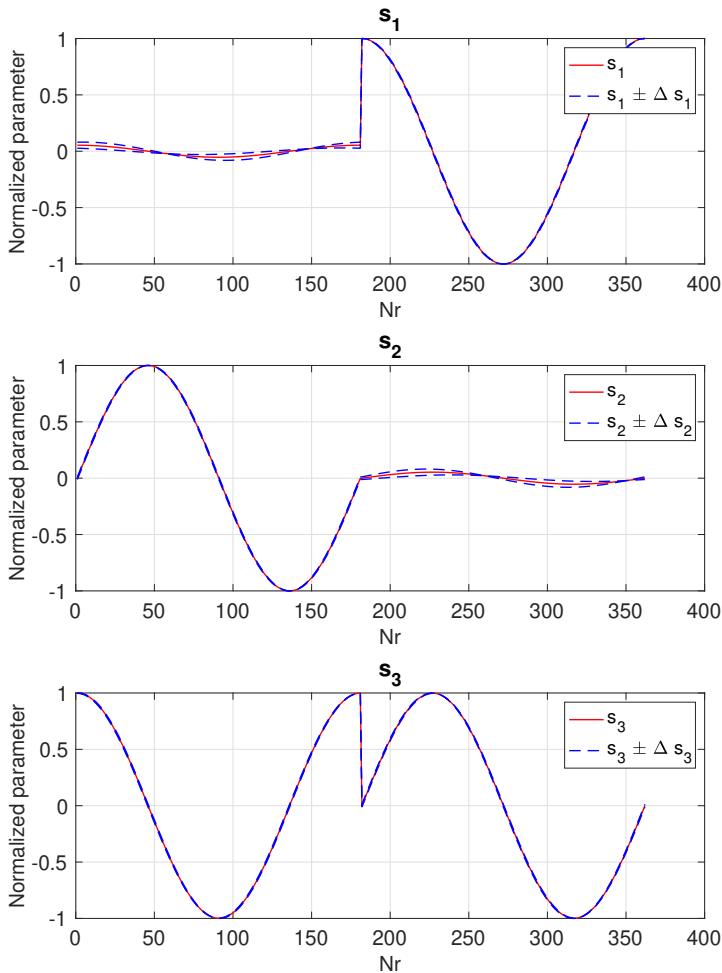


Figure 11.8: Maximal variation of the parameters of  $[S]$  (in blue) and ideal value (red). Until the number 180, the states are generated with the first orientation of the  $QWP$  and, after this, with the second configuration. We observe how the curves corresponding to the normalized Stokes parameters  $s_1$ ,  $s_2$ , and  $s_3$  deviate from the Eq. (11.15), and (11.16).

The misalignment of the instrument and the improper behavior of the  $QWP$  result in an inhomogeneous linear term. A  $QWP$  oriented at  $45^\circ$  generates a variable horizontal or vertical polarization component. On the other hand, a  $QWP$  at  $90^\circ$  produces a  $45^\circ$  or  $135^\circ$  linear component. For both configurations, the total degree of linear polarization never descends below 5%.

Assessing the error in estimating the incoming vectors' parameters is a relative task.



It depends on the orientation of the first linear polarizer,  $LP_1$ . The most affected parameter in the states generated with  $QWP$  at  $45^\circ$  shows a variation reaching 34% to the average of  $s_1$  for certain positions of the linear polarizer,  $LP_1$ . Still, for several orientations of  $LP_1$ , this variation is close to zero. Nevertheless, the variation is negligible for the other two parameters ( $s_2$  and  $s_3$ ). Overall, it is below 0.1%. The states generated with  $QWP$  at  $90^\circ$  seem even more problematic. In this case,  $s_2$ , the most impacted parameter, shows a variation that can reach even 42.5%, whereas the other two parameters also stay below 0.1%.

Despite the substantial variation of  $s_1$  and  $s_2$  in both configurations, the repercussions on the instrumental matrix are expected to be minimal. This is because the effect of these strong variations on the global state of polarization remains limited. Indeed, these variations are translated into an increase with a maximum of 2% of the  $DoLP$  for the chosen line of pixels. Nevertheless, the values of  $QWP$  parameters that best describe the minimum value of  $DoLP$ , the mean and maximum value across a line of pixels, also dictate the uncertainty of the demodulation. Therefore, by considering the variation of the incoming Stokes vector across a line of pixels, the relation (11.10) should be rewritten as:

$$\begin{cases} W_{mean}^{-1} = [S]_{mean} \cdot [I]^{-1} \\ W_{min}^{-1} = [S]_{min} \cdot [I]^{-1} \\ W_{max}^{-1} = [S]_{max} \cdot [I]^{-1} \end{cases} \quad (11.18)$$

where the vectors  $[S]_{mean}$ ,  $[S]_{min}$  and  $[S]_{max}$  are obtained with the parameters of the  $QWP$  that are providing a  $DoLP$  close to the average value across the line of pixels, to the minimum value, respectively the maximum. Each of these instrumental matrices will drive to a specific demodulated Stokes vector. The variation of the possible outcome represents the uncertainty of the results. Concerning the demodulation error, assessing it precisely in the given system configuration is impossible. Let us think, for instance, of the polarization states generated as a test with a rotating  $LP_1$  and the  $QWP$  oriented at  $30^\circ$ . Like in previous configurations, this polarization state will develop an inhomogeneous result along a line of pixels. However, we do not have the corresponding correction parameters for the  $QWP$  to track this inhomogeneity. We can only suppose that we stay within the same limits as in the previous cases as long as the system is not altered. Therefore, we may say again that the incoming polarization varies across the line of pixels between the limits imposed by the variation of the retardance and the fast axis.

Based on these hypotheses, we can build the possible outcome of a rotating  $LP_1$  and a  $QWP$  oriented at  $30^\circ$ . The results are presented in Fig. 11.9. We now notice that because all of the Stokes parameters exhibit a variation with a high amplitude, no such uncertainties as before are encountered. Again, the most affected parameter is that with the smallest amplitude,  $s_1$ . However, overall, the uncertainty with respect to the mean value stays below 1%.

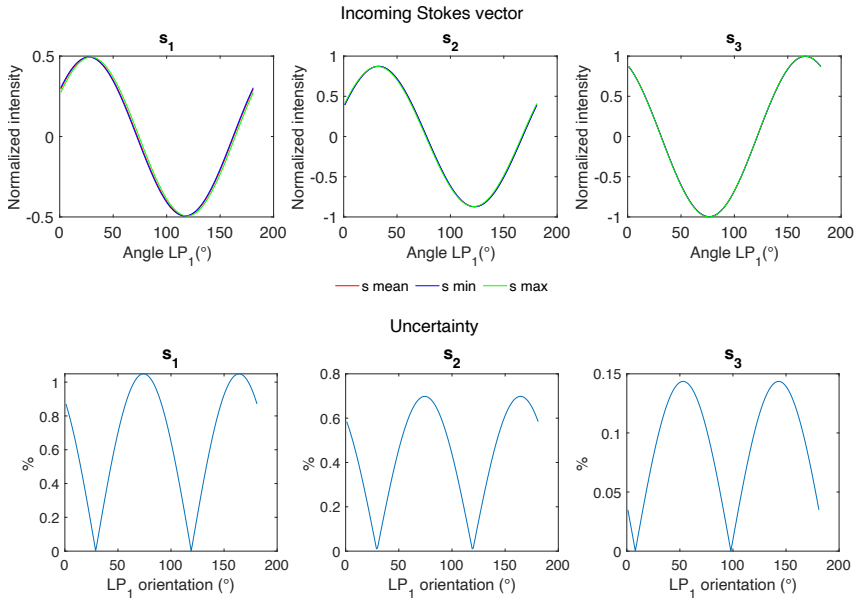


Figure 11.9: Incoming Stokes parameters (normalized value) corresponding to the states obtained through the rotation of  $LP_1$  for a  $QWP$  oriented at  $30^\circ$ . The values of the Stokes parameters were simulated starting from the retrieved characteristics of  $LP_1$  and the  $QWP$ . The uncertainty corresponds to the interval of variation of each parameter for every orientation of  $LP_1$ .

Nevertheless, because there is no other possibility to check the accuracy of the hypotheses made to build these vectors, we cannot tell with enough precision what is the real interval of variation across the line of pixels. Because of this, after demodulation, there is no reference after which to establish an error. To overcome this situation, a calibrated  $PSG$  generator must be used in the beginning to retrieve the instrumental matrix, and then the demodulation should be applied to well-known sources of polarization.

Despite the lack of precision in the  $PSG$  functioning and the misalignment assessment, which cannot be compensated by adjusting the  $QWP$  properties, the first tests for the demodulation are very promising. In this test, we have tried to retrieve the 180 states of polarization generated by rotating  $LP_1$  in front of a  $QWP$  oriented at  $30^\circ$ , states that are presented in Fig. 11.9.

The results of the demodulation process are presented in Fig. 11.10. If we look only at the mean values of the incoming and demodulated Stokes vectors, we observe that the relative difference between the parameters stays, on average, below 5% for most the orientations of  $LP_1$ . Despite the errors and misalignment present in our optical setup, these results demonstrate that demodulation of the polarimetric signal can be performed smoothly for any incident polarization. Access to a better quality polarization state generator and adopting the pixel-by-pixel instrumental matrix determination strategy can help improve the results and simplify the calibration procedure.

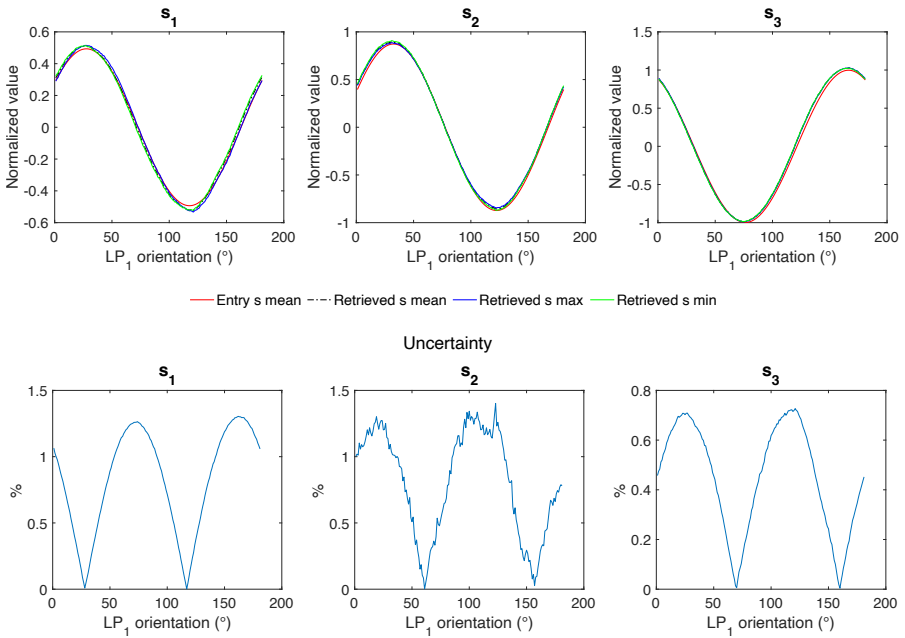


Figure 11.10: The first three graphics from the top present the mean value of the incoming Stokes parameters (red) obtained through simulation. The remaining curves show the retrieved parameters according to the  $[S]$  values used to compute  $W^{-1}$ . The second row of graphics shows the variation of the output Stokes parameters when the different instrumental matrices are used for demodulation.

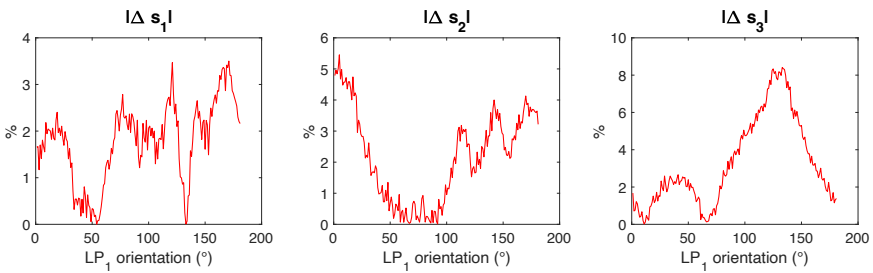


Figure 11.11: Relative difference between the simulated mean values of the Stokes parameters and the retrieved mean values.

### 11.3. METHOD II: OPPOSED STATES OF POLARIZATION

A more traditional way to find the modulation matrix is to use the opposed polarization states chosen from the Poincaré sphere. Therefore, following Eq. (11.3), if non-polarized light is passing through the system comprising the modulator and an analyzer oriented at an angle  $\theta$ , then the detected intensity by the pixel  $(k, l)$  can be expressed as:

$$I_{out} = \frac{1}{2} S_0 w_{00} \tag{11.19}$$

Therefore, after preliminary measurement of  $S_0$  in the absence of the modulator and the analyzer,  $w_{00}$  can be obtained for any  $(k, l)$  and for the desired orientation of the analyzer. Further, using step-by-step the incoming states  $\vec{S} = (S_0, \pm S_1, 0, 0)^T$ ,  $\vec{S} = (S_0, 0, \pm S_2, 0)^T$  and  $\vec{S} = (S_0, 0, 0, \pm S_3)^T$ , where  $T$  denotes the transposition operator, the rest of the terms of the modulation matrix can be retrieved.

For instance, an incoming Stokes vector  $\vec{S} = (S_0, \pm S_1, 0, 0)^T$  will provide, for any pixel  $(k, l)$ , the intensities :

$$I^\pm = \frac{1}{2} S_0 (w_{00} \pm w_{01}), \quad (11.20)$$

if we assume a total polarization ( $|S_1| = S_0$ ). From here, it can be inferred:

$$w_{01} = w_{00} \frac{I^+ - I^-}{I^+ + I^-}. \quad (11.21)$$

The same type of formula can be developed for the rest of the terms,  $w_{02}$  and  $w_{03}$ , by using total polarization at  $\pm 45^\circ$  and circular left and right, respectively.

This is a straightforward procedure for determining the matrix  $W$  corresponding to each pixel. Just like in the previous case, its success depends on the knowledge of the input vectors.



# BIBLIOGRAPHY

Boulbry, B., Ramella-Roman, J. C., & Germer, T. A. (2007). Improved method for calibrating a stokes polarimeter. *Appl. Opt.*, 46(35), 8533. <https://doi.org/10.1364/AO.46.008533>



# 12

## CONCLUSIONS AND PERSPECTIVES



A new method for the complete measurement of polarization at different wavelengths was explored in this research. This method will allow us to build compact, robust, and highly performant instruments which are suitable, among many other domains, for use in the space environment.

We started our exploration from an idea previously proposed in the literature about the possibility of conducting spectropolarimetric measurements with the help of a combination of birefringent prisms. We investigated this idea, providing scientific proof for its principle and exploring the different design possibilities. Analyzing figures of merit like the efficiency of the modulation scheme, the condition number, or the equally weighted variance, we identified the configurations leading to a highly accurate measurement of polarization. We also proved that, at least theoretically, this method of retrieving the polarization is close to an optimal one: it allows the determination of the Stokes parameters with equal and highest achievable precision.

In the end, we made the step from theory to practice, and we built a prototype of the central part of this method, the modulator. The objective was double-folded: to validate this polarization measurement approach and to learn what is happening with the polarized light that passes through such optical elements.

Both objectives were, at least partially, fulfilled. Many questions were answered, and many others arose along the way, requiring a deeper analysis of certain aspects. The experiments proved that the state of the incoming polarization can be retrieved using this approach, at least for a specific wavelength and certain bandwidth. At the same time, many lessons were learned that can help us improve this technique in the future, expand its field of applications, and explore new possibilities to apply its principles.

Five fundamental questions guided this research, and at least partial answers were provided.

### **1. Does the signal detected with an instrument using this method correspond to a single state of polarization?**

Solving the problem of the uniqueness of the solution is of paramount importance for this method of the retrieval of polarization. This can tell us if a unique intensity pattern in the detector plane characterizes every incoming polarization state.

The main "responsible" for the uniqueness is the modulation matrix of the instrument. We saw that this matrix relates the state of polarization of the incoming light and the detected intensity. The number of lines of this matrix depends on the number of pixels in the vertical direction over which the signal is spread. In addition, the values of the terms of this matrix are influenced by the wavelength and the spectral bandwidth, by the dimension of pixels, the angles of the prisms, the birefringence of the material, the orientation of the analyzer, etc. Overall, the problem of the solution's uniqueness reduces to the modulation matrix's characteristics.

Using multiple methods, we proved in Chapter 5 that the uniqueness of the solution characterizes an optical system employing a modulator in  $MgF_2$ . Multiple proofs were brought to this question. The most straightforward, adapted also for the experimental investigation, is based on the determination of the rank of the modulation matrix. Proving that this rank is four is a necessary and sufficient condition to demonstrate the uniqueness of the solution.

In addition, by exploiting the theoretical form of the terms of the modulation matrix in the ideal condition, the uniqueness of the solution was demonstrated in two ways. At first, the notion of Wronskian was used for this purpose. However, an equivalent proof can be obtained using the modulation functions' orthogonality.

## **2. How do potential instruments built according to this method behave in noisy conditions?**

The birefringent modulator proposed within this research is the main component responsible for the capacity to detect any state of polarization at various wavelengths. Composed of three birefringent prisms with fast axes that are differently oriented, this modulator ensures a continuous variation of the phase difference of the incoming light in a specific direction. Placing a linear polarizer after this modulator, the continuous variation of phase difference is converted into a variation of intensity in the same direction. In the end, this variation of the intensity, described with the help of the optical system's modulation matrix, ensures the polarization's determination. Theoretically, the "quality" of the modulation matrix can be tested for various values of the parameters involved in the modulation with the help of the condition number. Ideally, the condition number is  $\sqrt{20}$  for an optimal polarimeter. In Chapter 6, we also proved that the proposed method's condition number converges towards  $\sqrt{20}$  with the number of pixels.

The condition number offers only limited information about an instrument using this method of spectropolarimetry. Oversimplifying, we can say that it only informs about the possibility of inverting the modulation matrix to achieve the demodulation of the detected signal. However, it brings no information about the uncertainty that may affect the Stokes parameters. For this, analyzing the optical system in noise conditions is required. Such a study was conducted in Chapters 5, 6 and 7. Using different types of noise that may affect the detected signal, the uncertainty on the Stokes parameters was mapped as a function of the various parameters of the optical system. In this way, the values of the prisms' apex angles and the analyzer's orientations that can ensure the retrieval with equal precision of all the Stokes parameters were identified. In addition, it was proved that this method can ensure optimal noise mitigation.

## **3. Which procedures can be used to retrieve the polarization, and how reliable are they?**

It has been shown in Chapters 4, 5, and 6 that two procedures for retrieving polarization can theoretically be used within this method. One of these procedures supposes the fit of the detected intensity value with the theoretical function, and the second is based on determining the modulation matrix.

The first method requires a good knowledge of the optical system so that the theoretical function can correctly describe the passage of light through the different components. We used this method in the theoretical investigation of the spectropolarimeter. However, during the experimental stage, this procedure could not be applied.

The delivered modulator exhibited pronounced differences to the blueprint, differences which were not parametrized in the theoretical model and could not be investigated numerically in a short time. Also, during the experimental part, it was observed

that the Fresnel terms, ignored in the model built using the Mueller calculus, should not be overlooked.

These were the main reasons why, during the experimental part, the retrieved intensity pattern corresponding to various polarization states differed from the anticipated one. Consequently, the theoretical model could not be used to fit the experimental data to retrieve the polarization state.

The second demodulation method overpasses the effect of the overlooked Fresnel terms or the differences between the blueprints and the manufactured modulator. This method allows us to refer directly to the actual optical system. It requires the determination of the instrumental matrix, which comprises all the ignored or neglected effects. The difficulties brought by this method are mostly related to the knowledge of the polarization states used to retrieve the instrumental matrix. Therefore, it was pointed out that a calibrated polarization state generator is paramount for a reliable determination of this matrix.

#### **4. Can this method be experimentally implemented?**

The biggest challenge in translating this method of determining the polarization into practice is manufacturing the modulator. As a custom optical part that requires high optical manufacturing skills, finding a supplier ready to meet this challenge can be difficult. We found such a supplier, and the modulator manufactured was very close to specification.

The second important step in the practical realization is represented by the optical characterization of the modulator. The fact that we have the separate prisms of the modulator made this process easier. Thus, we managed to offer a detailed description of the variation of the phase difference and the fast axis's orientation in the modulator's two main prisms.

Finally, it was necessary to establish the instrumental matrix to demonstrate the ability to determine the polarization of light. Although we did not have a calibrated polarization generator, we completed this stage. The tests performed on 180 polarization states demonstrated the ability of this instrument prototype to determine all Stokes parameters. A complete set of measurements was carried to a single wavelength, using a spectral filter. For a broader confirmation of the project, the same type of measurements should be repeated at different wavelengths.

#### **5. How can it be exploited in the future?**

This remains an open question. Supposing that the full confirmation of the non-imaging working mode is achieved, an entirely new horizon opens. We have the basis to build very compact and robust non-imaging spectropolarimeters at that moment. Given the high compactness that can be achieved and the very small volume required by the polarimetric components, it can be imagined that such instruments will be compatible with various platforms, ranging from microscopes or ground telescopes to drones or satellites.

At the same time, it was mentioned in this thesis that an imaging working mode can be built using this method of determining the polarization. Various techniques exist today to achieve this new functionality. If such a step is made, the contribution of this instrument would be even more significant.

## 12.1. NEXT STEPS

The encouraging results exposed in this thesis represent the most essential steps for validating the new method of measuring the polarization of light. At the same time, they are opening the way towards multiple topics of research in this field. Questions arising from the observations made during the experimental part should be answered, and the investigations carried to a single wavelength should be extended to a broader spectrum. Moreover, the possibilities of achieving snapshot imaging spectropolarimetry or snapshot imaging Mueller matrix polarimetry should be explored. Achieving such capabilities could convert this method of measuring the polarization of light into a very versatile approach, with applications ranging from the space field to industry or medicine.

The most important steps that must be done next are:

- *Completing the theoretical model*

The experimental part of our research pointed out several differences between the results provided by the theoretical model of the modulator and the actual one. These differences originate in phenomena neglected in the theoretical investigation (like the Fresnel terms, the temperature, or the inhomogeneity of the birefringent media) or in the differences between the blueprints of the modulator and the manufactured specimen.

Thus, the theoretical model of the modulator should be corrected to include the effect of the neglected terms or the relative position of the prisms. Subsequently, this new model should be validated experimentally. Having a more precise theoretical model means, after all, a better understanding of the physical processes taking place in the optical components of the instrument. A better theoretical model can help us to apply this method to various instruments and to better understand the consequences of various constraints. In addition, an adequate theoretical model can be used in the demodulation process. If such a model is achieved, then the value of the intensity can be related correctly to the state of polarization of the incoming light. In the end, the analytical expression of the intensity can be used to fit the recorded data and to retrieve the Stokes parameters. Such a procedure can be more versatile than determining the instrumental matrix, as it can comprise the effect of wavelength, spectral resolution, temperature, or field of view.

Once the theoretical model is completed, it can be tested in the beginning on a non-imaging instrument. The spectropolarimeter developed by TNO and mentioned in Chapter 9 represents an excellent opportunity for this step. Using an optical prism to obtain the spectral separation of light, this design provides simultaneous access to various wavelengths. This instrument can be used without a precise theoretical description if the instrumental matrix is determined. However, its full potential is achieved only if this description is completed.

- *Developing the imaging capability*

Perhaps the most essential development of the method of accessing the polarization exposed in this thesis is its extension into the imaging working mode. This will enable the realization of the snapshot full Stokes imaging spectropolarimeter. It is a task that

remains to be done in the future. Many applications need today such capability. Astronomy, climatology, defense, industry, and medicine are just a few fields where snapshot imaging spectropolarimetry can play a major role. Several methods for achieving this capability, inspired by snapshot imaging spectrometry, were presented in this thesis. However, a more detailed investigation is needed. The different possibilities must be compared in order to identify which has the higher compatibility with the working mode of the modulator. In addition, because compactness and robustness are among the main qualities of this method, they should not be sacrificed while constructing the imaging working mode.

- *Mueller matrix imaging*

To push the usage domain even further, it can be easily proved that the imaging working mode also enables the snapshot Mueller matrix imaging. Through such a technique, all the terms of the Mueller matrix of a sample can be obtained almost instantly, in an imaging way, for various wavelengths. It is a unique capability, as it requires fewer input data to achieve the measurements compared to most of the existing instruments and does not need rotating parts. This is an application of tremendous importance in medicine, as it can help in the characterization of tissues and the diagnosis of different diseases.

These are just a few directions of evolution for this new method of measuring the polarization of light. Many other aspects can be considered and investigated along the way, offering new possibilities for development. We can cite replacing the analyzer with a polarizing beam splitter. Such a component could sacrifice the simplicity of the optical design for the benefit of higher accuracy. Even more, we can imagine replacing the modulator with a metasurface having the same capacity to modify the phase difference of light. This would enable the construction of highly compact instruments, presenting almost the same performance. All these are encouraging perspectives. Followed and investigated with faithfulness, they can lead to more performant and versatile ways of accessing this feature, which is the polarization of light. In the end, better and easier access to the polarization of light can be seen as a better understanding of the world around us.

**A**

**ADDENDUM**

## A.1. MUELLER CALCULUS

Throughout this research, we used Mueller matrices of different optical components (*LP*, *QWP*, *HWP*, *WP*). Certain differences can be found in the literature between these matrices, which come mainly from the definition of the direction of rotation and, thus, of the rotation matrix that allows the calculation of the Mueller matrices for different orientations. We based our work on the expressions used by (Hecht, 2017, Collett, 2005).

- Arbitrary wave plate of retardance  $\Delta\phi$  and orientation  $\theta$ :

$$\begin{pmatrix} 1 & 0 & 0 & 0 \\ 0 & C^2 + S^2 \cos(\Delta\phi) & CS(1 - \cos(\Delta\phi)) & -S \sin(\Delta\phi) \\ 0 & CS(1 - \cos(\Delta\phi)) & S^2 + C^2 \cos(\Delta\phi) & C \sin(\Delta\phi) \\ 0 & S \sin(\Delta\phi) & -C \sin(\Delta\phi) & \cos(\Delta\phi) \end{pmatrix}, \quad (\text{A.1})$$

where  $C = \cos(2\theta)$  and  $S = \sin(2\theta)$ .

- Mueller matrix of linear polarizer expressed in terms of absorption coefficients along  $x$  and  $y$  direction (Collett, 2005):

$$M_{LP}(p_x, p_y) = \frac{1}{2} \begin{pmatrix} p_x^2 + p_y^2 & p_x^2 - p_y^2 & 0 & 0 \\ p_x^2 - p_y^2 & p_x^2 + p_y^2 & 0 & 0 \\ 0 & 0 & 2p_x p_y & 0 \\ 0 & 0 & 0 & 2p_x p_y \end{pmatrix}, \quad (\text{A.2})$$

where  $p_{x,y} \in [0, 1]$ .

- Ideal linear polarizer (LP) with the transmission axis oriented along the  $x$ -axis ( $p_x = 1, p_y = 0, \theta = 0^\circ$ ):

$$M_{LP}(0) = \frac{1}{2} \begin{pmatrix} 1 & 1 & 0 & 0 \\ 1 & 1 & 0 & 0 \\ 0 & 0 & 0 & 0 \\ 0 & 0 & 0 & 0 \end{pmatrix}. \quad (\text{A.3})$$

- Ideal linear polarizer (LP) with the transmission axis oriented along the  $y$ -axis ( $p_x = 0, p_y = 1, \theta = 90^\circ$ ):

$$M_{LP}(90) = \frac{1}{2} \begin{pmatrix} 1 & -1 & 0 & 0 \\ -1 & 1 & 0 & 0 \\ 0 & 0 & 0 & 0 \\ 0 & 0 & 0 & 0 \end{pmatrix}. \quad (\text{A.4})$$

- Mueller matrix of a rotator (angle of rotation  $\theta$ ):

$$M_R(\theta) = \begin{pmatrix} 1 & 0 & 0 & 0 \\ 0 & \cos(2\theta) & \sin(2\theta) & 0 \\ 0 & -\sin(2\theta) & \cos(2\theta) & 0 \\ 0 & 0 & 0 & 1 \end{pmatrix}. \quad (\text{A.5})$$

- Linear polarizer oriented at an angle  $\theta$  with respect to the  $x$ -axis:

$$M_{LP}(\theta) = M_R(-\theta) \cdot M_{LP}(0) \cdot M_R(\theta) = \frac{1}{2} \begin{pmatrix} 1 & \cos(2\theta) & \sin(2\theta) & 0 \\ \cos(2\theta) & \cos^2(2\theta) & \cos(2\theta)\sin(2\theta) & 0 \\ \sin(2\theta) & \cos(2\theta)\sin(2\theta) & \sin^2(2\theta) & 0 \\ 0 & 0 & 0 & 0 \end{pmatrix}. \quad (\text{A.6})$$

- Linear polarizer oriented at  $\theta = 45^\circ$  with respect to the  $x$ -axis:

$$M_{LP}(45) = \frac{1}{2} \begin{pmatrix} 1 & 0 & 1 & 0 \\ 0 & 0 & 0 & 0 \\ 1 & 0 & 1 & 0 \\ 0 & 0 & 0 & 0 \end{pmatrix}. \quad (\text{A.7})$$

- Linear polarizer oriented at  $\theta = 135^\circ$  with respect to the  $x$ -axis:

$$M_{LP}(135) = \frac{1}{2} \begin{pmatrix} 1 & 0 & -1 & 0 \\ 0 & 0 & 0 & 0 \\ -1 & 0 & 1 & 0 \\ 0 & 0 & 0 & 0 \end{pmatrix}. \quad (\text{A.8})$$

- Quarter-wave plate ( $\Delta\phi = \frac{\pi}{2}$ ), fast axis horizontal ( $\theta = 0$ ):

$$M_{QWP}(0) = \begin{pmatrix} 1 & 0 & 0 & 0 \\ 0 & 1 & 0 & 0 \\ 0 & 0 & 0 & 1 \\ 0 & 0 & -1 & 0 \end{pmatrix}. \quad (\text{A.9})$$

- Quarter-wave plate, fast axis vertical ( $\theta = 90^\circ$ ):

$$M_{QWP}(90) = \begin{pmatrix} 1 & 0 & 0 & 0 \\ 0 & 1 & 0 & 0 \\ 0 & 0 & 0 & -1 \\ 0 & 0 & 1 & 0 \end{pmatrix}. \quad (\text{A.10})$$

- Quarter-wave plate, arbitrary fast axis orientation:

$$M_{QWP}(\theta) = \begin{pmatrix} 1 & 0 & 0 & 0 \\ 0 & C^2 & CS & -S \\ 0 & CS & S^2 & C \\ 0 & S & -C & 0 \end{pmatrix}, \quad (\text{A.11})$$

where  $C = \cos(2\theta)$  and  $S = \sin(2\theta)$ .



- Half-wave plate, fast axis horizontal ( $\theta = 0^\circ$ ):

$$M_{HWP}(0) = \begin{pmatrix} 1 & 0 & 0 & 0 \\ 0 & 1 & 0 & 0 \\ 0 & 0 & -1 & 0 \\ 0 & 0 & 0 & -1 \end{pmatrix}. \quad (\text{A.12})$$

- Half-wave plate ( $\Delta\phi = \pi$ ), fast axis vertical ( $\theta = 90^\circ$ ):

$$M_{HWP}(0) = \begin{pmatrix} 1 & 0 & 0 & 0 \\ 0 & 1 & 0 & 0 \\ 0 & 0 & 1 & 0 \\ 0 & 0 & 0 & -1 \end{pmatrix}. \quad (\text{A.13})$$

- Half-wave plate, arbitrary fast axis orientation::

$$M_{HWP}(\theta) = \begin{pmatrix} 1 & 0 & 0 & 0 \\ 0 & C^2 - S^2 & 2CS & 0 \\ 0 & 2CS & S^2 - C^2 & 0 \\ 0 & 0 & 0 & -1 \end{pmatrix}, \quad (\text{A.14})$$

where  $C = \cos(2\theta)$  and  $S = \sin(2\theta)$ .

### A.2. SPEX SPECTROPOLARIMETER

Another example of an instrument for measuring the polarization of light is the Spectropolarimeter for Planetary Exploration (SPEX). Developed in 2008, this instrument evolved into a version (SPEXone) that was already sent into space as part of NASA’s mission Plankton, Aerosol, Cloud, Ocean Ecosystem (PACE) (NASA, 2024). The instrument can simultaneously measure the light intensity, the degree of linear polarization, and the orientation of linear polarization.

Because in the literature, the spectral modulation is expressed in terms of the degree of polarization and angle of polarization, the Stokes components are embedded into these two terms, and an efficiency and condition number assessment cannot be made starting from the classical approach. The classical expression of the detected intensity (see Eq. 2.26) becomes here (Snik et al., 2009):

$$S(\lambda) = \frac{1}{2}s_0(\lambda) \cdot \left[ 1 \pm DoLP(\lambda) \cos \left( \frac{2\pi\delta(\lambda, T)}{\lambda} + 2 \cdot AoLP(\lambda) \right) \right], \tag{A.15}$$

where  $s_0(\lambda)$  is the detected intensity, which is related to the intensity of the incoming light  $S_0(\lambda)$  through the transmission term,  $t(\lambda)$ ,

$$s_0(\lambda) = S_0(\lambda)t(\lambda). \tag{A.16}$$

The sign from the relation (A.15) is dictated by the orientation of the polarizer (see Fig. A.1),  $DoLP$  is the degree of linear polarization,  $\delta(\lambda, T)$  is the combined retardance of the two multi-order retarders, and  $AoLP(\lambda)$  is the angle of the linear polarization.

The instrument remains a remarkable achievement through its compactness and robustness, if not by the theoretical estimations of the figures of merit, which remains to be done.

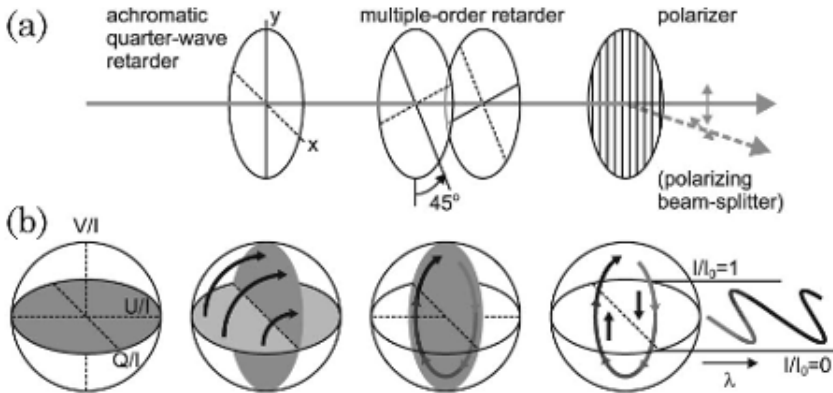


Figure A.1: SPEX schematic setup (a) and working principle (b). The solid lines from (a) correspond to fast axes orientations of the various wave plates. Source: (Snik et al., 2009)

The working principle of the instrument is described in Fig. 3.5. It contains a QWP with the transmission axis vertically oriented, followed by two multi-order wave plates

oriented at  $\pm 45^\circ$  with respect to the *QWP*. In the end, a polarizing beam splitter selects the two orthogonal components of the resulting polarizations and sends them in different directions.

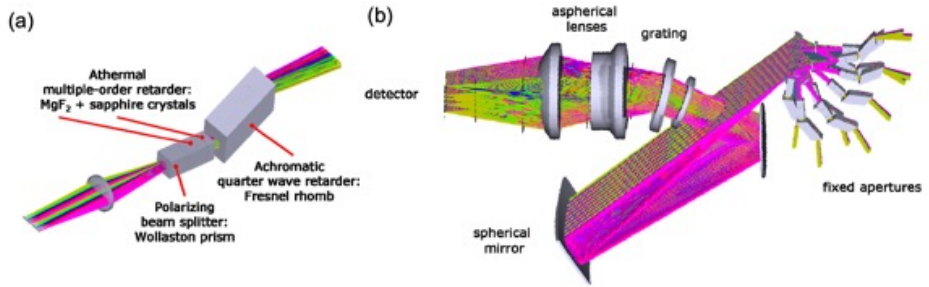


Figure A.2: Optical design of SPEX. Figure a) displays the polarimeter components while b) shows the entire instrument, containing also the spectrometer. Source: (Rietjens et al., 2010)

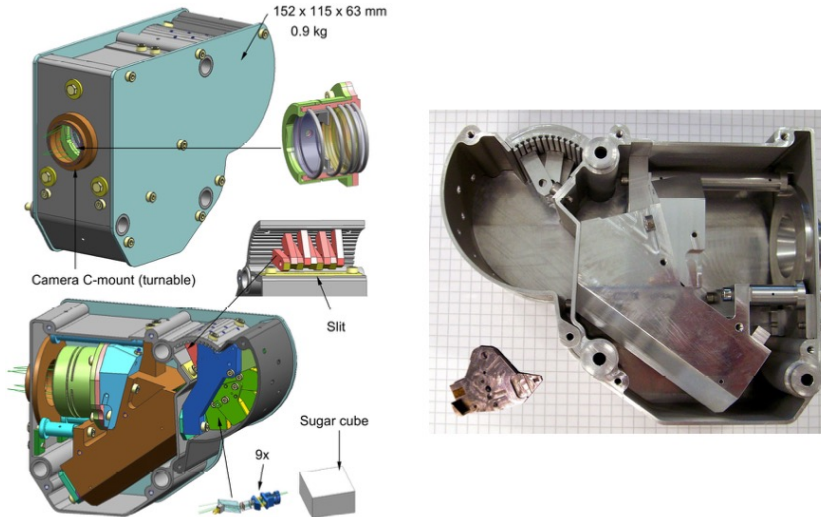


Figure A.3: Mechanical design of SPEX (left) and housing of the prototype (right). Source: (Rietjens et al., 2010)

Thus, the polarized light arriving from the left side is first impacted by the *QWP*. This orientation of the *QWP* facilitates the conversion between circular and  $\pm 45^\circ$  components. An incoming vector  $(S_0, S_1, S_2, S_3)^T$  is converted, ideally, into  $(S_0, S_1, -S_3, S_2)^T$ . Further, the first multi-order wave-plate, oriented at  $45^\circ$ , will leave the  $\pm 45^\circ$  polarization unaffected and alter the horizontal and vertical polarization by converting the circular component into a vertical one. This alteration is a function of the phase difference induced by the wave plate. The second multi-order wave plate will do the same thing as the first one but for the contrary sign. In the end, the polarizing beam splitter will select the

orthogonal components of the resulting vertical-horizontal linear polarizations modulated by the phase terms introduced by the multi-order wave plates. Thus, the intensity detected by the two detectors will depend on the  $S_0$ ,  $S_1$ , and  $S_2$  terms of the incoming light,  $S_1$  and  $S_2$  being spectrally modulated by the phase terms of the wave plates. To cover a large field of view, the instrument uses five viewports, oriented at  $0^\circ$ ,  $\pm 20^\circ$ , and  $\pm 50^\circ$ .

### A.3. OPTICAL PROPERTIES OF MAGNESIUM FLUORIDE

The theoretical simulations carried out in this thesis and the experimental works were based on a magnesium fluoride ( $\text{MgF}_2$ ) modulator. This is a birefringent crystal with a long tradition in polarization-related applications, presenting one of the highest birefringence in the spectral range  $0.13\ \mu\text{m}$ - $0.3\ \mu\text{m}$ . The variation of the refractive index of  $\text{MgF}_2$  with the wavelength can be accurately described by the Sellmeier dispersion formula:

$$n^2 - 1 = \sum_{j=1}^3 \frac{S_j \lambda^2}{\lambda^2 - \lambda_j^2}, \quad (\text{A.17})$$

where  $S_j$  and  $\lambda_j$  are the Sellmeier coefficients, experimentally determined.

According to the investigations carried out by Dodge (Dodge, 1984), for ordinary and extraordinary rays we have:

	O ray	E ray
$S_1$	0.48755108	0.41344023
$S_2$	0.39875031	0.50497499
$S_3$	2.3120353	2.4904862
$\lambda_1$	0.04338408	0.03684262
$\lambda_2$	0.09461442	0.09076162
$\lambda_3$	23.793604	23.771995

Table A.1: Sellmeier coefficients for  $\text{MgF}_2$  at  $19^\circ\text{C}$ . Source: (Dodge, 1984)

The impact of temperature on the refractive index of  $\text{MgF}_2$  was documented by (Tropf and Spie, 1995). Therefore, the Sellmeier coefficients  $S_i$  varies with the temperature like:

$$S_j = \sum_{n=0}^2 S_{j,n} T^n, \quad j = 1, 2, 3 \quad (\text{A.18})$$

The resonance terms  $\lambda_j$  are unaffected by the temperature and remain unchanged. The refractive indices can be computed with the Sellmeier formula using the new values of  $S_j$ .

The transmission of  $\text{MgF}_2$  is about 93% for the range  $0.2\ \mu\text{m}$ - $6\ \mu\text{m}$ . The prisms used by our instrument have a thickness that varies between 1 and 2 mm. From the point of view of transmission, this fact has no remarkable influence, at least in the visible field. As we can see in Fig. A.6, for two windows of 5 and 10 mm, a difference in transmission starts to show only above  $5\ \mu\text{m}$ . As a result, it is not expected to observe a variation in transmission along the vertical direction for the separate prisms studied here in the visible spectral range.

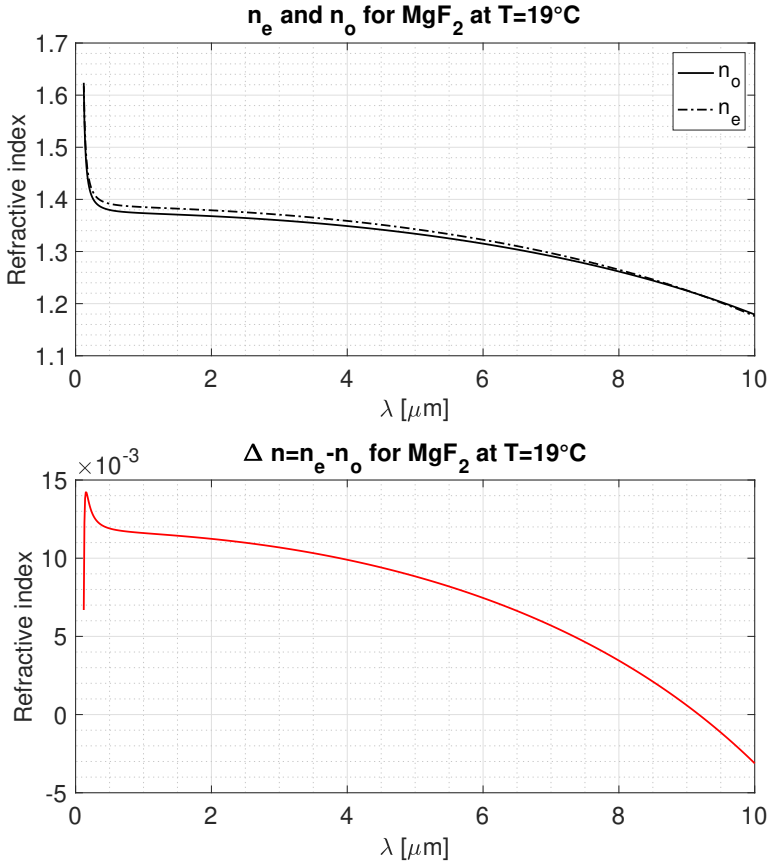


Figure A.4: Variation of the refractive indices of  $MgF_2$  with the wavelength, according to the Sellmeier model with Dodge parameters.

O ray: $93.2K \leq T \leq 473.2K$			
$n$	$S_{1,n}$	$S_{2,n}$	$S_{3,n}$
$n = 0$	0.49948850	0.38552565	2.3187214
$n = 1$	$-2.62692 \cdot 10^{-5}$	$3.30746 \cdot 10^{-5}$	$5.38686 \cdot 10^{-6}$
$n = 2$	$-4.99110 \cdot 10^{-8}$	$4.16987 \cdot 10^{-8}$	$-9.67447 \cdot 10^{-8}$
E ray: $93.2K \leq T \leq 473.2K$			
$n = 0$	0.42381630	0.49372874	2.4974978
$n = 1$	$-1.33435 \cdot 10^{-5}$	$1.87922 \cdot 10^{-5}$	$3.03125 \cdot 10^{-6}$
$n = 2$	$-7.58613 \cdot 10^{-8}$	$6.74060 \cdot 10^{-8}$	$-9.24950 \cdot 10^{-8}$

Table A.2: Sellmeier coefficients for  $n_e$  and  $n_o$  according to Tropf's model (Tropf and Spie, 1995)

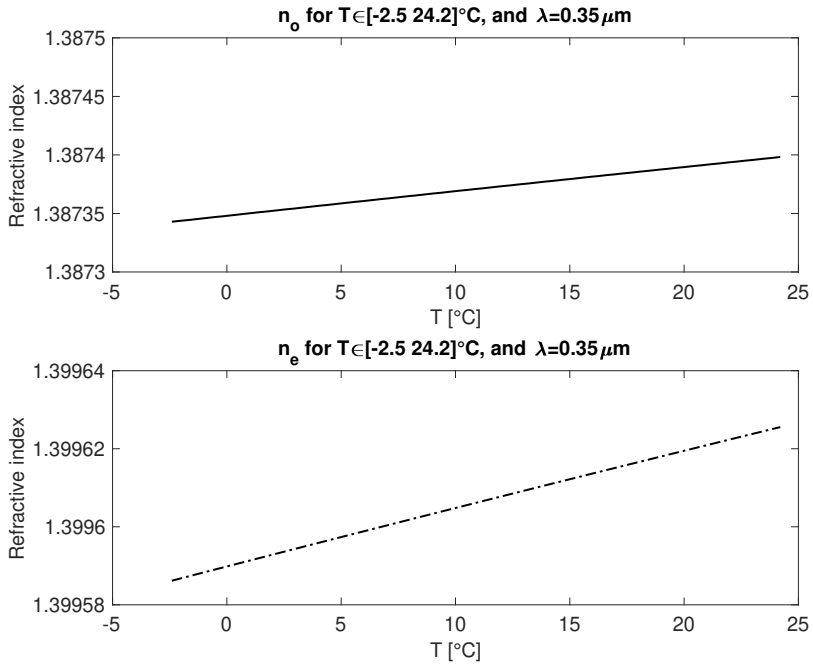


Figure A.5: Variation of the refractive indices of  $\text{MgF}_2$  with the temperature, when  $\lambda = 0.35 \mu\text{m}$ .

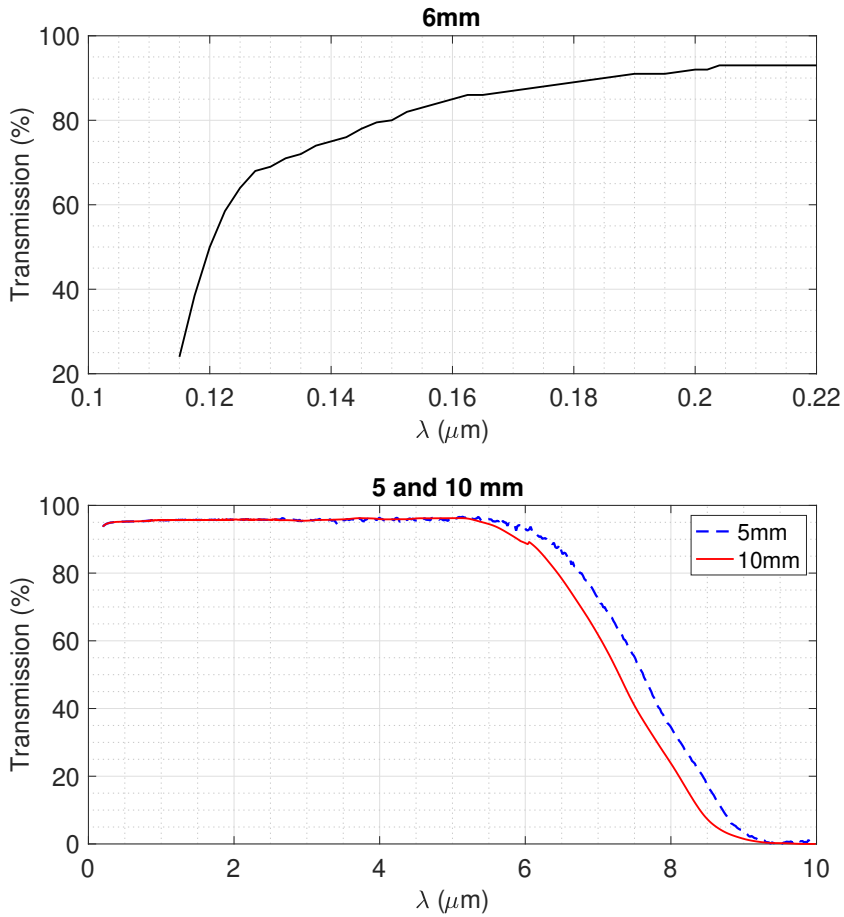


Figure A.6: Transmission of uncoated  $\text{MgF}_2$  for normal incidence. Data for  $0.1 \mu\text{m}$ - $0.22 \mu\text{m}$  interval correspond to a window of 6 mm thickness (Technologies, n.d.), whereas  $0.22 \mu\text{m}$ - $10 \mu\text{m}$  correspond to two thicknesses, 5 and 10 mm (Thorlabs, n.d.).



## A.4. EXPERIMENTAL SETUP: THE MAIN PROPERTIES OF THE OPTICAL COMPONENTS

The optical elements used in the experimental activities were:

- Source of white light
- Collimator (Achromatic doublet AC254-200-A-ML) from Thorlabs
- Filter
- Linear polarizer
- Quarter-wave plate
- Half-wave plate
- Camera

These elements were chosen following a radiometric budget that indicated the flux, transmission, and sensitivity needs.

### THE SOURCE

The light source was laser-driven, model EQ-99X-FC LDLS, from HAMAMATSU.



Figure A.7: The source of white light. Copyright ©2018 Energetiq Technology Inc.

This source is quite stable in the visible domain, delivering a power close to the maximum. Most of the measurements conducted in the experimental part used wavelengths of 515 nm and 633 nm, where the source emits between  $80 \mu\text{W}/\text{nm}$  and  $95 \mu\text{W}/\text{nm}$ .

Regarding the temporal stability of the source, the tests carried out for a maximum duration of four hours, using an integration time of 23 ms and a number of five frames, showed a variation of approximately 0.17% of the signal.

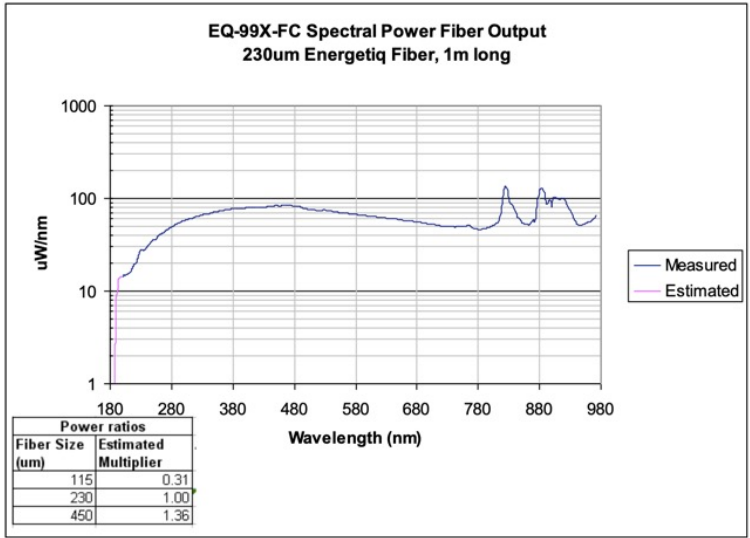


Figure A.8: Typical output spectrum of the source. Copyright ©2018 Energetiq Technology Inc.

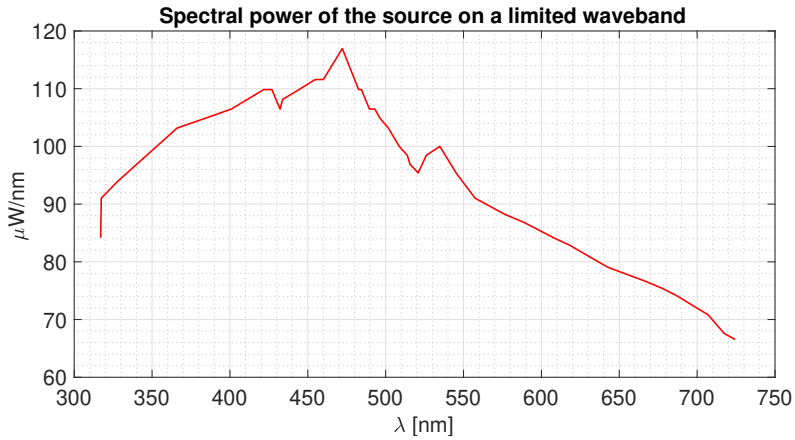


Figure A.9: Power output between 317 nm-724 nm based on the general output of the source presented in Fig.A.7.

### THE COLLIMATOR

The collimator used in the optical setup was an achromatic doublet AC254-200-A-ML from Thorlabs, with a focal length of 200 mm and 1-inch diameter.

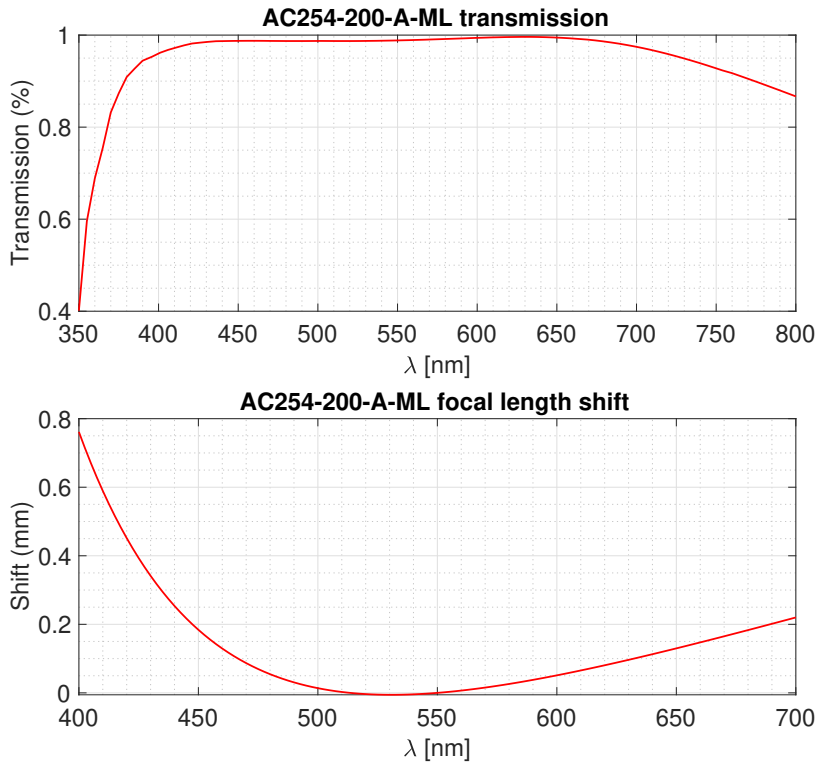


Figure A.10: Transmission and focal shift of the achromatic lens as a function of the wavelength. Data source: Thorlabs

## FILTERS

Two filters mainly were used during the laboratory tests and measurements: a hard-coated bandpass filter of central wavelength (CW) 514.5 nm and full width at half maximum (FWHM) 3nm, and another one of CW 633 nm and FWHM 3nm. The transmission of these two filters is illustrated in Fig. A.11.

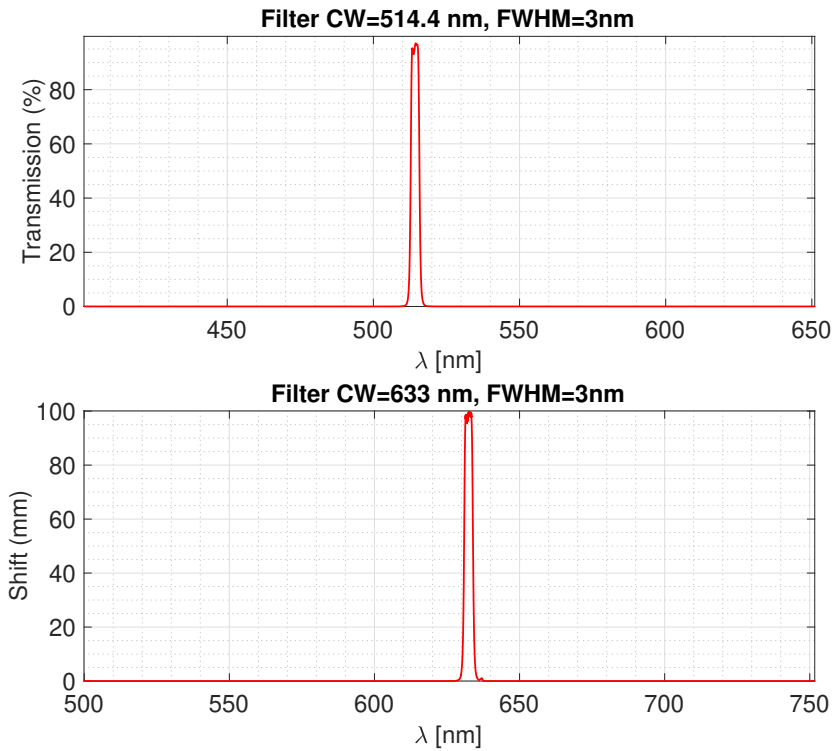


Figure A.11: Transmission of the two filters used in the experimental setup. Data source: Thorlabs.

### THE LINEAR POLARIZER

The polarizers used here were two ultra-broadband wire grid linear polarizers from Edmund Optics. These components' transmission and contrast ratios are presented in Fig. A.12. The polarizers can be on a very large spectral band, spanning from 300 nm to 3200 nm. In addition, they have a large angle of acceptance without depolarization ( $\pm 20^\circ$ ).

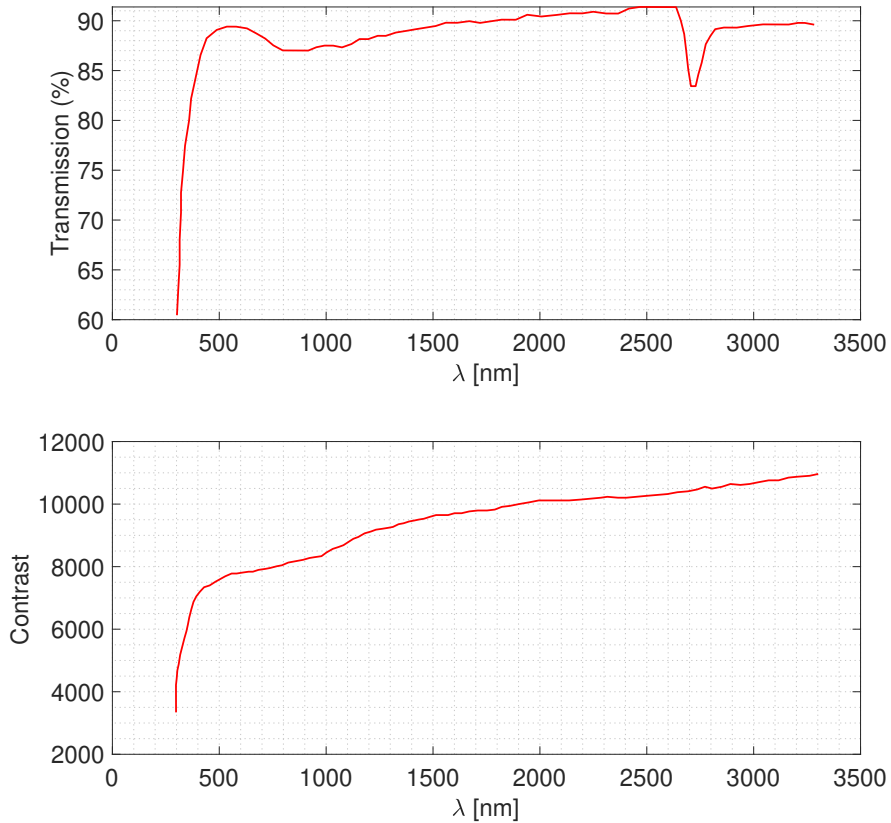


Figure A.12: Transmission and contrast ratio of the polarizers. Data source: Edmund Optics.

THE QUARTER-WAVE PLATE

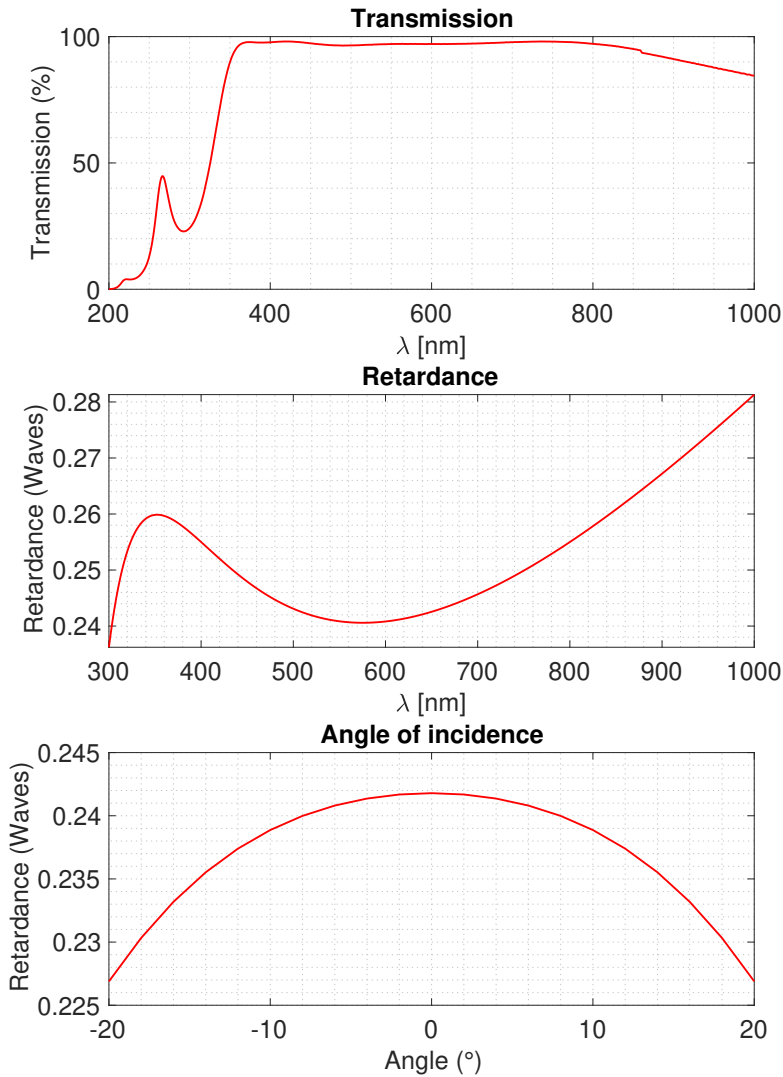


Figure A.13: Transmission, retardance, and impact of the angle of incidence for the achromatic QWP. Data source: Thorlabs.

A critical component of the optical setup was the quarter-wave plate. We used a mounted achromatic quarter-wave plate (AQWP10M-580) from Thorlabs, with a retardance accu-

racy of  $\lambda/300$ . The main properties of this optical element are summarized in Fig. A.13.

### THE CAMERA

The last component placed in the stream of light was the camera. This was a BFS-U3-123S6M-C USB 3.1 Blackfly S Monochrome Camera from FLIR. It has a resolution of 12.3 megapixels ( $4096 \times 3000$ ), and a pixel size  $3.45 \mu\text{m} \times 3.45 \mu\text{m}$ . The sensing area has  $14.3 \text{ mm} \times 10.35 \text{ mm}$ , and the frame rate is 30 fps. The exposure time can be set between  $10 \mu\text{s}$  and 30 s.

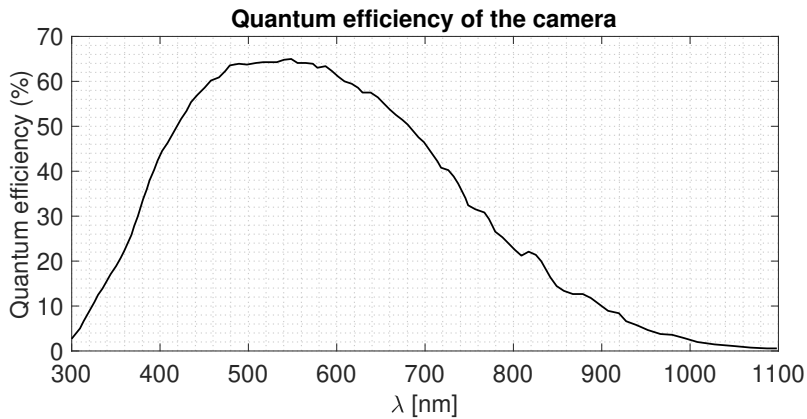


Figure A.14: Quantum efficiency and camera spectral response. Data source: <http://softwareservices.flir.com>

The detector quantum efficiency and spectral response are presented in Fig. A.14. For the wavelengths used during the laboratory measurements, 514.5 nm and 633 nm, the quantum efficiency is close to the maximum value.

# BIBLIOGRAPHY

- Collett, E. (2005). *Field guide to polarization*. SPIE. <https://doi.org/10.1117/3.626141>
- Dodge, M. J. (1984). Refractive properties of magnesium fluoride. *Applied Optics*, 23(12), 1980. <https://doi.org/10.1364/AO.23.001980>
- Hecht, E. (2017). *Optics* (5 ed). Pearson Education, Inc.
- NASA. (2024). *SPEXone polarimeter*. Retrieved October 6, 2024, from <https://pace.ocean-sciences.org/spexone.cgi>
- Rietjens, J. H. H., Snik, F., Stam, D. M., Smit, J. M., van Harten, G., Keller, C. U., Verlaan, A. L., & Laan, E. C. (2010). SPEX: THE SPECTROPOLARIMETER FOR PLANETARY EXPLORATION. *International Conference on Space Optics*. <https://doi.org/10.1117/12.2309231>
- Snik, F., Karalidi, T., & Keller, C. U. (2009). Spectral modulation for full linear polarimetry. *Applied Optics*, 48(7), 1337. <https://doi.org/10.1364/AO.48.001337>
- Technologies, A. (n.d.). *Magnesium fluoride: MgF2 windows and mgf2 lenses*. <https://www.alkor.net/MgF2.html> (accessed: 26.06.2024).
- Thorlabs. (n.d.). *Magnesium fluoride windows*. [https://www.thorlabs.com/NewGroupPage9.cfm?ObjectGroup\\_ID=5582](https://www.thorlabs.com/NewGroupPage9.cfm?ObjectGroup_ID=5582) (accessed: 26.06.2024).
- Tropf, W. J., & Spie, M. (1995). Temperature-dependent refractive index models for BaF<sub>2</sub>, CaF<sub>2</sub>, MgF<sub>2</sub>, SrF<sub>2</sub>, LiF, NaF, KCl, ZnS, and ZnSe. *Optical Engineering*, 34(5), 1369–1373. <https://doi.org/10.1117/12.201666>





# ACKNOWLEDGEMENTS

This work would not have been possible without continuous support from my family, promoters, supervisor, and colleagues. It was a complex course that navigated countless obstacles that were not among the easiest. The financing difficulties we faced at the beginning of the activity, the outbreak of the COVID-19 pandemic that reshaped our collaboration, and the transfer from the University of Liege to the Delft University of Technology (TU Delft) are just a few examples of these obstacles.

First, my gratitude goes to my promotor, Pieter Visser. He is the one who allowed me to continue the PhD project at TU Delft and to bring this research to a successful end. His help came at a critical moment when the continuation of the entire activity was in doubt due to financing difficulties.

The guidance my promotor, Jerome Loicq, provided, which allowed me to find a way through all these obstacles, is invaluable. Words can hardly express the gratitude I have for him. He never stopped believing in this project and the importance of our results, and he spared no effort to overcome the difficulties encountered. In addition, his clear vision of our project and constructive spirit helped me find a way forward when all the information became overwhelming or, on the contrary, seemed to lead to a dead end.

I have the same gratitude for my co-promotor, Pierre Piron. His tireless attention to detail, his experimental skills, and his competencies in polarimetry have helped me countless times to advance in research and practical implementation.

I want to thank Serge Habraken, my optics professor during college and master's, who, for a short time, also played the role of the promotor for the PhD. He is the one who opened my appetite for optics and space engineering and who offered me all the support during the period of the activity carried out within the Centre Spatial de Liège. Without him, none of this would have been possible.

I also have complete gratitude for the support, interest, and openness shown by TNO, our closest collaborator on this adventure. Their willingness to invest considerably financially and in person to transform our ideas into reality is a wonderful reason for joy and satisfaction. It is the first proof that our work matters and can be helpful. At the same time, it is the first door open to countless opportunities for learning, discovery, and innovation in spectropolarimetry.

In addition, I would like to thank my good friend, Colin Dandumont. Our small daily discussions from the period of activity at the Space Center in Liège brought an extra charm to my PhD, which I will always miss.

Last but not least, I am grateful to my wife for all her support and understanding. She has been by my side continuously all these years, putting behind me, most of the time, the difficulties of raising two small children. She was also a tireless listener. Countless times, she listened to all the arguments behind this research's most complex and arid calculations and not a few times did she help me identify the right path to follow.



# CURRICULUM VITÆ

## **Bogdan VASILESCU**

Bogdan Vasilescu was born in Craiova, Romania, in 1981. He was passionate about as much knowledge as possible, so he graduated for the first time from the Faculty of Philosophy of Babeş-Bolyai University (Cluj-Napoca, Romania) in 2004.

After several years of mass media and communication activity, he returned to his first love: Physics. He graduated from the Faculty of Physics of the University of Liège (Belgium) in 2019. Later, he followed a master's degree in Space Sciences at the same university.

Attracted by optics and its applications in space, he started a PhD in February 2019 at the University of Liège/Liège Space Center.

In parallel with the doctoral research, between April 2021 and July 2022, he also worked as an assistant in optics for the Space Center in Liège. It was an excellent opportunity to come into close contact with the world of space instruments. He was thus involved in the calibration of optical instruments (e.g., the SALTO project) and the analysis of key data parameters (KDP) for the 3MI instrument, part of ESA's Fluorescence Explorer (FLEX) project.

In July 2022, he transferred his PhD work to Delft University of Technology (TU Delft). In September 2024, he started a postdoctoral position at TU Delft, intending to refine the new polarization measurement method validated during his PhD.



# LIST OF PUBLICATIONS

## JOURNAL PAPERS

2. **Vasilescu, B.**, Piron, P., Loicq, J., *Performance analysis of a spectropolarimeter employing a continuous phase variation*, Optics Express, 31.13 (June.19, 2023), [10.1364/OE.487335](#).
1. **Vasilescu, B.**, Nazé, Loicq, J., *Solution uniqueness and noise impact in a static spectropolarimeter based on birefringent prisms for full Stokes parameter retrieval*, Journal of Astronomical Telescopes, Instruments, and Systems, 6.2 (Apr.23, 2020), [10.1117/1.JATIS.6.2.028001](#).

## CONFERENCE PAPAERS

3. **Vasilescu, B.**, Piron, P., Veenstra, A., Snel, R., Di Iorio, E., Ouellet, M., Chavet, Q., Ferrario, I., Loicq, J., *Experimental validation of a full Stokes spectropolarimeter for space applications*, Space Telescopes and Instrumentation 2024: Optical, Infrared, and Millimeter Wave (Proceedings of SPIE; Vol. 13092), Ed. by L. E. Coyle, S. Mat-suura, M. D. Perrin, [10.1117/12.3018645](#).
2. **Vasilescu, B.**, Nazé, Y., Rauw, G, Kintziger, C., Loicq, J., *Development of a space spectropolarimeter for full Stokes parameters retrieval*, Proc. SPIE 11852, International Conference on Space Optics — ICSO 2020, 118522J (11 June 2021), [10.1117/12.2599427](#).
1. **Vasilescu, B.**, Nazé, Loicq, J., *Development of a space spectropolarimeter for full Stokes parameters retrieval*, Proc. SPIE 11451, Advances in Optical and Mechanical Technologies for Telescopes and Instrumentation IV, 114513V (13 December 2020), [10.1117/12.2562102](#).

## ADDITIONAL PUBLICATIONS

1. Snel, R.C.,**Vasilescu, B.**, Di Iorio, E., Piron, P., Loicq, J., Ferrario, I., Silvestri, F., *Spectropolarimetry for space object identification*, Electro-optical and Infrared Systems: Technology and Applications XX, SPIE, 2023 ISBN: 978-1-5106-6703-7.